Quantum Metrology with a Molecular Lattice Clock and State-Selected Photodissociation of Ultracold Molecules

Chih-Hsi Lee

Submitted in partial fulfillment of the
requirements for the degree
of Doctor of Philosophy
in the Graduate School of Arts and Sciences

COLUMBIA UNIVERSITY

2020

ABSTRACT

Quantum Metrology with a Molecular Lattice Clock and State-Selected Photodissociation of Ultracold Molecules

Chih-Hsi Lee

Over the past few decades, rapid development of laser cooling techniques and narrow-linewidth lasers have allowed atom-based quantum clocks to achieve unprecedented precision. Techniques originally developed for atomic clocks can be extended to ultracold molecules, with applications ranging from quantum-state-controlled ultracold chemistry to searches for new physics. Because of the richness of molecular structure, quantum metrology based on molecules provides possibilities for testing physics that is beyond the scope of traditional atomic clocks.

This thesis presents the work performed to establish a state-of-the-art quantum clock based on ultracold molecules. The molecular clock is based on a frequency difference between two vibrational levels in the electronic ground state of $^{88}Sr_2$ diatomic molecules. Such a clock allows us test molecular QED, improve constraints on nanometer-scale gravity, and potentially provide a model-independent test of temporal variations of the proton-electron mass ratio. Trap-insensitive spectroscopy is crucial for extending coherent molecule-light interactions and achieving a high quality factor Q. We have demonstrated a *magic wavelength* technique for molecules by manipulating the optical lattice frequency near narrow polarizability resonances. This general technique allows us to increase the coherence time to tens of ms, an improvement of a factor of several thousand, and to narrow the linewidth of a 25 THz vibrational transition initially to 30 Hz. This width corresponds to the quality factor $Q = 8 \times 10^{11}$.

Besides the molecular quantum metrology, investigations of novel phenomena in state-selected photodissociation are also described in this thesis, including magnetic-field control of photodissociation and observation of the crossover from ultracold to quasiclassical chemistry.

Contents

List of Figures

List of Tables

Acknowledgments

I came to Columbia in the Fall of 2014. Now, five and a half years later, I felt so grateful for these incredible years and appreciated the opportunity to explore the exciting world of molecules. The journey in the Ph.D. studies is full of excitements, joys, and of course challenges. I would like to express my deepest gratitude to those who support me, encourage me, and accompany me along the way.

Firstly, I would like to give special thanks to my supervisor, Prof. Tanya Zelevinsky, for giving me the opportunity to work on the Sr experiment. Her wisdom and knowledge have led the experiment in the right direction. What I have learned from her is not only physics behind the experiment but also how to think as a scholar and a scientist. It is a truly precious experience working in her group. Thank you, Tanya.

The work in this thesis would not be possible without the corporation of the great team members. Dr. Stanimir Kondov joined the team as a postdoc in December 2016. We have done so many things together. We recovered the experiment from its breakdown in 2016. Also we took and analyzed a huge amount of data for photodissociation and molecular clock. I will never forget how exciting the moment it was when we found the first deeply bound ground state in March 2017. His knowledge of physics and optics has made the progress of molecular much smoother.

Kon Leung joined the team in August 2017 as a graduate student. His join strengthens the workforce of the team. Ever since he joined, he has been putting a lot of endeavor to the experiment. The experimental system upgrades wouldn't go so smoothly without him. I am very grateful to have Kon as my successor. With his knowledge and enthusiasm, I am sure he will lead to experiment to the next exciting level.

Christian Leidl, a visiting Master student from Germany, joined the group in June 2017. His efforts in building the lock system for the 780 nm cavity made the construction of the new generation master laser system a lot easier. Also, his endeavor in diagnosing the frequency comb helped elucidate the issue with frequency instability.

Dr. Hendrik Bekker joined the team as a postdoc in May 2019. He's been working on modeling the optical lattice spectrum with numerical methods. His model shines light on

the perplexing problem with clock state lifetime, which is of crucial importance for future development of the molecular clock. Also, he has been putting great efforts in helping figure out the lasting issue with the 780 nm laser system.

Emily Tiberi joined the group in November 2018. As a junior graduate student, she has done a great job of absorbing the knowledge on every inch of the experiment. Learning the setup of a metrology experiment is never easy and I am sure with her dedication and hard work, she will make excellent contributions to the experiment.

Many thanks go to Prof. Moszyński and his student Iwona Majewska for the wonderful collaboration. The weekly Skype meetings with them have been very insightful and helpful. The Sr experiment wouldn't have gone so smoothly without their inputs from the theory side.

Apart from my contemporaries, I would also like to thank my predecessors, Dr. Bart McGuyer and Dr. Mickey McDonald. They were the postdoc and senior graduate student working on the Sr experiment when I joined the group. Many thanks to them for leading me into the experiment. Their enthusiasm has inspired me a lot in the years of my graduate study.

I would also like to thank Dr. Gael Reinaudi, the first postdoc in the ZLab. I appreciate so much his kindness to visit when the experiment was down because of the shutter issue. His advice was very valuable and helpful for us to overcome the hard time. Besides, I also want to thank him for assisting transferring the lab control software to the new computer, which has facilitated the data-taking a lot.

Mentioning the shutter breakdown, I want to express my sincere thanks to Dr. Geoffrey Iwata and Rees McNally for giving me hands during the difficult time. Their knowledge and expertise in vacuum system have help avoiding many serious mistakes that I could have made without them.

Thank you all the ZLab members, Dr. Ivan Kozyryev, Konrad Wenz, Rees McNally, Mick Aitken, Sebastian Vazquez-Carson, Qi Sun for making the lab an incredibly pleasant place to work. Also, I would like to thank all of them for their cooperation to make the lab *A Quiet Place* when we were taking data. I know how ridiculous this request was but to keep all fourteen lasers in our experiment locked we really had no choice. I appreciate from the bottom of my heart for your understanding.

Thank you so much to my parents and my sister. Their unconditional love and support have always instilled me with confidence and driven me to pursue my goals. I can't describe in words how fortunate and grateful I feel to have you as my family.

I would also like to thank my lovely girlfriend, Liqiaonan Chen, for her love, accompany and encouragement. I appreciate her patience when I share both exciting and difficult moments in the lab.

Thank you my best friends in the physics department, Yihang Zeng, Shaowen Chen, and Qiang Han. The past five and half years wouldn't have been so joyful and colorful without your friendship.

I also want to thank all my friends. It's you that make my life in New York City so exciting.

To my family

Chapter 1

Introduction

1.1 Molecular lattice clock

A molecular lattice clock is a unique tool for precision measurements and fundamental physics test. Compared to atoms, which are governed purely by electronic interactions, molecules have additional internal degrees of freedom, resulting in richer spectra. Besides electronic interactions, nuclear dynamics of constituent atoms defines the molecular ro-vibrational structure, which makes molecule a special tool to test physics that is beyond the scope of current atomic lattice clocks [1, 2].

Over the past few decades atomic lattice clocks have undergone tremendous developments and are currently the most accurate timekeeping instruments. As of December 2019, the cutting-edge atomic clock exhibits relative precision of 2.5×10^{-19} [3], meaning that it would gain or lose no more than a second over the age of the universe. With this stability not only can it serve as a primary time standard, it also has a wide range of industrial applications and unique scientific importance.

Techniques originally developed for atomic clocks can be extended to ultracold molecules, with applications ranging from quantum-state-controlled ultracold chemistry [4–6] to searches

for new physics. In 2008 a molecule-based clock based on atomic clock techniques was proposed [7]. In this thesis I will discuss the first results with this type of clock. This work confirms the feasibility of the original proposal and lays down the foundation for further measurements including probing the drift of fundamental constants and testing the Standard Model.

1.1.1 What is a molecular clock and why is it interesting?

For a device to be claimed as a clock, it must possess two fundamental features. First, it needs to be highly precise. In other words, a clock must be based on a consistently robust and stable resonator. Quality factor (Q factor) is a good way to define stability. For a experiment that measures a frequency f with uncertainty δf the Q factor is defined to be

$$Q = \frac{f}{\delta f} \tag{1.1}$$

High Q factors have been demonstrated in many experiments. For instance, $Q = 5.2 \times 10^{15}$ has been achieved in atomic lattice clock and $Q > 10^{13}$ [10] has been realized in a molecular experiment. In our molecular clock $Q > 10^{11}$ has been demonstrated [9]. This is not the fundamental precision limitation. Higher quality factors can be obtained by reducing environmental perturbations and improving the spectra of critical lasers. A major part of this thesis will be devoted to discussing the attempts to push the precision of the molecular clock to the next era.

Second, a clock must be accurate, meaning that the measurement should be unbiased. In this thesis we also discuss the leading factors that cause measurement bias in our molecular lattice clock and how we tackle them.

So what is a molecular clock? How does it work? The molecular clock described in

this thesis is based on ultracold $^{88}Sr_2$ molecules trapped in an one-dimensional (1D) optical lattice. The heart of the clock consists of two different states in the molecular ground state potential. $^{88}Sr_2$ electronic ground states have lifetimes that are as long as a million years. Because of the longevity of the states an optical transfer between ground states forms an excellent clock resonator. Specifically, a high precision measurement of the relative binding energy of ground states is achieved via a two-photon Raman spectroscopy, depicted in Figure 1.1. Because of the long lifetimes, the natural linewidth of this Raman transition is essentially zero.

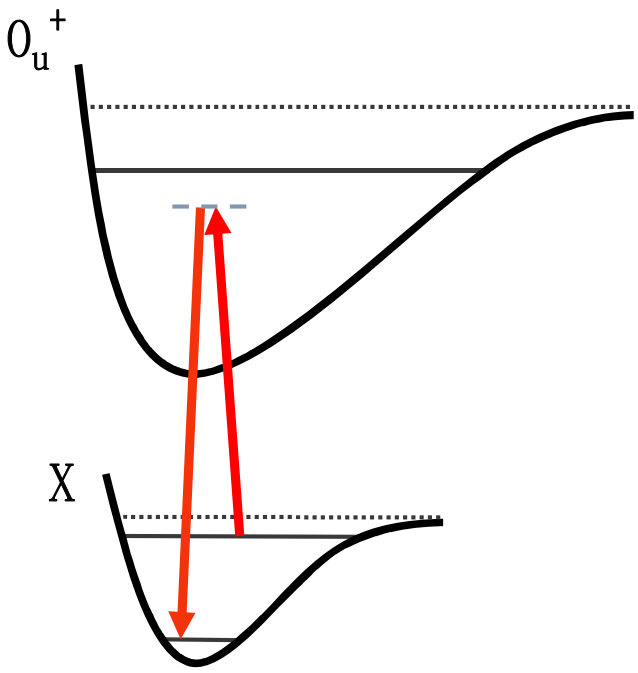

Figure 1.1: Precise measurement on relative binding energies in the ground state potential is carried out using two-photon Raman spectroscopy. A laser connecting the least bound ground state off-resonantly to an electronic excited state is shined on the molecules together with another laser connecting the deeply bound ground state to the excited state. If both lasers are detuned from the excited state by same amount, a two-photon coherent transition is driven and the molecules are transferred back and forth between the two ground states.

So what can we do with a molecular clock? Why do we need it if atomic clock is already very good? As mentioned earlier, molecules have a richer energy structure, which enables a molecular clock to probe new physics. With our molecular lattice clock, there are two aspects of physics that we are eager to test: probing the temporal drift of the proton-electron mass ratio and searching for a possible fifth force beyond the Standard Model.

1.1.2 Temporal drift of the proton-electron mass ratio

Precision measurement of ground state binding energies of the $^{88}Sr_2$ molecules reveals the possibility to test the temporal drift of the proton-electron mass ratio μ. Molecular vibrational energies are μ-dependent. Moreover, the dependence is stronger in the middle of the potential while it drops toward the top and bottom, as shown in Figure 1.2. Because of this varying dependence, $\dot{\mu}$ can be probed with precision measurements on *the relative binding energy between ground states*. If the drift of the relative energy is observed, a conclusion supporting a non-zero mass ratio drift can be drawn.

The varying dependency of binding energies on μ can be understood in the perturbed simple harmonic oscillator model. In a simple harmonic oscillator, the ground state binding energies corrected by the first-order perturbation are given by

$$E_\nu = \omega(\nu + \frac{1}{2}) - \chi_e\omega(\nu + \frac{1}{2})^2, \tag{1.2}$$

where ω is the vibrational constant, χ_e is the anharmonicity constant and ν is the vibrational level. The dependence of molecular parameters on μ has been well-known for decades [11]. In Equation 1.2, ω scales with $\mu^{-1/2}$ and $\chi_e\omega$ scales with μ^{-1}. These lead to the expression of the energy levels' μ dependence

$$\mu\frac{\partial E_\nu}{\partial \mu} = -\frac{1}{2}\omega(\nu+\frac{1}{2}) + \chi_e\omega(\nu+\frac{1}{2})^2 \tag{1.3}$$

The varying dependency of energy levels on μ is indicated from Equation 1.3. In the bottom of the potential where ν's are small, the μ dependency is dominated by the first term and thus the dependency increases with ν. As ν keeps growing, the second term increases and gradually offsets the effect from the first term. This reverts the increasing trend into a decaying trend, which makes the energy levels close to the potential threshold μ insensitive.

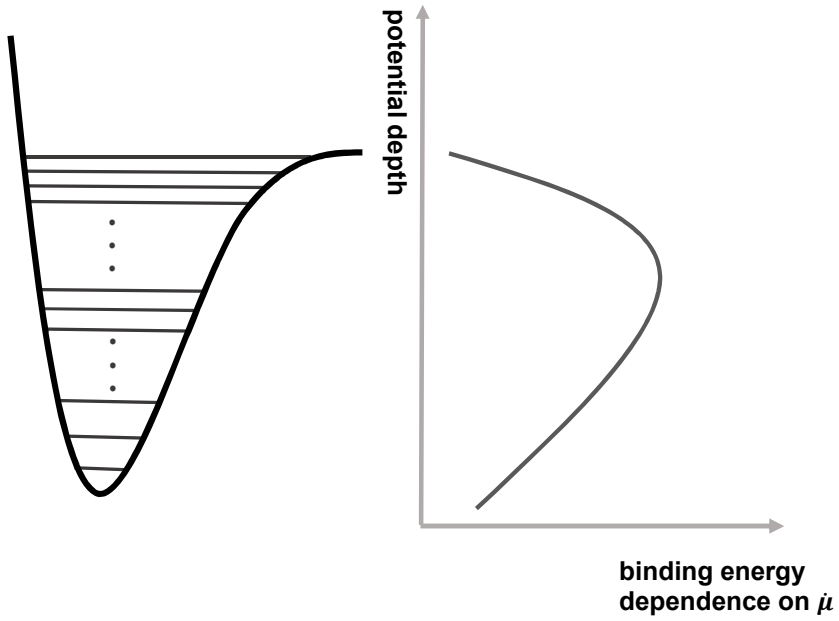

Figure 1.2: In the $^{88}Sr_2$ ground state potential, each state's binding energy has different sensitivity to $\dot{\mu}$. The sensitivity is weaker for shallow and deeply bound states than for intermediately-bound states. In consequence, if the proton-electron mass ratio changes, the relative binding energy from the middle of the potential will drift more than states from the top and bottom. Therefore by comparing the drift rate of binding energies we can probe the change rate of the mass ratio.

Moreover, it is worth noting that Equation 1.3 relates the sensitivity to the fractional change in the mass ratio to the fractional transition frequency uncertainty, $\delta\mu/\mu \sim \delta f/f$. Given that $^{88}Sr_2$ ground state potential is 30 THz deep, assuming a power broadened linewidth of 10 Hz and a signal to noise ratio of 100 would indicate a fractional uncertainty of $\sim 5 \times 10^{-15}/\sqrt{\tau}$ for testing $\dot{\mu}$, where τ is the integration time in seconds.

1.1.3 Searching for a fifth force

Apart from testing fundamental constants, molecular lattice clock also opens up the possibility for probing physics beyond the Standard Model. In the framework of the Standard Model, the nature of physics is formed with four fundamental interactions: gravitational, electromagnetic, strong nuclear and weak nuclear forces. Instead of these four interactions, modern theories have proposed the existence of a mass-dependent fifth force since mysteries such as dark energy and dark matter remain unsolved. With the molecular clock, precision measurements of Sr_2 ground state binding energies can serve as a platform for constraining the fifth force.

A molecular potential can be described by Born-Oppenheimer approximation

$$E_{\text{total}} \approx E_{\text{ele}} + E_{\text{vib}} + E_{\text{rot}} \tag{1.4}$$

where the total energy is the sum of the electronic, vibrational, and rotational interactions. Usually Equation 1.4 yields high enough precision but in order to search for the fifth force all the other contributions from the Standard Model need to be included. Table 1.1 lists the higher-order correction terms that are beyond the Born-Oppenheimer approximation.

How can we use a molecular clock to probe an unknown mass-dependent force? Of course we can measure binding energies with a single clock extremely precisely and compare

the results with *ab initio* calculations. On the experimental side this is not a problem. However, this would cause a lot of hassles on theory calculations. At molecular scale, the energy spectra are overwhelmed by mass-independent electromagnetic forces. It is therefore very hard to reproduce the binding energies accurately by theory alone. Fortunately there is another way to do it, which is to compare binding energies in molecules consisting of different strontium isotopes. Because the electronic structure is identical among the isotope family, mass-independent contributions can be canceled out by comparing different molecules so that the model will only be sensitive to mass-dependent contributions. To refrain from cooling fermion isotopes with nonzero nuclear spin, we focus on molecules based on bosonic isotopes. Strontium has three stable bosonic isotopes, i.e. ^{84}Sr, ^{86}Sr and ^{88}Sr, from which six different molecular clocks can be constructed. With ground state binding energies precisely measured for all six clocks, we can use part of the data to fit the quantum chemistry model and use the other to test the model. Any inconsistency from the fitting could imply the existence of a fifth force.

contribution	magnitude	effect on transition linewidth
adiabatic	$\mu = \mathrm{m}_e/\mathrm{m}_p$	$< 10^8$ Hz
nonadiabatic	μ^2	$< 10^3$ Hz
relativistic	$\alpha^2\mu$	$< 10^4$ Hz
QED	$\alpha^3\mu$	$< 10^2$ Hz
finite nuclear-size	$(r_c/a_0)^2$	$< 10^6$ Hz
higher order	$\alpha^4\mu$	< 10 Hz

Table 1.1: By comparing binding energies of ground states from molecular clocks of different isotopic mass we can preclude the effects from mass-independent contributions. Fitting molecular clocks based on different isotopes could reveal the existence of a fifth force.

1.1.4 Steps toward a molecular lattice clock

In this thesis the progress of constructing a molecular clock is presented in Chapters 2 to 7. A brief overview on what's covered in each chapter is provided below.

Molecular structure and experiment overview (Chapter 2) The structural features of $^{88}Sr_2$ molecules are governed by electronic, vibrational and rotational dynamics. Moreover, quantum statistics imposes certain restrictions on allowed quantum states. The experiments described in this thesis heavily rely on the optical transitions between bound states in different molecular potentials and therefore the knowledge in the molecular structure is crucial for interpreting the experimental results.

Performing spectroscopy on ultracold molecules is the key for achieving high-precision measurements. In our experiment ultracold $^{88}Sr_2$ molecules are produced from laser cooled Sr atoms via photoassociation. In order to achieve Doppler- and recoil-free spectroscopy the molecules are confined in a one-dimensional optical lattice trap. I will give a summary of laser cooling and trapping schemes used in our experiment as well as the methods for detecting and imaging the molecules.

Finally, a summary of the metrological equipment will be provided. It includes a frequency standard and a frequency comb. A stable frequency standard necessary for referencing the frequency components in the experiment and a frequency comb is required in the molecular clock to achieve a coherent clock transition. Because our comb is an older commercial model, it has a problem with a loosely-locked carrier-envelope offset frequency. To cope with this, special care has to be taken when performing phase locks with the comb. This knowledge is important for maintaining a good clock coherence.

Search for deeply bound molecular states (Chapter 3) The molecular clock operates on a frequency difference between two ground states. Therefore, the first challenge in building such a clock is to locate these states. Because of the sparsity of states, an efficient search method has to be adopted. To facilitate the search, a method based on Autler-Townes spectroscopy is applied. I will demonstrate that, with this method, we have precisely pinned down the location of five deeply bound ground states. This is a universal method which can be applied to the search for all the other ground states.

Implementation of a magic lattice trap (Chapter 4) To achieve long clock transition coherence, the clock state trap depths need to be matched. Because the $^{88}Sr_2$ ground state potential is over 30 THz deep, the clock state polarizabilities difference is inherently large. To compensate for this, the *magic wavelength technique* is developed. With the lattice laser tuned close to a lattice-driven transition, the polarizability of one of the clock states can be tuned to match the polarizability of the other clock state. When the polarizabilities are matched, the clock coherence is enhanced by several thousandfold and a 30 Hz transition linewidth is observed. Besides, direct one-photon spectroscopy on deeply bound excited states is performed, which corroborates the binding energy measurements of lattice-driven transition resonances.

Molecular clock stabilization and systematics (Chapter 5) To further increase the clock coherence, noise in the experimental system needs to be reduced. This includes the environmental noise in the lab, the noise in the master laser frequency, the noise in the laser spectra, probe laser intensity fluctuations, etc. I will explain how these noise sources affect the clock coherence and demonstrate the efforts to tackle them. With the noise greatly reduced, the precise determination of ground state binding energy becomes tenable. An example with a 25 THz deeply bound ground state will be provided.

Unexpected limits on clock state lifetime (Chapter 6) Even with all the efforts in reducing the experimental noise, the observed clock state lifetime is much shorter than what is expected. To explain the anomalous lifetime, I will discuss several ideas, including underestimation of lifetime from theory, accidental multi-photon scattering, and impurity of the lattice light spectrum. Systematic tests of clock state lifetime based on these ideas will be demonstrated. The most recent investigation has indicated that the culprit is likely the lattice light noise, which will be discussed in detail.

Measurements of dipole moments squared (DMS) (Chapter 7) The techniques developed for the molecular clock can be extended to measure transition strengths. I will demonstrate how these measurements are carried out. Knowledge in the transition strengths is important for carrying our more precise clock measurements. Also, well-measured transition strengths can be adapted to calibrate the molecular model, which would help point us toward the future directions of the molecular clock.

1.2 Ultracold photodissociation and quantum chemistry

In my first two and a half years at ZLab, I worked on another topic of ultracold strontium molecules, which was involved mysteries of state-selected photodissociation. When I joined ZLab in 2014, the Sr group was on an exciting journey of exploring ultracold strontium molecule photodissociation. This is the first experiment in the world that could perform dissociation of an *arbitrary* quantum state and reveal the molecular structure. The results were published in *Nature* [4]. I am honored to be part of the work not only because it improves the understanding of quantum-chemistry behavior but also because I had a chance to investigate and understand phenomena that couldn't be well explained by my predecessors. In this thesis, I discuss the solutions to these mysteries which make the story of quantum-

state-selected photodissociation complete.

Before describing the mysteries, here is a brief introduction to photodissociation. Photodissociation is a tool developed by chemists in the 1960's to study molecular structure by breaking the molecules with photons. Since its early stage of development, the *quasiclassical formula* has been suggested to describe the angular distributions of the fragments from diatomic molecule photodissociation [58–60]. In this approach the angular distribution is constructed by multiplying the conventional dipolar distribution [61, 62] for molecules prepared in spherically symmetric states or ensembles, $I(\theta) \propto 1 + \beta_{20} P_2^0(\cos\chi)$, by a probability density $|\Phi_i|^2$ of the initial molecular axis orientation, which gives

$$I(\theta, \phi) \propto |\Phi_i|^2 [1 + \beta_{20} P_2^0(\cos\chi)], \tag{1.5}$$

where $\chi = (\theta, \phi)$ is the polar angle defined with respect to the orientation of linear polarization of the photodissociating light and (θ, ϕ) are the (polar angle, azimuthal angle) defined according to the quantization axis that is fixed in the laboratory frame.

While the quasiclassical formula successfully predicted the results from several early experiments [63,64], it failed at other experiments [65]. Under what condition the quasiclassical formula holds or in what situation it fails hasn't been crystal clear until we performed the photodissociation on single quantum states at ZLab. In our experiment, the dissociation was performed on ultracold molecules, which greatly reduced the complexity encountered by early experiments with hot molecules. Besides, the capability of precisely populating molecules in single quantum states allowed research on pure-state dissociation and made the comparison of theory and experiment more feasible.

It is discovered that the quasiclassical model holds when *there is only one dissociation channel allowed by selection rules.* In the presence of multiple output channels, quantum

interference between these channels comes into play, which results in a failure of the quasi-classical model. A library of photodissociation experiments on all feasible Sr excited states is presented in Figure 4 of the Nature paper. By incorporating the quantum interference into the photodissociation model a complete agreement between experiment and theory was achieved.

So what's left? Among the breakthroughs, there were two sets of experiments that couldn't have been explained previously.

1.2.1 Magnetic-field tuned photodissociation

The first photodissociation mystery is the one-photon dissociation of weakly bound ground state molecules in the presence of a magnetic field. To demonstrate this puzzle, let's assume that the molecules are dissociated by a light with polarization that is parallel to the quantization axis. In this situation, the selection rules ensure that $\Delta m = 0$ and $\Delta J = 0,\ 1$ (note that $J = 0$ is forbidden for the 1_u and 0_u^+ potentials). There are two possible dissociation channels: $1_u(J = 1, m = 0)$ and $0_u^+(J = 1, m = 0)$. The $1_u(J = 1, m = 0)$ state wave function is proportional to $\sin^2(\theta)$ and the $0_u^+(J = 1, m = 0)$ state wave function is proportional to $\cos^2(\theta)$. As a result, the shape of the dissociated fragments should be described by simple trigonometric functions and the patterns should be independent of applied magnetic fields in the weak-field regime. However, the experimental observations contradict this intuition, as shown in Figure 1.3.

In Chapter 8 I discuss the solution to this puzzle and develop the theory that includes the effect of applied magnetic fields.

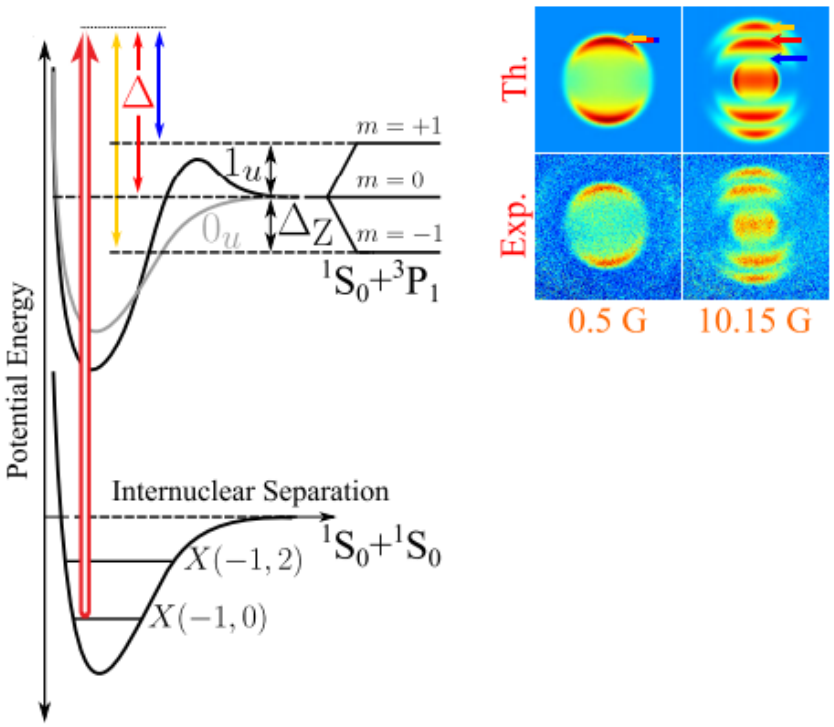

Figure 1.3: Photodissociation of weakly bound ground state molecules, denoted by X(-1,0), shows strong dependence of applied magnetic fields, indicating that our understanding of the photodissociation process was not complete. The theory which accommodates applied magnetic fields will be discussed in this thesis. Adapted from [5].

1.2.2 Crossover from ultracold to quasiclassical chemistry

Another mystery we encountered was the frequency dependence of one-photon dissociation of $J = 1$ molecules down to the $^1S_0 + ^1S_0$ continuum when shape resonances are absent.

A shape resonance is the phenomenon of quantum interference between dissociation channels in case of a quasibound state trapped by the potential barrier. Figure 1.4, for example, demonstrates a shape resonance observed for dissociation of $0_u^+(v = -3, J = 3, m_J = 0)$ molecules, where v is the vibrational quantum number, J is the total angular momentum, and m_J is the projection of J onto the quantization axis.

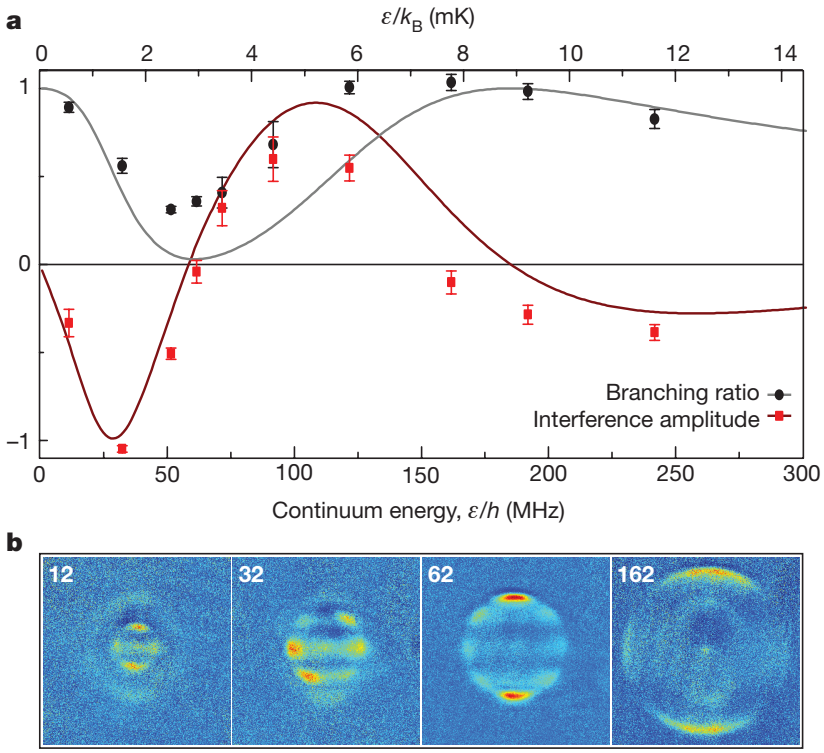

Figure 1.4: (a) Shape resonance for dissociation of $0_u^+(-3,3,0)$ molecules with a light field with polarization along the quantization axis. In this case selection rules lead to a single $m_J = 0$ but a mixture of $J = 2, 4$. The branching ratio and interference amplitude of this mixture evolve with dissociation energy. The shape resonance occurs at energy ∼66 MHz, where $J = 4$ output channel dominates the photofragment angular distribution. (b) Photofragment patterns at a few selected dissociation energies are presented. Energies labeled in white are in the unit of MHz. Adapted from [4].

In Figure 1.4, dissociation is launched with light where the polarization is parallel to the quantization axis. The selection rules for this case are $\Delta J = 0$ 1 and $\Delta m_J = 0$. Because of spin statistics, only even J's are allowed for the $^{88}Sr_2$ ground state molecules. In consequence, the molecules in the $0_u^+(-3,3,0)$ state can be dissociated into two output channels: $J = 2$ and 4. The angular distribution of the photofragments is then described by

$$|f(\theta,\phi)|^2 = |\sqrt{R}Y_{20}(\theta,\phi) + e^{i\delta}\sqrt{1-R}Y_{40}(\theta,\phi)|^2, \tag{1.6}$$

where Y_{Jm_J} is a spherical harmonic. As Figure 1.4 demonstrates, the amplitude R has an obvious dip at ∼66 MHz, which indicates a shape resonance where the fragment distribution is dominated by the $J = 4$ output channel.

Unlike this example, photodissociation from some states only has one allowed channel. For example, spin statistics only allows one reaction channel for $1_u(-2, 1, 0)$ molecules dissociation with horizontally polarized light. The relevant selection rules are $\Delta J = 0, 1$ and $\Delta m_J = 1, -1$. Because $J = 0$ ground state doesn't have sublevels that meet this condition, only the $J = 2$ output channel is allowed and there is no shape resonance. In this case, it could be expected that the photofragment angular distributions would be insensitive to the dissociation energy. However, our experiments proved otherwise, and the shape resonance is absent, the fragment patterns are *still* observed to be highly dependent on the dissociation energy.

In Chapter 9 I discuss the mechanisms that explain the evolution of photodissociation fragment angular distributions with dissociation energy. In these investigations, a clear crossover from the ultracold quantum mechanical to the quasiclassical regime of chemistry is observed.

Chapter 2

Molecular structure and experiment overview

2.1 Structure of $^{88}Sr_2$ molecules

Additional vibrational and rotational degrees of freedom results in a richer and more complicated molecular structure. The knowledge in the formation of molecular structure is crucial in interpreting the molecular transitions. In this section, I discuss the contents that are the most relevant to the experiments described in this thesis. More detailed discussions on the molecular structure can be found in [11, 16, 66].

The Hamiltonian of a physical system can be decomposed as the sum of contributions from different degrees of freedom. For molecules, the Hamiltonian can be written as

$$\hat{H} = \hat{H}_e + \hat{H}_v + \hat{H}_r, \tag{2.1}$$

where $\hat{H}_e$, $\hat{H}_v$,and $\hat{H}_r$ represent electronic, vibrational ,and rotational parts of Hamiltonian ,respectively.

The contributions in Equation 2.1 are decoupled in the Born-Oppenheimer approximation.

For a weakly bound diatomic strontium molecule, the electronic energy can be approximated as the sum of atomic electronic energies of two constituent atoms because the constituent atom size is a lot smaller than the molecular bond length. As for the vibrational energy, the energy level can be described by a quantum number v, which characterizes the molecular vibration frequency. In this thesis, I adopt the convention that $v = 0$ and $v = -1$ denote the deepest and shallowest state, respectively. Among all the energy degrees of freedoms, the rotational energy structure is the most complicated because it involves the various coupling of spin and orbital angular momenta of both electrons and nuclei. These angular momenta are summarized below:

- electronic orbital angular momentum, $\hat{L}$
- electronic spin angular momentum, $\hat{S}$
- total electronic angular momentum, $\hat{J}_e = \hat{L} + \hat{S}$
- rotational nuclei angular momentum, $\hat{R}$
- total molecular angular momentum, $\hat{J} = \hat{J}_e + \hat{R}$

Based on the electronic angular momenta, the projections of $\hat{L}$, $\hat{S}$,and $\hat{J}_e$ onto the internuclear axis are defined to be Λ, Σ ,and Ω, respectively. Note that $^{88}Sr_2$ molecule doesn't have hyperfine structure because of zero nuclear spin angular momentum. This is one of the major benefits of conducting metrology experiments using this molecule.

In different situations, the coupling strengths can vary a lot and thus different *good* quantum numbers are needed. In the following sections, the cases with electronic ground states and excited states of $^{88}Sr_2$ molecules will be discussed. More detailed and complete discussions can be found in [67].

2.1.1 Electronic ground state

The electronic ground state is best described by the quantum numbers $\hat{J}_e$, Λ, Σ, Ω, S and J. A widely-adopted notation for this case is denoted by

$$^{2S+1}|\Lambda|^{\pm}_{\Omega,g/u}, \tag{2.2}$$

where $\pm$ represents the sign of Σ and g/u indicates symmetry of the wavefunction (g/u stands for gerade/ungerade or even/odd).

There are several important features of electronic ground states. Since it is naturally the lowest energy state, the electronic energy asymptotes to that of the $^1S_0 + ^1S_0$ atomic state. Moreover, the molecule has no orbital and spin angular momentum ($\hat{L} = \hat{S} = 0$), therefore the projections of electronic angular momenta are zero ($\Lambda = \Sigma = \Omega = 0$). Furthermore, because two comprising atoms are in the same state and that ^{88}Sr is bosonic, it is naturally required that the wave function for ground state molecules should be *symmetric*. These lead to the notation for ground state molecules: $^1\Sigma^+_{0,g}$. In this thesis, the ground state potential is denoted by a simplified notation X and the ro-vibrational states are represented by $X(v, J, m_J)$, where v is the vibrational quantum number and m_J denotes the projection onto the internuclear axis of J. It should be emphasized that because the ^{88}Sr atom is bosonic, the symmetry in wavefunction only allows *even* J for $^{88}Sr_2$ electronic ground state [11, 14].

2.1.2 Electronic excited state

Electronic excited states can be very complicated. In this thesis, we only consider the simplest excited state that asymptotes to the $^1S_0$+$^3P_1$ threshold. In this case the total electronic angular momentum has $\hat{J}_e = 1$ with contribution from the excited $^3P_1$ atom. As a result, Ω, the projection of $\hat{J}_e$ onto the internuclear axis, can be either 0 or 1. Furthermore, because

the component atoms are in different states, the molecular wavefunction symmetry can be either *gerade* or *ungerade*. With these features, the notation for the electronic excited states are usually defined as [68, 70, 74]

$$|\Omega|^{\pm}_{g/u}, \tag{2.3}$$

where $\pm$ is only used for $\Omega = 0$ and denotes the molecular wavefunction symmetry. Note that $\pm$ here is different from the case of electronic ground state. Apparently two possible symmetry (ungerade/gerade) and two possible Ω (0/1) give four possible combinations (i.e. 0^+_u, 0^+_g, 1_u and 1_g). Among them, only 1_u and 0^+_u are electric dipole allowed from the ground state. In this thesis, we will focus on these two excited states.

The notation for excited states is the same as that for ground states. The ro-vibrational levels in the $1_u/0^+_u$ potential is labeled as $1_u(v', J', m'_J)$ and $0^+_u(v', J', m'_J)$, where v' is the vibrational quantum number and m'_J denotes the projection onto the internuclear axis of J'. The prime notation is adopted to distinguish excited states from ground states.

2.2 Experiment overview

At ZLab, the Sr_2 experiment was initially constructed in 2009. A complete description of how the experimental system was designed and setup can be found in [16]. Here I only make some brief remarks on the preparation of ultracold $^{88}Sr_2$ molecules. I will also describe the metrology equipment that is of crucial importance for the clock experiment.

2.2.1 Atomic Sr source

In our experiment, molecules are produced from ultracold atoms. The atoms come from an oven where two strontium cells are heated up to 600°C. The hot atomic vapor from the oven

is collimated by ∼180 microtubes in a nozzle before pouring into the vacuum tube. Right after the oven region is a mechanic valve (SG0063MCCF from Kurt J. Lesker). This valve was installed in 2016 to protect the strontium cells from being oxidized when the vacuum system is opened. Note that this valve can only hold up to 150°C so one has to be careful when running the oven at high temperature. After the mechanic valve lies the atomic shutter (L-0385 from Unibliz), which role is to block the hot atom beam during the lattice trapping time. As of December 2019, the atomic shutter is the one installed in 2016 after the previous shutter broke down after eight years of work. The shutter breakdown was a distressing memory because it caused a five-month delay in data taking. However, after this accident, a systematic shutter replacement procedure has been developed, which should make it a lot easier for the future (hopefully it will never be needed!). The replacement procedure is described in Appendix A. Right before the hot atom beam pours into the science chamber, it passes through a second mechanic valve. This valve is installed to prevent the atom beam from coating the Zeeman window when the experiment is off.

2.2.2 Atom cooling and trapping

In the following sections, I will briefly comment on how we cool and trap Sr atoms.

2.2.2.1 Zeeman slower

The Zeeman slower is constructed by a one-meter long tube and operates on the $^1S_0 \leftrightarrow {}^1P_1$ 461 nm transition. The 461 nm blue light is generated by frequency doubling a 922 nm IR laser provided by Sacher Lasertechnik. To generate sufficient power of blue light, the IR light is amplified by a tapered amplifier (TA) and frequency doubled in a homemade bow-tie cavity [16, 21, 22]. The laser is locked by saturated absorption spectroscopy in a strontium

galvatron vapor cell [18–20].

2.2.2.2 Blue MOT

Two stages of magneto-optical trap (MOT)'s are applied to cool strontium atoms. The first stage is the blue MOT, which operates on the 32 MHz broad 461 nm $^1S_0 \leftrightarrow {}^1P_1$ transition. The light source is the same as described in the Zeeman slower section. To increase the blue MOT loading efficiency, two repump lasers are applied to close loss channels. One repump works on the $^3S_1 \leftrightarrow {}^3P_2$ 679 nm transition and the other works on the $^3S_1 \leftrightarrow {}^3P_0$ 707 nm transition. In the blue MOT, there are usually 10^6 atom trapped at a temperature of 1 mK.

2.2.2.3 Narrow-line red MOT

After the first stage blue MOT cooling, the atoms are transferred to a red MOT. The red MOT operates on a narrow-line transition $^1S_0 \leftrightarrow {}^3P_1$, which has natural linewidth of 7.5 kHz. Due to this narrow linewidth, the red MOT can cool the atoms further down to $\sim$1 μK. Usually, there are $\sim 10^5$ atoms captured in the red MOT.

It is important to note that the red MOT laser also serves as the reference master laser for the experiment. The red MOT laser light is generated from a homemade ECDL and a fraction of the light is offset-locked to an ultra-low expansion (ULE) cavity. The stabilized red MOT laser light possesses a linewidth of $\sim$150 Hz.

2.2.2.4 Optical lattice

To suppress the Doppler shifts and achieve the recoil-free spectroscopy, the cooled atoms are loaded into an optical lattice trap. The lattice trap is constructed with a standing wave formed by retro-reflecting a laser beam and focusing the counter-propagating beams at the molecular cloud.

In our experiment, the lattice light is created by a homemade ECDL of wavelength 915 nm or 1064 nm. The ECDL output is amplified to ∼1 W by a TA, which works with diodes from Eagleyard Photonics. To achieve sufficient trapping, the lattice power usually runs at ∼200 mW and the beam waist is focused down to 29 μm at the molecular cloud. With this setup, there are usually 10^4 atoms trapped in the lattice. Although the TA design is an economic way to generate high power for trapping, it also incurs serious problems with impure spectrum. In our clock experiment, we have observed a limitation on the clock state lifetime imposed by the broad ASE noise from the TA. This issue will be discussed in depth in Chapter 6.

In an optical lattice, the trap depth is proportional to the real part of the polarizability. Moreover, to achieve recoil-free spectroscopy the lattice should work in the Lamb-Dicke regime. These concepts are commented below.

Trap depth and polarizability

Assuming a monochromatic laser light with frequency ω, the electric field of an optical lattice trap can be described by

$$\begin{aligned}\mathbf{E}(\mathbf{r},t) &= \mathbf{E}^{\text{forward}}(\mathbf{r})e^{-i\omega t} + \mathbf{E}^{\text{retro}}(\mathbf{r})e^{+i\omega t} \\ &= \hat{z}\left[E^{\text{forward}}(\mathbf{r})e^{-i\omega t} + E^{\text{retro}}(\mathbf{r})e^{+i\omega t}\right],\end{aligned} \tag{2.4}$$

where $\hat{z}$ is the polarization of the electric field, and $E^{\text{forward}}/E^{\text{retro}}$ are the complex amplitude of the forward/retro-reflected electric fields. For atoms that are exposed to this oscillating field, an atomic dipole moment $\mathbf{d}$ is induced

$$\mathbf{d} = \hat{z}\left[\alpha(\omega)E^{\text{forward}}(\mathbf{r})e^{-i\omega t} + \alpha(\omega)^{\dagger}E^{\text{retro}}(\mathbf{r})e^{i\omega t}\right], \tag{2.5}$$

where $\alpha(\omega)$ is the frequency-dependent complex atomic polarizability. The interaction of the dipole moment and the electric field generates a dipole potential

$$U_{dip}(\mathbf{r}) = -\frac{1}{2}\mathbf{d}(\mathbf{r}) \cdot \mathbf{E}(\mathbf{r}). \tag{2.6}$$

Plugging Equations 2.4 and 2.5 and applying rotating-wave approximation yields a time-averaged dipole potential

$$\begin{aligned} U_{dipole} &= -\frac{1}{2}\left[\alpha(\omega)E^{\text{forward}}(\mathbf{r})E^{\text{retro}}(\mathbf{r}) + \alpha(\omega)^{\dagger}E^{\text{forward}}(\mathbf{r})E^{\text{retro}}(\mathbf{r})\right] \\ &= -\text{Re}\left[\alpha(\omega)\right]|E^{\text{forward}}(\mathbf{r})|^2 \\ &= -\frac{1}{2\epsilon_0 c}\text{Re}\left[\alpha(\omega)\right] I(\mathbf{r}), \end{aligned} \tag{2.7}$$

where the last equation adopts the definition of lattice field intensity

$$I(\mathbf{r}) = 2\epsilon_0 c|E^{\text{forward}}(\mathbf{r})|^2, \tag{2.8}$$

assuming the index of refraction equal to 1. As Equation 2.7 demonstrates, the trap depth is proportional to the real part of the polarizability. Furthermore, the derivation doesn't require any atom-specific feature so this rule is also applicable to trapped molecules. Because the bound states in the $^{88}Sr_2$ molecular potentials have different polarizabilities, their trap depths in the optical lattice are also different. This leads to an issue of thermal broadening that limits the molecular clock coherence. A solution to this issue will be discussed in Chapter 4.

Trapping frequency and Lamb-Dicke parameter

Assuming the laser wavelength is λ, the electric field can be expressed as $E^{\text{forward}} = E_0\cos(kx)$, where $k = \frac{2\pi}{\lambda}$ and $\hat{x}$ is the laser propagation direction. Under the approximation that $kx \ll 1$, the time-averaged dipole potential in Equation 2.7 can be written as

$$U_{diople} = -U_0 \cos^2(kx) \sim -U_0(1 - k^2x^2). \tag{2.9}$$

This potential corresponds to a standard quantum simple harmonic oscillator with a longitudinal trapping frequency

$$\omega_{trapping} = \frac{2\pi}{\lambda}\sqrt{\frac{2U_0}{M}}, \tag{2.10}$$

where M is the mass of the molecule. Equation 2.10 has several critical implications. First, it can be considered as an indicator of the tightness of the lattice trap. The Lamb-Dicke parameter is defined as $\eta = \sqrt{\frac{\omega_{recoil}}{\omega_{trapping}}}$ [23, 25], where the recoil frequency $\omega_{recoil} = \frac{\hbar k^2}{2M}$. In the Lamb-Dicke regime, $\eta \ll 1$, the trapping frequency is a lot larger than the recoil frequency, which is a critical criterion for recoil-free spectroscopy. Second, from Equations 2.7 and 2.10, the trap depth and thus the polarizability can be directly backed out. In our experiment, the trapping frequency is obtained via sideband spectroscopy [13]. Given a lattice with a power of $\sim$ 200 mW and beam waist $\sim$29 μm, the trapping frequency is around $2\pi \times 70$ kHz, which corresponds to a $U_0/h \sim 0.8$ MHz trap depth, where h is the Planck constant.

2.2.3 Production of ultracold molecules

In our experiment, molecule production is realized via photoassociation [74], where a pair of atoms absorb a photon and bound together into a molecule on an excited 0_u^+ state. Because the excited state has excellent wave function overlap (i.e. large Franck-Condon factors) with a few certain weakly bound ground states, the excited molecules quickly decay to those ground states via spontaneous emission. An illustration of producing $X(-2, 0)$ molecules with photoassociaiton via the $0_u^+(-5, 1)$ state is shown in Figure 2.1.

The time duration of the photoassociation pulse is critical in molecule production. If the pulse is too short, the number of molecules is too little, which would lead to a weak signal. However, if the pulse is too long, the photoassociation process would incur excessive heating on the molecules [13]. Typically, with a photoassociation laser intensity of 3 W/cm^2, a pulse duration of 2 ms is optimal for producing $X(-1, 0)$ molecules and 500 μs for $X(-2, 0)$ molecules. With photoassociation, approximately 5,000 molecules are prepared at $\sim$5 μK at the electronic ground states. The non-associated atoms are wiped away with the resonant 461 nm blue MOT light.

Huge wave function overlaps between excited states and ground states is crucial for photoassociation. This benefit only exists for states near the asymptote of the potential. Wave function overlaps drop significantly toward the bottom of the potential, therefore populating molecules on a deeply bound ground state requires an alternative method. This topic is discussed in Chapter 3.

2.2.4 Molecule detection and imaging

In our experiment, the molecules are detected with the recovery scheme [83]. To do this, a bound-to-free laser is shined on ground state molecules to break them into atoms for absorption imaging. Typically, the molecules are recovered into the $^1\mathrm{S}_0 + ^3\mathrm{P}_1$ threshold and the strong $^1\mathrm{S}_0 \leftrightarrow {}^1\mathrm{P}_1$ cycling transition is utilized for imaging. Note that this method only works for weakly bound molecules because transitions from deeply bound ground states into excited thresholds are inefficient. To detect molecules on a deeply bound state, the molecules have to be transferred to a weakly bound state before being recovered.

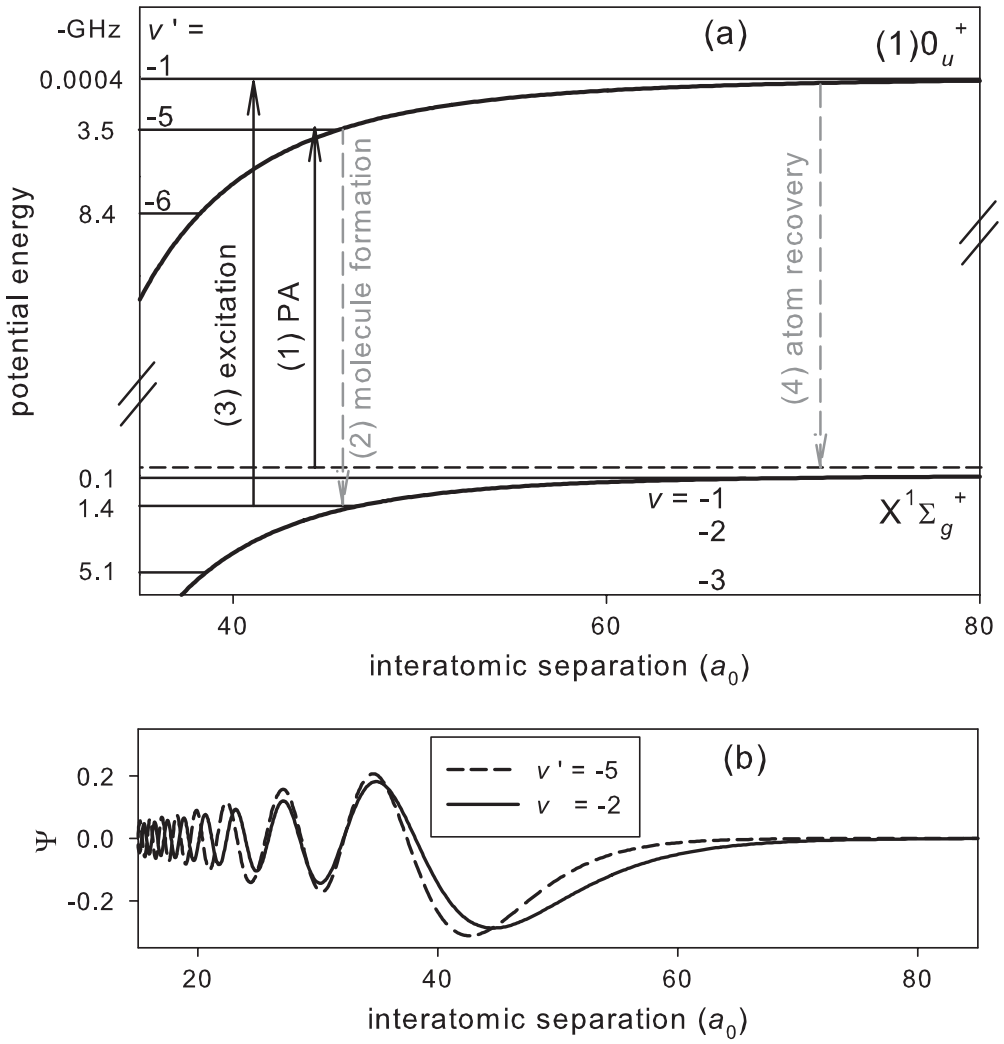

Figure 2.1: Sr_2 molecule production and detection. (a) (1) Ultracold atoms are bound into molecules and excited onto specific 0_u^+ states by a photoassiciation pulse. (2) Due to a large Franck-Condon factor, molecules on $0_u^+(v' = -4, 1)$ and $0_u^+(v' = -5, 1)$ efficiently decay to $X(v = -1, J = 0, 2)$ and $X(v = -2, J = 0, 2)$ states, respectively. (3) To detect molecules, a recovery pulse is applied to dissociate the molecules via the $^1S_0 + ^3P_1$ threshold. (4) Excited atoms decay down to the ground state and absorption images are created with the 461 nm cycling laser. (b) Wave function overlap of $0_u^+(v' = 5)$ and $X(v = -2)$ state. The large Franck-Condon factor is the key for photoassociation. Adapted from [71].

2.2.5 Frequency standard

In our experiment, the frequency standard is provided by a GPS-disciplined 10 MHz crystal oscillator (Connor-Winfield, the FTS500 Xenith TBR), which offers a frequency inaccuracy of tens parts per trillion. This frequency standard generates a 10 MHz sinusoidal wave output from an intrinsically low jitter voltage-controlled crystal oscillator (VCXO) and all metrologically important components in the experiment are referenced to this frequency standard.

2.3 Frequency stabilization and optical frequency comb

In this section, a brief review of our frequency comb and a summary of essential operation notes are provided. A frequency comb is a broad laser spectrum consisting of $sim10^5$ of discrete and repetitive lines with well defined frequencies. The rapid development of frequency combs has allowed linking radiofrequency standards to optical frequencies and hence has tremendous impacts on the fields of frequency metrology and precision measurements [77]. Nowadays, frequency combs are commercially available at a wide range of spectra from microwave to ultraviolet with available repetition frequencies ranging from 10 MHz to over 1 THz [78]. These make the frequency comb a tool that is almost inevitable for metrology experiments.

2.3.1 Frequency comb operation

The comb that we have been working with is the model of FC1500-250-WG provided by Menlo Systems. This model operates with the femtosecond comb technique, where a pulse on the fs level circulates in a laser cavity. This circulating pulse leads to an output of a sequence of repetitive pulses which envelope travels at its group velocity and the carrier travels at its phase velocity. In the frequency domain, this sequence of output pulses corresponds to a

spectrum of equally spaced lines. Assuming the repetition time of the pulse train is T and that the carrier wave oscillates at frequency ω_c, the spacing between two adjacent lines, i.e. repetition rate, is $\omega_{\mathrm{RR}} = \dfrac{2\pi}{T}$ and the electric field at time t of this sequence of pulses can be described by

$$E(t) = \mathrm{Re}\left[A(t) \cdot \exp(-i\omega_c t)\right] = \mathrm{Re}\left[\sum_n A_n \cdot \exp(-i(\omega_c + n\omega_r)t)\right], \tag{2.11}$$

where $A(t)$ is the periodic envelope function satisfying $A(t+T) = A(t)$ and A_n is its n-th Fourier component.

In general, it is not required that the group velocity be equal to the phase velocity. In the case where they differ, a newly generated pulse acquires an additional phase shift $\Delta\phi$. This phase shift results in the so-called carrier-envelope offset (CEO) in the frequency domain

$$\omega_{\mathrm{CEO}} = \omega_{\mathrm{RR}}\Delta\phi, \tag{2.12}$$

which leads to the mathematical description of the frequency spectrum

$$\omega_n = \omega_{\mathrm{CEO}} + n\omega_{\mathrm{RR}} \tag{2.13}$$

Conventionally the expression with units of Hz is adapted

$$f_n = f_{\mathrm{CEO}} + nf_{\mathrm{RR}} \tag{2.14}$$

Equation 2.14 links two radio frequencies f_{CEO} and f_{RR} to an optical frequency f_n. In our comb, the CEO frequency $f_{\mathrm{CEO}} = 20$ MHz and repetition rate $f_{\mathrm{FF}} \sim 250$ MHz. With these radio frequencies well-stabilized, the frequency spectrum forms *a series of stable references* to which an optical light source can be locked.

2.3.2 Comb spectrum generation

In the model of our comb, the octave-spanning supercontinuum frequency band ranges from 1000 nm to 2100 nm. To convert this comb spectrum into the visible band, the part near 1560 nm is frequency-doubled through a second harmonic generation (SHG) to 780 nm. Then the frequency-doubled light is coupled to a photonic crystal fiber (PCF) where the visible octave spectrum is generated. One thing to note about SHG process is that the frequency doubling process only works for the CEO frequency whereas the repetition rate remains unchanged. This is because the sum frequency generation is the dominant process in SHG [79]. As a result, the comb spectrum generated in the visible range can be written as

$$f_m = 2f_{\mathrm{CEO}} + mf_{\mathrm{RR}}, \tag{2.15}$$

where m is an non-negative integer.

2.3.3 Offset frequency detection and repetition rate stabilization

Frequency detection and stabilization are crucial for frequency combs. In Menlo combs, the repetition rate is directly measured and the offset frequency is measured via the $f-2f$ scheme. The mode with mode number n is frequency doubled and beat with the mode with mode number $2n$. The beat note $(2f_{\mathrm{CEO}} + 2nf_{\mathrm{RR}}) - (f_{\mathrm{CEO}} + 2nf_{\mathrm{RR}})$ is then the offset frequency.

For stabilizing the frequencies, the offset frequency and repetition rate are locked separately. The repetition rate can be stabilized to either an RF reference or an optical reference, depending on experiment purpose. The lock is performed with a cavity piezo element along with a fast intra-cavity electro-optic modulator feedback, which provides high bandwidth locking. For the work described in this thesis, the repetition rate is optically locked to the 150 Hz master laser line. On the other hand, the offset frequency is always stabilized to RF

reference and the lock is achieved with pump current feedback. This lock scheme doesn't allow high-bandwidth lock and thus the linewidth of the offset frequency is limited to ~400 kHz. Even though the repetition rate lock is fast and tight, the low bandwidth lock for the offset frequency leads to a shaky comb spectrum. Figure 2.2 illustrates the effect of a loosely locked offset frequency. In this illustration, the repetition rate is stabilized by phase-locking the nearest comb mode m to the reference laser frequency f_0. The fast lock of repetition rate indicates a constant beat note frequency f_{beat} between the m-th comb mode and the reference laser

$$2f_{CEO} + mf_{RR} - f_0 = f_{beat}. \tag{2.16}$$

From Equation 2.16, we can see the instability in the offset frequency is translated to the repetition rate

$$\delta f_{RR} = \frac{2\delta f_{CEO} - \delta f_0}{m} \approx \frac{2}{m}\delta f_{CEO} \tag{2.17}$$

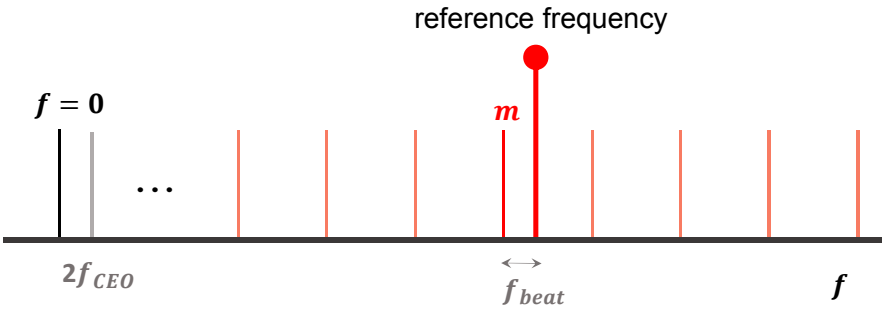

Figure 2.2: Illustration of jittering comb spectrum caused by a broad offset frequency

To tackle the repetition rate uncertainty arising from the jittering offset frequency, Menlo Systems provides an lock scheme with the so-called *CEO subtraction* method. The idea is to use $f_{beat} = f_{\mathrm{CEO}}$ for the repetition rate lock. In this scheme, the f_{CEO} terms on both sides of Equation 2.16 can be canceled out so that the repetition rate would be more stabilized. However, there is an apparent flaw in the design. The frequency supplied for the beat note is $1 \times f_{CEO}$ but what is actually needed is $2 \times f_{CEO}$. Because of this flaw the comb spectrum, jittering can't be fully removed. Very fortunately, it turns out that with this single CEO subtraction the comb works fine (at least for now), a stability on the order of 10^{-14} has been observed. Our Master student Christian Liedl performed a thorough diagnosis on this issue. Readers can consult his thesis [17] for more details.

Besides adopting the f_{CEO} subtraction method to stabilize the repetition rate, another technical measure is necessary to cope with the jittering f_{CEO} when locking spectroscopic lasers to the frequency comb. Because the whole comb spectrum jitters with the offset frequency, lasers locked to the comb inherits this instability, leading to notorious coherence issues. To deal with this problem, the f_{CEO} is utilized to lock the laser beat note, as illustrated in Figure 2.3. Note that in this scheme, the sign of the beat note is opposite to that of f_{CEO} to correctly cancel the frequency instability. With a positive f_{CEO}, for example, the beat note for the laser lock is $-f_{CEO}$. When f_{CEO} increases, the comb spectrum moves to higher frequencies. In this scenario, the beat note grows by the same amount but in the opposite direction, which compensates the change in f_{CEO} and stabilizes the spectroscopic laser frequency.

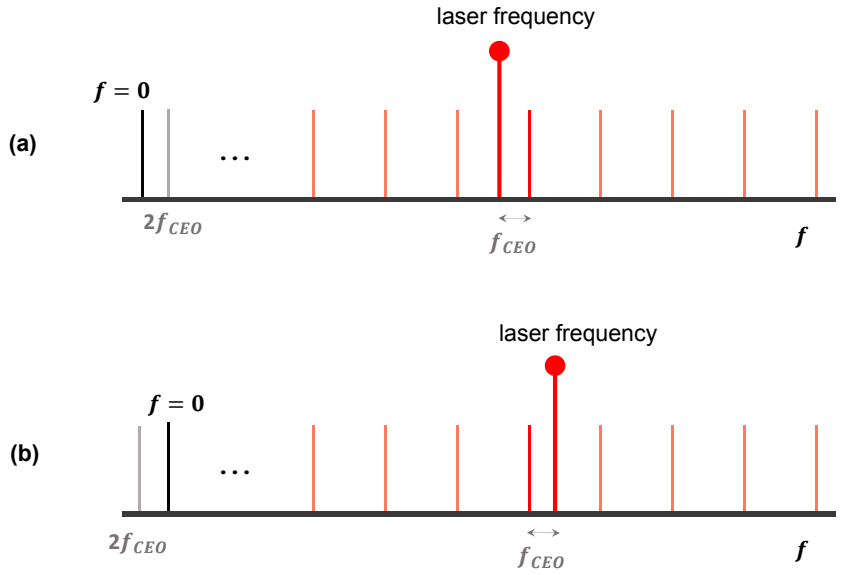

Figure 2.3: To eliminate the instability from the offset frequency, the f_{CEO} was sent to lock the laser frequency. Also, the sign of the beat note is chosen to be opposite of f_{CEO} in order to correctly cancel the frequency instability. (a) For $f_{CEO} > 0$, the laser frequency is locked on the red side of the comb reference. (b) For $f_{CEO} < 0$, the laser frequency is locked on the blue side of the comb reference.

Like the CEO subtraction scheme for locking the repetition rate, in principle the lasers should be locked with the $2 \times f_{CEO}$ subtraction scheme. However, due to the design of the comb we haven't found a reliable way to do it. In this thesis, for a laser that is stabilized to the frequency comb, it is locked with $1 \times f_{CEO}$ if not suggested otherwise.

2.3.4 Comb mode number determination

The comb mode number is determined by comparing the frequency comb counter values and the wavelength meter reading.

Assuming the laser of interested is locked to the n-th comb tooth with a beat note of f_{beat}, the frequency of this laser is then $2f_{CEO} + nf_{RR} + f_{beat}$. This frequency has to be consistent

with that measured by the wavelength meter f_w

$$f_w = 2f_{CEO} + nf_{RR} + f_{beat}, \tag{2.18}$$

from which the comb tooth number can be determined

$$n = \frac{f_w - 2f_{CEO} - f_{beat}}{f_{RR}} \tag{2.19}$$

One subtle thing to keep in mind is that our wavelength meter drifts from day to day. Therefore the wavelength reading should be calibrated by a well-determined transition, for instance the $^3\mathrm{P}_1$ intercombination transition or the $^1\mathrm{P}_1$ blue MOT transition. A real example on determining the comb tooth number is provided in Section 4.2.3.

Chapter 3

Search for deeply bound molecular states

In this chapter, I describe an efficient way to search for the deeply bound ground states. Searching for deeply bound states is not an easy task because of the sparsity of states. The depth of the $^{88}Sr_2$ ground state potential is >30 THz and, according to *ab initio* calculations, the level spacing at the bottom of the potential is more than 1 THz. In other words, searching for the deeply bound states is like looking for a needle in a haystack. The search would be fruitless and time-wasting if a wrong method is adopted. So what is the more efficient way to do it?

Before discussing the search method, let us review the simpler case when looking for excited states. In this situation, the search can be done simply by monitoring the depletion from ground state molecules. With molecules populated on a certain ground state, a laser connecting that ground state is scanned through the region where the excited state is suspected to be. In the meantime, a recovery pulse is applied to count how many molecules stay in the ground state. When the depletion laser hits the transition, the molecules are pumped into the excited state so that a drop in the recovery signal can be observed. The process is

illustrated in Figure 3.1.

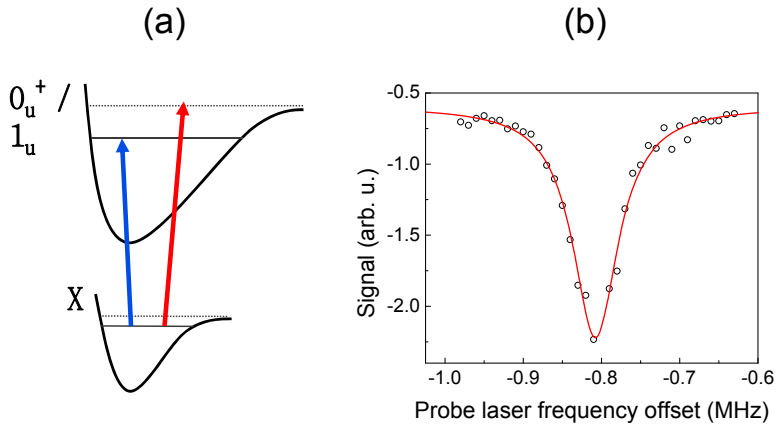

Figure 3.1: One-photon spectroscopy can be adapted to search for weakly bound excited states. With molecules populated on a certain ground state, a laser connecting that ground state (navy) is scanned through the region where the desire state is suspected to be. In the meantime a recovery laser (red) is applied to count the molecule number in the ground state. When the depletion laser hits the transition the molecules are pumped into the excited state and a drop in the recovery signal will be observed.

In general, this direct depletion method works well for excited state search. However, for searching deeply bound ground states, this method becomes unrealistic. The analogy of direct depletion in the context of ground state search is the coherent two-photon Raman spectroscopy. This is naturally a more difficult method of spectroscopy because it not only involves more photons to drive the transition, but also requires a frequency comb to achieve the coherence. Due to these complexities, the Raman transition is not an ideal tool for ground state search. In the next section I will describe an alternative search method that is based on the Autler-Townes spectroscopy.

3.1 Autler-Townes spectroscopy

3.1.1 The principle of Autler-Townes spectroscopy

The Autler-Townes effect was discovered in the 1950s when a split in a molecular microwave transition was observed when one of the involved states was coupled to a resonant field. The fact that it does not require the involved laser fields act coherently makes the Autler-Townes spectroscopy an excellent tool for ground state search.

Figure 3.2 demonstrates an illustration for the Autler-Townes spectroscopy. When the coupling field is absent, the $|e\rangle$ state remains unperturbed, therefore the laser probing the $|g\rangle \rightarrow |e\rangle$ transition resolves only one peak. In the presence of the coupling laser that couples $|r\rangle$ and $|e\rangle$ states, the field interaction perturbs the molecular Hamiltonian. With the rotating wave approximation the Hamiltonian can be written as

$$H = \hbar\Delta \left|e\right\rangle \left\langle e\right| + \frac{\hbar\Omega}{2}(\left|e\right\rangle \left\langle r\right| + \left|r\right\rangle \left\langle e\right|), \tag{3.1}$$

where Δ is the detuning of the coupling laser from $|r\rangle \rightarrow |e\rangle$ transition and Ω is the Rabi frequency of the coupling laser. The Hamiltonian described by Equation 3.1 has energy eigenvalues

$$E_{\pm} = \frac{\hbar\Delta}{2} \pm \frac{\hbar\sqrt{\Omega^2 + \Delta^2}}{2} \tag{3.2}$$

The above derivation shows that the coupling field results in a split in both $|e\rangle$ and $|r\rangle$ states (The splitting of $|r\rangle$ can be understood by symmetry). As a result of this split, the probe laser connecting the $|g\rangle$ state scans through a doublet instead of a peak. This phenomenon is the Autler-Townes effect. Before describing how this spectroscopy is applied to find deeply bound ground states, let us discuss some observations of Equation 3.2.

- The dependence of doublet energies on coupling laser detuning form a hyperbola.
- The state splitting only depends on coupling laser intensity and frequency detuning. The fact that it is independent of pulse time duration makes the Autler-Townes spectroscopy a fantastic tool for the state searching.
- At resonance ($\Delta = 0$) the state splitting is symmetric, i.e. $|E_+| = |E_-|$ and the energy gap between the doublets is equal to the coupling laser Rabi frequency, i.e. $E_+ - E_- = \hbar\Omega$.
- At large detuning, Autler-Townes spectroscopy asymptotes to the two-photon Raman spectroscopy. At $\Delta \to \pm\infty$, one of the doublets approaches to the original state while the other is pushed further out. It is therefore expected that the transition strengths to each of the doublets would be different.

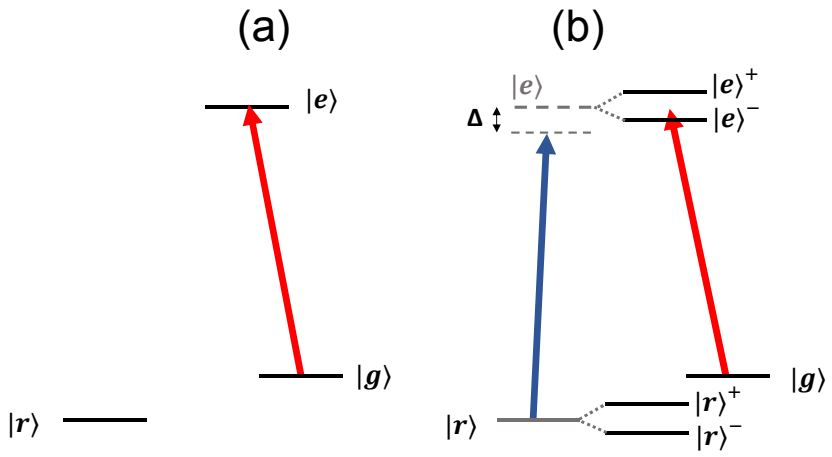

Figure 3.2: (a) Without the coupling laser (blue) $|e\rangle$ state is unperturbed and thus only one peak is observed when scanning the probe laser (red). (b) In the presence the coupling laser, the molecule-light interaction is coupled into the Hamiltonian, resulting in state splittings of $|e\rangle$ and $|r\rangle$ states. Consequently, a doublet is observed when scanning the probe laser.

3.1.2 Search for deeply bound states

In this section, I discuss how we use the Autler-Townes spectroscopy to find deeply bound ground states.

To find the states, the Autler-Townes effect is utilized in reversed order, as shown in Figure 3.3. Molecules are initially populated on a weakly bound ground state $|v_0\rangle$ and a probe laser is tuned on resonance of the transition to an excited state $|v'\rangle$. Due to the resonant

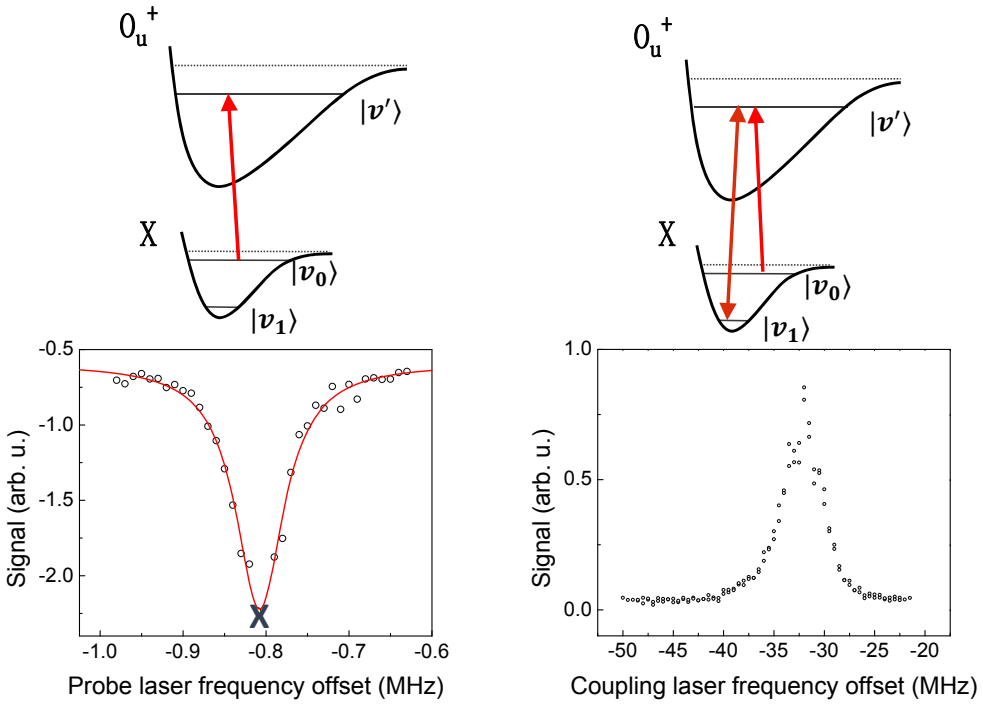

Figure 3.3: Demonstration of state searching using Autler-Townes effect. Firstly, the probe laser (red) is scanned through an excited state $|v'\rangle$ and parked on the transition resonance (the grey cross). Then the coupling laser (orange) is scanned through to perturb the molecular states. As the coupling laser comes close enough to the $|v_1\rangle \rightarrow |v'\rangle$ resonance, because of Autler-Townes effect, it will split the $|v'\rangle$ state. As a result, the probe laser will no longer be resonant, therefore the molecule recovery signal will rise.

probe laser, the recovery signal is depleted. Note that the probe laser intensity should be just enough for a good signal depletion. A proper probe intensity is critical because reducing power broadening on the probe transition results in a higher sensitivity to the signal from new states. With the depletion spectroscopy set up, the coupling laser is scanned through the $|v_1\rangle \rightarrow |v'\rangle$ transition. As the coupling laser comes close enough to the resonance, its light field starts perturbing the molecular Hamiltonian, leading to level splitting in the excited state. As a result of the splitting, the probe laser will no longer be resonant, therefore an increase molecule recovery signal will be observed.

The step size at which the coupling laser frequency is swept is critical here. As described, the success of this method relies on the Hamiltonian perturbation from the coupling light fields, so scanning the coupling laser with an exceedingly large step size would risk the missing of the resonance. The optimal step is the one that is large enough to make an efficient search but not too large that the sensitivity is compromised. An estimation on the optimal step is provided below.

Given a linewidth γ for the $|v_0\rangle \rightarrow |v'\rangle$ depletion transition, we want at least a minimum shift of one full linewidth from the Autler-Townes effect to observe a noticeable signal change. For a red-detuned coupling laser ($\Delta < 0$), the E_+ component is closer to the original level so for the shift to be larger than γ it requires that

$$\frac{\hbar\Delta}{2} + \frac{\hbar\sqrt{\Omega^2 + \Delta^2}}{2} > \hbar\gamma$$

which yields $\Delta > -\frac{\Omega^2 - 4\gamma^2}{2\gamma}$. By symmetry, we have $\Delta < \frac{\Omega^2 - 4\gamma^2}{2\gamma}$ for blue-detuned region. This suggests that the optimal scanning step be the joint interval of these two regions, which is

$$\text{optimal scan step} = \frac{\Omega^2 - 4\gamma^2}{2\gamma} \approx \frac{\Omega^2}{2\gamma}, \tag{3.3}$$

assuming a coupling Rabi frequency that is larger than the probe depletion linewidth. Given a coupling laser intensity of $\sim$ 1W/cm^2 and a 80 kHz depletion transition linewidth, the optimal scan step is $\sim$ 2 MHz. This is a convenient searching step size which can be achieved with a manually-controlled piezo.

Table 3.1 summarizes the binding energies of five deeply bound ground states that are found with this method.

vibrational level v	rotational level J	binding energy (THz)
8	0	23.013,0(1)
7	0	24.031,1(1)
6	2	25.070,581(1)
6	0	25.073,538,149(2)
5	0	26.138,6(1)
4	0	27.228,2(1)

Table 3.1: Binding energy of a few deeply bound ground states found with Autler-Townes spectroscopy

A few comments about these binding energy measurements:

- The binding energy here is counted from the $^1S_0 + ^1S_0$ threshold.
- The vibrational levels v is assigned according to the comparison with theoretical calculations done by Prof. Robert Moszynski's team at Warsaw University.
- To map out the whole ground state potential what we need to do is simply changing the frequency of the coupling laser. Given that usual optical diodes can cover a range

of ∼5 nm, it requires about seven diodes to probe all the ground states.

- The precision in the measurements is limited by the wavelength meter uncertainty except for the two states with $v = 6$. For these two states, the binding energies are determined with molecular clock metrology. Determination of the clock state binding energy requires descriptions of critical experimental system stabilization schemes, which will be discussed in Section 5.2.3.2. The same technique can be extended to all the other ground states.

3.1.3 A test of Autler-Townes spectroscopy

In the previous section, ground state search via Autler-Townes spectroscopy applied in the reversed order is demonstrated. With the success of precisely locating the deeply bound ground state, the iconic avoided-crossing behavior in Autler-Townes spectroscopy can be studied. Figure 3.4 demonstrates an example where the $X(-2, 0) \rightarrow 0_u^+(-5, 1)$ transition is probed while the coupling laser perturbs the molecular Hamiltonian through the $X(6, 0) \rightarrow 0_u^+(-5, 1)$ transition. Throughout the experiment the coupling laser power is fixed at 330 μW with a beam waist of 150 μm, which corresponds to an intensity of 0.47 W/cm^2. The avoided-crossing behavior is obtained by scanning the probe laser at a variety of coupling laser frequencies. As expected from previous discussions, the doublet frequencies are well-captured by the hyperbolic function form described by Equation 3.2. Moreover, the spectroscopy collected with several selected coupling frequency shows how transition strengths can vary for the doublet.

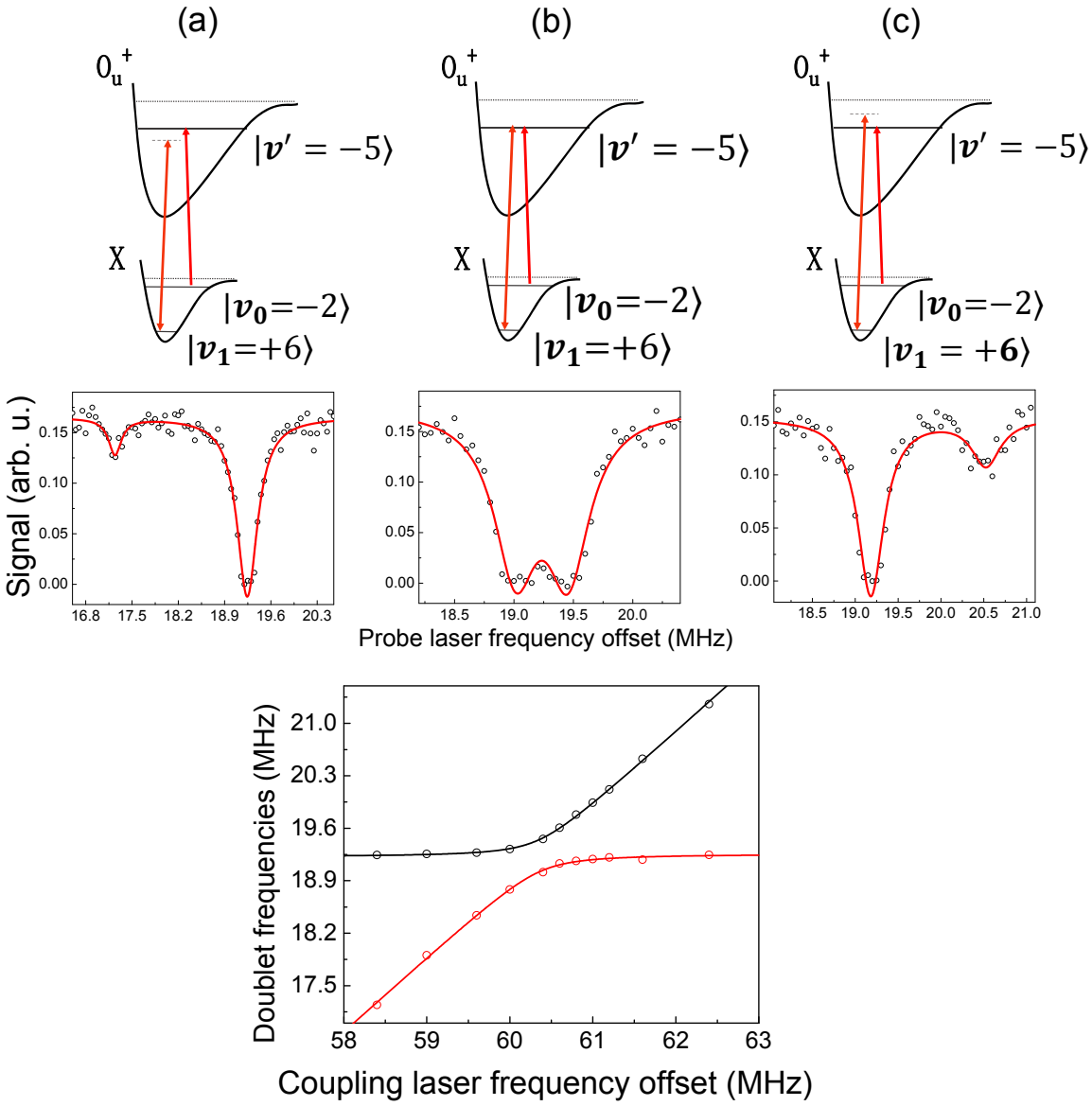

Figure 3.4: Examination of Aulter-Townes effect with a deeply bound ground state. The probe laser probes the $X(-2,0) \rightarrow 0_u^+(-5,1)$ transition while the coupling laser perturbed the molecular Hamiltonian through the $X(6,0) \rightarrow 0_u^+(-5,1)$ transition. (a) When it is red-detuned, a peak appears on the red side of the resonance. (b) When it is on resonance, two doublets are symmetric about the resonance frequency. (c) When it is blue-detuned, a peak appears on the blue side of the resonance. The dependency of doublet frequencies as a function of coupling laser detuning is shown in the bottom.

3.2 Two-photon Raman spectroscopy

In our experiment, molecules are transferred to deeply bound ground states via two-photon Raman transitions. As suggested in the Autler-Townes spectroscopy, when the coupling laser detuning is large, one peak is pushed away from the one-photon probe resonance. At the limit of $\Delta \ll \Omega$ the pushed away doublet is driven coherently by both involved lasers. In this chapter I will discuss this two-photon process and demonstrate state transfers with this technique.

3.2.1 The principle of Raman spectroscopy

A two-photon Raman transition involves two lasers with frequencies ω_1 and ω_2 where these two beams act on molecules at the same time and drive a transition coherently. Here we focus on the situation which applies to our experiment, the Λ-*configuration*, as depicted in Figure 3.5. In a Λ-configuration, the Raman process drives a transition via a virtual state

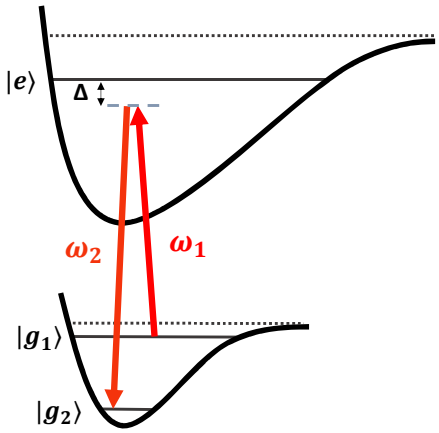

Figure 3.5: In a Λ-configuration, two lasers drive a two-photon transition via a virtual state and the energy between the initial and final states is determined by the energy difference between two involved lasers.

(or an intermediate state) and the energy difference between the initial and final state is $\hbar(\omega_2 - \omega_1)$. It is important to note that the virtual state only serves as an auxiliary purpose. No molecule is excited to that state.

The behavior of a Raman transition can be described by a straightforward method that treats each leg of the transition as a one-photon process. In a two-level system which consists of two states $|g\rangle$ and $|e\rangle$, a laser with frequency ω driving the molecules initially populated on the $|g\rangle$ state will lead to a time-dependent population on $|e\rangle$ state [12]

$$c_e(t) = \frac{\Omega}{2}\left[\frac{1-\exp(i(\omega_0+\omega)t)}{\omega_0+\omega} + \frac{1-\exp(i(\omega_0-\omega)t)}{\omega_0-\omega}\right] \tag{3.4}$$

where ω_0 is the transition frequency and Ω is the probe laser Rabi frequency. With rotating-wave approximation, Equation 3.5 can be approximated to

$$c_e(t) \sim \frac{\Omega}{2}\left[\frac{1-\exp(i(\omega_0-\omega)t)}{\omega_0-\omega}\right] \tag{3.5}$$

Now let us extend this to the two-photon Raman process. Consider the case in Figure 3.5, the first laser that connects state $|g_1\rangle$ to state $|e\rangle$ results in

$$c_e(t) \sim \frac{\Omega_{g_1,\,e}}{2}\left[\frac{1-\exp(i(\omega_{e,\,g_1}-\omega_1)t)}{\omega_{e,\,g_1}-\omega_1}\right], \tag{3.6}$$

where $\omega_{a,\,b}$ denotes energy difference $\omega_a - \omega_b$ between two states a and b and $\Omega_{g_1,\,e}$ represents the Rabi frequency of the first laser beam. Substituting Equation 3.6 into the time-dependent Schrödinger equation and applying the rotating-wave approximation yields

$$\begin{aligned} i\frac{\partial}{\partial t}c_2(t) &= \Omega_{g_2,\,e}\cos(\omega_2 t)\exp(-i\omega_{e,\,g_2}t)c_e(t) \\ &\sim \frac{\Omega_{g_1\to e}\Omega_{g_2,\,e}}{4(\omega_{e,\,g_1}-\omega_1)}\left[\exp(i(\omega_2-\omega_{e,\,g_2})t) - \exp(-i(\omega_{g_1,\,g_2}+\omega_1-\omega_2)t)\right], \end{aligned} \tag{3.7}$$

Note that $\omega_1 - \omega_{e,g_1}$, which will be denoted by Δ, is the difference between the first probe laser frequency and the $|g_1\rangle \rightarrow |e\rangle$ transition frequency. Similarly, $\omega_{g_1,g_2} + \omega_1 - \omega_2$, which will be denoted by δ, represents the frequency detuning from the Raman transition resonance condition. With Δ and δ, Equation 3.7 can be rewritten as

$$i\frac{\partial}{\partial t}c_2(t) = -\frac{\Omega_{g_1,e}\Omega_{e,g_2}}{4\Delta}\left[\exp(i(\Delta-\delta)t) - \exp(-i\delta t)\right] \tag{3.8}$$

Integration of Equation 3.7 yields

$$c_2(t) = \frac{\Omega_{g_1,e}\Omega_{e,g_2}}{4\Delta}\left[-\frac{1-\exp(i(\Delta-\delta)t)}{\Delta-\delta} + \frac{1-\exp(-i\delta t)}{\delta}\right] \tag{3.9}$$

For a near-resonant Raman transition, the Raman laser frequencies are tuned close to the frequency difference between the Raman states, under which condition it is reasonable to assume $\Delta \gg \delta$. With this, Equation 3.9 can be approximated to

$$c_2(t) \sim \frac{\Omega_{eff}}{2}\left[\frac{1-\exp(-i\delta t)}{\delta}\right], \tag{3.10}$$

where Ω_{eff} is the effective Rabi frequency defined by

$$\Omega_{eff} = \frac{\Omega_{g_1,e}\Omega_{e,g_2}}{2\Delta} \tag{3.11}$$

Comparing Equation 3.5 and 3.10 reveals the fact that the state population function for a two-photon transition is identical to the one for a one-photon transition. In a two-photon transition, the transition strength is described by the effective Rabi frequency, which is proportional to the Rabi frequency of individual Raman legs and inversely proportional to the common detuning.

3.2.2 Raman spectroscopy with deeply bound ground states

In this section, a demonstration of ground state transfer via a two-photon Raman transition is exhibited. In this example, the molecules are transferred from $X(-2,0)$ state to $X(6,0)$ state and two lasers with wavelength 689 nm and 651 nm are used to drive the transition. To make the Raman probe lasers coherent, the lasers have to be phase-locked to the same reference frequency. To technically achieve this, a frequency comb is employed. As illustrated in Figure 3.6, the 689 nm probe laser is directly locked to the master laser. However, since the 651 nm laser frequency is too far away from the master laser frequency, the only way to phase-lock it

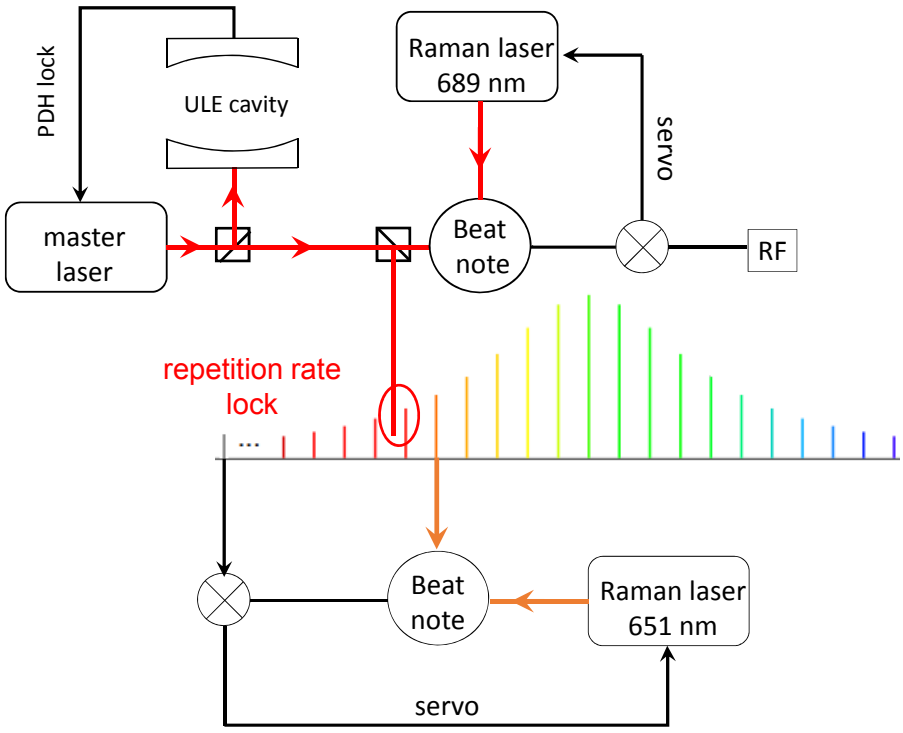

Figure 3.6: Schematic configuration of frequency comb stabilization and Raman probe lasers locking. The 689 nm probe is directly phase-locked to the master laser and the 651 nm probe is stabilized with the frequency comb.

is via the frequency comb. Because the frequency comb is stabilized by the master laser, the coherence between 689 nm and 651 nm probes is achieved. With coherent probe lasers, the two-photon Raman transition is obtained, shown in Figure 3.7. In this demonstration, molecules are initially populated on the $X(-2,0)$ state and the two-photon transition to $X(6,0)$ state is driven with Raman probe lasers blue-detuned from the $0_u^+(-5,1)$ state by 10 MHz.

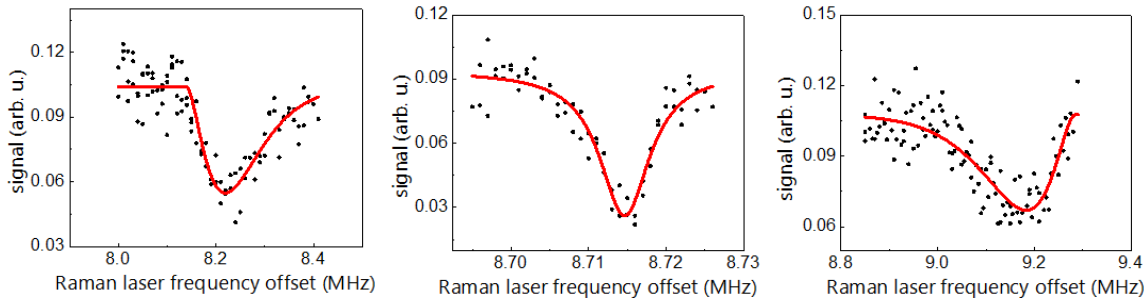

Figure 3.7: Two-photon Raman transition lineshapes between $X(-2,0)$ and $X(6,0)$ states recorded at several lattice frequencies. The Raman transition is driven with Raman lasers detuned by 10 MHz from the $0_u^+(-5,1)$ state. The mismatch in the Raman state polarizabilities results in a clear feature of thermal broadening in the lineshape. Also, the transition frequency varies with the lattice frequency because of lattice light shift. The horizontal axis is the frequency offset of the first Raman laser.

A key feature in the lineshapes is the skewness resulted from thermal broadening. Since the energy difference between the Raman states is over 20 THz, there is a huge mismatch in the Raman states' polarizabilities. Due to this polarizability mismatch, the optical lattice causes severe inhomogeneous broadening. The lineshapes in Figure 3.7 are fit to a thermal broadening model described in detail in [13, 14]. Eliminating this broadening mechanism is crucial for getting a narrow transition line and a method called the *magic-lattice technique* is adopted to accomplish this goal.

Chapter 4

Implementation of a magic lattice trap

4.1 AC Stark shift and magic trapping

The magic lattice trap is a key concept for lattice clocks. In a magic lattice trap, the polarizabilities of the clock states are equal. This technique has led to a breakthrough in the precision of optical atomic lattice clock [73]. In ZLab, ultra-narrow one-photon molecular transitions have also been demonstrated with a magic trap [10], which opens a new regime of molecular metrology. In this chapter I will discuss how to achieve this state-insensitive magic lattice trap for the molecular clock.

Just like the DC Stark shift, an oscillating electric field induces light shifts on energy levels. In an optical lattice trap, the dynamic AC Stark shift on the level $|a\rangle$ induced by a laser trapping field is described by [72]

$$\delta E_a = -\alpha_a(\omega_L)(\frac{\varepsilon_L}{2})^2 + \text{higher-order terms}, \tag{4.1}$$

where ω_L and ϵ_L denote the frequency and amplitude of the laser fields, respectively. The

state-dependent factor α_a is the dynamic polarizability, which is described by

$$\alpha_a(\omega) = \sum_b \frac{|\langle a|\,\mathbf{d}\cdot\hat{\varepsilon}\,|b\rangle|^2}{E_b - E_a - \omega} + \sum_b \frac{|\langle a|\,\mathbf{d}\cdot\hat{\varepsilon}\,|b\rangle|^2}{E_b - E_a + \omega}, \tag{4.2}$$

where $\mathbf{d}$ is the dipole operator, E_i denotes energy levels of all possible states and $\hat{\varepsilon}$ represents the laser field polarization. Equation 4.2 suggests that the dynamic polarizabilities can be tuned with lattice laser frequency, which is the heart of the polarizability matching.

A mismatch in state polarizabilities hurts the performance of the molecular clock in two aspects. First, as suggested in Equation 2.7, a polarizability mismatch means that trap depths for the clock states are unequal. Because the lattice trap is not perfectly harmonic, unequal trap depths result in carrier frequencies that are dependent on lattice motional states. This varying carrier frequencies lead to the inhomogenous broadening [13, 14], which lineshape is demonstrated in Chapter 3. Due to this broadening mechanism, the clock transition cannot be narrowed below 50 kHz, which is far away from the sub-mHz fundamental limit. Second, the unbalanced polarizability leads to a huge systematic error on the frequency measurements. As a result, a nonzero differential light shift is generated. Equation 4.3 describes the differential light shift for the $|1\rangle \rightarrow |2\rangle$ transition

$$\delta\nu_{12} = -\frac{\alpha_1(\omega_L) - \alpha_2(\omega_L)}{h}\left(\frac{\varepsilon_L}{2}\right)^2 \tag{4.3}$$

As $\alpha_1(\omega_L) \neq \alpha_2(\omega_L)$, the differential light shift is lattice-power dependent. Recall the molecular clock relies on the relative binding energy between ground states to probe minuscule change in fundamental physical quantities; such a systematic error is not acceptable in the clock measurements.

Regarding these concerns, the necessity for a magic lattice trap is clear. In the next

section, I will discuss how to achieve a *magic* trap where the polarizabilities are equal for the clock states.

4.1.1 Polarizability matching

The possibility of achieving the magic lattice lies in the fact that dynamic polarizabilites are trap laser frequency dependent. As described in Equation 4.2, the frequency dependence is particularly large when the trap laser is near resonances. Assume the lattice frequency is close to the $|g\rangle \rightarrow |k\rangle$ transition. Then the dynamic polarizability behavior of $|g\rangle$ is dominated by the near-resonance term

$$\alpha_g(\omega) = \frac{|\langle g|\,\mathbf{d}\cdot\hat{\varepsilon}\,|k\rangle\,|^2}{E_k - E_g - \omega} + \underbrace{\left(\sum_{b\neq k}\frac{|\langle g|\,\mathbf{d}\cdot\hat{\varepsilon}\,|b\rangle\,|^2}{E_b - E_g - \omega} + \sum_b \frac{|\langle g|\,\mathbf{d}\cdot\hat{\varepsilon}\,|b\rangle\,|^2}{E_b - E_g + \omega}\right)}_{\text{background term}} \tag{4.4}$$

Since the lattice frequency is tuned near resonance, the $|g\rangle$ polarizability can be modified in a huge range, as illustrated in Figure 4.1. Moreover, due to the large energy spacing between molecular states, while the lattice frequency is being tuned, the background term that consists of the contributions from the other resonances remains fairly constant. This has a beneficial implication: for a clock transition consisting of two arbitrary ground state, the point at which the polarizabilities for both states are matched can be determined by tuning the lattice frequency around a lattice-driven transition resonance. This special lattice wavelength is the so-called *magic lattice wavelength*.

However, not all lattice-driven transitions are suitable for polarizability tuning. For instance, transitions from a weakly bound ground state to a weakly bound excited state ruin the lattice trapping, which would lead to significant molecule scatterings. Also, transitions from a deeply bound ground to a weakly bound excited state would suffer from insufficient

transition strength. As stated in Equation 4.4, the tunability of polarizability is proportional to the dipole transition moment, therefore the polarizability tunability would be very limited with a weak lattice-driven transition. To avoid this limitation, the lattice-driven transitions adopted in this thesis are transitions from deeply bound ground states to deeply bound excited states, as illustrated in Figure 4.2. In the following section, I will discuss the steps toward realizing the magic lattice trap.

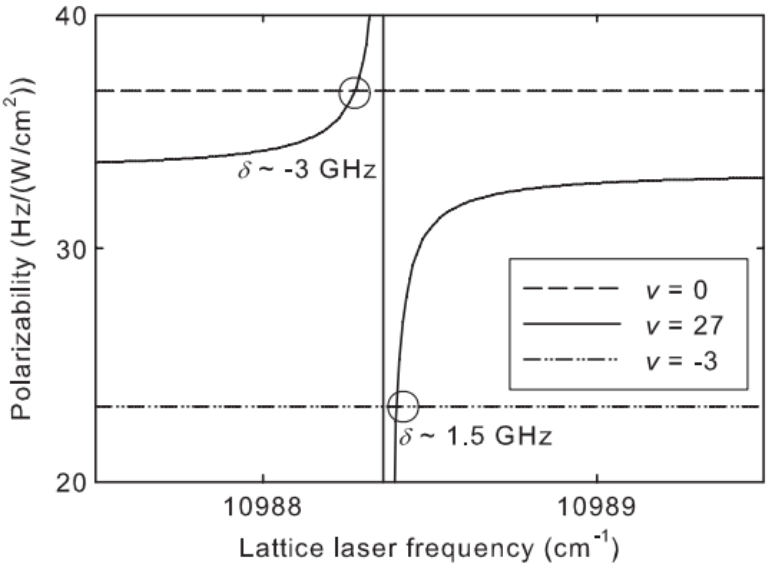

Figure 4.1: In this illustration, the polarizability $X(27,0)$ state is tuned with a 919 nm lattice. The dynamic polarizability of the ground state can be modified in a huge range with the lattice laser tuned close to a resonance. Because the energy difference between clock states is huge, while the polarizability of one state is being tuned, the polarizabilities of the other states remain fairly constant. At $\delta \sim -3$ GHz, the polarizability is tuned to match that of $X(-3,0)$ state and at $\delta \sim 1.5$ GHz, the polarizability is tuned to match that of $X(0,0)$ state. Adapted from [7].

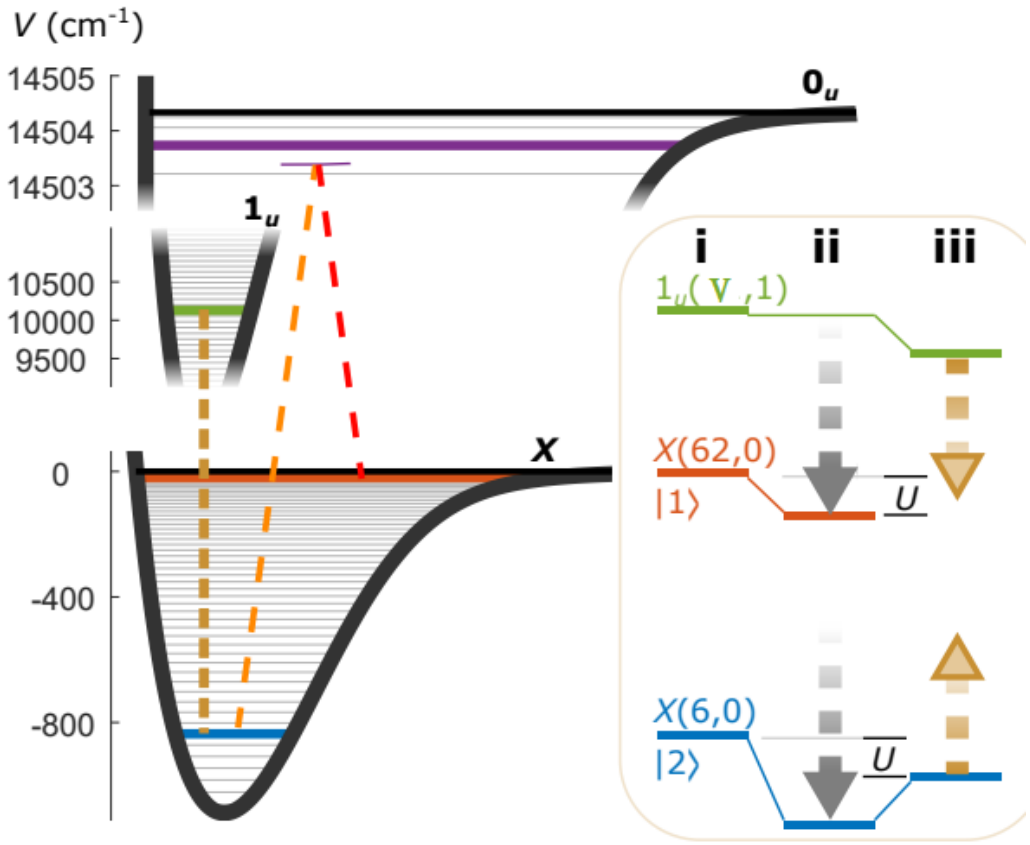

Figure 4.2: For the work described in this thesis, deeply bound 1_u states are used for tuning clock states polarizabilities. In this figure, a two-photon Raman transition is driven between $X(-1,0)$ and $X(6,0)$ via $0_u^+(-4,1)$. To match the clock state polarizabilities, the lattice is parked near the $X(6,0) \rightarrow 1_u(24,1)$ resonance. Inset: (i) states involved in this clock transition (ii) clock state energies are shifted down by different amounts in the lattice as indicated with grey arrows (iii) but at a magic wavelength, $X(6,0)$ is additionally up-shifted (yellow arrows) so that its trap depth U is equal to that of $X(-1,0)$. Adapted from [9].

4.2 Search for deeply bound 1_u states

To achieve a magic lattice trap, bound states with binding energies >10,000 cm^{-1} in the 1_u potential are employed [9]. This is not a unique choice; any transition with sufficient transition strength can do the job. A benefit of using deeply bound 1_u states is their large binding energies. According to the *ab initio* calculations [76], no other ungerade potential asymptoting to $^1S_0 + ^3P_1$ atomic level is as deep as ∼10,000 cm^{-1}. This precludes the possibility of accidental influence from states in another potential.

4.2.1 Search schemes

To search for the deeply bound 1_u states, a method based on the lattice-induced light shifts is employed. The concept is similar to the ground state search with Autler-Townes spectroscopy. In this search scheme, the lattice laser connects the deeply bound clock state to a deeply bound 1_u state. As the lattice is close to the transition resonance, it induces a light shift δf on the deeply bound ground state

$$\delta f = \frac{1}{4}\frac{\Delta\Omega_L^2}{\Omega_L^2/2 + \Delta^2 + \gamma^2/4} \sim \frac{\Omega_L^2}{4\Delta}, \tag{4.5}$$

where Ω_L is the lattice-induced Rabi frequency, Δ is the detuning from the nearest 1_u level which natural linewidth is γ.

Figure 4.3 illustrates the schematic for the deeply bound 1_u state search. Initially, a depletion is set up with the two-photon transition from a weakly bound to a deeply bound ground state. As the lattice frequency is tuned close to a lattice-driven transition from the bottom clock state to a 1_u state, a light shift is induced on the bottom clock state so that an increase in the depletion signal is observed.

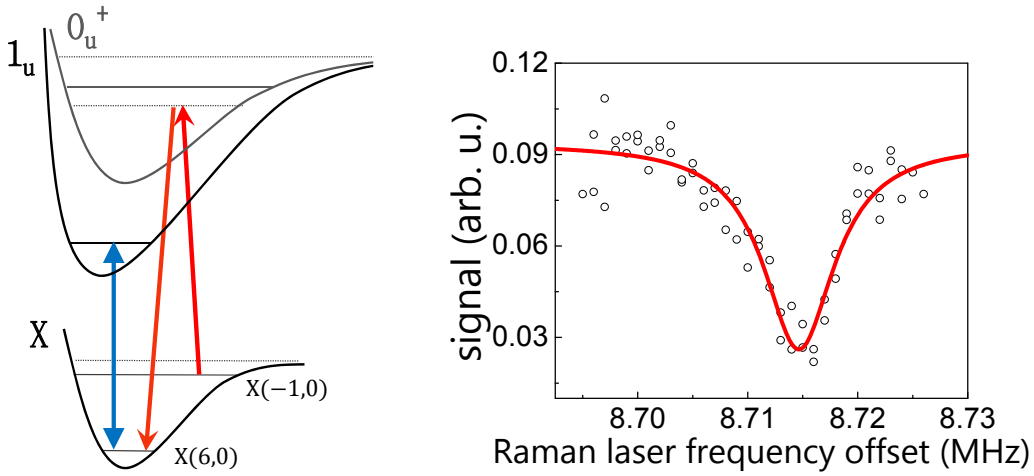

Figure 4.3: The method via lattice-induced light shift is employed to search for deeply bound 1_u states. Initially a depletion is setup with the two-photon Raman transition (red and orange) from weakly bound $X(-1,0)$ to deeply bound $X(6,0)$ (right). With the Raman transition kept at resonance, the lattice frequency is tuned to look for the 1_u states. As the lattice laser is close to a lattice-driven transition (blue), a light shift is induced on the deeply bound state. Due to this induced light shift, the original Raman transition is no longer on resonance and thus a signal increase can be observed.

With this light shift method, several deeply bound 1_u states have been located. Table 4.1 summarizes the binding energy for those states. Several months after these light shift measurements were carried out, another lattice system was constructed. With the new lattice system, the original lattice laser can be used as a spectroscopic laser, which allows an alternative way to measure binding energies with one-photon spectroscopy. The comparison of binding energies measured with light shift method and one-photon spectroscopy is presented in Section 4.2.3.

vibrational level v'	rotational level J'	binding energy (THz)
26	1	129.584,5(1)
25	1	131.757,4(1)
24	1	133.943,8(1)
23	1	136.143,2(1)
...	...	...
7	1	173.083,9(1)
6	1	175.499,2(1)
5	1	177.926,8(1)

Table 4.1: Binding energy of deeply bound 1_u states measured with lattice-induced light shifts. The binding energies are calculated with respect to the $^1\mathrm{S}_0 + ^3\mathrm{P}_1$ threshold.

Several comments about these measurements:

- The precision for these measurements is limited by the wavelength meter uncertainty. With direct one-photon spectroscopy, the binding energies can be determined with higher precision. A detailed data analysis for backing out the binding energies will be presented in Section 4.2.2.

- Assigning vibrational levels for deeply bound 1_u states is not as straightforward as for the deeply bound ground states. In the case with ground states, the assignments are based on comparisons of measurements and *ab initio* calculations. The level numbers quoted in the Nature Physics publication [9] are also based on these comparisons. However, it has been realized that the complexities in the excited potentials make such comparisons less reliable for assigning levels to deeply bound excited states. Recently, a more accurate way for assigning deeply bound 1_u states has been developed. This topic will be discussed in Section 4.2.4.

- The readers may be anticipating the avoided-crossing from Autler-Townes doublet like what is demonstrated with ground states. However, observing such behavior is challenging in the case when the lattice light also serves as the probe laser. As the lattice frequency approaches the lattice-driven transition resonance, a huge polarizability shift is induced on the deeply bound ground state, which makes it impossible to collect spectroscopy. To resolve the Autler-Townes doublet, it requires the separation in the role of the probe laser and the trapping laser, which will be examined in Section 4.2.5.

- Binding energy measurements are performed with deeply bound states in two different regions in the 1_u potential. Among the 1_u states, we would like to find the one that is the best in maintaining the clock transition coherence. Even though a lattice-driven transition can help match the clock state polarizabilities, it could impose other limitations on the clock coherence from the issues such as frequency instability and accidental multi-photon loss. The criteria for selecting good lattice-driven transitions are explored in Section 4.3.3.

4.2.2 Binding energies of deeply bound 1_u states

In this section, the analysis on the binding energy of deeply bound 1_u states is demonstrated. As described in Equation 4.5, the light shift changes with lattice frequency detuning in an anti-symmetric manner: a positive light shift is induced with a blue-detuned lattice and vice versa. Therefore, by fitting the light shift, the resonance frequency can be obtained. Figure 4.4 illustrates the lattice-induced light shift on the $X(-1,0) \rightarrow X(6,0)$ Raman transition with $X(6,0) \rightarrow 1_u(24,1)$ as the polarizability-tuning transition.

The fitting in Figure 4.4 yields a pretty tight error of $\sim$10 kHz on the transition resonance frequency. However, the actual uncertainty is larger than this since the lattice frequencies in

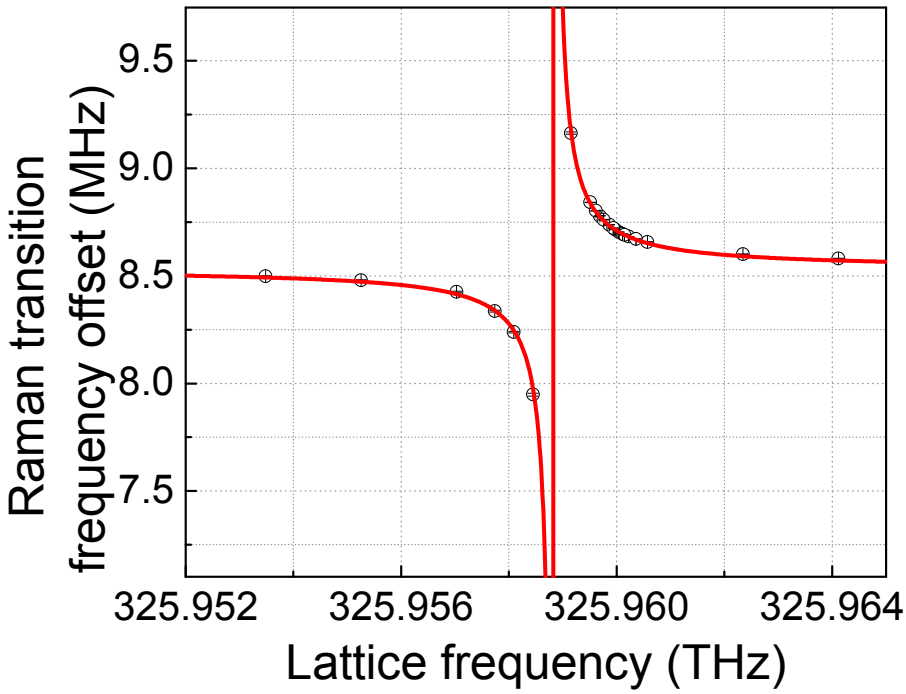

Figure 4.4: Dramatic light shift of the $X(-1,0) \rightarrow X(6,0)$ Raman transition occurs as the optical lattice is tuned across the $X(6,0) \rightarrow 1_u(24,1)$ transition. The binding energy of the 1_u state can be obtained from fitting the dispersive curve. By fitting this data to Equation 4.5, a resonance frequency of 325.958,824,720(5) THz is yielded.

Figure 4.4 are obtained from the wavelength meter (WS6 200 MC from HighFinesse), which is subject to an intrinsic uncertainty of 100 MHz.

Figure 4.5 illustrates the schematic for calculating the binding energy of the 1_u state. With the resonance frequency obtained from fitting the light shift curve, the 1_u state binding energy can be calculated with pre-determined $X(6,0)$ state binding energy and the $^1\mathrm{S}_0 + ^3\mathrm{P}_1$ threshold energy. Here the $X(6,0)$ binding energy is adapted from Table 3.1 and the $^1\mathrm{S}_0 + ^3\mathrm{P}_1$ intercombination line is assumed to be 434.829,121,313(10) THz according to reference [80]. With these numbers, the binding energy can be calculated as follows

$$\text{B.E.} = \text{intercombination line} - (\text{ground state B.E.} + \text{lattice frequency})$$

$$= 434.829,121,313(10)\ \text{THz} - [-25.073,513,155(5)\ \text{THz} + 325.958,82(1)\ \text{THz}]$$

$$= 133.943,8(1)\ \text{THz}$$

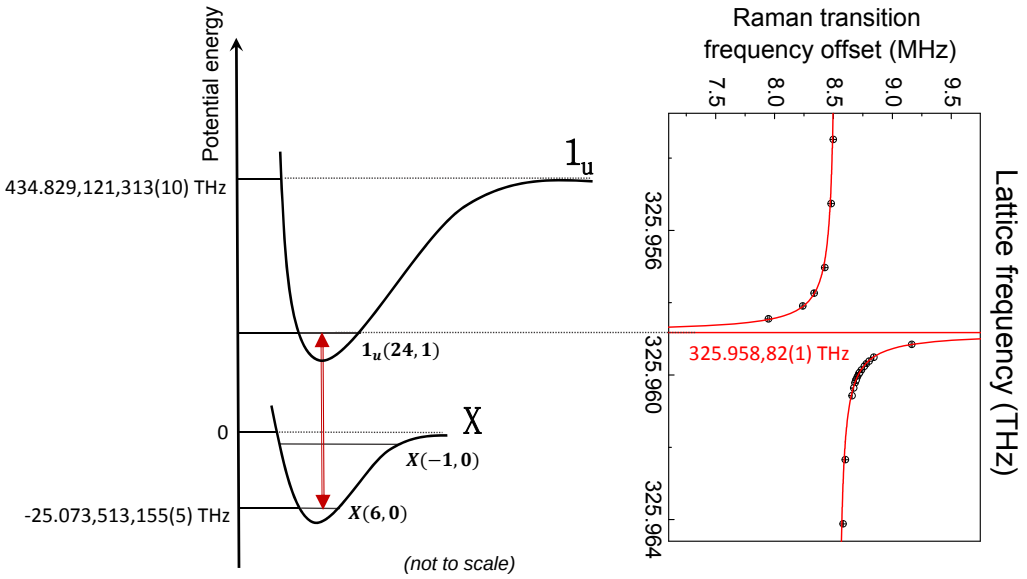

Figure 4.5: The 1_u state binding energy can be backed out by the light shift fitting result together with the pre-determined deeply bound ground state binding energy.

Although the precision on 1_u state binding energies is limited, the lattice frequency for a magic trap can be determined much more precisely. In Section 4.3.2 I will demonstrate how a 10 kHz uncertainty in determining magic frequency can be achieved with differential light shift. Figures 4.6 and 4.7 summarize the light shift dispersive curves for all seven deeply bound 1_u states that have been found.

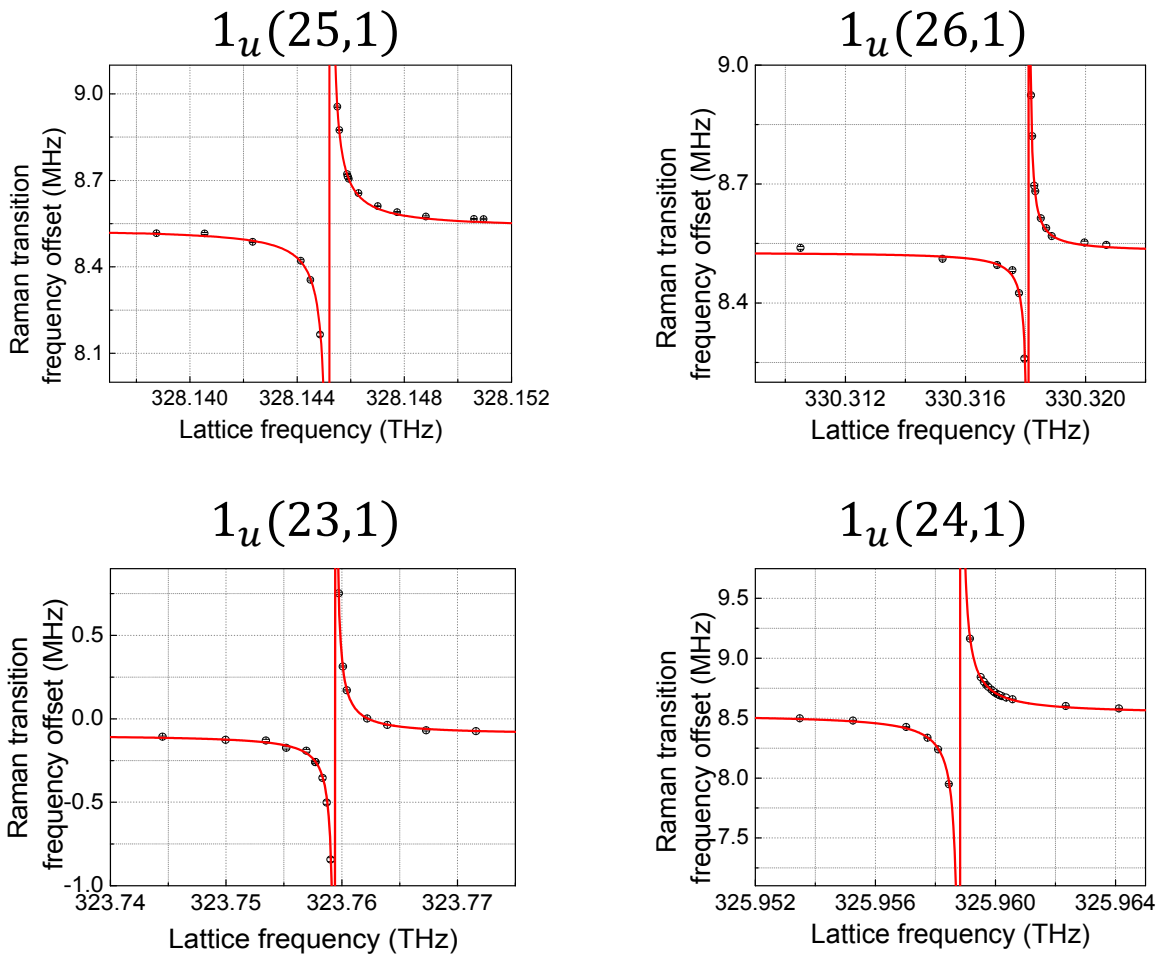

Figure 4.6: Light shifts due to lattice-driven transitions from $X(6,0)$ to $1_u(v'$=23,24,25,26;J'=1). The lattice frequency for these resonances is

vibrational level v'	lattice frequency (THz)	lattice wavelength (nm)
26	330.318,104,041(5)	907.587,1(2)
25	328.145,206,020(5)	913.596,9(2)
24	325.958,824,720(5)	919.724,9(2)
23	323.759,417,264(5)	925.972,9(2)

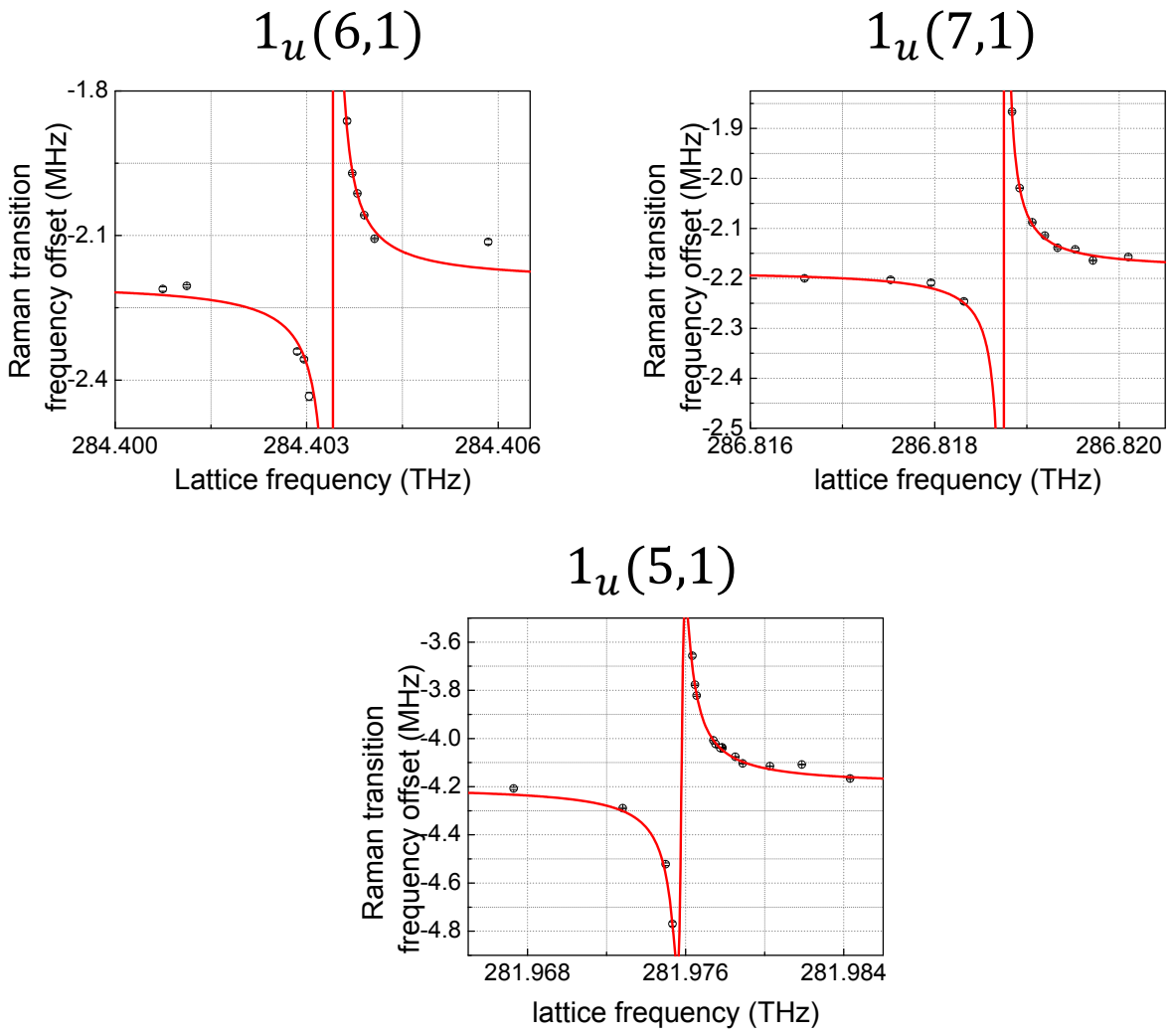

Figure 4.7: Light shifts due to lattice-driven transitions from $X(6,0)$ to $1_u(v'$=5,6,7;J' =1). The lattice frequency for these resonances is

vibrational level v'	lattice frequency (THz)	lattice wavelength (nm)
7	286.818,749,337(5)	1045.233,1(2)
6	284.403,412,893(5)	1054.109,9(2)
5	281.975,790,174(5)	1063.185,1(2)

4.2.3 Direct one-photon spectroscopy

In this section, the 1_u states binding energies measured with one-photon depletion spectroscopy are presented. To perform depletion spectroscopy, another infrared laser system was constructed for lattice trapping and the original infrared light could serve as a spectroscopic laser. The binding energy measured with this method is not subject to the wavelength meter uncertainty. As later demonstrated in this section, an uncertainty of $\sim$1 MHz on the binding energies can be obtained with depletion spectroscopy.

The original motivation for performing one-photon spectroscopy on deeply bound 1_u states is to resolve the Autler-Townes doublet. This has the importance in constructing the molecular clock because it provides an accurate way to measure the transition strength. The topic on transition strength measurement is discussed in Chapter 7. As high precision for excited state binding energies is not of crucial importance in the context of the molecular clock, only a few states in Table 4.1 will be replicated in this section.

Figure 4.8 illustrates the scheme for a 1_u state depletion spectroscopy. The molecules are initially populated on the $X(6,2)$ state via a two-photon Raman transition. To collect the spectroscopy, an infrared laser with wavelength $\sim$919 nm is scanned through the $1_u(24,1)$ state. Because the spectroscopic laser is phase-locked to the comb, its frequency can be well determined and controlled. One caveat about this measurement is that the lattice trap is not magic for this transition and thus a nonzero differential light shift is present. To cope with this systematic bias, the spectroscopy is performed with two different lattice power, from which the actual transition frequency can be extrapolated.

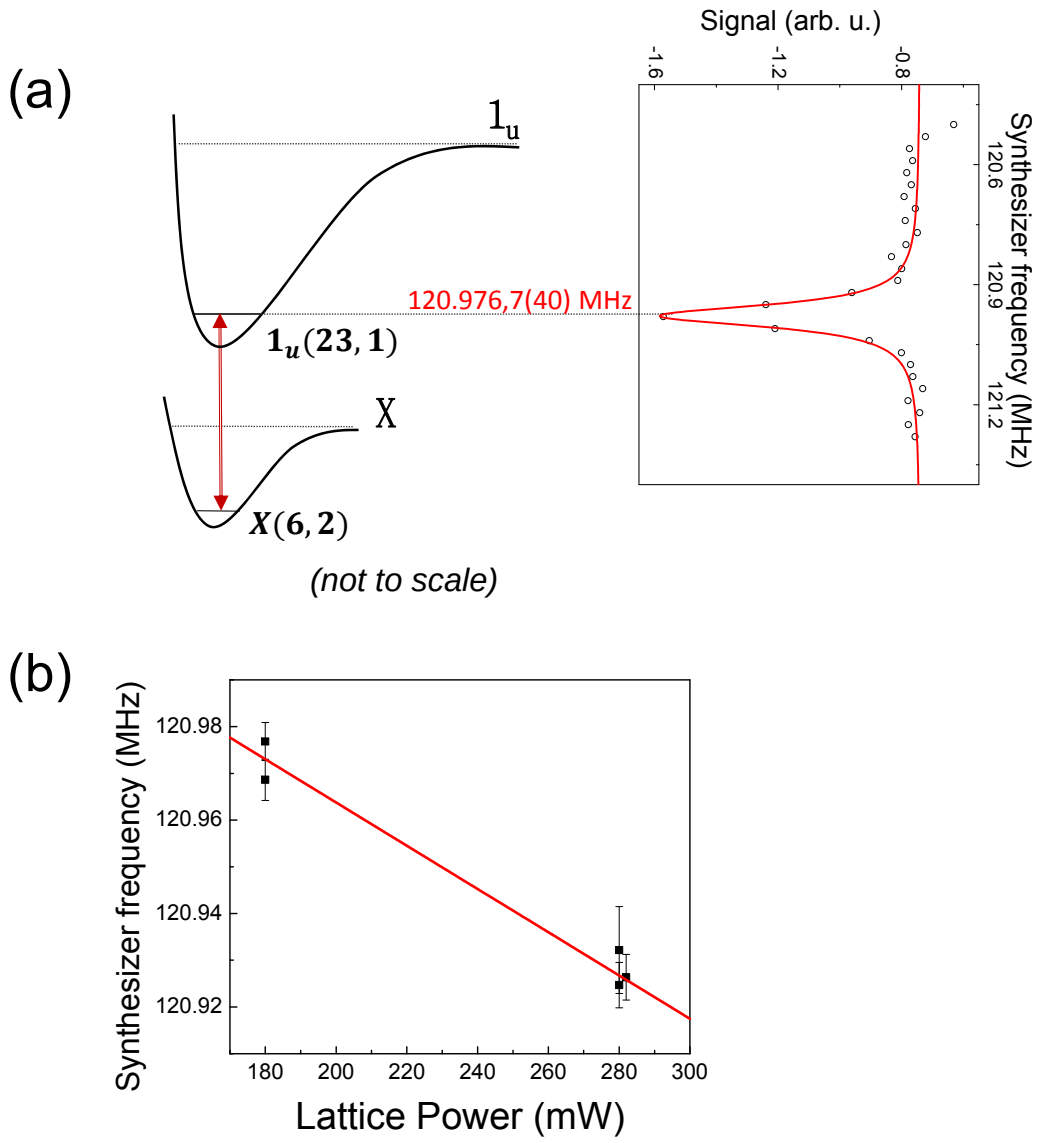

Figure 4.8: Probing the 1_u state with one-photon depletion spectroscopy. (a) With the probe laser phase-locked to the frequency comb, the 1_u state binding energy can be determined more precisely. (b) To cope with the systematic bias due to a non-magic lattice, the spectroscopy is performed with two different lattice power, from which the actual transition frequency can be extrapolated. In the fit the slope is $-0.46(4)$ kHz/mW and the intercept is 121.06(1) MHz.

Note that the synthesizer frequency in Figure 4.8 doesn't directly mean the actual spectroscopic laser frequency but it has to do with how the laser is scanned. Figure 4.9 illustrates the setup of the infrared probe laser. Explanation of how the setup scheme is crucial for binding energy calculations.

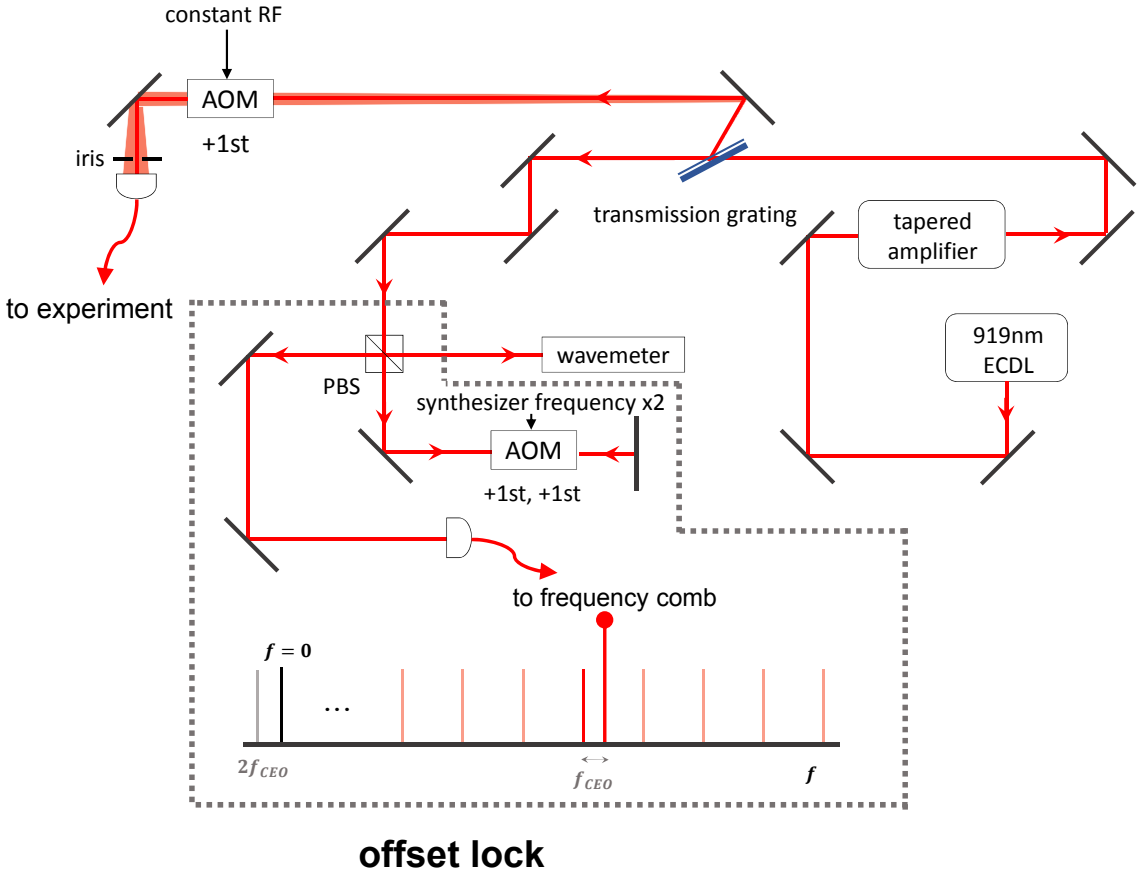

Figure 4.9: Schematic configuration of the infrared probe light system. The laser is offset-locked to the frequency comb, which is done with optics inside the grey area. To obtain the depletion spectroscopy, an acousto-optic modulator (AOM) is scanned by a frequency synthesizer which output goes through a frequency doubler. The other AOM before the experiment fiber is in place to serve as a shutter and it is controlled by a constant RF frequency. The transmission grating is irrelevant to the binding energy measurement. Its purpose will be discussed in Chapter 5).

The setup for this infrared laser system is of crucial importance for the molecular clock. The laser light is initially generated from an ECDL and amplified by a TA. After the TA a transmission grating is in place. The purpose of this grating is irrelevant to the binding energy measurement but is crucial for tackling the issue with background noise in the TA spectrum. Its operation principle is described in Section 5.1.2. Typically more than 90% of the laser beam can be diffracted into the +1st order and be used for the experiment. The small non-diffracted portion transmits the grating and is employed for the offset locking scheme.

In the offset locking scheme, the laser beam goes through an acousto-optic modulator (AOM) that is controlled by a frequency synthesizer. Note that the output of the synthesizer is frequency-doubled to match the specification of the AOM. The modulated beam from the AOM is coupled to the frequency comb and phase-locked to the nearest comb tooth. It is important to note that in this experiment the f_{CEO} was locked on the negative side, which means case (b) in Figure 2.3 applies.

The steps for calculating the $1_u(23, 1)$ state binding energy are described below. Firstly, the laser frequency *before the offset lock* is read by the wavelength meter to be $f_0 = 925.9813$ nm. Note that the wavelength meter needs to be calibrated by the atomic transition. When the spectroscopy was collected, the wavelength meter read the $^1\mathrm{S}_0 + ^1\mathrm{P}_1$ transition as $\frac{1}{2} \times 921.9233$ nm. The actual wavelength for this atomic transition is well-known, which should be $\frac{1}{2} \times 921.9240$ nm. According to this, the wavelength of the infrared probe laser should be corrected to $f_0^{\mathrm{corr}} = 925.9820(3)$ nm. On the other hand, the frequency comb counter read the f_{CEO} and f_{RR} as 20 MHz and 250,011,947.117,85(12) Hz, respectively. With these numbers, the comb tooth number to which the spectroscopic laser is locked can be backed out. Since the laser was locked on the *blue side* of the comb tooth, we have

$$\underbrace{f_0^{\text{corr}} + 4f_{\text{synthesizer}}}_{\text{raw frequency shifted by offset lock.}} = \underbrace{-2f_{\text{CEO}} + Nf_{\text{RR}}}_{\text{frequency of the N-th comb tooth}} + f_{\text{CEO}},$$

which indicates $N = 1,294,964.96(42) \sim 1,294,965$.

With the comb tooth number backed out, the rest part is straightforward. In Figure 4.8(b), the transition resonance frequency is obtained to be $f_{\text{synthsizer}} = 121.06(1)$ MHz, therefore the laser frequency seen by the molecules is

$$\underbrace{-2f_{\text{CEO}} + 1,294,965f_{\text{RR}}}_{\text{reference freq.}} + \underbrace{f_{\text{CEO}}}_{\text{b.n.}} - 4f_{\text{synthsizer}} + \underbrace{f_{\text{shutter}}}_{\text{80 MHz for this state}}$$
$$= 323.756,296,86(4) \text{ THz}$$

With the $X(6,2)$ binding energy listed in Table 3.1, the $1_u(23,1)$ state binding can be calculated to be

$$434.829,121,311(10) \text{ THz} - [-25.070,581(1) \text{ THz} + 323.756,296,86(4) \text{ THz}]$$
$$= 136.143,375(1) \text{ THz}$$

With the depletion spectroscopy the uncertainty in determining 1_u state binding energy is reduced to $\sim$1 MHz, corresponding to $Q \sim 10^9$. Note that this limit is not fundamental. Even more precise measurements can be obtained by reducing the power broadening and with a magic lattice trap.

The binding energy obtained in this way is consistent with that obtained through the light shift measurements. Table 4.2 summarizes the comparison between these two methods with three 1_u states.

v	J	light shift measurement	one-photon spectroscopy
26	1	129.584,5(1)	129.584,620(1)
24	1	133.943,8(1)	133.943,644(1)
23	1	136.143,2(1)	136.143,405(1)

Table 4.2: Comparison of 1_u state binding energies obtained with light shift measurement and one-photon spectroscopy. Binding energies are in the unit of THz. The shutter AOM frequency is 110 MHz for $v' = 24, 26$.

4.2.4 Vibrational number assignment for deeply bound 1_u states

In this section, I discuss the vibrational level assignments for deeply bound 1_u states. In the Nature Physics paper, the four 1_u states with binding energy around 130 THz in Table 4.1 are assigned to $v' = 19, 20, 21$ and 22. These assignments are given based on the comparison of measured transition frequencies and *ab initio* calculations. However, it turns out that this comparison method only works for ground states but not for excited states. With the previous assignments, the binding energies of 1_u states agreed well with the theoretical model but the measured transition dipole moments squared (DMS) between $X(6, 0)$ and 1_u states were very off from predictions. The discrepancies in binding energies were within 1 GHz whereas the DMS's could be off by orders of magnitude. This seemly contradictory observation is due to the fact that the 1_u potential depth was not characterized precisely enough.

The improved method for assigning deeply bound 1_u states takes into account the DMS's more seriously. With carefully measured DMS's for multiple lattice-driven transitions, the molecular model has been calibrated. With this calibration, it turns out the 1_u potential depth is actually deeper and thus several very deeply bound ground states in the bottom of the potential are found missing in the original model. According to the calibrated model, the new assignments listed in Table 4.1 are obtained. Figure 4.10 illustrates the comparison

of measured and predicted DMS's. The fact that the trend in measured DMS's agrees nicely with theory indicates the new assignments are very likely the *only possible choices*. As shown in Figure 4.10, the DMS's exhibit an obvious oscillatory behavior with state levels. In other words, a slight miss in the level assignment would lead to dramatic different DMS's.

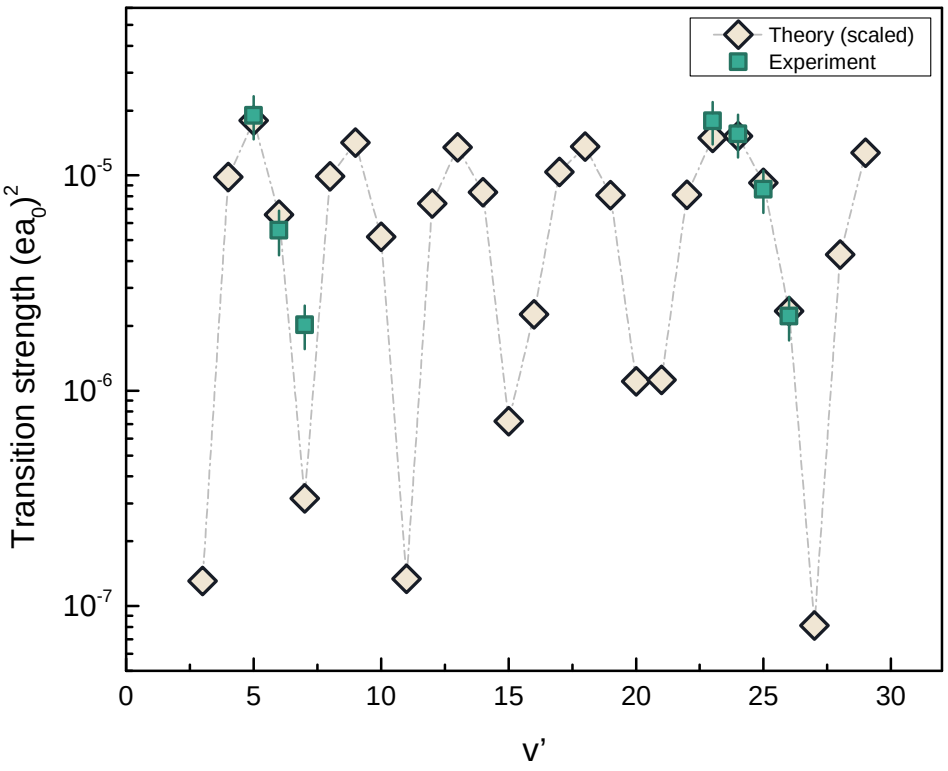

Figure 4.10: Comparison of measured 1_u states' transition dipole moments squared (DMS) and *ab initio* model. Calibrating the model with new found deeply 1_u states helps characterizing the potential better. According to the calibrated model, the new assignments listed in Table 4.1 are obtained.

4.2.5 Three-photon Autler-Townes spectroscopy

In this section, the Autler-Townes spectroscopy with the deeply bound 1_u transitions is presented. This is one of the most difficult spectroscopy that's been carried out in Sr experiment at ZLab.

As previously described, Autler-Townes spectroscopy is created when depletion spectroscopy is perturbed by a coupling laser. In the case of deeply bound ground states, it takes three photons to accomplish the spectroscopy: the depletion process is the two-photon Raman transition from a weakly to a deeply bound ground state and the coupling is a transition connecting the deeply bound ground state to a deeply bound 1_u state. Figure 4.11 illustrates a demonstration where the Raman transition between $X(-1, 0)$ and $X(6, 0)$ state is taken as the probe transition and $X(6, 0) \rightarrow 1_u(24, 1)$ is adopted for the coupling transition.

There are several factors that make obtaining this spectroscopy challenging. First of all, the coupling laser couldn't be too strong, which means an additional laser is needed for trapping. Including more lasers naturally adds complexity to the experiment. Secondly, phase-locking the lattice is untenable because the lattice is in the 1064 nm region, which is out of the comb supercontinuum range. In consequence, Raman transition can't be run at the magic wavelength and thus not only is the S/N ratio greatly sacrificed, but the signal sensitivity is also reduced. Last but not least, to pin down the location of 1_u state resonances, direct one-photon spectroscopy is required. However, this is beyond the capability of the experiment sequence controller so at the time when we took this data a person had to sit down at a corner of the lab and very carefully tuned the laser frequency by hand. (This was not easy and took us some efforts to get rid of human phase slips.) Considering these difficulties, we are grateful in the success of achieving this three-photon Autler-Townes spectroscopy.

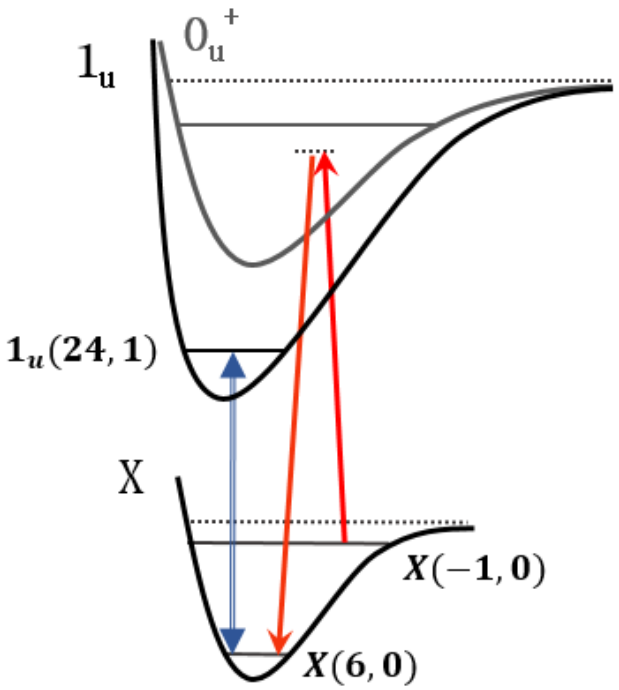

Figure 4.11: Schematics for the three-photon Autler-Townes spectroscopy. The data shown in this section is from the experiment where a two-photon Raman transition from $X(-1,0)$ to $X(6,0)$ state is perturbed by an infrared transition from $X(6,0)$ to $1_u(24,1)$ state. When the infrared probe approached the transition resonance, the laser field was coupled to the molecular Hamiltonian and thus the bottom ground state is split.

Figure 4.12 demonstrates the results of the spectroscopy. To get this data, at each infrared laser frequency, the *first Raman laser* was scanned. We could have also scanned the second Raman laser but we made our choice simply because the first Raman laser power was more stable when being scanned. Note that scanning the first Raman laser implies the common detuning of the Raman transition would be different as the infrared frequency is altered. The experiment described now was not sensitive to this subtlety but one should be careful in choosing the right laser to scan when a fixed common detuning is needed.

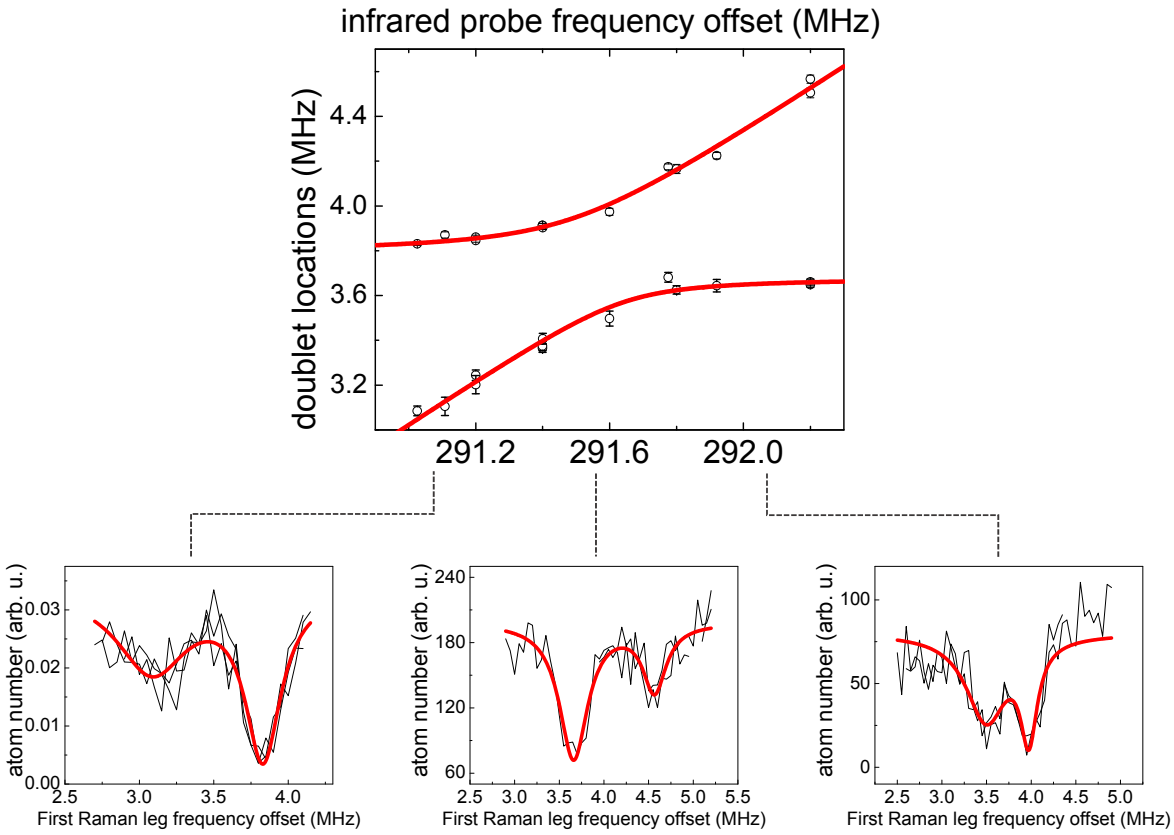

Figure 4.12: A demonstration for three-photon Autler-Townes spectroscopy. Here the two-photon Raman transition between $X(-1,0)$ and $X(6,0)$ state is taken as the probe transition and $X(6,0) \rightarrow 1_u(24,1)$ is adapted for the coupling transition. At each coupling laser frequency, the first Raman laser frequency is scanned for the Autler-Townes doublets.

4.3 Characteristics of a magic lattice trap

With deeply bound 1_u states found, a lattice that is magic for the clock transition can be achieved. In this section, several characteristics of a magic trap are presented, including clock transition lineshape and differential light shifts. At the end of this section, the criteria for good lattice-driven transitions will also be explored.

4.3.1 Clock lineshape with a magic trap

The polarizability of the deeply bound ground state is strongly modified as the lattice-driven transition is close to resonance. When the lattice-driven transition is far from the resonance, the clock transition suffers from inhomogeneous broadening. As the lattice is at the magic wavelength, the inhomogeneous broadening is eliminated and thus the transition linewidth becomes a lot narrower. If the lattice frequency is too close to resonance, the polarizability of the bottom ground state is over tuned and an inhomogeneous broadened lineshape reoccurs.

Figure 4.13 exhibits the lineshape evolution of $X(-1,0) \rightarrow X(6,0)$ clock transition as the lattice frequency is scanned through the lattice-driven transition resonance $X(6,0) \rightarrow 1_u(24,1)$. The polarizability of $X(6,0)$ state is *initially larger* than that of $X(-1,0)$ state, which implies the lower clock state is more deeply trapped. To have a homogeneous trap, it is expected that the magic wavelength occurs on the *blue side* of the lattice-driven transition. In Figure 4.13(a), the lattice is way blue-detuned, resulting in an inhomoegneous broadened clock transition lineshape. As the lattice comes closer to the resonance, shown in (b), the polarizability mismatch is alleviated so that the inhomogeneous effect is diminished, leading to a narrower linewidth. In (c) the lattice reaches the magic wavelength, at which case the inhomogeneous effect is completely eliminated and thus the lineshape becomes symmetric and the linewidth is greatly reduced. As the lattice frequency keeps moving toward the resonance, the lattice becomes non-magic again. Also, since the polarizability of the lower state is over tuned, an inverted inhomogenous broadened lineshape occurs. When the lattice frequency is tuned across the resonance, the relative polarizability is inverted back and the original asymmetric lineshape reoccurs, as shown in (e) and (f).

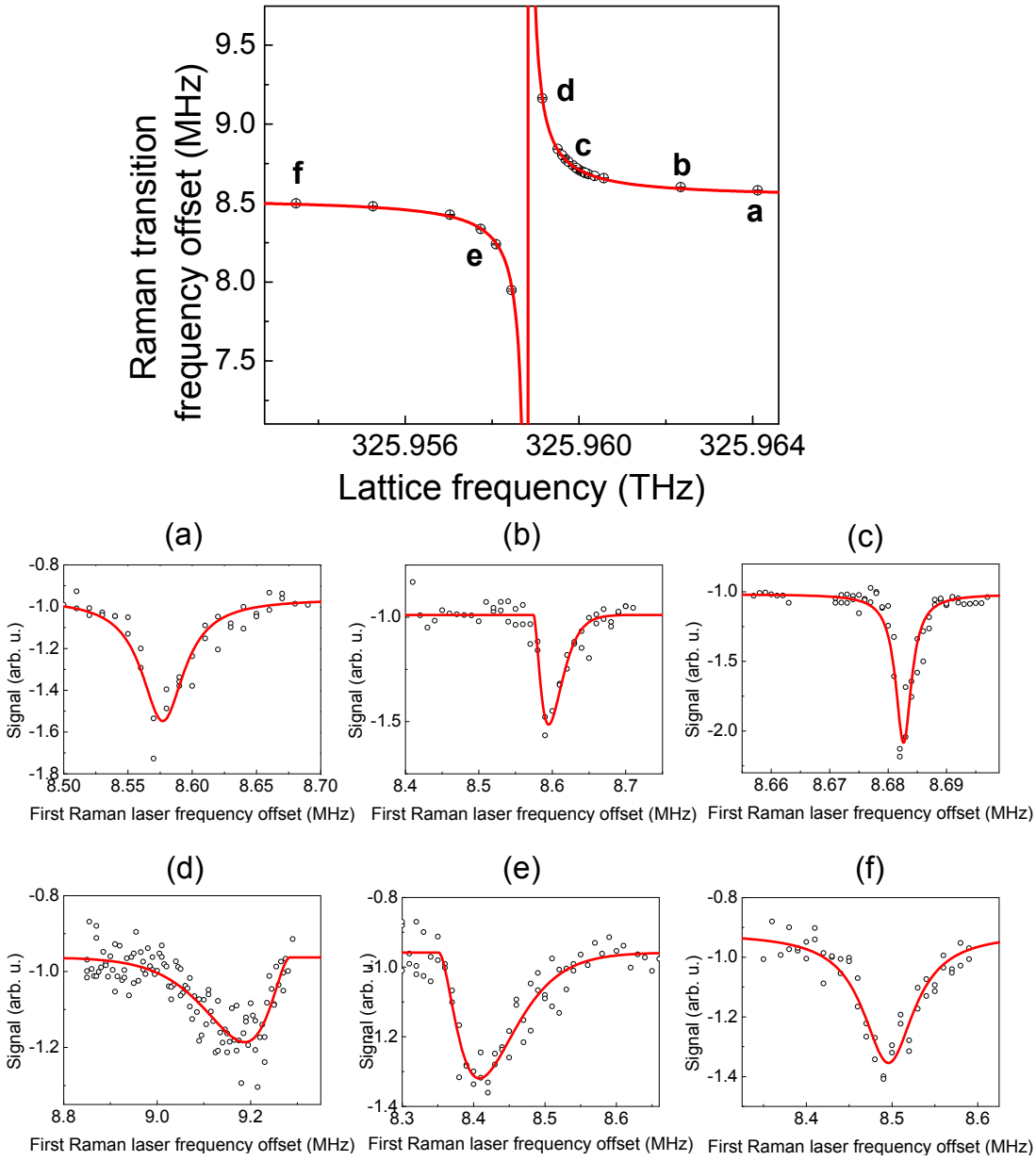

Figure 4.13: Two-photon Raman transition lineshapes at different lattice frequency. Since the polarizability of the lower clock state is initially larger, the magic wavelength is expected to appear on the blue side of the transition.

Figure 4.14 demonstrates the dependence of the clock transition linewidth on the lattice frequency. At the magic wavelength, the linewidth is reduced from over 100 kHz down to less than 2 kHz. Note that this data is taken with a software-locked lattice. In Section 4.3.2 it will be demonstrated that the linewidth can narrowed down to sub 100 Hz with a phase-locked lattice.

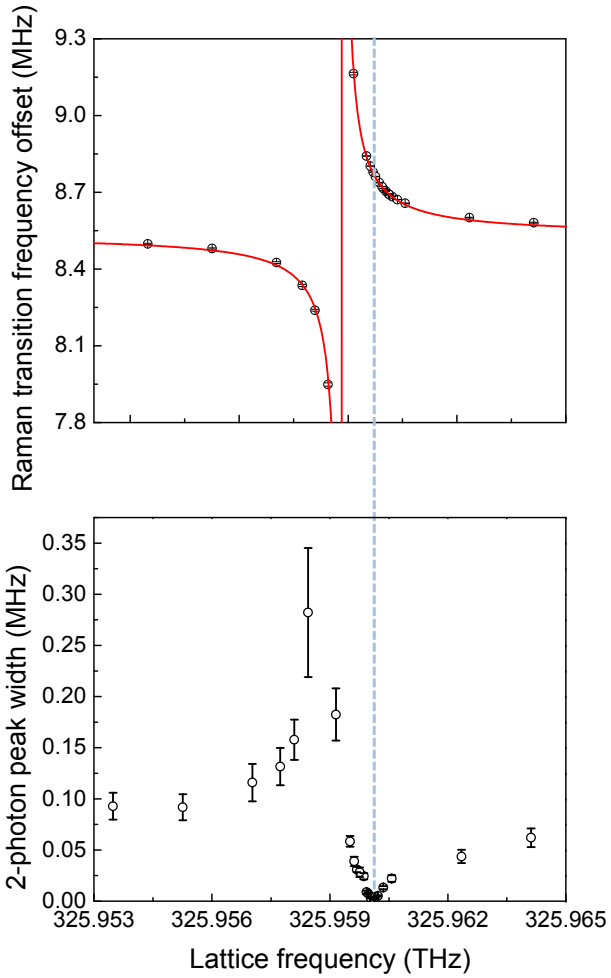

Figure 4.14: Two-photon Raman transition linewidth as a function of lattice frequency. At the magic wavelength, the linewidth is greatly reduced from over 100 kHz down to < 2 kHz. This data was taken with a software-locked lattice.

4.3.2 Differential light shift

In the previous section, it has been proven that the mismatch in clock state polarizabilities can be overcome by tuning the lattice frequency at the magic wavelength. Also, the more precise the magic wavelength is determined, the more narrow the linewidth is. In this section, a method to precisely pin down the magic wavelength using the differential light shift is explored.

In Section 4.1, the AC Stark shift for a two-photon transition is derived. As Equation 4.3 suggests, the differential light shift induced by the optical lattice is proportional to lattice power and clock state polarizability mismatch. This dependence of differential light is an iconic feature that characterizes a magic trap and has been demonstrated in different clock experiments [31–33]. Due to its high sensitivity to polarizability mismatch, measuring the differential light shift offers a reliable way to determine the magic wavelength.

Figure 4.15 demonstrates the magic wavelength determination. In (a), the $X(-1,0) \rightarrow X(6,0)$ clock transition frequency is measured with various lattice frequencies at high and low lattice power. The lattice frequency is tuned near the $X(6,0) \rightarrow 1_u(23,1)$ resonance and the power is varied between 180 mW and 90 mW. Since the lattice frequency is tuned near a resonance, the clock state polarizability mismatch is strongly modified according to the lattice frequency. As a result, the difference in differential light shifts between high and low lattice power would also be different. In (b), the light shift difference is plotted against lattice frequency. In this figure, the magic wavelength is the x-intercept, where the difference in light shifts between low and high lattice power vanishes.

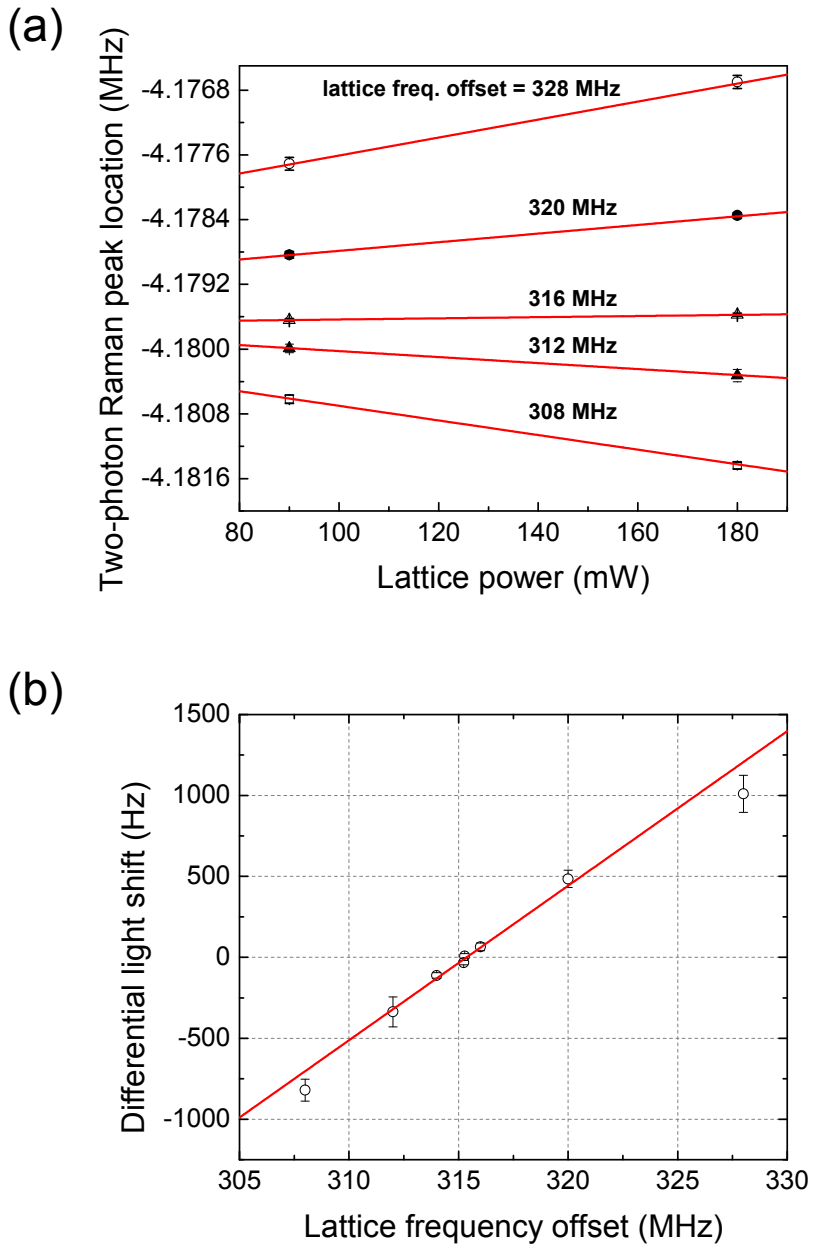

Figure 4.15: Determination of magic wavelength via differential light shift. (a) At each lattice frequency, the light shifts are measured with 90 mW and 180 mW lattice power. Because the polarizability mismatch is modified by the $X(6,0) \rightarrow 1_u(23,1)$ resonance, the difference in the light shifts varies with the lattice frequency. (b) The difference in the light shifts as a function of lattice frequency is shown. The magic wavelength is the x-intercept, where the polarizability difference is zero. The fitted line indicates the magic wavelength happens when the lattice frequency offset is at 315.36(12) MHz.

The accuracy of determining the magic wavelength this way depends on the Raman transition linewidth. The data in Figure 4.15 is taken with a $\sim$ 800 Hz Raman linewidth, which yields an uncertainty of 120 kHz, or a fractional error of 3×10^{-10}, in the magic wavelength. Using a narrower linewidth would increase the sensitivity to light shifts and thus help determine the magic wavelength with even higher accuracy.

4.3.3 A series of magic lattice traps

In Section 4.2, the search for lattice-driven transitions is presented. All of those resonances can serve the purpose of equalizing the clock state polarizabilities. However, there are indeed some lattice-driven transitions that possess unique characteristics, make them a better choice for the purpose of the molecular clock. In general, a good lattice-driven transition should possess two qualifications: (1) it maintains good frequency stability on the clock transition and (2) it minimizes off-resonance scattering on the clock states. In this section, these criteria for good lattice-driven transitions will be explored.

frequency stability transfer

First of all, a good lattice-driven transition should prevent transferring frequency instabilities to the clock Raman transition. To match the polarizabilities, the lattice has to sit on the side of the lattice-driven transitions. Due to the steep slope of the light shift curves, the lattice frequency instability is encoded on the clock transition. This frequency instability transfer can be quantified as

$$\delta f = s_m \times \delta f_{lattice}, \tag{4.6}$$

where s_m is the slope of polarizability curve at the point of magic wavelength. A good

lattice-driven transition for the molecular clock is the one that is the least sensitive to lattice instability. In other words, it should have the minimum curve slope at the magic wavelength. Equivalently, this transition is also the one that has the largest lattice-driven Rabi frequency. This is manifest from the light shift equation. In Equation 4.5, the light shift is approximated as $\delta f = \frac{\Omega_L^2}{4\Delta}$, where Ω is the lattice-driven Rabi frequency and Δ is the lattice detuning from the transition resonance. For a given pair of clock states, the required light shift f_m for matching the polarizabilities is fixed and the magic lattice trap occurs at

$$\Delta_m = \frac{\Omega_L^2}{4f_m}. \tag{4.7}$$

From Equation 4.7, the curve slope at the magic wavelength can be calculated

$$s_m = \frac{d}{d\Delta}\delta f\Big|_{\Delta=\Delta_m} = \frac{4f_m^2}{\Omega_L^2}. \tag{4.8}$$

Equation 4.8 implies that stronger transitions lead to smaller curve slopes and thus are better choices for the molecular clock.

Figure 4.16 compares four different lattice-driven transitions. The lattice couples $X(6,0)$ to $1_u(v' = \{23-26\}, J' = 1)$ and the clock transition is formed with $X(-1,0)$ and $X(6,0)$ states. For each transition, the light shift on the $X(6,0)$ state is plotted against the lattice detuning from resonance. The measurements are performed at lattice power of 200$\sim$230 mW. From this demonstration, the $1_u(23,1)$ resonance implies the gentlest slope while the $1_u(26,1)$ implies the steepest slope. To compensate for the polarizabilities unbalance, the bottom clock state should be up-shifted by $f_m \sim$200 kHz. Because f_m is state-independent, the curve slope at the magic wavelength is inversely proportional to DMS, which is nicely corroborated by Figure 4.10.

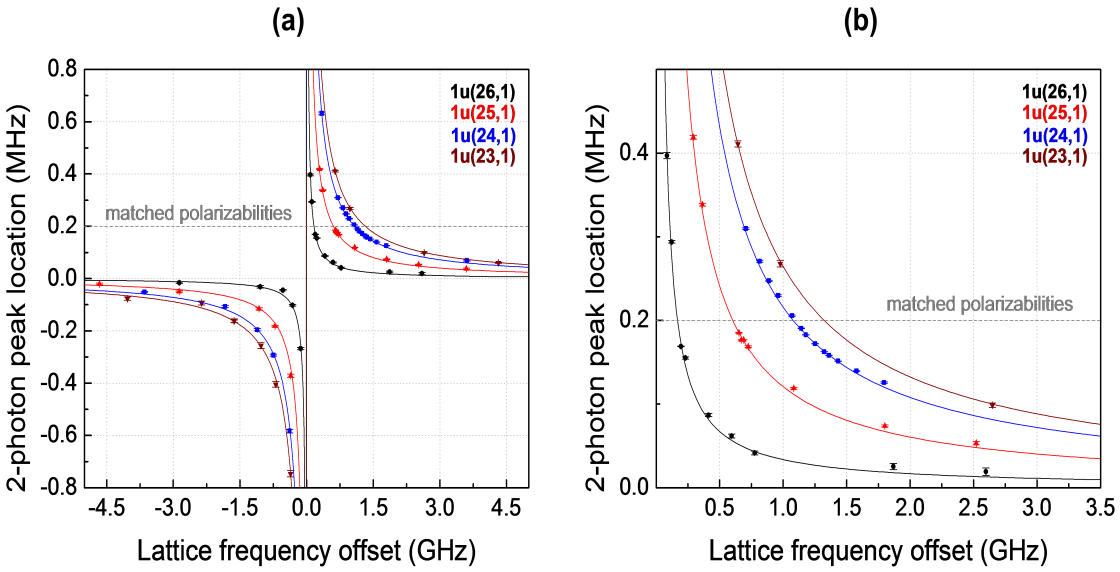

Figure 4.16: Comparison of several lattice-driven transitions. (a) Measured light shifts on the $X(-1,0) \rightarrow X(6,0)$ clock transition versus lattice light detuning are demonstrated with multiple lattice-driven transition from $X(6,0)$ to $1_u(v' = \{23-26\}, J' = 1)$ resonances. The vertical axis refers to the detuning of the first Raman laser. The measurements are performed with lattice power of 200∼230 mW. (b) A zoom-in look at (a). Transitions that have larger DMS's results in larger magic lattice detuning and leads to gentler curve slope at magic wavelength.

off-resonant scattering

Besides frequency stability transfer, the off-resonant scattering is another critical factor for selecting a good lattice-driven transition. Lattice light is a strong and focused beam with intensity typically > 3 kW/cm^2. Although at the magic wavelength the lattice light is off-resonant by ∼1 GHz, its strong intensity could still cause photon scatterings, leading to limits on the clock state lifetime. Therefore good lattice-driven transitions are the ones that induce the least scattering.

For a laser light that is detuned from a transition $|g\rangle \rightarrow |k\rangle$ by frequency Δ, the off-resonant scattering rate Γ_{scatt} can be written as

$$\Gamma_{scatt} = \frac{\gamma_k}{2} \frac{s}{1 + s + \frac{4\Delta^2}{\gamma_k^2}}, \tag{4.9}$$

where γ_k is the natural linewidth of the $|k\rangle$ state and s is the saturation parameter defined by $s = \dfrac{2\Omega_{kg}^2}{\gamma_k^2}$. According to the *ab initio* calculations performed by Prof. Robert Moszynski's team at the University of Warsaw [76], the natural linewidth of deeply bound 1_u states is on the order of 5 kHz, which is tiny compared to usual lattice frequency detuning at the magic wavelength ($\Delta_m \sim 1$ GHz). Therefore the far detuned approximation is applicable for a magic lattice trap, simplifying Equation 4.9 to be

$$\Gamma_{scatt} \approx \frac{\gamma_k \Omega_L^2}{4\Delta^2} = 4 f_m^2 \frac{\gamma_k}{\Omega_k^2}, \tag{4.10}$$

where Δ_m is given by Equation 4.7.

The natural linewidth originates from the limited lifetime due to spontaneous emissions. The $|k\rangle$ state can decay to many different states $|i\rangle$. The sum of the coupling between the dipole moments d_{ki} and the vacuum determines the spontaneous decay rate [25]

$$\gamma_k = \sum_i \frac{4\alpha}{3e^2c^2} \omega_{ki}^3 |d_{ki}|^2, \tag{4.11}$$

where $\alpha \sim 1/137$ is the fine structure constant, c is the speed of light in vacuum and e is the electron charge. With this expression for the natural linewidth, Equation 4.7 can be rewritten as

$$\Gamma_{scatt} = \left(\frac{32\alpha\epsilon_0\hbar^2 f_m^2}{3e^2cI}\right)\omega_{gk}^3 \frac{\sum_i \omega_{ki}^3 |d_{ki}|^2}{\omega_{kg}^3 |d_{kg}|^2} \tag{4.12}$$

Note that the Rabi frequency $\Omega_{gk}^2 \equiv \frac{|d_{gk}|^2 I}{2\epsilon_0 c\hbar^2}$ is adopted, where I is the laser light intensity and ϵ_0 is the permittivity of free space. Equation 4.12 has a striking implication. The off-resonant scattering rate is *inversely-proportional to* the frequency-weighted branching ratio of dipole moment squared (DMS). In other words, good lattice-driven transitions are the ones that have a large branching ratio of transition strength.

In conclusion, a good lattice-driven transition should satisfy two qualifications. It should possess a strong transition strength so that the Raman transition could be insensitive to the instability in the lattice frequency. Also, it should have a large frequency-weighted DMS branching ratio for suppressing the one-photon lattice scattering.

4.4 Power of magic lattice trapping

In this section, the consequences of a magic lattice are exhibited. First, with a magic lattice, the clock transition linewidth can be narrowed down to sub-100 Hz level. Second, due to the enhanced coherence time, population flopping between clock states, or Rabi oscillations, can be observed.

In the demonstrations illustrated in this section, the lattice-driven transition $X(6,0) \rightarrow 1_u(24,1)$ is applied on the $X(-1,0) \rightarrow X(6,0)$ clock transition driven with a common detuning 25 MHz from $0_u^+(-4,1)$. As exhibited in Figure 4.16, this transition has a good dipole transition moment, which yields the curve slope of 1.8×10^{-4}. Also, this transition induces a mild one-photon scattering rate of $\sim$1 Hz, according to *ab initio* calculations on 1_u lifetimes and branching ratios. With this scattering rate, a Raman linewidth of 1 Hz and a clock

lifetime of > 150 ms are expected.

4.4.1 Sub-100 Hz narrow line

According to the derivation in Section 3.2, the behavior of a two-photon Raman transition is equivalent to that of a one-photon transition. In a Raman transition from $|g_1\rangle \rightarrow |g_2\rangle$ via a virtual state $|e\rangle$, the first laser connects $|g_1\rangle$ to $|e\rangle$ with detuning Δ and the second laser connects $|g_2\rangle$ to $|e\rangle$ with detuning Δ. The transition strength of this Raman transition is given by the effective Rabi frequency Ω_{eff}

$$\Omega_{eff} = \frac{\Omega_1 \Omega_2}{2\Delta}, \tag{4.13}$$

where Ω_1 and Ω_2 are the one-photon Rabi frequency of the first and second laser, respectively. Furthermore, the effective laser intensity is defined with first laser intensity I_1 and second laser intensity I_2 as

$$I_{eff} = \sqrt{I_1 I_2} \tag{4.14}$$

With this definition, the effective Rabi frequency is proportional to the effective lattice intensity $\Omega_{eff} \propto I_{eff}$. This is slightly different from its counterpart of one-photon transition, where the Rabi frequency is proportional to the square root of laser intensity.

Due to the analogy to a one-photon transition, the lineshape of a two-photon Raman transition can be described by a Lorentzian profile with a full width at half maximum (FWHM) of $\sqrt{\gamma^2 + \Omega_{eff}^2}$, where γ here is the asymptotic linewidth probed with zero laser power. Note that it is not strictly equivalent to the natural linewidth. Systematic loss mechanisms such as lattice scattering, two-body collision, etc. are included in this parameter. As described in

the previous section, the first-leading loss mechanism is expected to be the lattice scattering, which would limit the asymptotic linewidth to be on the order of 1 Hz. When the effective Rabi frequency is large compared to the asymptotic linewidth, it dominates the FWHM of the two-photon transition, leading to the fact that the FWHM acts proportionally to the effective power. This is the so-called *power broadening regime*.

Figure 4.17 demonstrates the dependence on effective intensity of a two-photon Raman transition linewidth. In this measurement, the Raman probe laser beam waist is fixed to be 150 μm. The fact that the linewidth shows a linear dependence on effective power indicates the asymptotic linewidth is narrower than what has been probed. Figure 4.18 exhibits a narrow clock transition linewidth of 32 Hz taken with an effective power of $\sim$20 nW.

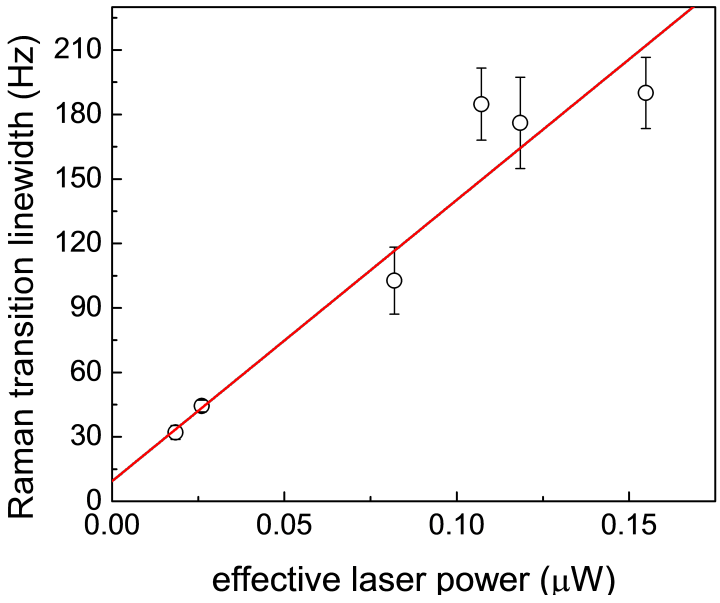

Figure 4.17: Examination of asymptotic linewidth of a two-photon Raman transition. The fact that the linewidth shows a linear dependence on effective power indicates the asymptotic linewidth is narrower than what has been probed.

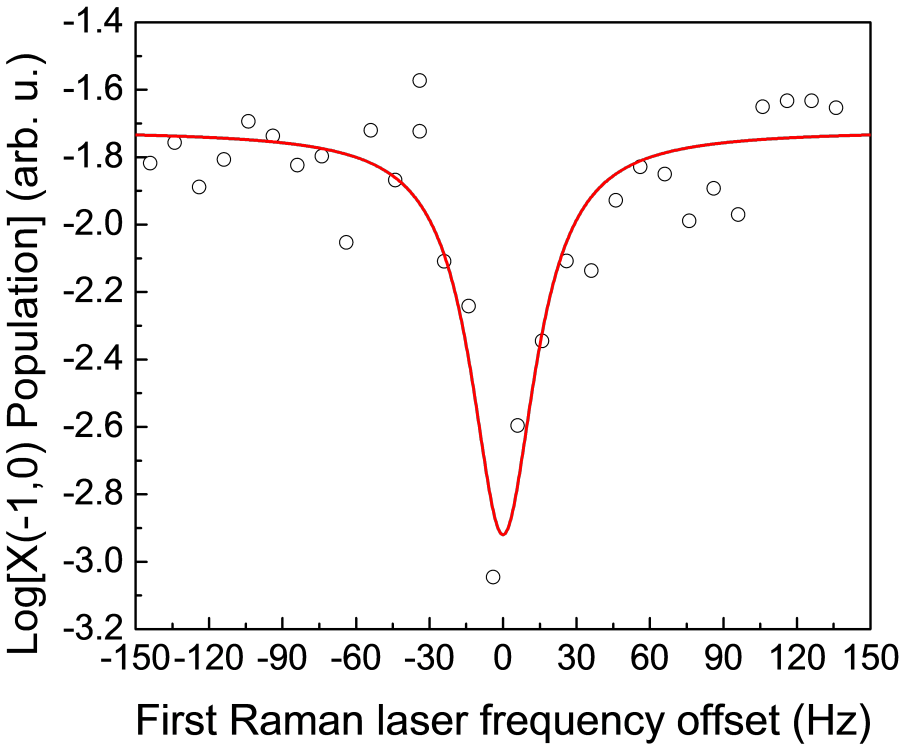

Figure 4.18: A narrow lineshape of a two-photon Raman transition. This trace exhibits a 32 Hz linewidth, which is the record of our lab as of 2019. The fact that the linewidth still shows linear dependence on effective power indicates the asymptotic linewidth is narrower than what we could have probed. At zero frequency offset, the actual detuning on the first Raman laser frequency is -4.554,936(1) MHz.

There is an important technical note to mention for this measurement, which is the method to crank down the probe powers. Since the usual power meters are not reliable at the nW level, weak powers can't be directly measured faithfully. A more precise alternative method to control weak laser powers is to use calibrated neutral-density (ND) filters. To do that, the ND filters are initially calibrated at high power. The exact attenuation can be well-calibrated by measuring the powers with and without an ND filter. Since the attenuation is fairly insensitive to power, the calibrated ND filters can be used to precisely control weak laser powers.

4.4.2 Rabi oscillation across the molecular potential

In this section I discuss the realization of Rabi oscillations in the molecular clock. In an ideal two-level system with $|1\rangle$ and $|2\rangle$ states, there is no population loss. When this system is driven on resonance, the optical Bloch equations that describe the system are

$$\dot{\rho_{11}} = 2\Omega\rho_{12}$$

$$\dot{\rho_{22}} = -2\Omega\rho_{12}$$

$$\dot{\rho_{12}} = -i\frac{\Omega}{2}(\rho_{22} - \rho_{11}),$$

where Ω is the Rabi frequency. Assuming $\rho_{11} = 1$ and $\rho_{22} = 0$, the optical Bloch equations have analytic solution

$$\rho_{11}(t) = \cos^2\frac{\Omega t}{2}$$
$$\rho_{22}(t) = \sin^2\frac{\Omega t}{2} \tag{4.15}$$

Detailed discussions on the analytic description of Rabi oscillations can be found in references [26,27]. Equations 4.15 indicates that the population oscillates with a frequency of Ω between two states. This is the so-called Rabi oscillations. This phenomenon has been demonstrated in a wide variety of systems [10, 28–30].

With the technique of magic lattice, the coherence time of our molecular clock has been dramatically enhanced. The enhanced coherence, together with the fact the lifetime of the clock states is as long as a million years, makes the Raman transition between clock states essentially a light-coupled two-level system, which enables the observation of Rabi oscillations. The Rabi oscillation in the molecular clock is unique in the sense that *it is quantum state flopping across almost an entire ground potential well.* The entire ground state potential is 30

THz deep and the flopping between states that are over 20 THz apart has been achieved. The same technique can be applied to achieve flopping between any pair of states and the Rabi oscillation between the least and the most deeply bound states is undoubtedly achievable.

There are several important notes for realizing Rabi oscillations in the molecular clock.

- Firstly, the lattice trap has to be as magic as possible to maintain the coherence. To achieve great coherence, one should use the narrowest possible lineshape to determine the magic frequency.

- Secondly, low lattice power is strongly favored in order to observe high quality Rabi oscillations. As Chapter 6 demonstrates, although a magic lattice drastically enhances the coherence, an excessive population loss is still present. This is actually quite surprising and unexpected. Further researches have concluded that this loss originates from the background noise of the lattice laser, therefore running the lattice at low power can alleviate the loss effect. In addition to low lattice power, the background noise of the lattice laser should be attenuated with a diffraction grating and a spectrum clean-up cavity. These will be discussed in Chapter 5.

- Thirdly, the two-photon Rabi frequency should be chosen properly. If it is too small, then the flopping rate is slow, which makes observing the Rabi oscillations difficult. On the other hand, if the Rabi frequency is too large, the Raman lasers could result in unwanted loss mechanisms. For instance, in the example that I will demonstrate, the first Raman laser connects $X(-1,0)$ and $0_u^+(-4,1)$ with 25 MHz detuning. The $X(-1,0) \rightarrow 0_u^+(-4,1)$ transition has a large Franck-Condon factor. Therefore, if excessive power is dumped into this Raman leg, an unwanted heating on the $X(-1,0)$ molecules is induced and thus the coherence time is limited. This point will be revised

in Chapter 6.

- Fourthly, the Raman laser powers should be at the *balanced power ratio*. As I will discuss in Sec 5.2, the balanced power ratio is the ratio between Raman laser powers that eliminates the systematic light shift induced by the Raman lasers. Typically weak Raman lasers are required to precisely determine the magic frequency. However, to keep the Rabi frequency in the proper range, larger Raman laser powers are necessary. Therefore, if the Raman powers don't follow the balanced power ratio, the magic frequency determined with low Raman power wouldn't be accurate for high Raman power, which leads to undesirable decoherence.

- Last but not least, all sources of decoherence should be properly taken care of. This including stabilizing the Raman probe powers and maintaining the frequency stability transfer. These technical issues will be detailed in Chapter 5.

Figure 4.19 demonstrates Rabi oscillations between $X(-1,0)$ and $X(6,0)$ states. The clock transition is driven with a detuning of 25 MHz from $0_u^+(-4,1)$ and the effective Rabi frequency is 500 Hz. To achieve the magic trap, the $X(6,0)$ polarizability is modified with the lattice-driven transition to $1_u(24,1)$ state. In order to reduce the loss due to lattice laser noise, the lattice was running with 110 mW. Also, a diffraction grating and a spectral clean-up cavity are in place.

As demonstrated in Figure 4.19, a few cycles of population flopping have been achieved. This is exciting but there are also some worrisome observations. First, even with a well-determined magic lattice frequency, the molecular lifetime is only 30 ms, which is a lot shorter than what was expected. Besides, the trace shows a limited coherence time of 10 ms. The culprit to the coherence time issue has been to be the frequency comb locking quality.

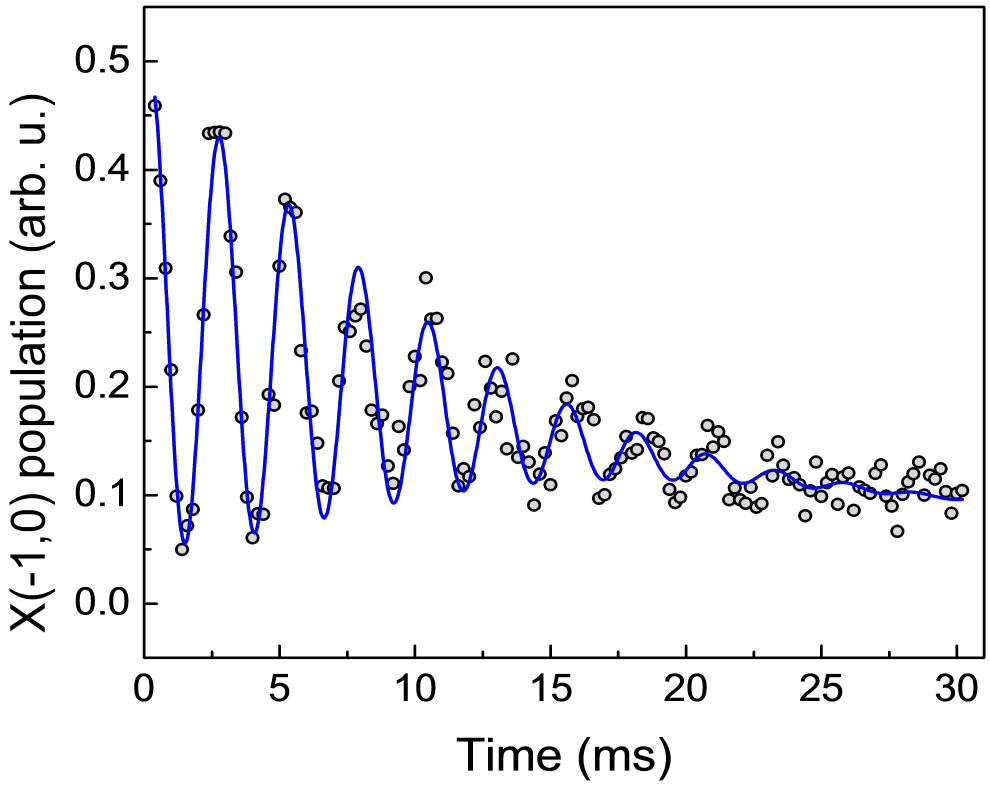

Figure 4.19: Rabi oscillations between $X(-1,0)$ and $X(6,0)$. The energy separation between these two states is ~25 THz. The trace is fit to a function form $A\exp(-t/T_l)\,[1+\exp(-t/T_c)\cos(\omega t+\phi)]$, which suggests an overall molecular lifetime of 26 ms and a coherence time of 12 ms. The fitted Rabi frequency is 410(1)Hz. Error bars are not shown because each point is an average of only two experimental realizations.

By stabilizing the repetition rate with a stronger beat note, the issue with coherence time is alleviated. However, the issue with limited clock state lifetime is a lot more puzzling. Further investigations have suggested that the issue may arise from the background noise in the lattice laser spectrum. This topic will be explored in Chapter 6.

Discussion on the Rabi oscillation fit function

In the Rabi oscillations just presented, we have seen that, albeit with a magic lattice trap, a non-negligible population loss and a limited coherence time are still present. To incorporate these observations, the model of state flopping requires a slight adjustment. First, to reflect the limited clock state lifetime, decay terms (labeled in red) need to be included in the optical Bloch equations.

$$\dot{\rho_{11}} = \Omega\rho_{12}$$

$$\dot{\rho_{22}} = -\Omega\rho_{12} - \Gamma\rho_{22}$$

$$\dot{\rho_{12}} = -i\frac{\Omega}{2}(\rho_{22} - \rho_{11}) - \frac{\Gamma}{2}\rho_{12},$$

where Γ is the population loss rate from the clock state that is connected by the lattice light. This set of optical Bloch equations yields an analytic solution

$$\rho_{11}(t) = \frac{1}{4\Omega'^2}e^{\frac{-\Gamma t}{2}}\left(\Gamma\sin\frac{\Omega' t}{2} + 2\Omega'\cos\frac{\Omega' t}{2}\right)^2 \tag{4.16}$$

$$\rho_{22}(t) = \frac{4\Omega^2}{\Omega'^2}e^{\frac{-\Gamma t}{2}}\sin^2\frac{\Omega' t}{2} \tag{4.17}$$

where $\Omega' = \sqrt{\Omega^2 - \Gamma^2/4}$. Assuming $\Gamma \ll \Omega$, in which case a few flopping cycles could occur before the molecules die out, the population that we detect, i.e. ρ_{11}, approximates to

$$\rho_{11}(t) \approx \frac{1}{2}e^{\frac{-\Gamma t}{2}}\left[1 + \cos(\Omega t)\right] \tag{4.18}$$

To model the decoherence, two approaches are provided below. The first method is the heuristic model, which is adapted for the Nature Physics publication and the second method is a newer model that explains decoherence from the aspect of spatial nonuniformity in Raman lasers.

1. Heuristic model

In this model, the decoherence is explained by spontaneous emission from the clock state. Let's consider an extreme situation where the population on $|2\rangle$ decays *only* to $|1\rangle$. In this situation, the optical Bloch equations are described by

$$\dot{\rho_{11}} = \Omega\rho_{12} + \Gamma_c\rho_{22}$$

$$\dot{\rho_{22}} = -\Omega\rho_{12} - \Gamma_c\rho_{22}$$

$$\dot{\rho_{12}} = -i\frac{\Omega}{2}(\rho_{22} - \rho_{11}) - \frac{\Gamma_c}{2}\rho_{12}$$

This set of equations can be solved analytically with solutions

$$\rho_{11}(t) = \frac{1}{2}\left[1 + e^{-\frac{3t}{4\Gamma_c}}\cos(\Omega t)\right] \tag{4.19}$$

$$\rho_{22}(t) = \frac{1}{2}\left[1 - e^{-\frac{3t}{4\Gamma_c}}\cos(\Omega t)\right] \tag{4.20}$$

Note that the above solutions are obtained with initial conditions $\rho_{11}(0) = 1$ and $\rho_{22}(0) = 0$.

Now, what about the situation where a population loss and decoherence are both present? In this case the optical Bloch equations are

$$\dot{\rho_{11}} = \Omega\rho_{12} + \Gamma_c\rho_{22}$$

$$\dot{\rho_{22}} = -\Omega\rho_{12} - (\Gamma_l + \Gamma_c)\rho_{22}$$

$$\dot{\rho_{12}} = -i\frac{\Omega}{2}(\rho_{22} - \rho_{11}) - \frac{\Gamma_l + \Gamma_c}{2}\rho_{12},$$

where Γ_l represents the population loss and Γ_c reflects the decoherence. Unfortunately, this set of equations cannot be solved analytically but close scrutiny on Equations 4.18 and 4.19 reveals a heuristic guess. In the situation where only population loss is present, the exponential decay factor appears before the parenthesis. In the situation where only

decoherence exists, however, the exponential decay factor appears before the oscillatory cosine term. Based on this it is reasonable to guess the solution for $\rho_{11}(t)$ should have the following form.

$$\rho_{11}(t) = Ae^{\frac{-\Gamma_l t}{2}}\left[1 + e^{\frac{-3\Gamma_c t}{4}}\cos(\Omega t)\right], \tag{4.21}$$

where A is a proper coefficient. Note that this function form is the one that was used for the Nature Physics publication and it is also the fitting function adopted in Figure 4.19.

2. Raman lasers' spatial nonuniformity

Another approach is to consider decoherence from the aspect of the nonuniformity in Raman laser intensities. A laser with a nonuniform intensity leads to a Rabi frequency gradient seen by the molecules. Due to the geometry of the lattice trap, it is reasonable to model the Rabi frequency as $\Omega(r) = \Omega_0 + \delta\Omega(r)$, where r is the radial distance from the center of molecule cloud. Since the Raman laser beam size is usually a few times larger than the cloud size, we can only keep the first leading term of $\delta\Omega(r)$. In consequence, the $\cos(\Omega t)$ term in Equation 4.18 approximates to

$$\cos\left[(\Omega_0 + \delta\Omega(r))t\right] \approx \cos(\Omega_0 t)\cos(\delta\Omega(r)t) \approx \cos(\Omega_0 t)\left[1 - \frac{(\delta\Omega(r)t)^2}{2}\right] \tag{4.22}$$

Since the Rabi frequency is now spatial dependent, the population on $|1\rangle$ is therefore the ensemble average of molecules

$$\begin{aligned}\rho_{11}(t) &= \int_D \frac{1}{2}e^{\frac{-\Gamma t}{2}}\left[1 + \cos(\Omega t)\right] n(r)d^2r \\ &\approx \frac{1}{2}e^{\frac{-\Gamma t}{2}}\Bigg[1 + \cos(\Omega_0 t)\underbrace{\left[1 - t^2\int_D \frac{(\delta\Omega(r))^2}{2}n(r)d^2r\right]}_{\approx\cos(\Gamma_c t)}\Bigg],\end{aligned}$$

where $n(r)$ is the normalized spatial density of the molecules that satisfies $\int_D n(r)d^2r = 1$ and $\Gamma_c \equiv \left[\int_D (\delta\Omega(r))^2 n(r)d^2r\right]^{0.5}$ is the coherence rate. In short, modeling the Rabi frequency distribution the population we detect is

$$\rho_{11}(t) = \frac{1}{2}e^{\frac{-\Gamma t}{2}}\left[1 + \cos(\Gamma_c t)\cos(\Omega_0 t)\right] \tag{4.23}$$

To compare this model with the heuristic approach, one can apply the approximation $\cos x \sim e^{-x^2/2}$ for small x to replace $\cos(\frac{t}{\Gamma_c})$ and obtain

$$\rho_{11}(t) = \frac{1}{2}e^{\frac{-\Gamma t}{2}}\left[1 + e^{\frac{-(\Gamma_c t)^2}{2}}\cos(\Omega_0 t)\right] \tag{4.24}$$

Figure 4.20 demonstrates the fitting result with Equation 4.24.

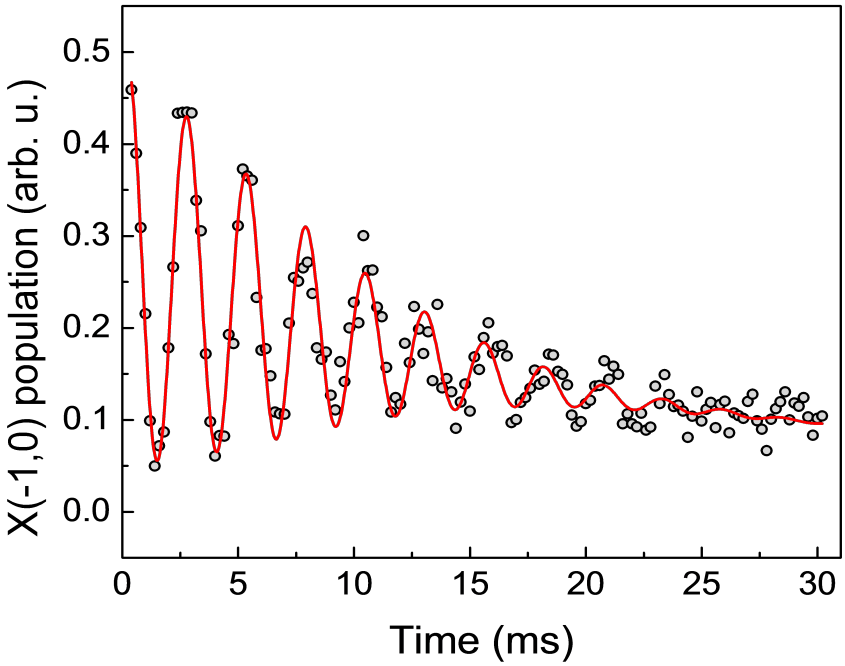

Figure 4.20: Rabi oscillations that is fit to Equation 4.24. The fit suggests an overall molecule lifetime of 18 ms, a coherence time of 15 ms and Rabi frequency of 410(1) Hz. The trace is the same as in Figure 4.19.

Figure 4.21 compares the fits with two models we just discussed. The fitted Rabi frequency and coherence time are quite consistent in both models while the discrepancy in molecule lifetime is larger than that in the coherence time. In the heuristic model the lifetime is 26 ms whereas in the intensity model it is 18 ms. Simply by looking at the trace, the lifetime of 18 ms seems to be more reasonable. Indeed, the intensity model yields better fitting statistics with the R square exceeding 0.99.

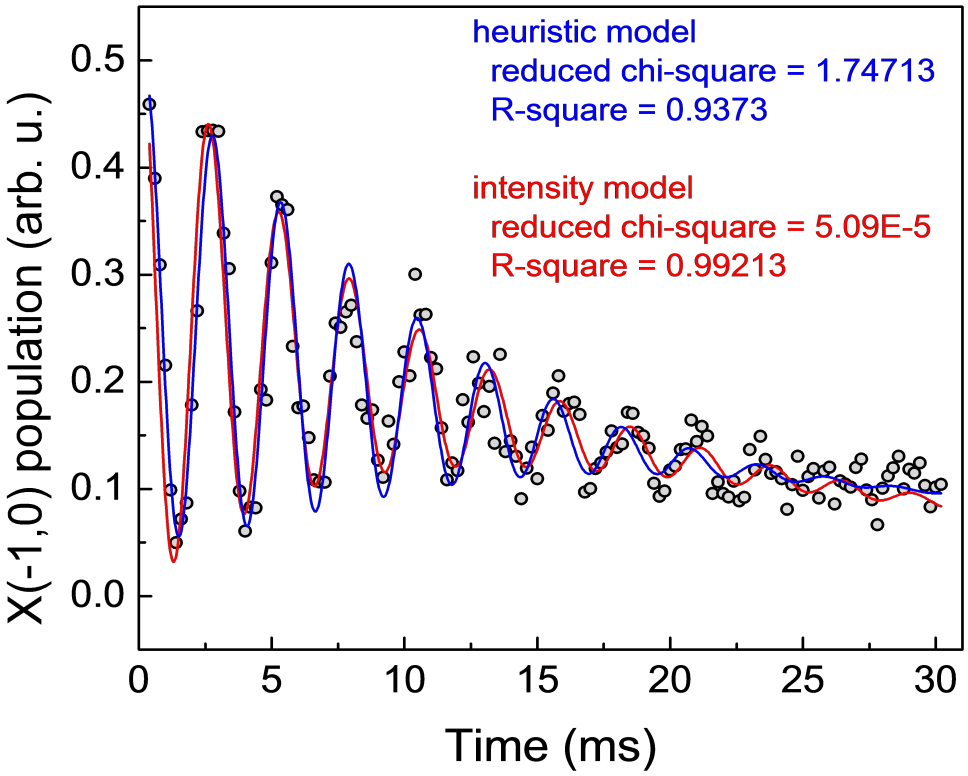

Figure 4.21: Comparison of two fitting models for Rabi oscillations

Chapter 5

Molecular clock stabilization and systematics

Great frequency stability and high controllability of the experimental system need to be ensured to perform high-quality precision measurements and reduce systematics. In this chapter I discuss the experiment upgrades that we have implemented in the past few years. These upgrades have enhanced the stability of the experiments and enabled the measurements of systematics. At the end of this chapter, I will also discuss some leading contributions for systematics, from which binding energy of deeply bound ground states can be precisely-determined.

5.1 Experimental system stability

The experiment upgrades that have implemented mainly fall into three categories. First, the stability of the master laser has been greatly enhanced. This was achieved by improving the temperature feedback system for the ULE cavity. Second, endeavors have been put to reduce the background noise of the lattice laser spectrum. The attempts include implementing a diffraction grating and a spectral clean-up cavity. Lastly, the stability of the probe lasers has

been improved by reducing optical fiber noise and stabilizing the laser intensities.

5.1.1 Master laser temperature stabilization

As described in Chapter 2, the frequency reference in our experiment is provided by the master laser which frequency is stabilized to a ULE cavity. Over the past decade, the stability of the master laser has been sufficient for our purpose, but for molecular clock experiments it turns out that this stability is not enough. The stability limit in the master laser frequency comes from the temperature control of the ULE cavity. Ever since the cavity was built, the temperature controller has only allowed for one way feedback; the cavity could only be heated up whereas it could not be cooled down. To maintain the cavity at a stable (or semi-stable) temperature, the set point was about three °C higher than the lab temperature. As the cavity temperature dropped below the set point, the heaters attached to the cavity were engaged to raise it up. However, when the cavity temperature was higher than the set point, no feedback servo could bring it down so it had to rely on natural dissipation for the temperature to drop down.

This temperature instability leads to the cavity frequency instability. For a ULE cavity, the fractional stability of the resonant frequency f is related to the fractional cavity length L stability by

$$\frac{\delta f}{f} = -\frac{\delta L}{L} \tag{5.1}$$

Moreover, the fractional length stability is given by [34, 35]

$$\frac{\delta L}{L} = a/2(T - T_0)^2 + b/3(T - T_0)^3 \tag{5.2}$$

where T_0 is the zero-crossing temperature and a and b are parameters related to the cavity's

coefficient of thermal expansion (CTE) α.

$$\alpha(T) = a(T - T_0) + b(T - T_0)^2, \tag{5.3}$$

where the linear coefficient a is typically around 2×10^{-9} K^{-2} and the quadratic coefficient b is typically around -1×10^{-11} K^{-3} [34].

Given the dependence of CTE on the temperature, the drawback of a one-way servo is clear. First, the frequency stability is vulnerable to lab temperature fluctuations. The lab temperature feedback is not always stable. When the lab temperature control breaks down, the lab temperature spikes, which would push up the ULE cavity temperature. Due to the lack of cooling function, the rise in cavity temperature cannot be compensated and would thus lead to huge frequency drifts. Second, the cavity couldn't be stabilized at the zero-crossing temperature. Suggested by Equation 5.2, the fractional frequency stability is minimized at the zero-crossing temperature T_0. However, it has been realized that the zero-crossing temperature of our ULE cavity is lower than the lab temperature set point by around 2 °C. This means the cavity couldn't be run at the zero-crossing temperature unless the cooling function on the cavity temperature servo was implemented.

There are several ways to implement the cooling function. It can be as straightforward as to open the vacuum chamber and attach a TEC element to the cavity. However, it is a bit risky in that such intrusive movement could ruin the vacuum and damage the cavity. Alternatively, we adopted a milder way, which was to place several TEC's underneath the vacuum system to cool the whole chamber. Figure 5.1 presents the implementation of TEC's. To sufficiently cool the vacuum system, eight TEC's are arranged into a configuration where four pairs of TEC's in series are connected in parallel, as shown in (a). This configuration makes the best use of the output power of the PTC10 controller, the temperature controller

provided by Stanford Research Systems. The TEC system is servo-ed by a spare PTC10 output channel for PID feedback. To ensure even thermal distribution, the TEC's are placed symmetrically underneath the vacuum system, as demonstrated in (b).

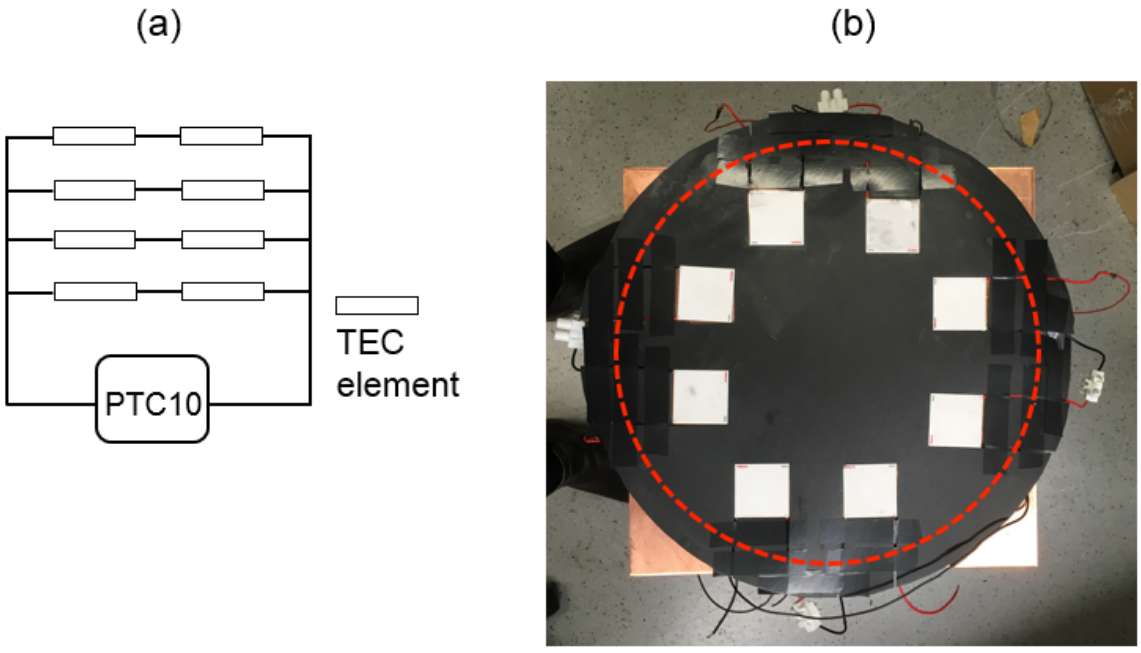

Figure 5.1: Design of the TEC system for cooling the ULE cavity's vacuum system. (a) Eight TEC's are placed in the configuration where four pairs of TEC's in series are connected in parallel. (b) To ensure even thermal distribution, the TEC's are placed symmetrically underneath the vacuum system. The dotted orange circle denotes the size of the vacuum chamber. A black rubber plate is utilized to protect the TEC's from being crashed by the vacuum chamber.

Besides adopting the optimal TEC layout, proper thermal sensors layout and efficient heat dissipation are also critical for achieving efficient thermal control. To ensure correct temperature reading, four TH10K thermistors from Thorlabs are placed equally spaced around the bottom of the vacuum chamber, as shown in Figure 5.2(a). These four thermistors are connected in parallel to perform average temperature reading. By doing this way, the local thermal fluctuations can be averaged out so that the temperature reading can be more precise and reliable.

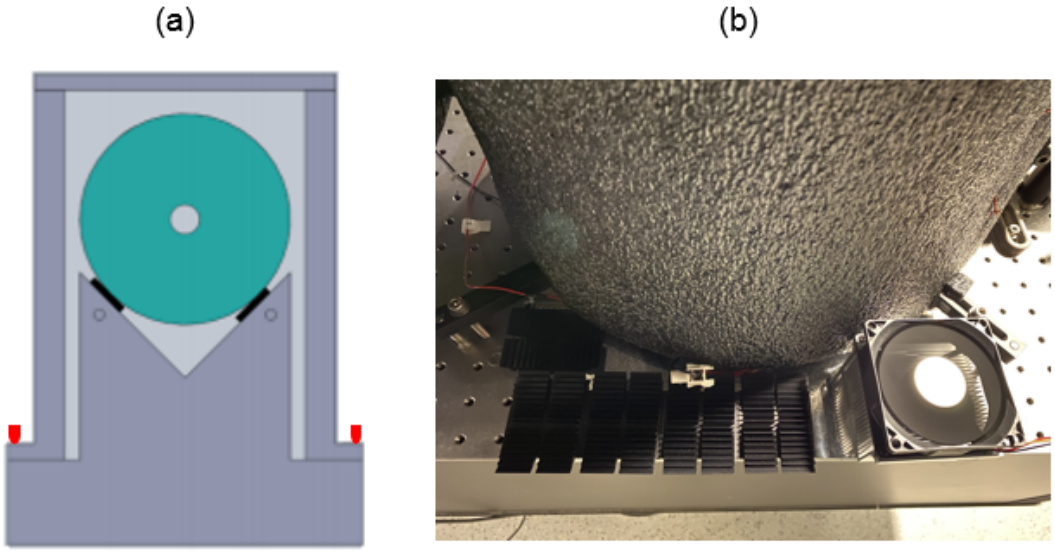

Figure 5.2: (a) To correctly measure the temperature, four thermistors are equally-spaced placed around the vacuum chamber (labeled in red, only two thermistors are plotted for simplicity). The thermistors are connected in parallel to average out local thermal fluctuations. Adapted and edited from [16] (b) For efficient heat dissipation, the TEC system is placed on an aluminum plate on which a fan and a bunch of heat sinks are placed to speed up heat dissipation.

Due to the large thermal capacity of the vacuum chamber, it is necessary to have efficient heat dissipation. We were not aware of this at our first attempt when we simply had the TEC's in direct contact with the optical table. However, it turned out that the optical table is not efficient at dissipating heat as we expected. As a result of the inefficient heat dissipation, a lot of heat was accumulated underneath the vacuum chamber, which prevented the temperature from dropping down to the sweet spot. To resolve this issue, we applied thermal paste on both sides of the TEC's and have the TEC system sandwiched by two layers of aluminum plates. Also, on a bottom layer of the aluminum plate a fan and a bunch of heat sinks are placed to speed up heat dissipation, as shown in Figure 5.2(b).

With the cooling function implemented, the ULE cavity temperature can be stabilized at the zero-crossing temperature. Figure 5.3 exhibits the fractional frequency stability of

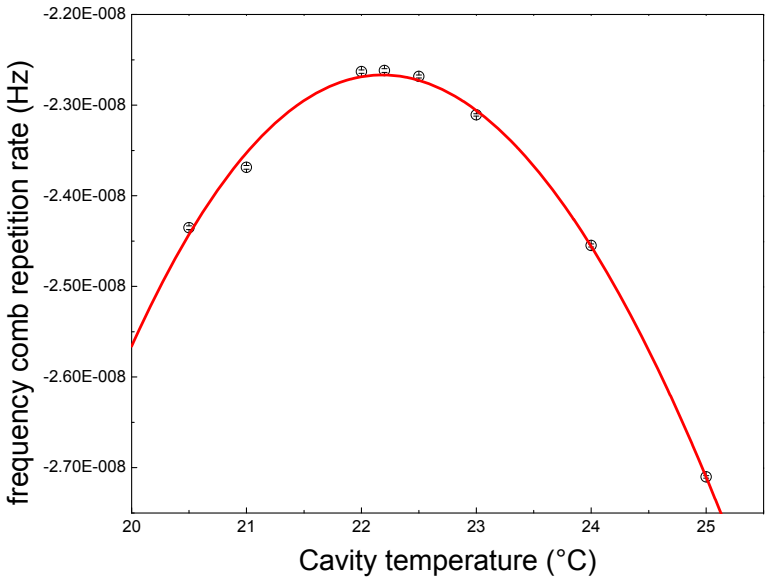

Figure 5.3: The frequency comb repetition rate is measured at each cavity temperature. Fitting the curve to Equation 5.2 yields the zero-crossing temperature of 22.18(5)°C and CTE coefficients $a = 1.20(6) \times 10^{-9}$ K^{-2} and $b = -4(4) \times 10^{-11}$ K^{-3}.

master laser as a function of cavity temperature. The frequency is measured with the frequency comb. At each temperature, the frequency comb repetition rate is stabilized to the master laser. Because the same comb tooth was used every time, the fractional stability of the master laser is consistent with that of the repetition rate. By fitting the curve with Equation 5.2, it yields yields the zero-crossing temperature of 22.18(5)°C and CTE coefficients $a = 1.20(6) \times 10^{-9}$ K^{-2} and $b = -4(4) \times 10^{-11}$ K^{-3}.

Figure 5.4 compares the master laser stability with and without the cooling function. The upper trace is the comb repetition rate recorded by the counter when the master laser cavity

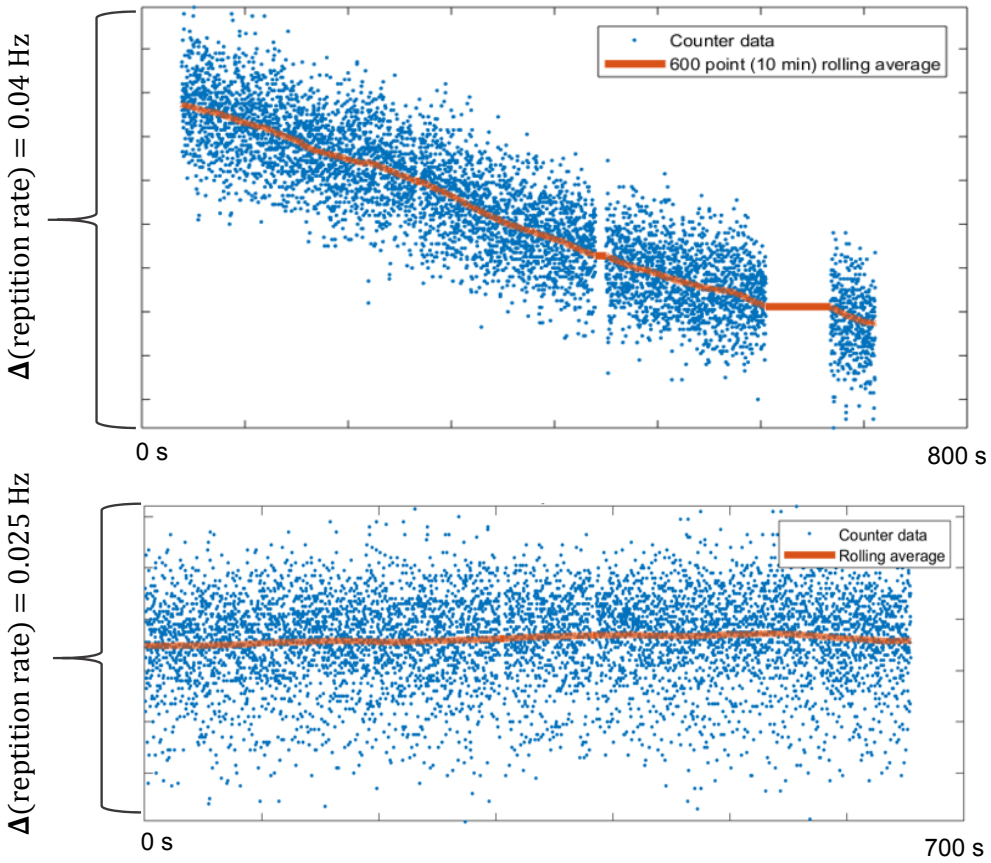

Figure 5.4: Stabilizing the ULE cavity at zero-crossing temperature greatly enhances the frequency stability of the master laser. The frequency comb repetition rate is recorded by the comb internal counter. Upper/bottom trace is taken without/with the cooling function.

is not at the zero-crossing temperature and the bottom trace is taken with the zero-crossing temperature. Stabilizing the ULE cavity at the zero-crossing temperature drastically enhances the average master laser frequency stability by an order of magnitude. However, due to the thermal delay time, the issue with reference frequency instability is not fully resolved. Figure 5.5 demonstrates a strong correlation between ULE cavity temperature servo output and the clock transition frequency. To achieve even better reference laser stability, a ULE cavity with faster temperature control feedback is necessary. In our experiment, the next generation of frequency reference will be provided by a Fabry-Perot cavity by Stable Laser Systems, which not only allows a well-designed temperature servo but also a linewidth of 1 Hz.

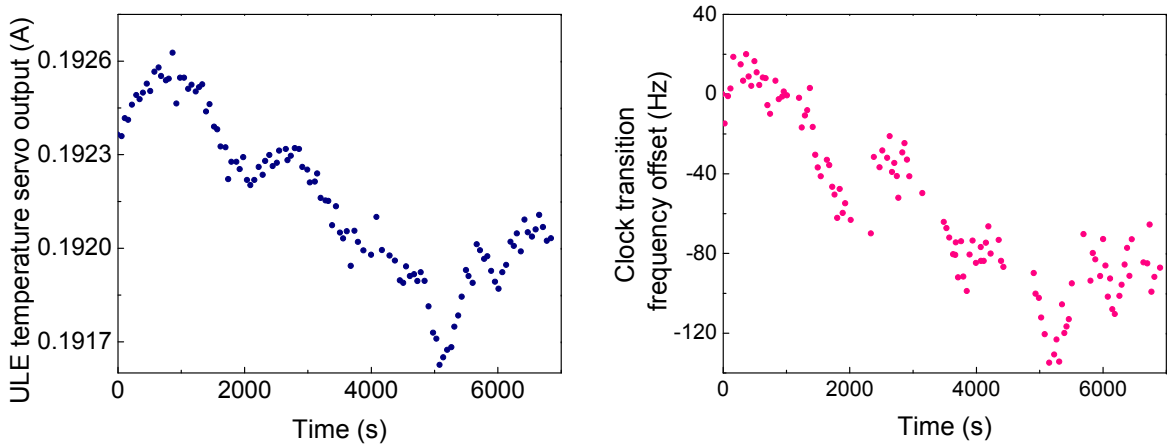

Figure 5.5: Running the ULE cavity at the zero-crossing temperature has stabilized the reference frequency by an order of magnitude. However, the issue with reference frequency instability is still not fully solved due to the thermal delay time. Here a strong correlation between (a) the cavity temperature servo output and (b) the clock transition frequency offset is demonstrated. Here the frequency offset is relative to the transition frequency measured at 0 s.

5.1.2 Lattice transmission grating

Because the lattice light is a key factor for the molecular clock precision, its spectrum purity is of critical importance. Actually, our recent investigations have suggested that the impurity of the lattice light has attributed to the short lifetime of the clock states. In the following two sections I will discuss our attempts to clean the lattice light spectrum.

As discussed in Chapter 2, our lattice laser is generated from an external-cavity diode laser and is amplified by a tapered amplifier (TA). A TA is an economical way to generate high laser power but it has its own drawback. As the TA is pumped by a seed light, the luminescence from spontaneous emission light can be optically amplified to high power level, producing the amplified spontaneous emission (ASE) [36–39]. This unwanted noise is problematic in our experiment. Usually, the spectrum of ASE spans over 10 THz, which can potentially cover a few deeply bound excited states and thus contribute to unwanted photon scatterings. As illustrated in Figure 5.6, as the lattice trap is tuned to magic via a

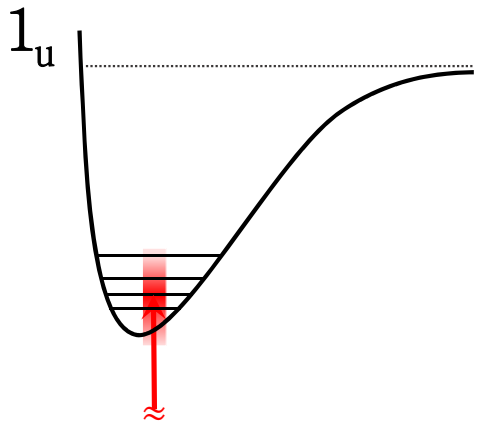

Figure 5.6: The wide spectrum of the ASE can cover a few deeply bound 1_u states. This leads to unwanted scatters and limitations on the clock state lifetime.

lattice-driven transition, the nearby states would cause unwanted scatters on the clock states.

To clean up the ASE noise, our first attempt is to install a transmission grating. The grating we chose is the model T-1850-915s-3210-93 provided by LightSmyth Technologies. This grating has a line density of $d = 1850$ lines/mm and allows diffraction efficiency of $> 90\%$ in an incident light wavelength range of (865 nm, 965 nm). Figure 5.7 depicts the schematics of how this grating works. As laser light incidents on the transmission grating, all diffracted orders appear on the other side of the grating. For simplicity, only the 0th and 1st orders are shown.

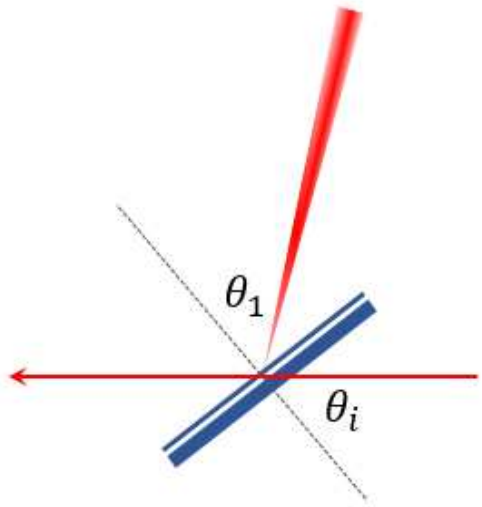

Figure 5.7: Schematics for a transmission grating. As laser light incidents on the transmission grating, all diffracted orders appear on the other side of the grating. The incidence angle θ_i and diffracted angle of the 1st order beam θ_1 is defined according to the norm vector of the grating surface.

As the transmission grating is blazed, the diffraction on a laser with wavelength λ is described by

$$d(\sin\theta_i + \sin\theta_n) = n\lambda, \tag{5.4}$$

where θ_i is the incidence angle and θ_n is the diffraction angle for the n-th order. The grating is designed to work in the Littrow configuration where the +1st order is maximized. In other words, when the diffraction efficiency is maximized, we have $\theta_i = \theta_1$. Plugging this into Equation 5.4 and using $d = 1/1850$ mm and $\lambda = 919$ nm, we obtain $\theta_1 \approx 58.2$ degrees. Now let's estimate how much spread in wavelength the transmission grating can filter out. After the beam is diffracted out, it takes a distance for the spectrum to spread out. Typically in our experiment the diffracted beam travels by a distance of 80 cm before being coupled into a single-mode optical fiber. Moreover, a pinhole is placed at the front of the fiber coupler to block the unwanted spread-out spectrum. A conservative estimate assumes a spatial range of 1 mm that can go through the pinhole and the fiber coupler. These lead to a selective angle range of $\Delta\theta = 1$ mm / 80 cm $\approx 1.3 \times 10^{-3}$ radians. By differentiating the grating equation, this implies a selective wavelength range of

$$\Delta\lambda = d\cos\theta_1\Delta\theta_1 \approx 0.37 \text{ nm}. \tag{5.5}$$

Note that as the diffraction efficiency is maximized, the incidence angle is no longer changed and therefore only $\sin\theta_1$ term contributes when differentiating the grating equation. This result implies that the transmission grating can filter out ± 0.18 nm of ASE noise relative to the carrier peak by spreading out the diffracted beam by a half meter. For $\lambda = 919$ nm, this corresponds to ± 64 GHz. Figure 5.8 shows the effects of the transmission grating on the

lattice light spectrum.

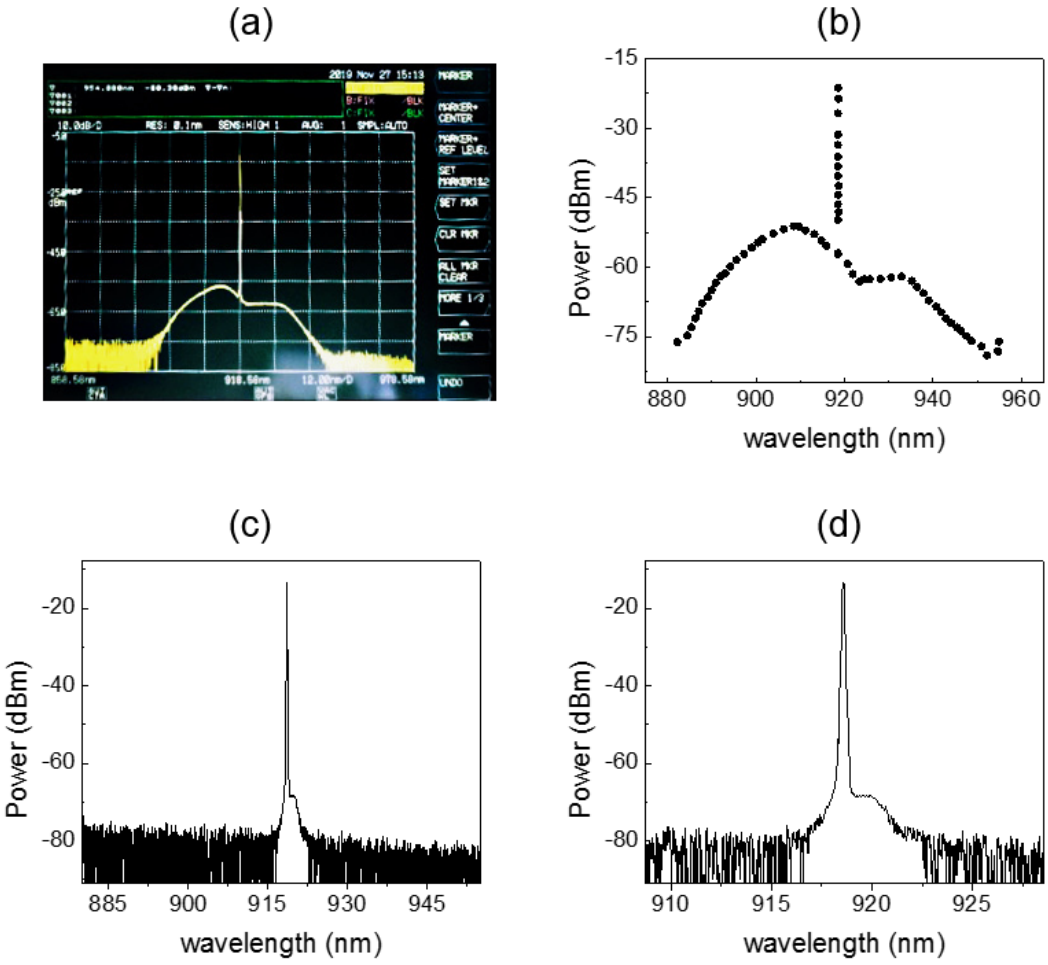

Figure 5.8: With the transmission grating installed, the lattice light spectrum is greatly cleaned up. In this demonstration, a lattice light of $\lambda = 919$ nm is diffracted by the grating. After a beam travel distance of 80 cm the diffracted beam passes through a pin hole and gets coupled into a single-mode optical fiber. The laser spectrum is measured with an optical spectrum analyzer. In (a) the grating is not installed and a ASE noise that spans 50 nm wide is observed. In (b) a recovered data from (a) is shown. This is a trace extracted from the image because the original data is corrupted. (c) The spectrum measured with the transmission grating installed. (d) zoom in of (c).

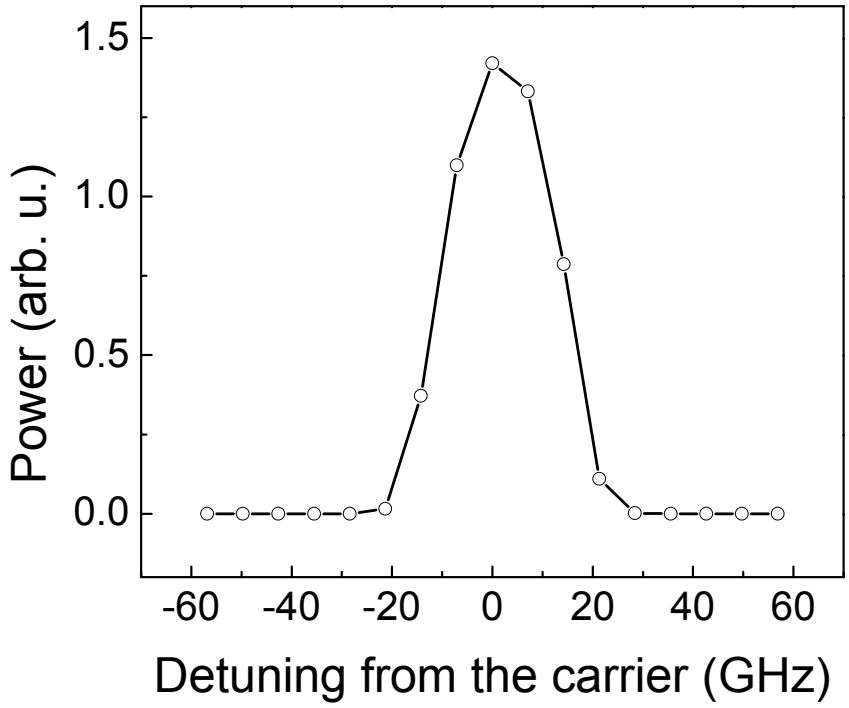

Figure 5.9: A zoom-in look of the spectrum cleaned by the transmission grating. The suppression threshold of the ASE noise is observed to be $\sim \pm 20$ GHz.

As demonstrated in Figure 5.9, the suppression threshold of the ASE noise is observed to be $\sim \pm 20$ GHz. This is helpful in reducing the scattering rate. The vibrational level spacing in the bottom region of 1_u potential is ~ 3 THz, which means, with the suppression from the grating, only the scattering due to the lattice-driven transition state will remain. A demonstration of how much installing the transmission grating could enhance the clock state lifetime is presented in Chapter 6. Although installing a grating alleviates the scattering issue, totally eliminating it requires a lot more effort. As we see from Chapter 4, the magic frequency is typically ~ 1.5 GHz away from the resonances, therefore using a grating to completely suppress this scattering would require an impractically long beam travel distance. This leads to the necessity of a spectral clean-up cavity.

5.1.3 Lattice spectral clean-up cavity

To suppress the scattering from the lattice-driven transition resonance, a Fabry-Perot cavity is implemented to clean the lattice spectrum. The cavity is constructed with two spherical mirrors from CVI Laser Optics and standard optics components from Thorlabs. The mirrors used for the cavity are the model PR1-920-98-0537 which has a curvature radius of 0.2 m, reflectivity of 98%, and clear face diameter of 0.5 inches. Due to the mirror geometry, the cavity is designed in the confocal configuration, which schematic is shown in Figure 5.10. Note that the cavity doesn't have to be in the confocal design and actually the concentric design should work even better. We chose these mirrors simply because not many choices that allow high reflectivity were available in the market.

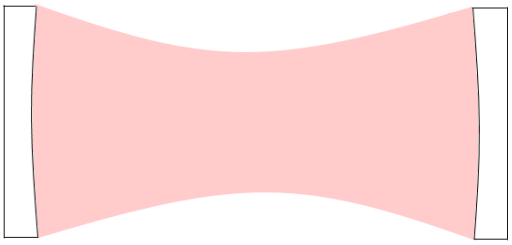

Figure 5.10: The clean-up cavity is designed in the confocal configuration where two identical curved mirrors with large radius of curvature face each other.

To lock the cavity length, one of the mirror is glued to a ring piezoelectric actuator, shown in Figure 5.11(a) and (b). The other mirror is placed in a half-inch tube which allows adjustable cavity length, shown in Figure 5.11(c) and (d).

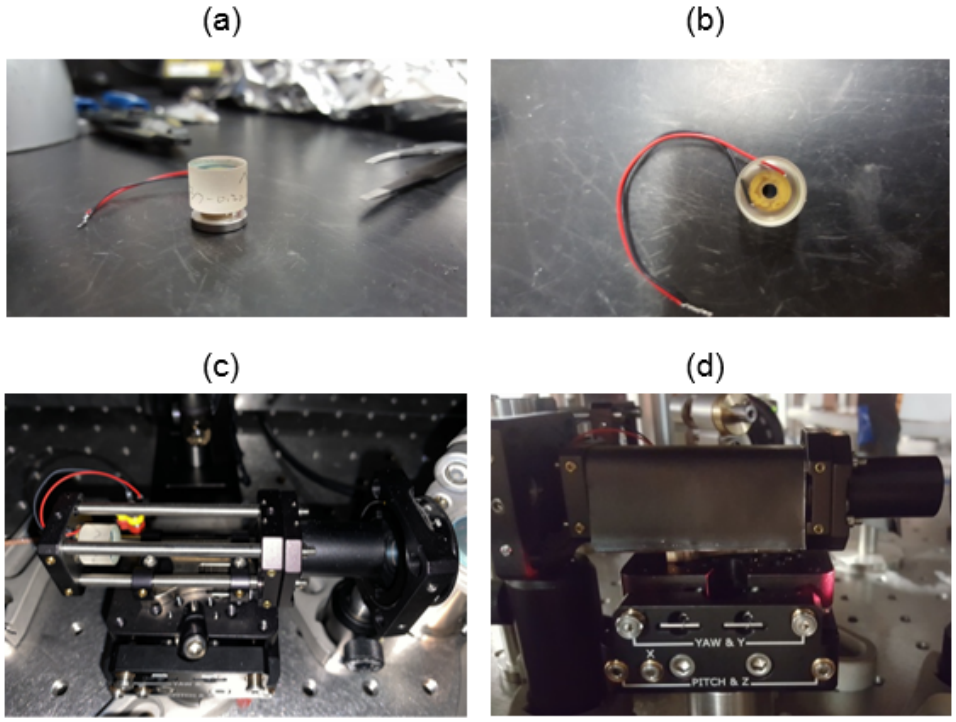

Figure 5.11: The spectral clean-up cavity consists of two spherical mirrors. One is glued to a ring piezo to lock the cavity length and the other one is placed in a tube, which allows adjustable cavity length. (a) side view and (b) top view of the mirror with piezo. (c) The overall setup of the cavity. (d) The cavity is usually covered with a piece of protective black paper.

For the work described in this thesis, the cavity length is set to be $L \sim 5.7$ cm, which corresponds to a free-spectral range (FSR) of

$$\text{FSR} = \frac{c}{2L} = 2.6 \text{ GHz} \tag{5.6}$$

The finesse of the cavity is determined by the circulating power loss after one round trip. In our cavity, the mirror reflectivity is 98%, which leads to a $\rho \approx 4\%$ loss per round trip. As a result, the finesse of the cavity can be determined as

$$\mathcal{F} = \frac{\pi}{1-\sqrt{\rho}} \approx 155 \tag{5.7}$$

An FSR of 2.6 GHz and finesse of 155 indicate that the FWHM of the cavity resonance is about 17 MHz. With this finesse and resonance linewidth, the cavity should suppress the scatterings from all lattice-driven transitions. In Chapter 6, I will examine how much the clean-up cavity would help with the lifetime issue.

Besides the design of the cavity itself, the locking system and beam mode-matching are also important. The cavity is locked with the Pound-Drever-Hall (PDH) technique, which schematic is depicted in Figure 5.12. The diffracted beam from the transmission grating is phase modulated by a 30.3 MHz homemade electro-optic modulator (EOM) before being

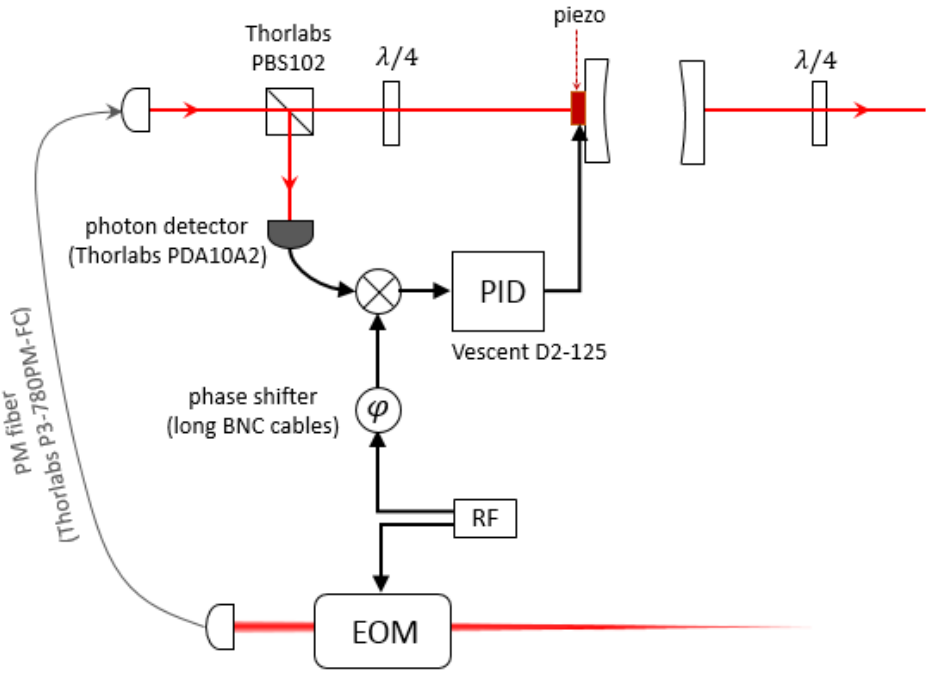

Figure 5.12: Schematic of PDH lock for the clean-up cavity. Beam mode-matching optics is omitted.

coupled into the optical fiber. The cavity is placed after the fiber where the beam quality is excellent and coupling into the TM_{00} Gaussian mode is easily achieved.

Last but not least important is the beam mode-matching. Good mode-matching is critical for obtaining efficient cavity coupling. In the experiments described in this thesis, the mode-matching optics is placed between the output optical fiber and the cavity. The beam coming out from the fiber coupler is collimated and has a beam waist of 1.45 mm. Right after the fiber coupler a convex lens with focal length 100 mm and a concave lens with focal length -50 mm shrink the beam waist at the center of the clean-up cavity to 140 μm. The mode-matching optics system is depicted in Figure 5.13.

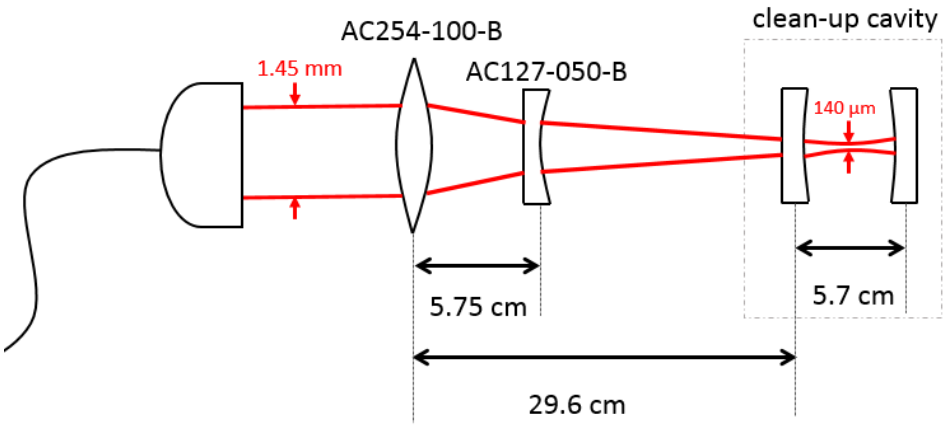

Figure 5.13: Mode-matching lens system for the clean-up cavity. This lens system is placed right after the fiber coupler and before the PHD lock system. The optics for PDH lock is omitted for simplicity.

Note that the clean-up cavity can be placed before and after the fiber. It had been placed after the fiber simply because of space consideration. Actually, in the latest version of the experiment, the cavity has been relocated before the fiber, where the fiber coupling can help suppress transverse modes generated from the cavity.

5.1.4 Fiber noise cancellation

High stability of frequency reference is crucial in clock experiments. In our experiment, the fundamental frequency stability limit is subject to the master laser, which resonance has an intrinsic $\delta f \sim 150$ Hz linewidth. A benefit of Λ-type Raman spectroscopy is its resistance to reference frequency instability. Assume Raman laser wavelengths of λ_1 and λ_2, the effective frequency instability Λ-type Raman spectroscopy is

$$|\frac{\lambda_1 - \lambda_2}{\lambda_2}|\delta f \tag{5.8}$$

In our usual two-photon spectroscopy, Raman laser wavelengths are 689 nm and 651 nm. These correspond to a frequency drift of ~ 10 Hz. Ideally, in the pursuit of high-precision measurements, this reference instability is the leading order precision limitation.

A critical criterion that validates the above statement is that no phase noise is induced as the light is distributed. In our experiment, the laser light production, the frequency comb, and the science vacuum chamber are spread over different optical tables. To distribute the frequency stability across the experiment, the frequency reference needs to be transferred from one optical table to another. A polarization-maintaining single-mode optical fiber is an ideal transmission medium for this task. However, this is also where the noise comes in. The light phase in optical fibers is sensitive to environmental noise, such as mechanical pressure, acoustic noise, local temperature gradient, etc. [40]. As laser light travels through an optical fiber, these environmental noises causes fluctuations in the index of refraction of the fiber and thus broaden the laser light spectrum. The resulting phase noise is typically on the order of 100 Hz to 1 kHz, therefore the noise on every metrologically important fiber must be actively compensated with the fiber noise cancellation technique that was first demonstrated in [41].

The environmental perturbation on the index of refraction of the fiber affects the optical fiber length (OPL). These noises are local and time-dependent

$$\text{OPL} = \int_{\mathcal{S}} n(\mathbf{r}, t) dr, \tag{5.9}$$

where $n(\mathbf{r}, t)$ is the index of refraction of the fiber and $\mathcal{S}$ denotes the fiber path [42]. Equation 5.9 leads to a phase shift on the laser that travels through the fiber

$$\varphi(t) = 2\pi \frac{OPL}{\lambda}, \tag{5.10}$$

where λ is the laser wavelength.

In order to cancel the fiber noise, a fraction of the transmitted light is retro-reflected back into the fiber and beat with a fraction of the non-transmitted light. Assuming the back-reflected light experiences the same OPL, the fiber-induced phase noise written on the laser after a round trip is then $2\varphi(t)$. Note that this assumption is valid only for short fibers. In our experiment, all metrologically important fibers are shorter than 10 m, which implies a travel time of $(10\text{m}) \times \frac{1.5}{c} \approx 50$ ns, given a typical index of refraction 1.5 for optical fibers. This travel time is a lot shorter than the time scale of lab noises, which is usually on the order of ~ 50 ms. Thus it is reasonable to assume the OPL stays constant as the light travels through the fiber.

The beat note detection between the back-reflected and non-transmitted beams is performed with the self heterodyne measurement [43]. A self heterodyne measurement is usually utilized to measure single-frequency laser linewidth. It typically involves a long optical fiber and an AOM. First the laser is split into two beams. One of the beams is sent through the fiber and frequency modulated by an AOM. Both beams are combined onto a photodiode

which records the beat note. Due to the time delay resulted from the long fiber, the transmitted beam becomes independent from the non-transmitted beam, therefore the beat note between these two beams reveals the linewidth of the laser. In the heterodyne measurement performed for the fiber noise, however, the situation is a bit different. The optical fibers used in the experiment are short so that the delay time is almost negligible compared to the laser coherence time. As a result, the beat note observed doesn't represent the laser linewidth but reflects the fiber-induced noise.

Figure 5.14(a) depicts the optics for our fiber noise cancellation. The beams are split from an AOM that is driven by a voltage-controlled oscillator (VCO) at $f_{\mathrm{AOM}} = 80$ MHz. The +1st order light is coupled into an optical fiber and $\sim 10\%$ of the transmitted light is back-reflected into the fiber. On the other hand, the 0th order output from the AOM forms the non-transmitted light and is fully reflected back to the AOM. From the second pass through the AOM, the 0th order of the back-reflected transmitted beam and the -1st order of the non-transmitted beam are beat with each other, which beat note is detected by a fast photodiode. After the whole process, the transmitted beam acquires a frequency shift of $f_{\mathrm{AOM}} + 2\varphi(t)$ and the non-transmitted beam acquires a phase of $-f_{\mathrm{AOM}}$. Upon beating these two beams, the beat note is $2f_{\mathrm{AOM}} + 2\varphi(t)$.

Figure 5.14(b) shows the locking scheme. To extract the fiber noise, the beat note is mixed with a $2f_{\mathrm{AOM}}$ RF signal generated by a direct digital synthesizer (DDS). The DDS is the 409B model by Novatech and it is referenced to a Rb atomic clock that has a frequency instability of 10^{-12}. Since the frequency variance in the DDS is negligible compared to the scale of fiber noise, the mixed signal is simply $2\varphi(t)$. This DC error is then fed into a PI circuit which output modulates the VCO frequency to compensate the fiber noise. Figure 5.15 illustrates the comparison of the power spectral density (PSD) with and without the

fiber noise cancellation.

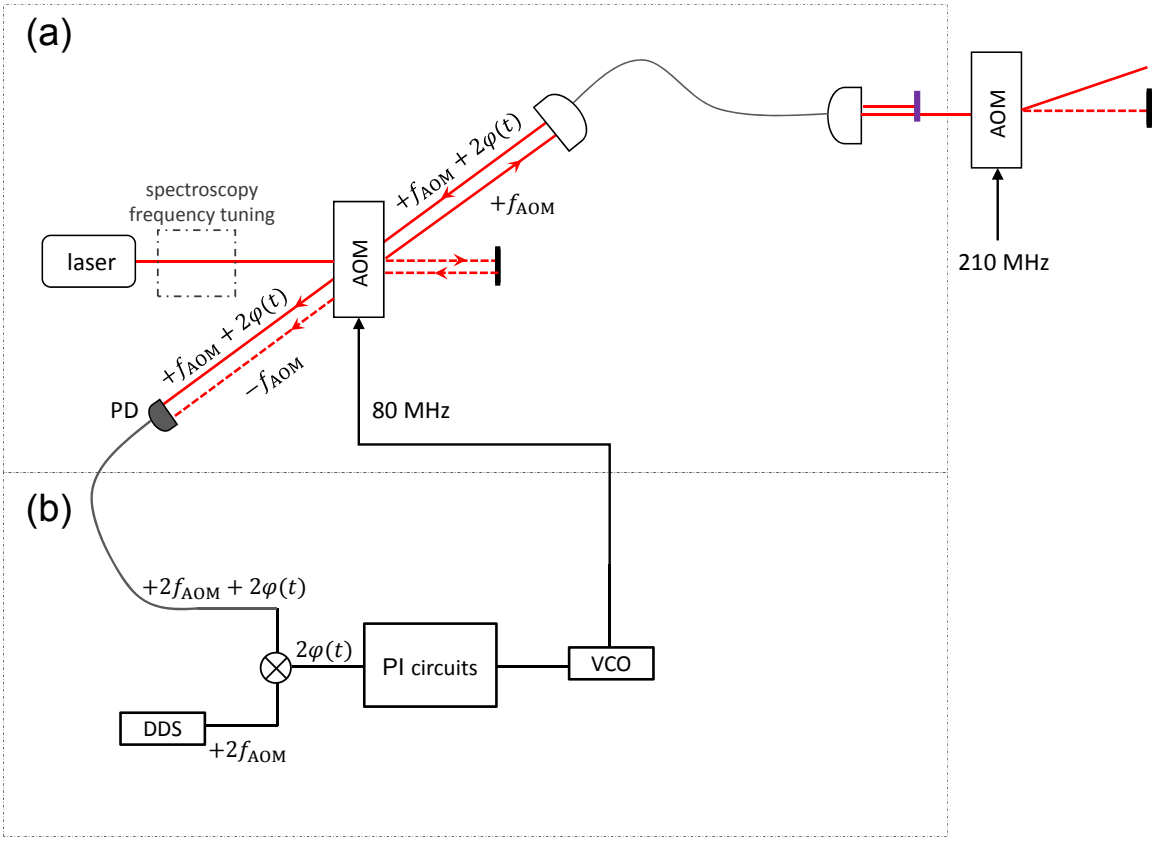

Figure 5.14: The setup for fiber noise cancellation. In (a) the optics for fiber noise cancellation is demonstrated. The fiber noise is probed with a self heterodyne measurement. The beat note between the transmitted and non-transmitted beams recorded by the photodetector (PD) is $2f_{\mathrm{AOM}} + 2\varphi(t)$. In (b) the lock design is shown. The beat note recorded by the PD is mixed with a strict DDS frequency to extract the fiber noise $2\varphi(t)$. The nearly DC signal is taken by the PI circuits which output modulates the VCO frequency to cancel the fiber noise.

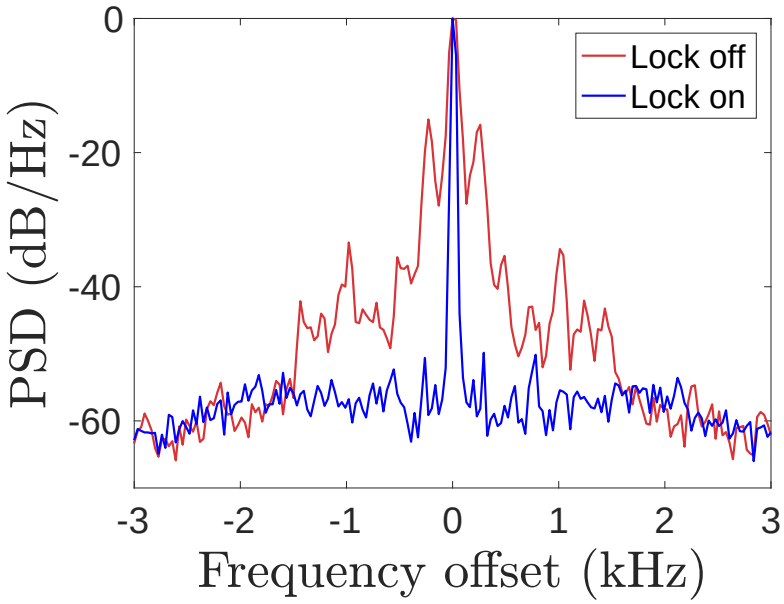

Figure 5.15: Power spectral density (PSD) with and without the fiber noise cancellation.

It is important to note that, with the fiber noise cancellation installed in the system, the probe beam shutter has to be arranged differently. Since AOM's allow nanosecond rise time, it is an ideal component for a shutter that precisely controls the laser pulse time. In the situation without the fiber noise cancellation, the spectroscopy tuning AOM served the role of the laser shutter. However, with the fiber noise cancellation implemented, the shutter AOM needs to be relocated because continuously interrupting the laser would ruin the fiber noise lock. To achieve this, an extra shutter AOM is placed after the output fiber coupler, as shown in Figure 5.14. The AOM is driven by a constant 210 MHz RF and the +1st order output beam goes into the experiment. Due to the additional AOM, the resulting frequency shifts have to be carefully taken into account when calculating the binding energies. An example will be demonstrated in Section 5.2.3.

5.1.5 Probe power stabilization

Aside from frequency stability, probe laser intensity stability also plays a critical role in achieving good coherence. For a two-photon Raman transition, the effective Rabi frequency is given by Equation 4.13, which indicates the Rabi frequency is proportional to the square root of the multiplication of laser intensity from each of the Raman beams. Straightforward error propagation implies that the probe laser intensity instability contributes to the Rabi frequency instability by

$$\frac{\delta\Omega_{eff}}{\Omega_{eff}} = \frac{1}{\sqrt{2}}\frac{\delta P}{P}, \tag{5.11}$$

where P is the Raman laser power and it is assumed that the intensity stability is identical for both Raman lasers. For instance, a $\sim$10% fluctuation in the probe laser intensity leads to $\sim$7% temporal fluctuation in the Rabi frequency.

The phase of Rabi oscillations comes from the time integral of the Rabi frequency so the accumulative Rabi frequency fluctuation results in a phase noise that limits the coherence time. With a fluctuating Rabi frequency $\Omega(t) = \Omega_0 + \delta\Omega(t)$, the corresponding Rabi oscillation is

$$\text{state population} \propto \cos^2\left(\int_0^t (\Omega_0 + \delta\Omega(\tau))\, d\tau\right) \tag{5.12}$$

The dephasing caused by Rabi frequency fluctuation can be demonstrated with a toy model where the fluctuation is treated as a Gaussian process. Assuming a fractional Rabi frequency stability of κ, the dimensionless parameter $\eta(t) \equiv \frac{\delta\Omega(t)}{\Omega_0}$ denotes the Gaussian process and is expressed as

$$\eta(t) = \mathcal{N}(0, \kappa) \tag{5.13}$$

In this model, the Rabi oscillation can be written as

$$\text{state population} \propto \cos^2\left[\Omega_0\left(t + \int_0^t \eta(\tau)d\tau\right)\right] \tag{5.14}$$

It can be shown that the accumulative phase noise term is a Gaussian random variable

$$\int_0^t \eta(\tau)d\tau = \mathcal{N}(0, \kappa t) \tag{5.15}$$

The dephasing time is defined by the time duration at which the standard deviation of the accumulative phase noise reaches 2π. In other words,

$$T_{\text{dephasing}} \equiv \frac{2\pi}{\kappa\Omega_0} \tag{5.16}$$

For Rabi oscillations with $\Omega_0 = 1$ kHz, a $\kappa = 7\%$ fractional stability leads to 90 ms dephasing time.

Besides instantaneous stability, laser intensities also suffer from long-term drift. Along the way from where laser light is generated to the science chamber, there are many things that need to be maintained in high quality to prevent drifts in laser intensities. These include laser mode, phase locking stability, fiber coupling efficiency, etc. Without active stabilization, a 20% drift in laser intensity in the course of 2 hours is likely to happen. This amount of intensity drift would shift the transition resonance and ruin the clock measurements. As I will discuss in Section 5.2.1, the light shift induced by Raman probe lasers is $\frac{\Omega_p^2}{4\Delta}$, where Ω_p is the one-photon Rabi frequency and Δ is the common detuning in the Raman spectroscopy. So, how much resonance shift would the probe intensity drift lead to? Let's assume a narrow

Raman transition with a linewidth of 50 Hz that is driven with $\Delta = 25$ MHz. To achieve $\Omega_{eff} = 50$ Hz, the Rabi frequency from each of the Raman lasers have to be

$$\Omega_p = \sqrt{2\Delta\Omega_{eff}} = \sqrt{2 \times 25 \text{ MHz} \times 50 \text{ Hz}} = 50 \text{ kHz},$$

assuming equal Rabi frequency between Raman probe lasers. A 20% intensity drift in one of the laser beams would lead to a $0.2 \times \frac{(50 \text{ kHz})^2}{4 \times 25 \text{ MHz}} = 5$ Hz systematic light shift. Therefore, an uncontrolled Raman laser intensity would not only result in dephasing in Rabi oscillations, but also contribute to a non-negligible systematic error in clock measurements.

Laser intensity stabilization is vital to avoid these scenarios. Figure 5.16 illustrates the scheme for active intensity stabilization. Stable laser intensity is accomplished by engaging feedback on the amplitude of the RF signal that drives the spectroscopy AOM. After the optical fiber, a small fraction of probe laser is picked off and detected by a fast photodetector (PD). The intensity reading from the PD, I_{PD}, is sent to a high-speed servo controller (LB1005-S by Newport) where it is coupled to an adjustable internal reference, I_{ref}, that determines the intensity lock set point. To stabilize the intensity, the coupled signal $I_{\text{ref}} - I_{\text{PD}}$ is fed into a voltage variable attenuator (ZX73-2500-S+ by Mini-Circuits) which controls the RF amplitude. When $I_{\text{PD}} = I_{\text{ref}}$ a constant attenuation is applied on the RF amplitude so that the intensity is stable. While $I_{\text{PD}} > I_{\text{ref}}$ the attenuator reduces the RF amplitude more to compensate for the intensity variance and vice versa. With this stabilization scheme, the fractional instability of Raman probe laser intensities has been reduced to less than 1%. Moreover, since the stabilized intensity is controlled by the servo box's internal reference, the long-term intensity drift has also been eliminated.

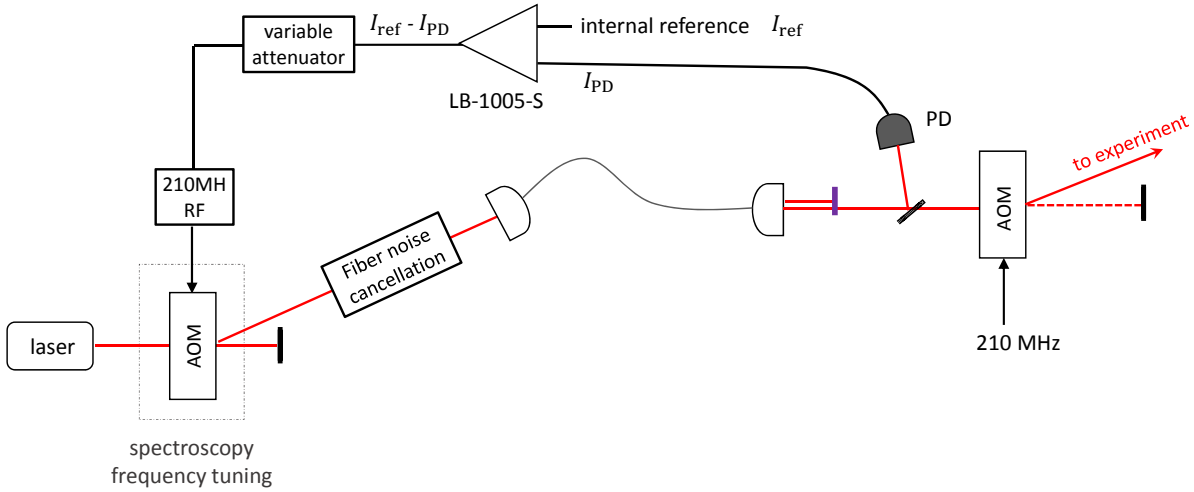

Figure 5.16: Schematic of probe laser intensity stabilization. A small fraction of probe laser is detected by a photodetector (PD). The intensity reading from the PD is coupled to an adjustable reference in the servo box to generate an error signal. According to the error signal, the variable attenuator adjusts the RF attenuation to compensate for the intensity variance.

5.2 Clock systematic effects

With these stabilization schemes implemented, the experimental system has been much better controlled, which has enabled the measurements of clock systematics. In this section, I mainly discuss the systematic effect from Raman probe intensities and briefly touch the effect of molecule collisions.

5.2.1 Probe laser intensities

The Stark shift due to Raman probe lasers is a major source of systematic bias [44,45]. In a Λ-type Raman transition described in Figure 3.5, the light shifts induced by the probe beams can be eliminated when the probe intensities are at the *balanced ratio*, at which the Rabi

frequencies of both Raman beams are equal, i.e. $\Omega_1 = \Omega_2$.

This can be understood intuitively. Assume a Raman transition with probe lasers red-detuned from the virtual state. In the measurements described in this section *we keep the second Raman laser frequency constant while tuning the first Raman laser frequency to probe the light shifts.* When the first Raman laser intensity increases, the induced light shift lowers the energy of the initial clock state $|g_1\rangle$, shown in Figure 5.17(a). Therefore the first Raman laser frequency needs to be larger in order to compensate for this light shift and maintain the resonance. Similarly, when the second Raman laser intensity increases, the induced light shift lowers the energy of the final clock state $|g_2\rangle$, shown in Figure 5.17(b). To compensate for the light shift, the first Raman laser frequency has to be smaller. Here comes

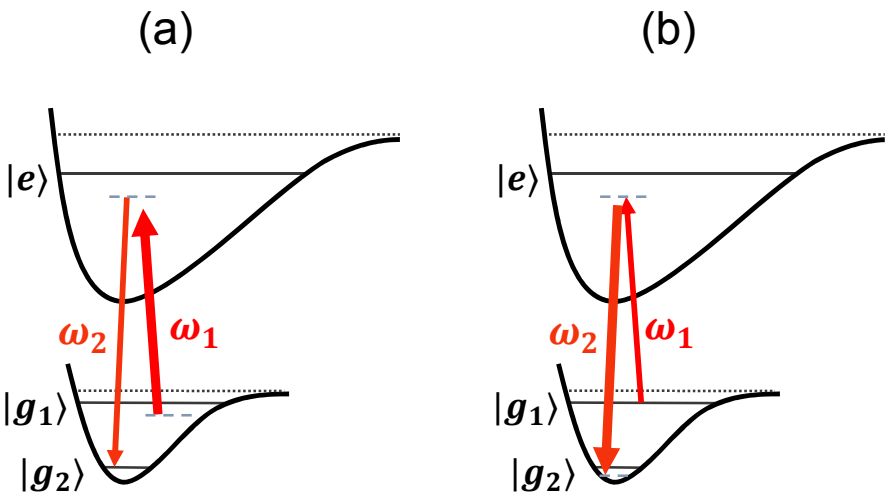

Figure 5.17: Illustration of schematic bias due to probe beam AC Stark shift. If the second Raman laser frequency ω_2 remains fixed, (a) the laser frequency ω_1 needs to be *larger* in order to compensate for the light shift induced by a stronger first Raman laser. Similarly, (a) the laser frequency ω_1 needs to be *smaller* in order to compensate for the light shift induced by a stronger second Raman laser.

the interesting conclusion. Because the light shift direction is opposite and that the shift is proportional to Rabi frequency square, the light shifts from both lasers are canceled out if the Rabi frequencies are matched.

When the Rabi frequencies are matched, it indicates that the probe beam intensities ratio is the inverse of the DMS ratio. This is because Rabi frequency, by definition, is proportional to the multiplication of dipole moment and electric field amplitude. In other words, $\Omega \propto (d \times E)$, where d is the dipole moment and E is electric field amplitude. Adopting the definition of laser intensity from Equation 2.8, when $\Omega_1 = \Omega_2$, we have

$$d_1\sqrt{I_1} = d_2\sqrt{I_2}, \tag{5.17}$$

Hence,

$$\frac{I_1}{I_2} = \frac{d_2^2}{d_1^2} \tag{5.18}$$

Figure 5.18 demonstrates the probe beam light shift at different intensity ratios. In this measurement, the Raman transition is formed by $|g_1\rangle = X(-1,0)$, $|g_2\rangle = X(+6,0)$ and $|e\rangle = 0_u^+(-4,1)$, in which setup the DMS ratio is $\frac{d(|g_1\rangle, e)^2}{d(|g_2\rangle, e)^2} = R_0$. The light shift is measured with high and low probe intensities while fixing the probe intensity ratio at $0.5R_0, R_0$ and $2R_0$. As demonstrated, the light shift is consistent with zero when the probe intensity ratio is equal to R_0.

Since the balanced probe intensity is directly linked to Raman transition DMS's, precise understanding in transition strengths is critical for eliminating the probe beam light shift. In Chapter 7, methods for precisely measuring transition strengths will be explored.

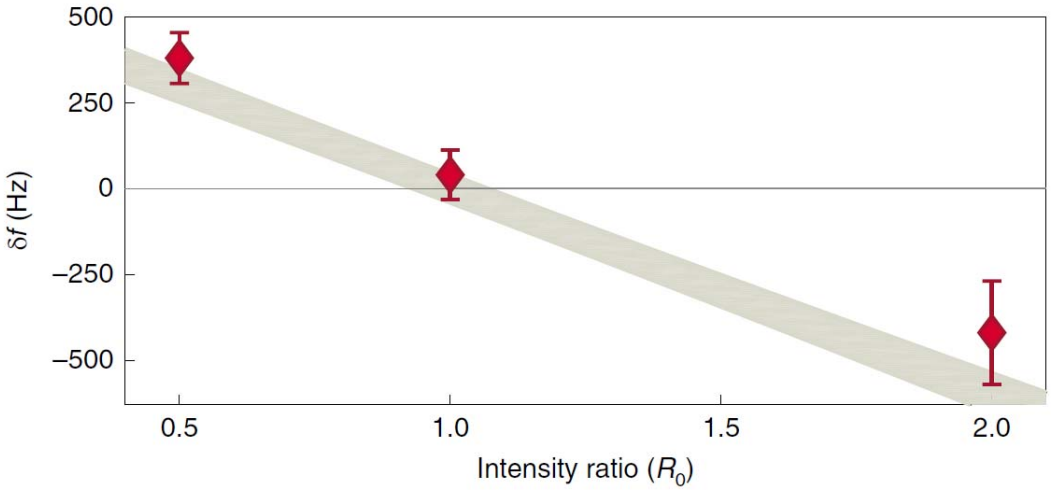

Figure 5.18: Demonstration of probe beam light shift at different intensity ratios. The light shift is measured with high and low probe intensity while keeping the intensity ratio at several regime. At the probe intensity ratio where the individual Rabi frequencies are equal, the light shift is consistent with zero. Adapted from [9].

5.2.2 Collisional frequency shifts

Apart from Raman probe beam light shift, the collisional frequency shift is another systematic uncertainty that we have investigated. It's been demonstrated in many types of experiments that collisions would lead to density dependent frequency shifts [46–50].

To probe the collisional shift, the narrow clock transition frequency is recorded with different molecular density, shown in Figure 5.19 and the molecular density is varied by tuning the blue MOT loading time. In this measurement, the loading time is varied between 400 ms to 5,000 ms and the molecular density is represented by the recovery signal strength. As demonstrated, the resolved resonance frequency doesn't have obvious dependence on molecular density, which indicates that the molecular clock accuracy is not limited by collisions under current precision.

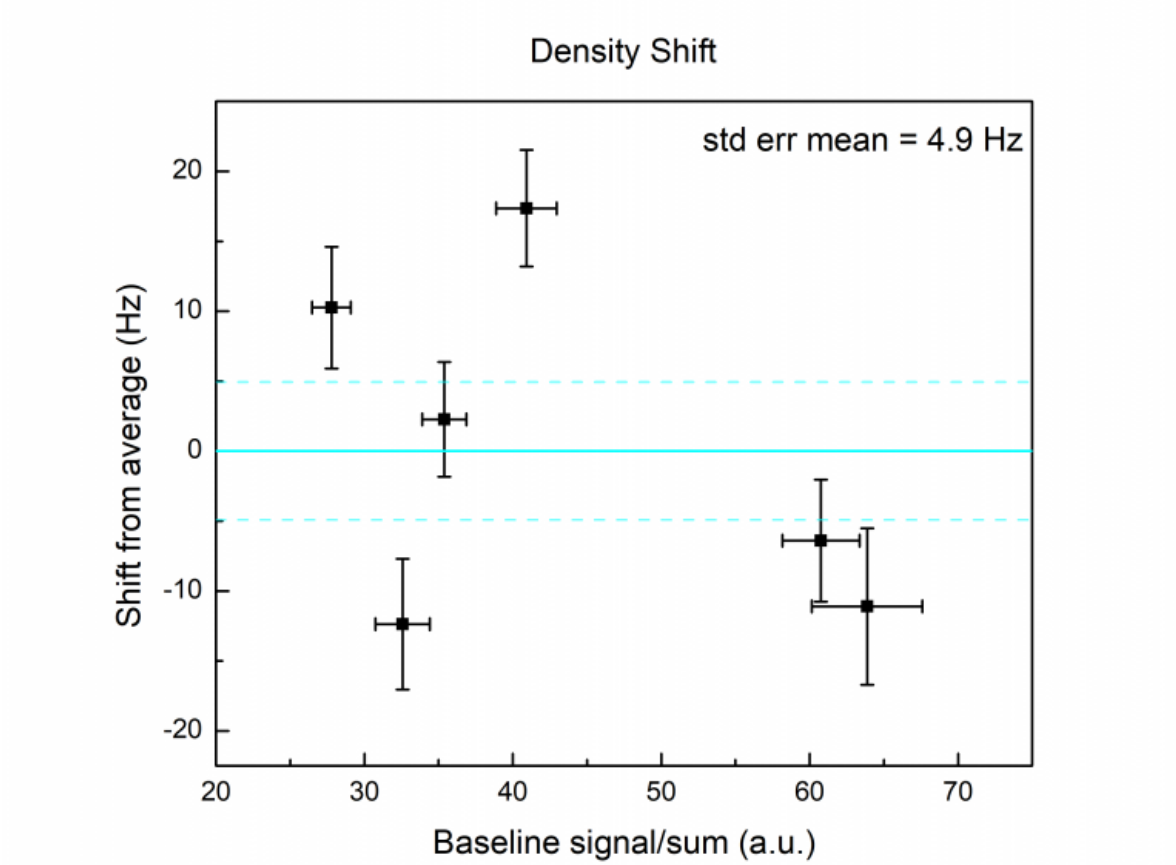

Figure 5.19: Demonstration of collisional frequency shift in the molecular clock. The clock transition frequency is measured with a variety of molecular density. In this measurement, the molecular densities is controlled by the blue MOT loading time.

5.2.3 Determination of the $X(6,0)$ state binding energy

In this section, I demonstrate the calculation of binding energy of $X(6,0)$ state from the $X(-1,0) \rightarrow X(6,0)$ clock transition. This analysis is based on the 30 Hz clock transition lineshape shown in Section 4.4.1, where the Raman probe intensities are controlled at the balanced ratio. The logic in this calculation is universal to all the other ground states. To perform binding energy calculations, one must keep the following points in mind.

- The lattice-induced light shift must be eliminated. This can be accomplished either by extrapolating the spectroscopic resonance frequency to zero lattice power or with the magic lattice trap technique. Due to the enormous polarizability difference, a magic lattice is strongly preferred when probing binding energies of deeply bound states via two-photon spectroscopy.

- All the other systematics must be carefully coped with. In this section, the two-photon spectroscopy is obtained with the balanced probe power intensities, which eliminates the probe beam Stark effect.

- All frequency shifters must be included in the calculation. Along the beam paths, a lot of frequency shifts take place for a variety of reasons, including spectroscopic tuning, laser beam shutters, fiber noise cancellations, etc. Everything should be properly included to achieve accurate calculations.

5.2.3.1 Metrology system

To carry out the calculations, the metrology system has to be explained in detail. As previously elaborated, the frequency stability is set by the master laser. All the probe lasers are stabilized to the master laser in different ways. First, the first Raman laser (689 nm) is directly phase-locked to the master laser, shown in Figure 5.20. When driving the clock transition, the phase lock beat note is set to be $f_{b_1} = f_1 - f_{\text{master}} = -712.4$ MHz. To perform spectroscopic sweep, the laser beam undergoes a double pass system which takes {-1st,-1st} orders from an AOM driven by a (210 MHz + det_1) frequency. According to Figure 4.18, an overall frequency detuning $\text{det}_1 = -4.554,936(1)$ MHz is applied at the transition resonance. Moreover, the fiber noise cancellation and the laser beam shutter AOM's lead to a shift of +80 MHz and +210 MHz respectively on the laser frequency.

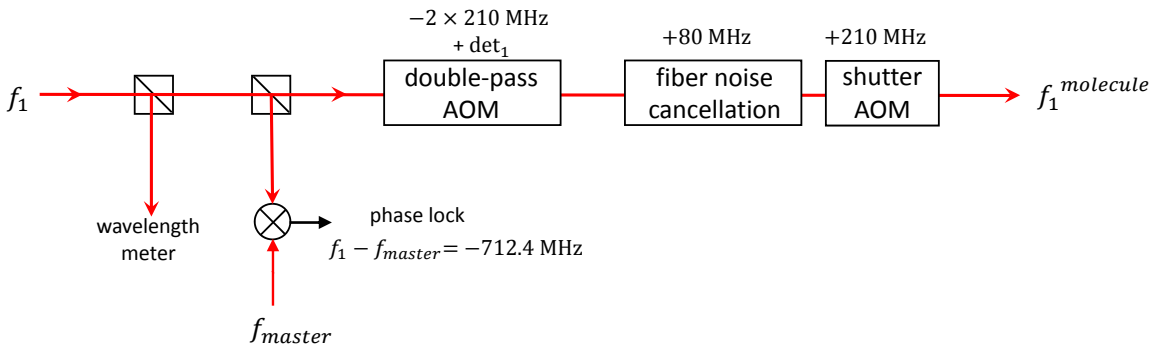

Figure 5.20: Schematic of first Raman laser lock system.

To reference the frequency comb stability to the master laser, a fraction of the master laser light is led to the frequency comb table via an optical fiber to stabilize the com repetition rate. Before the fiber coupler a fiber noise cancellation system is set up, which leads to a +80 MHz frequency shift, shown in Figure 5.21.

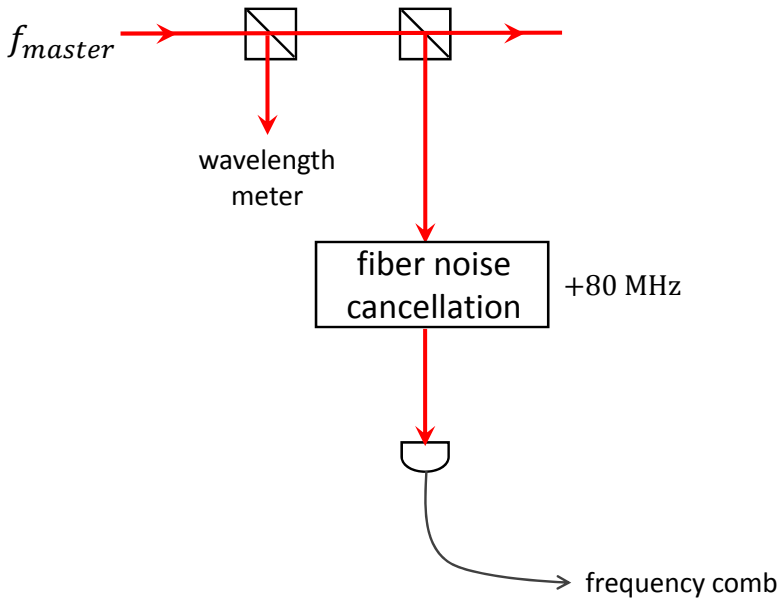

Figure 5.21: Schematic of frequency comb repetition rate stabilization with the master laser.

The second Raman laser (651 nm) is stabilized to the frequency comb. The lock system for the second Raman laser is pretty similar to that for the first Raman laser with only some tiny differences. First, the sweeping AOM is centered at 80 MHz and the double pass scheme takes {+1st,+1st} orders. Second, the fiber noise cancellation AOM is centered at 210 MHz. Last, the wavelength meter measures the laser wavelength *right before* the fiber coupling. A schematic for the second Raman laser lock is shown in Figure 5.22. Note that at the resonance, an frequency detuning $\text{det}_2 = -13.4$ MHz is applied on the spectroscopy AOM.

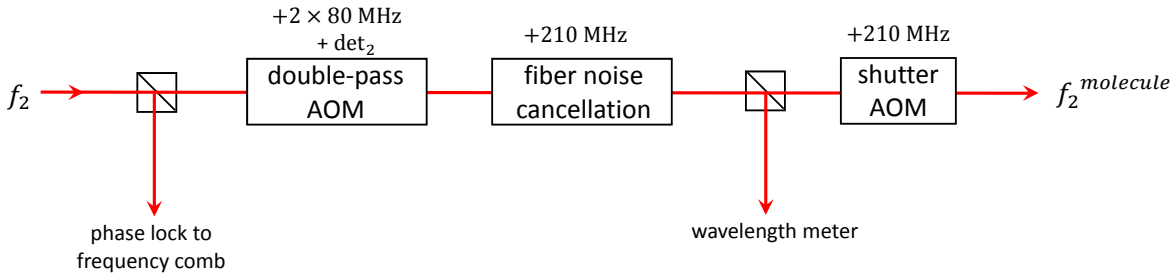

Figure 5.22: Schematic of second Raman laser lock system.

5.2.3.2 Binding energy relative to the $X(-1,0)$ state

With the metrology system elaborated, the binding energy calculation becomes straightforward. First, let's back out the number of comb tooth N_{master} that is used for stabilizing the repetition rate. The master laser frequency is determined by the $^1\text{S}_0 \rightarrow {}^3\text{P}_1$ atomic transition, which is $\lambda_{master} = 689.449,2$ nm read by the wavelength meter. Also, when the clock transition spectroscopy is taken, the repetition rate recorded by the frequency comb internal counter is $f_{RR} = 250,011,945.69(2)$ Hz and the CEO frequency f_{CEO} is locked on the *negative side*, corresponding to the case in Figure 2.3(b). Note that to lock the repetition rate, the locking scheme *with* $1\times$*CEO frequency subtracted* is adopted, which means the beat note between the master laser and the N_{master}-th comb tooth is

$$(f_{master} + 80\text{MHz}) - f_{N_{master}} = f_{CEO} + 40 \text{ MHz} \tag{5.19}$$

In other words,

$$\left(\frac{c}{\lambda_{master}} + 80 \text{ MHz}\right) - (N_{master} f_{RR} - 2f_{CEO}) = 20 \text{ MHz} + 40 \text{ MHz}, \tag{5.20}$$

which yields $N_{master} = 1,739,233$. Therefore we have the master laser frequency

$$f_{master} = N_{master} f_{RR} - f_{CEO} - 40 \text{ MHz} \tag{5.21}$$

The Raman laser frequencies *seen by the molecules* can also be determined in a straightforward manner. According to Figure 5.20, the first Raman laser frequency f_1 is determined by $f_1 - f_{master} = -712.4$ MHz. The frequency the molecules see is the one undergoes the seris of frequency shifts

$$\begin{aligned} f_1^{molecule} &= f_1 - 2 \times 210 \text{ MHz} + \det_1 + 80 \text{ MHz} + 210\text{MHz} \\ &= f_{master} - 712.4 \text{ MHz} - 2 \times 210 \text{ MHz} + \det_1 + 80 \text{ MHz} + 210\text{MHz} \\ &= N_{master} f_{RR} - f_{CEO} - 886.954,936(1) \text{ MHz} \end{aligned} \tag{5.22}$$

To determine the second Raman laser frequency, we need to back out the number of comb tooth to which the second Raman laser is locked. The wavelength meter reads the second Raman laser wavelength to be 651.8625 nm. According to Figure 5.22, we can set up the equation for comb tooth number

$$\left(\frac{c}{\lambda_{second}} - 210\text{ MHz} - 160\text{ MHz} - \det_2\right) - (N_{second} f_{RR} - 2f_{CEO}) = +f_{CEO}, \tag{5.23}$$

which yields $N_{second} = 1,839,516$. Note that the positive sign on the right hand side of Equation 5.23 comes from the fact that f_{CEO} is locked on the negative side. Therefore, the second Raman laser frequency f_2 can be determined as

$$f_2 = N_{second} f_{RR} - f_{CEO} \tag{5.24}$$

and the frequency that the molecules see is

$$\begin{aligned} f_2^{molecule} &= N_{second} f_{RR} - f_{CEO} + 160\text{ MHz} + 210\text{ MHz} + 210\text{ MHz} + \det_2 \\ &= N_{second} f_{RR} - f_{CEO} + 566.6\text{ MHz} \end{aligned} \tag{5.25}$$

The relative binding energy between the clock states, namely $X(-1,0)$ and $X(6,0)$, can then be calculated as

$$\begin{aligned} \text{relative B.E.} &= f_2^{molecule} - f_1^{molecule} \\ &= (N_{second} - N_{master})\, f_{RR} + 566.6\text{ MHz} + 886.954,936(1)\text{ MHz} \\ &= 25.073,401,504(2)\text{ THz} \end{aligned} \tag{5.26}$$

5.2.3.3 Absolute binding energy

The absolute binding energy of $X(6,0)$ state can be backed out by adding the binding energy of $X(-1,0)$ state to the relative energy. So far, the most accurate measurement of $X(-1,0)$

binding energy is 136.644,7(50) MHz [14], therefore the absolute binding energy of $X(6,0)$ can be calculated to be

$$\begin{aligned} \text{X(6,0) binding energy} &= 25.073,401,504(2)\ \text{THz} + 136.644,7(5)\ \text{MHz} \\ &= 25.073,538,149(2)\ \text{THz} \end{aligned} \tag{5.27}$$

Although eventually the precision on absolute binding energies will be constrained by the benchmark state, precise relative binding energies are sufficient to serve the purpose of the molecular clock.

Chapter 6

Unexpected limits on clock state lifetime

In Chapter 4 I demonstrate Rabi oscillations between a shallow and a deeply bound ground state. With a magic lattice trap, the inhomogeneous effect is eliminated, which increases the coherence time by three orders of magnitude. However, a unexpectedly short lifetime that is only $\sim$10 ms is observed for the clock states. In this chapter I explore the reasons behind this anomalous lifetime puzzle.

Let's first elaborate on how direct measurement of ground state lifetime is carried out. For shallow ground states, the measurement is straightforward. After the molecules are populated on a certain ground state, a duration of wait time is applied before the molecules are recovered into atoms and counted. Therefore, the molecule lifetime can be backed out by fitting the molecule recovery curve as a function of the wait time. The time sequence of this measurement is demonstrated in Figure 6.1. For deeply bound ground states, the scenario is more complicated. Because directly populating molecules on a deeply bound state is difficult, transferring them from a shallow ground state is (so far) the only way to produce deeply bound molecules. Also, since the bound-to-free coupling is too weak for deeply

bound ground states, direct recovery is not practical, therefore it requires transferring deeply bound molecules back to a shallow state to count the molecule number. As a result of these

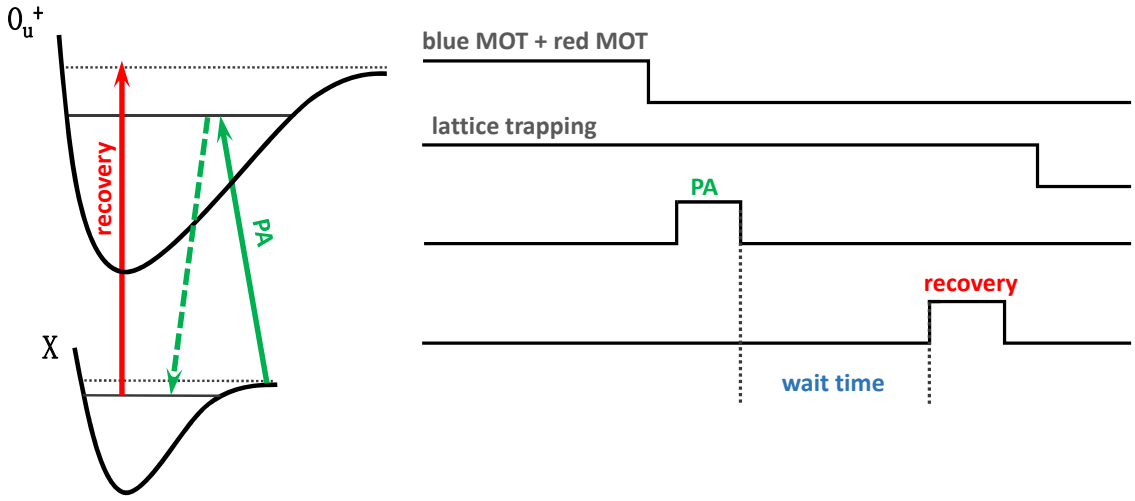

Figure 6.1: Time sequence for shallow ground state lifetime measurements. The lifetime of a shallow ground state can be backed out by varying the wait time inserted between molecule production and recovery. Note that a wiping pulse is applied after the photoassociation (PA) pulse to clean up leftover atoms. This pulse is not shown for simplicity.

limitations, several things have to be taken care of in order to perform accurate measurements on deeply bound ground state lifetime. First, a good signal noise (S/N) ratio has to be ensured. Due to the complexity of state transfer, the signal in this kind of experiment is typically very weak. To compensate for the poor signal, an extra atom loading time is usually required. A typical loading time used for carrying out ground state lifetime is 800 μs for shallow states and 5 s for deeply bound states. Second, the molecules left on the initial ground state have to be properly cleaned up. Due to the limited state transfer efficiency, a small fraction of molecules are left on the initial state after the transfer. If the leftover

molecules are not cleaned up, the lifetime measurements will be contaminated. A typical way to accomplish the cleanup is to shine a pulse in which the recovery light and the strong cycling 461 nm $^1P_1$ transition light are both on. The recovery pulse breaks the leftover molecules into atoms and the 461 nm light wipes out the atoms. Usually, a wipe pulse of 800 μs is sufficient for a complete wipe out but one should always confirm no residual molecules are left before carrying out the measurement. The time sequence for deeply bound ground state lifetime measurement is demonstrated in Figure 6.2.

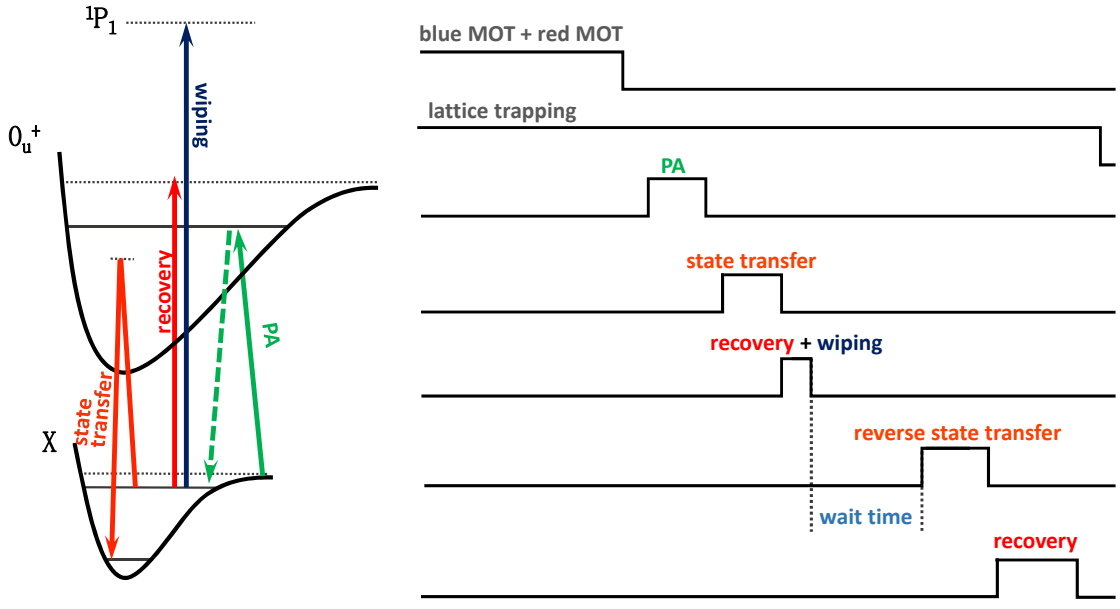

Figure 6.2: Time sequence for deeply bound ground state lifetime measurements. The situation is more complicated than measuring the shallow ground state lifetime. Population of deeply bound molecules relies on a state transfer process. To prevent the leftover molecules from disturbing the measurements, a wipe pulse consisting of the recovery light and the 461 nm $^1P_1$ transition light is applied to clean them up. The wait time is defined from the end of wipe pulse to the beginning of the second state transfer pulse. Note that another wiping pulse is applied right after the photoassociation (PA) pulse to clean up leftover atoms. This pulse is not shown for simplicity.

6.1 Ground state decay models

In this section I discuss the ground state decay mechanisms. The loss mechanisms discussed in this chapter are categorized into the one-body type and the two-body type.

6.1.1 One-body loss

In a 1D lattice trap, there are usually a few molecules trapped in one lattice site. Let's first consider the situation where multi-body interactions are weak and negligible. This approximation is usually enough to explain most of the ground state decays. Under this approximation, the molecule decay originates from one-body mechanisms, including molecule natural decay, molecule-light interactions and background gas collisions. Note that the background gas collision is categorized as an one-body mechanism because it doesn't involve interactions between molecules in the lattice [52]. The decay of molecules in the lattice trap can be described by the differential equation

$$\dot{\rho} = -\left(\Gamma_0 + \Gamma_c + \sum_k \Gamma(\omega_k)\right)\rho, \tag{6.1}$$

where ρ represents the local density of molecules in the lattice and Γ_0, Γ_c, and $\Gamma(\omega_k)$ denote the decay rate due to natural lifetime, background collisions and molecule interaction with laser k, respectively. Integrating Equation 6.1 yields

$$\dot{N} = -\left(\Gamma_0 + \Gamma_c + \sum_k \Gamma(\omega_k)\right)N, \tag{6.2}$$

where N is the total number of molecules in the lattice trap. Equation 6.2 has the solution $N(t)$ described by

$$N(t) = \exp\left[-\left(\Gamma_0 + \Gamma_c + \sum_k \Gamma(\omega_k)\right) t\right] N(0), \tag{6.3}$$

Not all decay mechanisms considered in Equation 6.3 contribute equally. Let's discuss the contributions from each mechanism.

- First, the natural decay is so slow that it can be neglected in the work discussed in this thesis. According to *ab initio* calculations, the natural lifetime of ground states is over a million years and thus it is reasonable to neglect its contributions to the decay rate.

- Second, the decay due to molecule-light interaction depends on the laser frequency and intensity. The light scattering rate is described by Equation 4.9

  $$\Gamma(\omega_k) = \frac{\gamma_k \Omega_k^2}{\gamma_k^2 + 2\Omega_k^2 + 4(\omega_k - \omega_0)^2},$$

  where γ_k is the natural lifetime of the excited state to which the laser k addresses and ω_0 is the resonant transition frequency. The contribution from the light scattering dominates the molecular decay when the laser intensity is large or the laser frequency is close to a transition resonance. In the context of the molecular clock, the two-photon Raman clock transition is formed by two lasers that are detuned from the virtual state. If the Raman lasers are too close to the virtual state, the one-photon scattering will limit the clock state lifetime. However, if they are too far away from the virtual state, the effective Rabi frequency would be too small, which makes it hard to observe high-quality Rabi oscillations. Fortunately, the one-photon scattering rate decreases with $\frac{1}{\Delta^2}$ while the effective Rabi frequency scales with $\frac{1}{\Delta}$. It is therefore possible to find a proper Δ so that the effective Rabi frequency is not too small and also the Raman probe laser scattering is well suppressed. In this thesis, the typical virtual state for the

clock transition is $0_u^+(-4,1)$ state, which has natural linewidth γ ~30 kHz. Assuming driving Rabi oscillations with balanced probe Rabi frequency of 150 kHz and detuning $\Delta = 25$ MHz, the effective Rabi frequency is $\sim$ 230 Hz. Under these conditions the Raman probe laser scattering is $\sim \frac{(30\text{ kHz})\times(150\text{ kHz})^2}{4\times(25\text{ MHz})^2} = 0.27$ Hz, corresponding to a lifetime of ~0.6 s, which satisfies the requirement pretty well.

- Third, the molecule lifetime is capped by the background gas collisions [55]. The optical lattice is implemented in a vacuum of 10^{-9} Torr, corresponding to a gas density of 10^7 cm^{-3}. Because of the lattice trap depth is typically ~50 μK, the elastic collisions between trapped the ultra-cold molecules and the residual hot gas transfer enough momentum to kick out the trapped molecules from the trap. In a vacuum

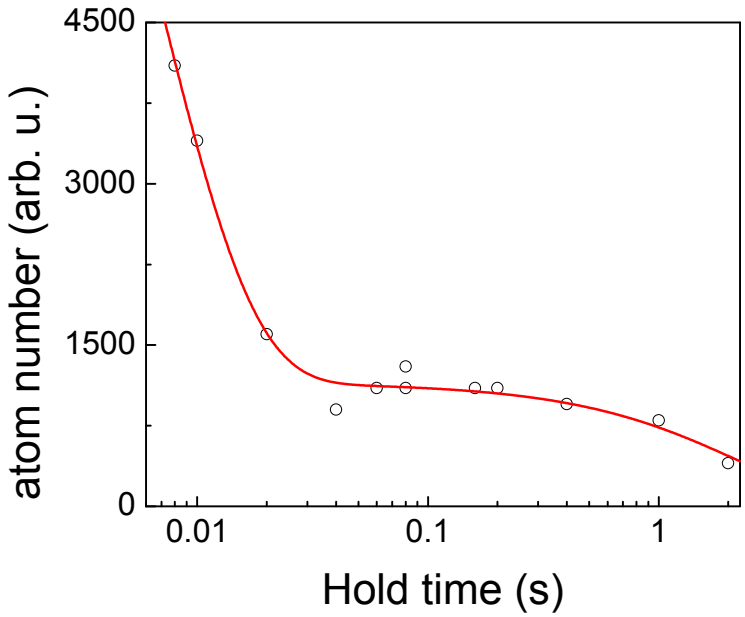

Figure 6.3: The background limited lifetime is measured with the time-of-flight method. The trace is fit to a double decay model, which suggests the hot atoms escape from the trap in 6.5(9) ms ant that the cold atoms can stay trapped for 2.2(6) s.

of 10^{-9} Torr, the background limited lifetime is on the order of a few seconds [53, 54]. In Figure 6.3, the background limited lifetime of our optical lattice is characterized. Note that in this measurement, it is the decay of trapped atoms that is measured but the loss mechanism and the decay timescale of atoms are similar to those of molecules. In Figure 6.3, the data is fit to a double exponential decay model. It is because the lattice initially traps a group of hot atoms which escapes from the trap quickly. For the colder atoms that we care about, they can stay in the trap for as long as 2.2(6) s.

6.1.2 Two-body inelastic collisional loss

In the one-body loss model, it is assumed that no collision between trapped molecules is present. However, in the situation where multiple molecules are trapped in the same lattice sites, the collisional effect has to be taken into account. To model the decay rate, an additional collisional term is added to the loss differential equation [52, 54].

$$\dot{\rho} = -\left(\Gamma_0 + \Gamma_c + \sum_k \Gamma(\omega_k)\right)\rho - \beta\rho^2, \tag{6.4}$$

where β is the collisional parameter. Integrating Equation 6.4 yields

$$\dot{N}(t) = -\left(\Gamma_0 + \Gamma_c + \sum_k \Gamma(\omega_k)\right)N(t) - \beta\int_V \rho(\mathbf{r},t)^2 d^3r, \tag{6.5}$$

With the assumption of constant molecule temperature, Equation 6.5 can be solved by

$$N(t) = \frac{N(0)\exp(-\Gamma t)}{1 + \dfrac{N(0)\kappa}{\Gamma}\left[1 - \exp(-\Gamma t)\right]}, \tag{6.6}$$

where κ is a parameter depending on effective lattice site volume and $\Gamma = \Gamma_0 + \Gamma_c + \sum_k \Gamma(\omega_k)$ is the one-body decay rate [56].

6.2 Shallow ground state lifetime

In this section I discuss the lifetime measurements for the two shallowest ground states. These measurements are well described by the two-body collisional loss mechanism and suggest a molecular lifetime of ∼100 ms.

6.2.1 $X(-1,0)$ state lifetime measurement

Figure 6.4 demonstrates the lifetime measurement of $X(-1,0)$ state. In this measurement, around 7000 $X(-1,0)$ molecules are produced and spread over ∼700 lattice sites. With this

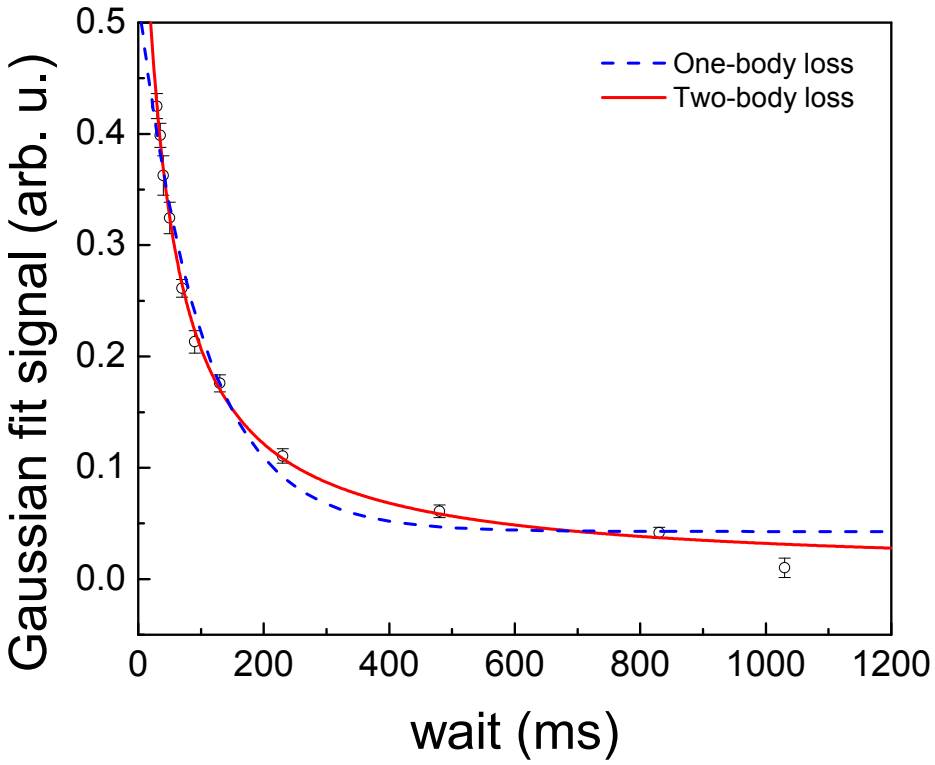

Figure 6.4: Measurement of $X(-1,0)$ state lifetime clearly suggests a two-body loss mechanism which yields a $1/e$ lifetime of ∼100 ms. The lifetime can be longer if less molecules are produced in the optical lattice.

lattice density, a two-body collisional lifetime of ∼100 ms is observed. To reduce the shot-to-shot noise, each point on the trace is obtained from averaging five consecutive shots. This lifetime is a lot longer than that observed in the clock experiments so it can be concluded that the collisional loss is not the culprit of the short lifetime issue.

6.2.2 $X(-2,0)$ state lifetime measurement

Figure 6.5 demonstrates the lifetime measurement of $X(-2,0)$ state. The lifetime of this state is dominated by the two-body collisional loss and a very similar $1/e$ lifetime of ∼100 ms is observed. This trace is taken under the same condition as Figure 6.4.

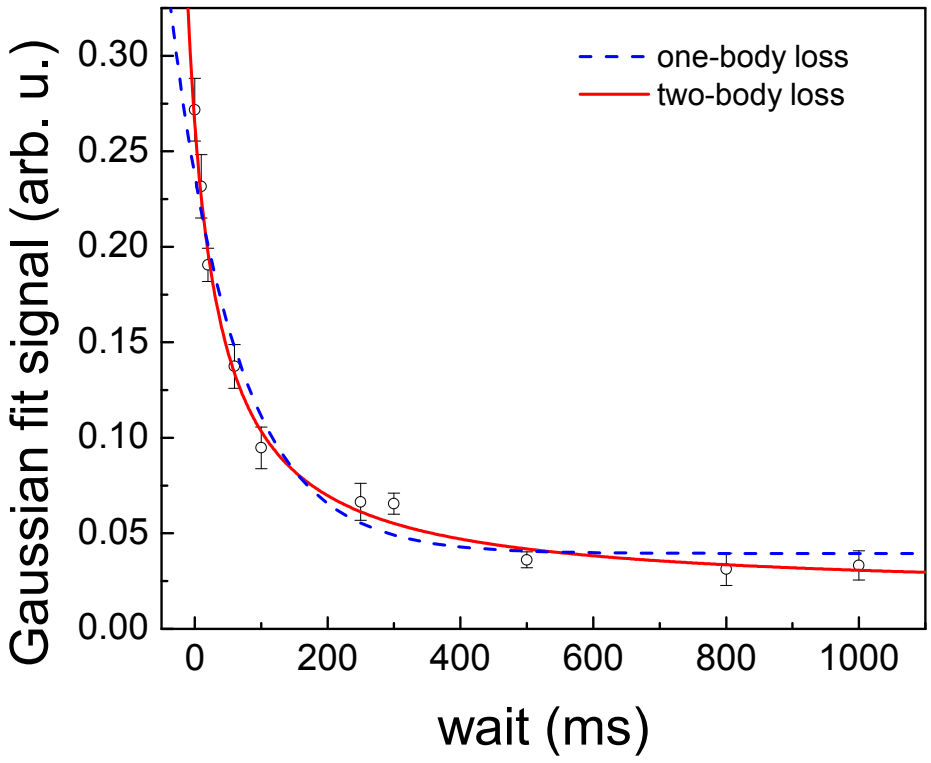

Figure 6.5: Measurement of $X(-2,0)$ state lifetime clearly suggests a two-body loss mechanism which yields a $1/e$ lifetime of ∼100 ms. The lifetime can be longer if less molecules are produced in the optical lattice.

6.2.3 Scattering from Raman lasers

In this section I examine the scatterings due to Raman probe beams. From this discussion, the natural linewidth of the Raman virtual state can be backed out. As previously elaborated, recent theoretical calculations have suggested a natural linewidth for shallow 0_u states be in the range of $12 \sim 30$ kHz. Given linewidth on this level, in a Raman spectroscopy where the common detuning $\Delta \sim 25$ MHz the clock state lifetime limit due to probe scatterings is on the order of 600 ms. To verify this estimation, an experimental test of linewidth is carried out.

Figure 6.6 illustrated the measurement of $X(-1,0)$ state lifetime versus probe power. In this measurement, a bound-to-bound laser is detuned from the $X(-1,0) \rightarrow 0_u^+(-4,1)$ transition by 25 MHz and the ground state lifetime is measured at a variety of bound-to-bound laser power. The bound-to-bound laser has beam size of $\pi(80.9 \times 97.4)$ μm^2 at the molecular cloud. As demonstrated, the scattering exhibits a clear linear dependence on the bound-to-bound power, which corroborates the scattering formula.

Under the conditions that $\Delta \gg \gamma$ and $\Delta \gg \Omega$, the scattering rate described by Equation 4.9 can be approximated to $\Gamma \approx \dfrac{\gamma\Omega^2}{4\Delta^2}$. The natural linewidth of the $0_u^+(-4,1)$ state can be obtained from this relation because, by definition, the Rabi frequency squared is $\Omega^2 = \dfrac{DMS \times E^2}{h^2} = \dfrac{DMS \times 2I}{h^2\varepsilon_0 c}$, where the laser intensity I is related to the electric field by $I = \frac{1}{2}\varepsilon_0 c E^2$. With techniques discussed in Chapter 7, the DMS for $X(-1,0) \rightarrow 0_u^+(-4,1)$ transition is precisely measured to be 1.97×10^{-3} $(ea_0)^2$. Therefore the natural linewidth can be directly deduced from the slope obtained from fitting the scattering as a function of bound-to-bound power. In Figure 6.6 the fitted slope is 0.35(4) Hz/μW, which results in a natural linewidth of 44(4) kHz. Note that this method of linewidth fitting can be improved

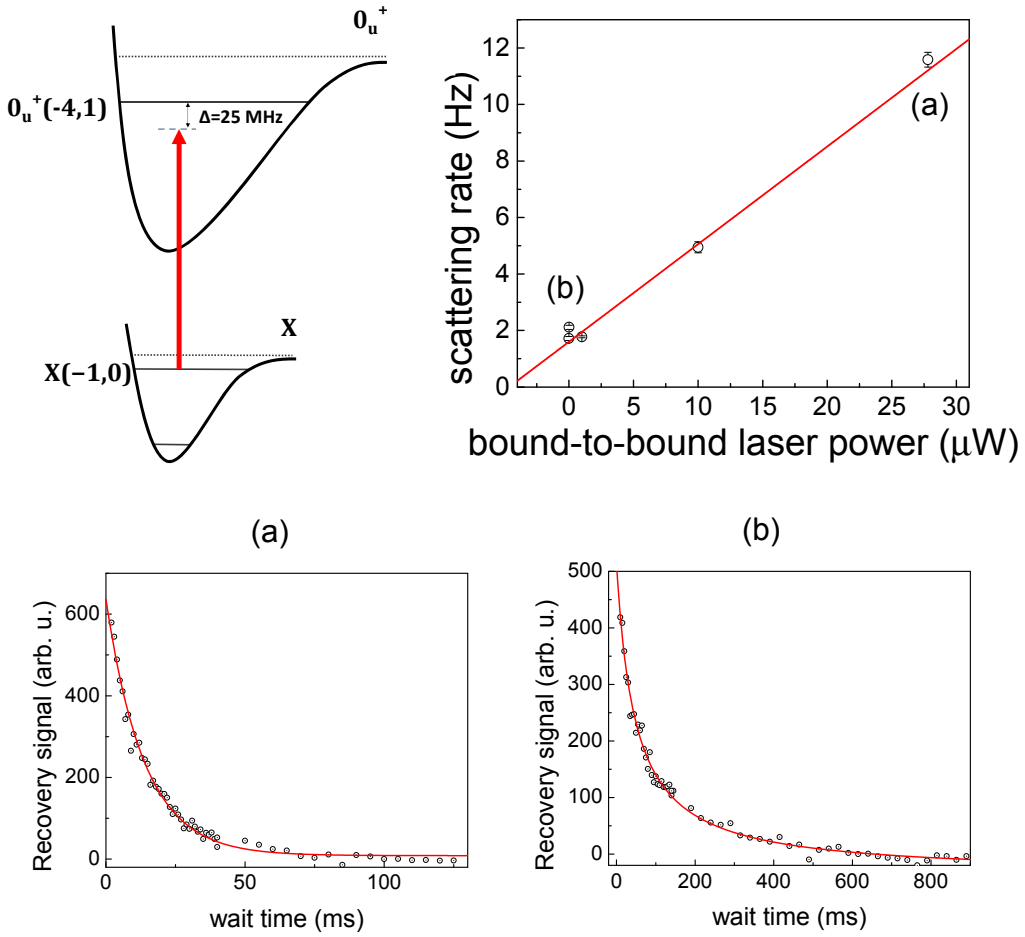

Figure 6.6: Scattering rates on the $X(-1,0)$ molecules are measured with various bound-to-bound laser power. In this measurement, the bound-to-bound laser is detuned from the $0_u^+(-4,1)$ state by 25 MHz, which is the usual setting for the Raman spectroscopy discussed in this thesis. At each bound-to-bound laser power, the scattering rate is deduced from a single exponential fit. The scattering rate has a clear linear dependence on bound-to-bound power, which agrees with the scattering theory with large detuning. The fitted slope of the dependency is 0.35(4) Hz/μW. Molecule decay traces are shown for two extreme case. In (a) the bound-to-bound power is 27.8 μW and the trace is well described by the one-body loss model. In (b) no bound-to-bound power is applied and the decay trace is characterized by the two-body loss model.

by plotting the scattering rate as a function of Rabi frequency, in which way the uncertainties in the DMS and the beam size measurements can be avoided. So far, the most accurate linewidth measurement for this state was obtained with a direct depletion spectroscopy in a magic trap, which yields 23(1) kHz [14]. The fact that the measured linewidth value has the same order of magnitude as the theory prediction precludes the possibility that the Raman probe scattering is the leading factor accounting for the short clock lifetime.

6.3 Deeply bound ground state lifetime

In the previous section, the possibility that the shallow clock state results in the lifetime problem is precluded, therefore the bottom clock state must be the culprit to this puzzle. The loss mechanism is a bit more complex for the bottom state because there is an additional light, the lattice light, that connects the state. Since the lattice light is detuned closely to a resonance, it could lead to unwanted scattering. In this section, it will be proved that the lattice light is very likely to be the reason that causes the short clock lifetime but, unfortunately, the actual loss mechanism has not been fully clear. Although the problem hasn't been fully resolved, I will discuss the investigations that have been carried out so far and hopefully these clues will help elucidate the perplexing mystery.

6.3.1 Theoretical prediction

Let's first estimate the scattering rate due to the magic lattice light. According to the latest theoretical prediction by Prof. Robert Moszynski's team, the natural linewidth for the $1_u(v' \sim 23, J' = 1)$ states is typically on the order of 5 kHz. Assume a lattice Rabi frequency of 30 MHz, the one-photon scattering rate due to the lattice is

$$\Gamma_{lat.} = \frac{\gamma\Omega^2}{4\Delta^2} = \frac{5\text{ kHz} \times (30\text{ MHz})^2}{4\Delta^2}, \tag{6.7}$$

where Δ is the lattice detuning from the lattice-driven transition resonance. As demonstrated in Chapter 4, for the lattice to be magic for the clock transition, the lattice laser is typically detuned from the resonance by ~ 1.3 GHz. This yields a scattering rate of ~ 4.2 /s, which corresponds to a lifetime of ~ 240 ms. Surely this scattering is too weak to explain the lifetime issue but this estimation is based on several assumptions.

- First, it assumes the natural linewidth prediction is correct. The scattering rate is proportional to linewidth and therefore a wrong linewidth would lead to an incorrect scattering estimation.

- Second, it assumes only one-photon scattering is present. If there is other higher-order loss mechanisms, the scattering rate would be underestimated.

- Third, it treats the lattice light as an ideal laser with zero linewidth. However, from Section 5.1.2 we have seen that the lattice light has a huge messy background noise due to the tapered amplifier. This background noise could scatter molecules and lead to a shortened clock state lifetime.

6.3.2 Surprising experimental observations

Let's first examine some measurements of deeply bound state lifetime, from which we can have some clues on what is happening. In Figure 6.7, $X(6,0)$ state lifetime is measured as a function of the lattice frequency. The lattice is detuned from the $1_u(23,1)$ state by a variety of amounts while the lattice Rabi frequency is kept constant at 24 MHz. There are two surprising findings in this measurement.

- When the lattice is far from resonances, the lattice scattering is negligible and thus the molecular lifetime is expected to be in the regime where two-body loss dominates. However, it is observed that the molecular lifetime is capped at $\sim$ 50 ms, which is shorter by a factor of two than the typical collision-limited lifetime demonstrated in Figure 6.4 and 6.5.

- Suggested by Equation 6.7, the lattice-limited lifetime should get longer as the lattice detuning increases. This trend is observed but the rate at which the lifetime increases is way lower than what is expected. For example, at $\Delta = 10$ GHz, the observed lifetime is $\sim$23 ms whereas the one-photon model predicts almost zero scattering.

The discrepancy in the saturated lifetime has been explained. It is actually due to the background noise of the lattice laser. Although the lattice is detuned by a few hundred GHz from all nearby resonances, the lattice ASE background, which spans over a few THz, can still scatter the molecules. In Section 6.3.3, a test the collision-limited lifetime for the deeply bound ground state will be demonstrated *with the background cleaned by the transmission grating*. The slow rising of the lifetime, however, is more perplexing and the reason behind it still remains unclear. A hidden TA noise structure near the carrier could explain this observation but proving this hypothesis is challenging. Directly detecting this spectrum structure requires 1 GHz resolution, which is technically difficult for an optical spectrum analyzer. An alternative way around this is to put in a spectral clean-up cavity to suppress the noise level. In Section 6.4.3.2, I will discuss the effects of the cavity on the lifetime. Besides TA noise, a more complex loss mechanism, for instance a two-photon process, could also cause a short clock state lifetime and this topic will be discussed in Section 6.4.2.

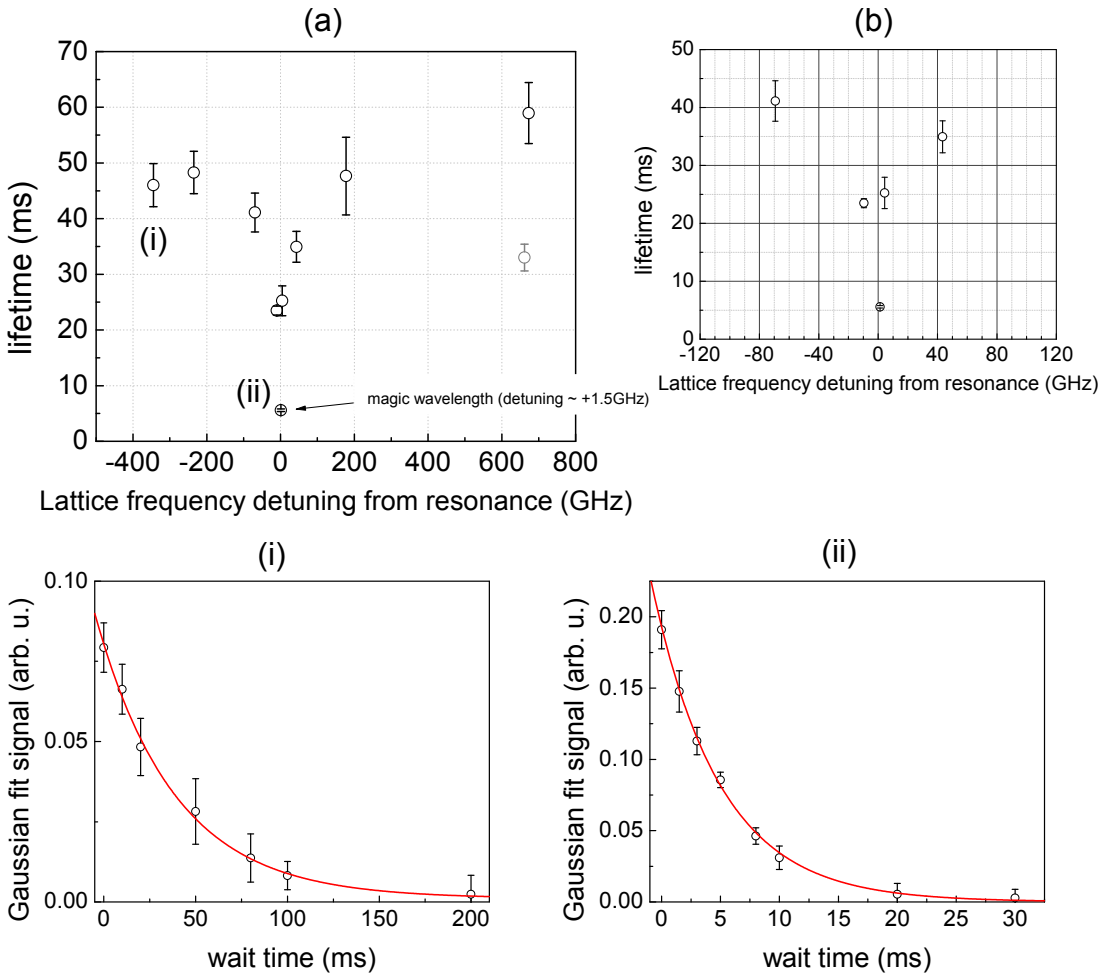

Figure 6.7: $X(6,0)$ state lifetime is measured with the lattice laser frequency detuned from the $1_u(23,1)$ state resonance by a variety of amounts. Throughout the experiment the lattice power is fixed at 175 mW, which corresponds to a Rabi frequency of 24 MHz. The lattice frequency is software-locked to the wavelength meter except for the magic frequency where the lattice is phase-locked to the frequency comb. In (a) the lattice frequency is tuned in a range of ± 200 GHz across the resonance. The lifetime levels off at 50 ms as the lattice is far-detuned from the resonance. In (b) a zoom in look reveals a very slow increase rate of lifetime that is surprisingly contradictory to Equation 6.7. Two examples of $X(6,0)$ molecule decay with (i) $\Delta = -344$ GHz and (ii) $\Delta = +1.5$ GHz (magic lattice) are demonstrated. The traces are fitted to single-exponential one-body model.

6.3.3 Inelastic collisional loss

Figure 6.8 demonstrates the two-body collision loss for the deeply bound $X(6,0)$ state. To suppress the ASE noise scattering, the background noise is cleaned up with the transmission grating. Note that in this measurement the spectral clean-up cavity is not in place and thus the ASE noise within ± 20 GHz around the carrier is not cleaned up, according to Figure 5.9. To suppress the excessive loss, the lattice is detuned from the nearest 1_u state by $\Delta = 1$ THz. Since the lattice is non-magic for the clock transition, an efficient π-pulse to populate $X(6,0)$

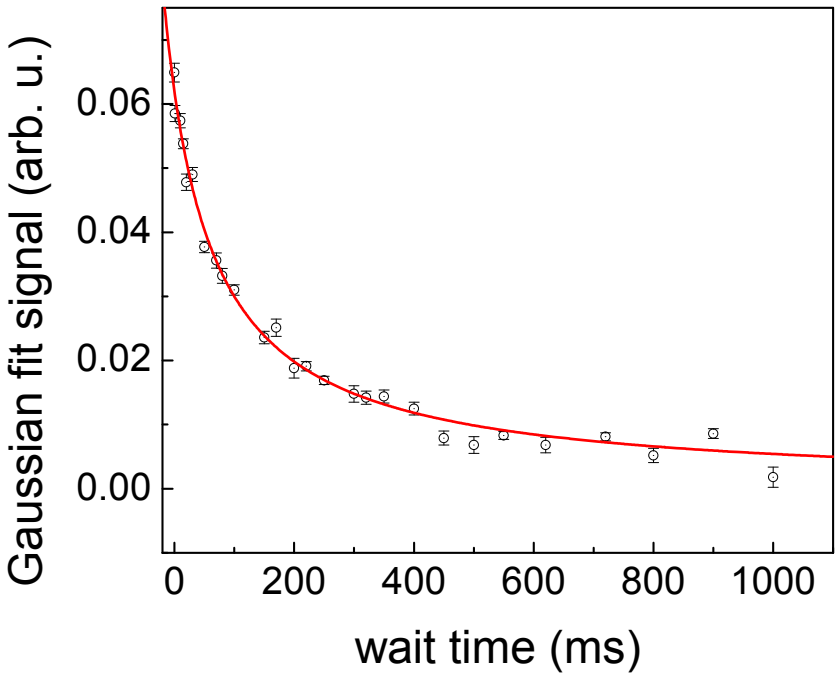

Figure 6.8: Two-body collisional loss for deeply bound $X(6,0)$ state. The tapered amplifier ASE noise is cleaned by the transmission grating. In this measurement, the lattice is detuned from the nearest 1_u state by $\Delta = 1$ THz. The decay trace is fitted to the two-body loss model described by Equation 6.6, which yields a $1/e$ lifetime of 140 ms. The lifetime is longer than that of shallow ground states because of lower molecular density.

molecules is not tenable. To cope with this, a long Raman pulse, or called a dephasing pulse, is applied to transfer the molecular states. As a result of the less efficient state transfer, the $X(6,0)$ molecule density is lower than the initial molecular cloud, therefore the collision-limited lifetime is expected to be longer than that demonstrated with shallow ground states. This is corroborated in Figure 6.8 where a $1/e$ lifetime of 140 ms is observed.

6.3.4 Scattering from Raman lasers

In Section 6.2.3, I discuss the Raman probe scattering rate on the shallow clock state and examined that the measured natural linewidth of the $0_u^+(-5,1)$ state agrees with the theoretical prediction. A beauty of Λ-type Raman transition is the symmetry between Raman legs. At balanced Raman intensity, the Raman probe scattering rate on the deeply bound clock state is essentially the same as that on the shallow state because both Raman legs share the same virtual state. Therefore, in the situation where the first Raman laser doesn't cause problematic scattering, it is automatically guaranteed that the second Raman laser is safe unless one or both Raman beams *talk* to the wrong clock state, via accidental nearby resonances.

6.4 Possible solutions to the puzzle

Previously I discuss several possible reasons that would lead to the clock lifetime issue. They include (a) incorrect natural linewidth prediction, (b) complex scattering mechanism and (c) the tapered amplifier ASE noise. In this section I will elaborate on these points in more detail and discuss our attempts to tackle them.

6.4.1 Incorrect natural linewidth prediction

The first and most intuitive guess is that the theoretical predictions on deeply bound 1_u state natural linewidth are incorrect. Most recent $^{88}Sr_2$ molecular model predicts linewidth of ∼5 kHz for $1_u(\sim 24, 1)$ states. If the actual linewidth is broader, it will directly lead to a higher scattering rate. How can we know something about the linewidth from the experiment? In this section I present two methods for measuring the linewidth of deeply bound 1_u states. The first one is a direct measurement via the depletion spectroscopy and the second one employ the clock state scattering curve.

6.4.1.1 Direct measurement of 1_u state natural linewidth

The direct measurement of deeply bound 1_u state linewidth is performed with depletion spectroscopy on $X(6, 0)$ state. Figure 6.9 demonstrates the measurement of $1_u(24, 1)$ state lifetime. To avoid power broadening, the 919 nm $X(6, 0) \rightarrow 1_u(24, 1)$ depletion transition is driven by a probe intensity of 7.6 mW/cm^2. Furthermore, the measurements are performed with a high and a low lattice power so that the natural linewidth can be deduced by extrapolating to zero power. This is necessary because making a magic lattice for this depletion transition was beyond the capability of the experiment. Because the frequency band of 1054 nm is outside the frequency comb supercontinuum, the lattice can't be stabilized to the comb and thus making a magic lattice for clock transition is untenable.

As demonstrated, extrapolating to zero lattice power suggests a natural linewidth of ∼83 kHz for the 1_u state. Although the lattice is non-magic for the depletion transition (as corroborated by the non-zero differential light shift), lattice power extrapolation should take out the effect from the inhomogeneous broadening and yield the natural linewidth. However, there are several factors that make drawing a conclusion from this measurement

difficult. First, since a magic trap is not tenable for this transition, the ground state transfer is inefficient, leading to the restriction of poor S/N ratio for the experiment. Second, the tunability of the lattice power is limited. For the 1054 nm lattice, the lowest power to maintain sufficient trapping is around 150 mW. Due to this limited tuning range, interpreting the measurements is difficult.

In the following section, I will demonstrate an alternative method that is not subject to these technical limitations.

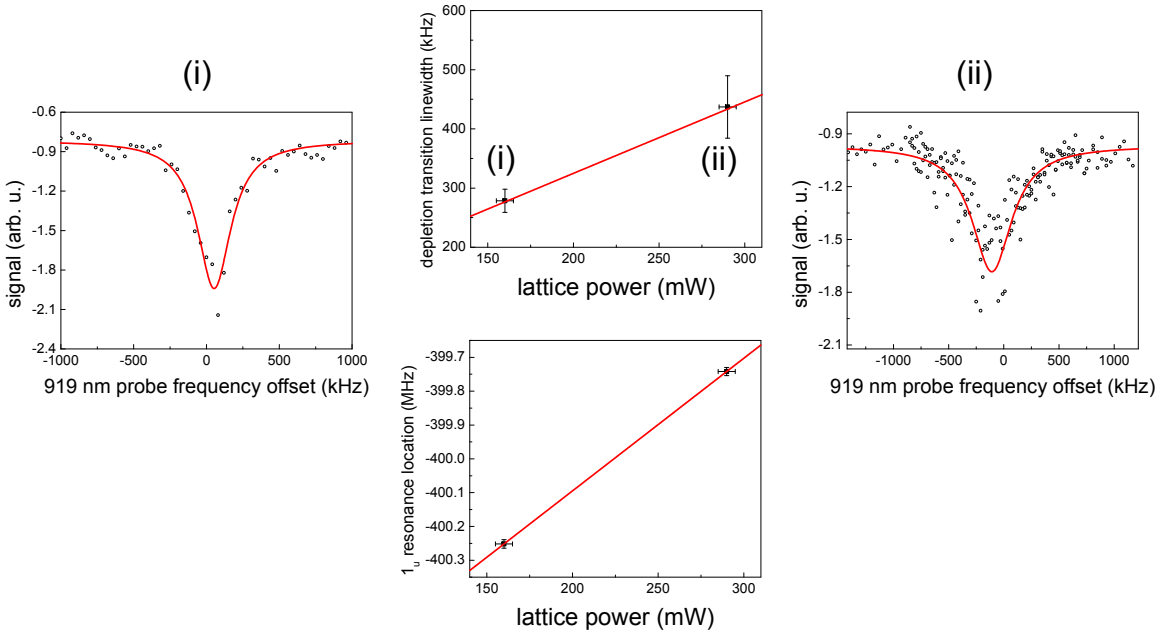

Figure 6.9: Direct extrapolating measurement of $1_u(24,1)$ state lifetime with depletion spectroscopy. In this measurement, the lattice laser wavelength is 1054 nm. To avoid power broadening, the 919 nm $X(6,0) \rightarrow 1_u(24,1)$ depletion transition is driven by a probe power of 200 nW, corresponding to an intensity of 7.6 mW/cm^2. The depletion transition linewidth (top) and frequency offset (bottom) are measured with a high and a low lattice power. Extrapolating to zero lattice power suggests a natural linewidth of ∼83 kHz for $1_u(24,1)$ state. Obtaining a reliable error bar requires more data points. The depletion traces for both high and low lattice power are shown as labeled.

6.4.1.2 Detuning dependence of scattering rate

Let's recall that the off-resonant scattering rate reads $\Gamma = \frac{\gamma\Omega^2}{4\Delta^2}$, where γ is in the unit of Hz. Also, a lifetime τ is related to the scattering rate Γ by the relation $\tau = \frac{1}{2\pi\Gamma}$. Thus, while keeping the Rabi frequency constant, the natural linewidth can be backed out by fitting the lifetime as a function of detuning.

In Figure 6.10, the $X(6,0)$ state lifetime is measured with a variety of lattice frequency near the $1_u(26,1)$ state resonance. Throughout the experiment, the lattice power is fixed at 165 mW, which corresponds to a Rabi frequency of 8.3 MHz. Note that this transition has a DMS of 2.22×10^{-6} $(ea_0)^2$, which is obtained with techniques discussed in Chapter 7. The

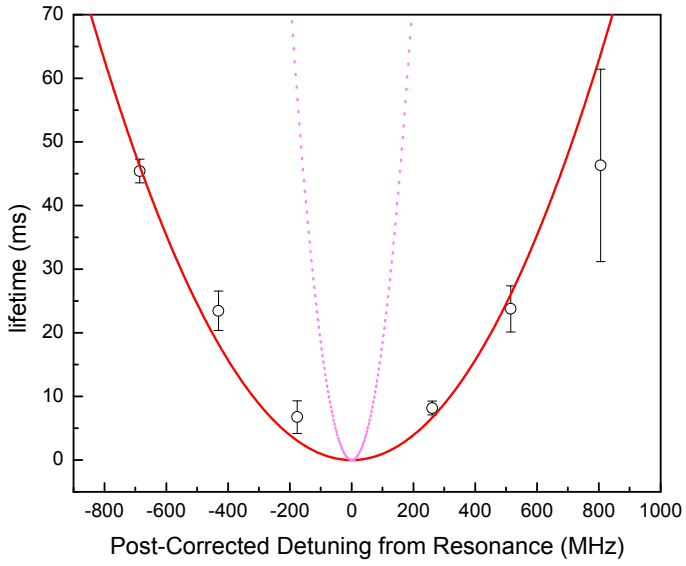

Figure 6.10: Lifetime of $X(6,0)$ molecule is measured with different lattice frequency near the $1_u(26,1)$ state resonance. In this measurement both transmission grating and spectral clean-up cavity are in place. The lattice Rabi frequency is kept constant at 8.3 MHz. The data is fitted to $\tau = \kappa(\Delta - \Delta_0)^2$, which yields a natural linewidth of 94(6) kHz for the $1_u(26,1)$ state. Dotted curve is calculated with the theoretical linewidth.

data is fitted to a function form of

$$\tau = \kappa(\Delta - \Delta_0)^2, \tag{6.8}$$

where $\kappa \equiv \dfrac{2}{\pi\gamma\Omega^2}$ and Δ_0 denote the scattering factor and frequency offset for the resonance, respectively. As expected, the lifetime fits well to the parabolic function where a scattering factor $\kappa = 9.8(6) \times 10^{-5}$ ms/(MHz)^2 is yielded. This scattering factor indicates a surprisingly large linewidth of 94(6) kHz compared to 5 kHz predicted by the theory. Before jumping into a conclusion, let's examine the same measurements performed with other 1_u states.

In Figure 6.11, the same measurements performed with $1_u(7,1)$ and $1_u(24,1)$ state resonances are presented. Similar to the $1_u(26,1)$ resonance, the backed out lifetimes for these two states are also very large. The linewidth for $1_u(7,1)$ and $1_u(24,1)$ states is 100(38) kHz and 239(60) kHz respectively whereas the theoretical predictions are both below 3 kHz. All these measurements suggest consistent observations of broad lifetime for deeply bound 1_u state, which implies the theory is very messed up. However, it is very unlikely that the theory is so wrong. Several reasons includes:

- First, the theory predictions for the binding energies and DMS's are both excellent. An uncertainty of 10^{-5} in binding energy has been achieved for all found deeply bound ground states and excited states. Also, as shown in Chapter 7, the DMS's prediction error is typically on the order of 20%. These indicate that both the number of decay channels and the decay strengths are well characterized. Under this circumstance, the natural linewidth predictions are unlikely to be off by over two orders of magnitude.

- Second, the natural linewidth for a weakly bound excited state has been examined in Section 6.2.3, where the experimental value corroborates the theoretical prediction within an order of magnitude. Intuitively, the natural linewidth of deeply bound states

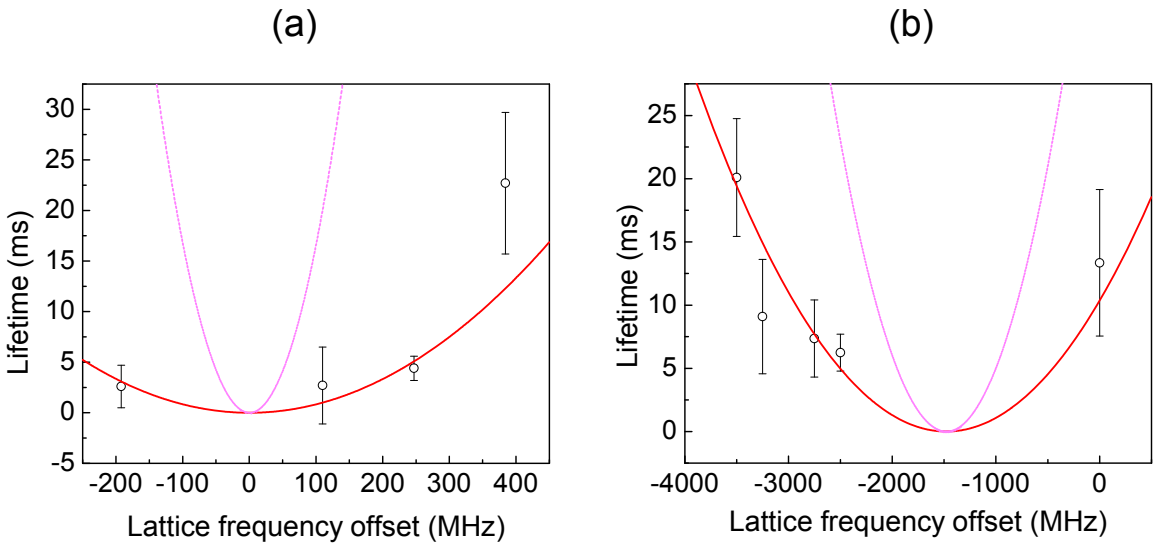

Figure 6.11: Lifetime of $X(6,0)$ molecule is measured with different lattice frequency near the $1_u(7,1)$ and $1_u(24,1)$ state resonances. Both transmission grating and spectral clean-up cavity are in place in these measurements. The lifetime curves are fitted to $\tau = \kappa(\Delta - \Delta_0)^2$. In (a) the data is taken with $1_u(7,1)$ state and the lattice Rabi frequency is kept constant at 8.9 MHz. The fitted linewidth is 100(38) kHz, where the large error bar comes from the poor laser mode at this wavelength. In (b) the data is taken with $1_u(24,1)$ state and the lattice Rabi frequency is kept constant at 24.1 MHz. The fitted linewidth is 239(60) kHz. Dotted curves are calculated with theoretical linewidth.

should be even narrower than that of weakly bound states because of less efficient decay channels and weaker decay strength. Weakly bound excited molecules can decay to a number of weakly bound ground states whereas the number of efficient decay channels for deeply bound excited molecules is significantly lower. Moreover, the decay strength from deeply bound states is weaker because the states are further away from the atomic threshold. Therefore, the natural linewidth of deeply bound 1_u states is unlikely to be as wide as a few hundred kHz.

6.4.2 Accidental two-photon transitions

Another hypothesis for the excessive loss is a two-photon scattering into higher excited potentials. As illustrated in Figure 6.12, with the lattice laser connecting $X(6,0)$ to $1_u(24,1)$, two-photon processes from the laser light can scatter the $X(6,0)$ molecules into the continuum of ^{1}D potential. In this section I explore the possibility of this scattering mechanism.

6.4.2.1 Power dependence of scattering rate

An important signature of a two-photon process is the lattice power dependence of the scattering rate. The effective Rabi frequency for a two-photon process is

$$\Omega_{eff} \sim \frac{\Omega_{X-1_u}\Omega_{1_u-^1D}}{\delta}, \tag{6.9}$$

where δ is the laser detuning from the intermediate 1_u state. The two-photon scattering rate is proportional to the effective Rabi frequency squared and the density of states above dissociation continuum [57].

$$\Gamma^{two-photon} = \frac{\pi}{2}\Omega_{eff}^2 D(f), \tag{6.10}$$

where $D(f)$ is the density of states in the continuum with energy f. Since the effective Rabi frequency is proportional to the lattice power, if the two-photon process dominates the loss, a scattering rate exhibiting a quadratic dependence on power should be observed. Figure 6.13 demonstrates a measurement showing a quadratic dependence of clock state lifetime with lattice power. Actually this is the reason we ascribed the excessive molecule loss to the two-photon scattering in the Nature Physics publication [9]. In this measurement, the $X(6,0)$ molecule lifetime is measured with various lattice powers while the lattice frequency is fixed at $1_u(24,1)$ state magic wavelength. Although a quadratic dependence of lifetime on

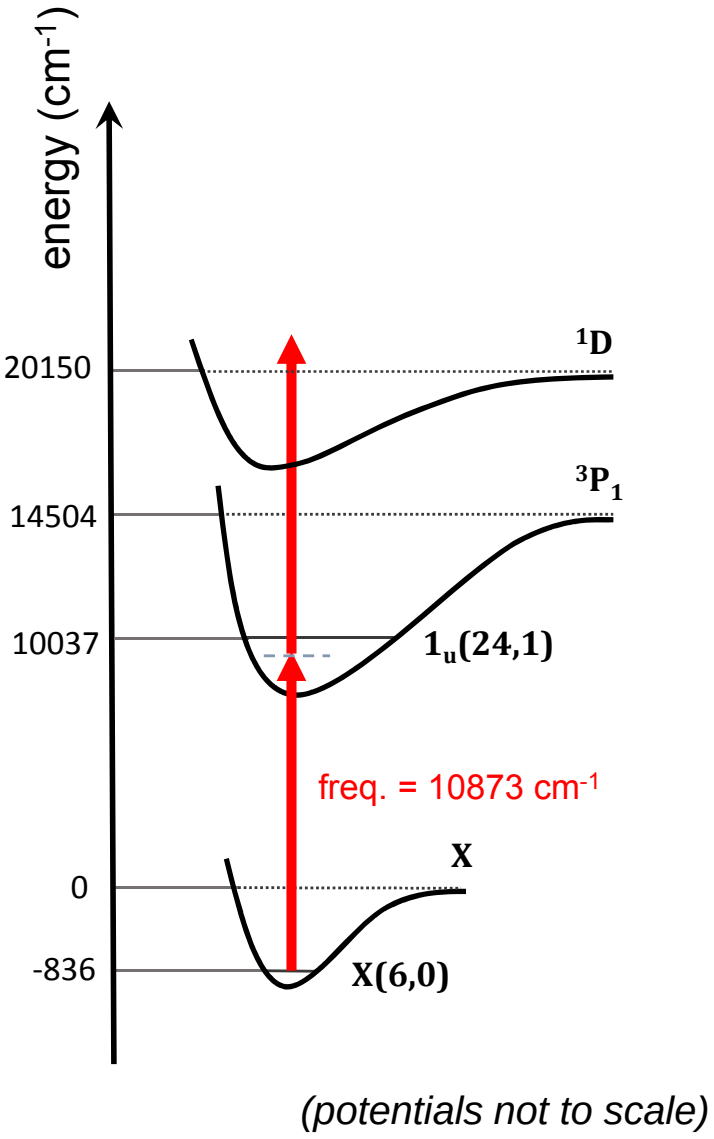

Figure 6.12: Illustration of a two-photon scattering into higher excited potentials. Constructing a magic lattice with $1_u(24,1)$ state, for example, leads to a two-photon into ^{1}D potential continuum by a dissociation energy of 760 cm^{-1}, or 23 THz.

power seems to be clear in Figure 6.13, the conclusion about the two-photon scattering has become suspicious for the following reasons.

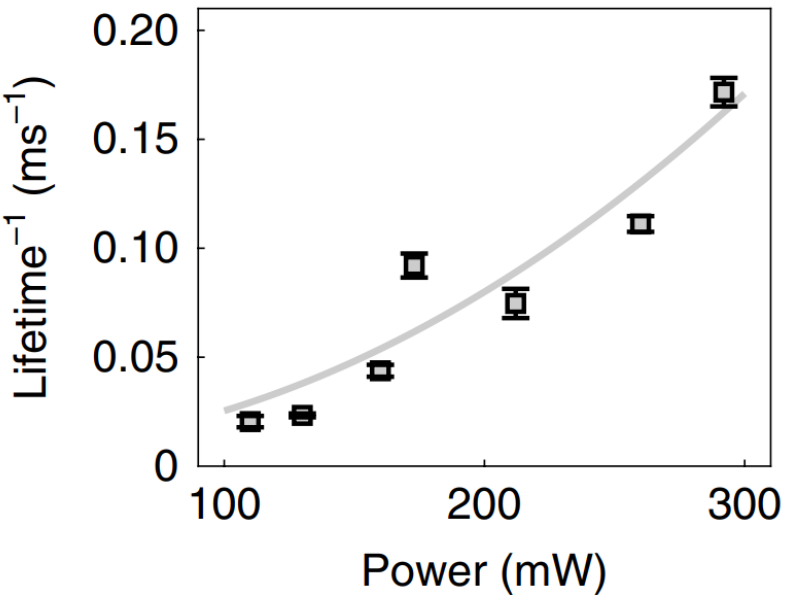

Figure 6.13: A suspicious quadratic dependence of scattering rate on lattice power. This data is the Figure 3(c) in the Nature Physics publication [9]. Here the $X(6,0)$ molecule lifetime is measured with various lattice power while keeping the lattice frequency at the $1_u(24,1)$ state magic wavelength. This data set is suspicious because it is taken without cleaning up the lattice ASE noise.

First, the main reason for that the existence of two-photon losses becomes suspicious is the reproducibility of the experiment. At the time when data in Figure 6.13 was taken, we didn't realize the issues with tapered amplifier ASE noise so the data was taken *without neither the transmission grating nor the clean-up cavity.* After the lattice spectrum is cleaned up, the quadratic dependence has no longer been observed. Figure 6.14 demonstrates a more careful measurement of $X(6,0)$ state with both the grating and the clean-up cavity installed. In this measurement, the lifetime is measured with various 919 nm probe laser powers while the laser is tuned near the $X(6,0) \rightarrow 1_u(24,1)$ transition resonance. As shown, an obvious linear power dependence is present. Second, if the picture of two-photon losses is correct, a substantially

longer clock lifetime should be observed in the situations where two-photon decay channels are closed. However, the measurements described in the next section contradict this hypothesis, which casts more doubts on the existence of two-photon losses.

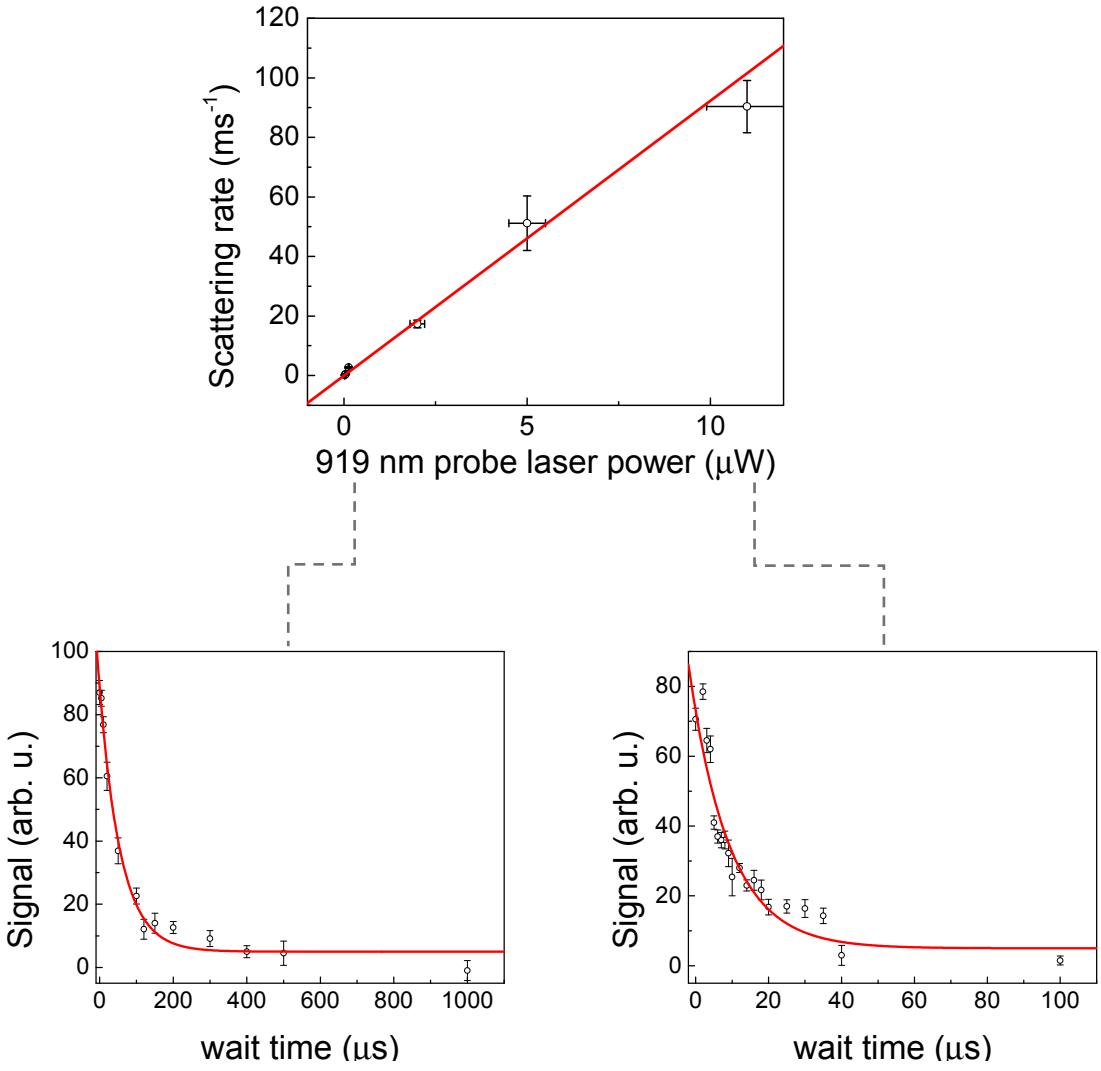

Figure 6.14: Lifetime measurements taken with the grating and the clean-up cavity disproves the existence of two-photon loss by showing linear dependence on power. Here the $X(6,0)$ state lifetime is measured with various power for the 919 nm probe laser that is tuned near the $X(6,0) \rightarrow 1_u(24,1)$ transition resonance. Lifetime curves in this measurement are fitted to the one-body loss model.

6.4.2.2 More deeply bound 1_u states for magic lattice

A critical examination of the existence of two-photon scatterings is to investigate the molecular lifetime with different magic wavelengths. Table 6.1 lists the continuum energies of

$1_u(v', 1)$ state	transition frequency	^{3}P	^{3}D$_1$	^{1}D
26	11,018	6,696	3,041	1,050
25	10,946	6,552	2,897	906
24	10,873	6,406	2,751	760
23	10,799	6,258	2,603	612
7	9,567	3,794	139	-1,016
6	9,487	3,634	-21	-1,176
5	9,406	3,472	-183	-1,338

Table 6.1: Continuum energies of two-photon dissociation from $X(6, 0)$ state into three lowest lying excited potentials. All numbers are in the unit of wavenumber (cm^{-1}). Negative values mean that the dissociation is below the potential threshold. The transition frequency indicates the one-photon frequency.

two-photon dissociation from $X(6, 0)$ state via different 1_u states into three lowest-lying excited potentials. As demonstrated, with 1_u states that are very close to the bottom of the potential, the two-photon process into some of the possible dissociation channels is suppressed. A state which is particularly worth testing is the $1_u(5, 1)$ state. With this state, the two-photon dissociation energy is only higher than the ^{3}P threshold. The ^{3}P decay channel is not worrisome because a detailed theory calculation has suggested a negligible decay rate with dissociation energy larger than 3,000 cm^{-1}. With these said, if two-photon scattering is the culprit accounting for the short lifetime issue, the magic lattice achieved with $1_u(5, 1)$ state would significantly prolong the $X(6, 0)$ molecule lifetime. However, the experiment

contradicts this hope. In Figure 6.15, the lifetime is measured with a lattice detuned from $1_u(5,1)$ state by 8.4 GHz. The lattice power is fixed at 210 mW, corresponding to a Rabi frequency of 27 MHz. Assuming a natural linewidth of 5 kHz, the scattering rate can be calculated to be $\sim 2\pi \times 0.01$ /s. However the fit on the decay trace suggests a scattering rate of $2\pi \times 17(4)$ /s, which indicates that the two-photon processes is not the culprit to the lifetime issue.

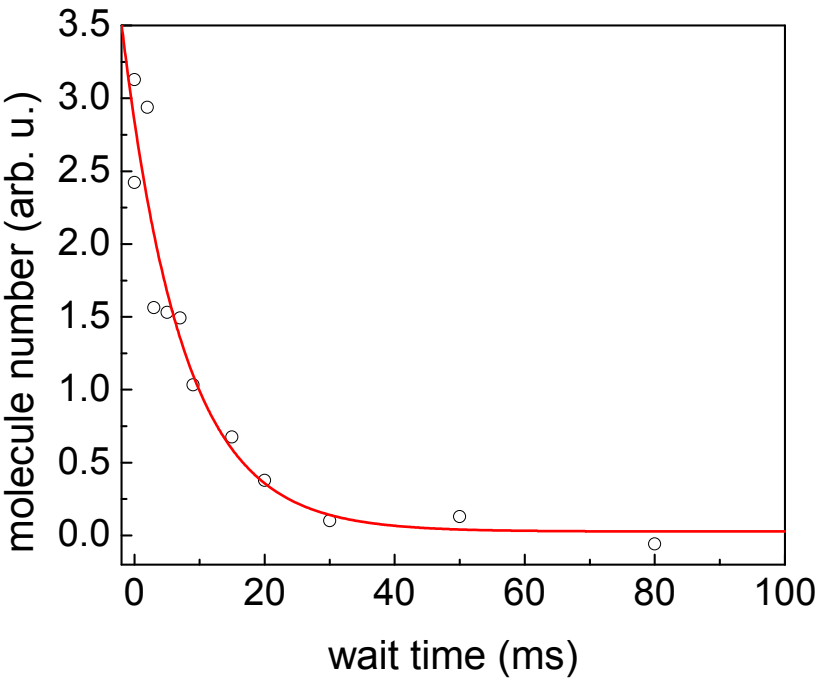

Figure 6.15: $X(6,0)$ molecule lifetime is measured with a lattice detuned from the $1_u(5,1)$ state by 8.4 GHz. In this situation, the two-photon processes is suppressed thus the scattering should be dominated by the one-photon process. In this measurement the lattice Rabi frequency is 8.4 MHz. Assuming a natural linewidth of 5 kHz, the one-photon scattering rate is calculated to be $\sim 2\pi \times 0.01$ /s. However, the decay fit suggests a scattering rate of $2\pi \times 17(4)$ /s. The trace is fitted to the one-body loss model.

Readers may wonder if bound-to-bound two-photon transitions could happen and lead to scatterings. This was actually what we thought after the measurement with $1_u(5,1)$ state was carried out. However, the most recent *ab initio* calculations suggest against this hypothesis. In the situation with the $1_u(5,1)$ state, the two-photon processes into bound states in the three closest potentials, i.e. ^{3}D, ^{1}D and ^{1}P, all have scattering rates below 10^{-5} Hz unless an accidental resonance is driven. Therefore, the conclusion about the hypothesis of the two-photon scattering can be made more clearly now: even though such a loss mechanism could exist, it is not the leading factor that limits the clock lifetime now.

6.4.3 Spectral noise in the lattice laser light

The background noise in the lattice light could also cause unwanted molecule scattering. In Chapter 5, I discuss the ASE noise generated from the tapered amplifier. I also show that this broad noise does exist in our lattice laser light. In this section I will demonstrate how this noise can be (partially) cleaned up by the transmission grating and the spectral clean-up cavity and how a cleaner lattice light spectrum directly leads to a longer molecule lifetime. Indeed, the ASE noise is the only suspect that has concrete evidence to show its relation with the short lifetime. However, what makes the lifetime issue so perplexing is that there are still some measurements that the ASE noise can't explain.

6.4.3.1 Transmission grating

First, let's see the effect of the transmission grating. Figure 6.16 compares the lifetime measured with and without the grating. As demonstrated in Section 5.1.2, the transmission grating truncates the ASE noise, allowing only a small window near the carrier to be coupled into the lattice fiber. As a result, only the resonance that is the closest to the lattice frequency

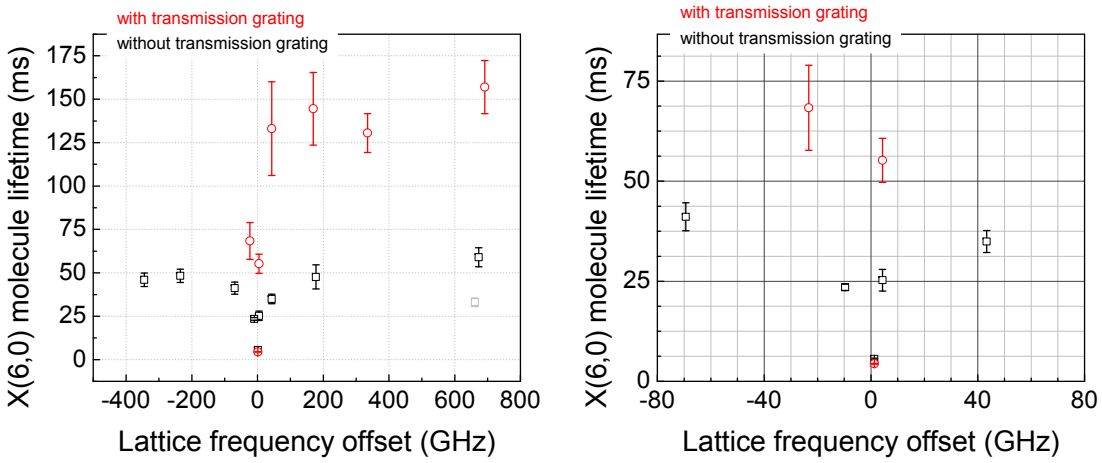

Figure 6.16: $X(6,0)$ molecule lifetime is measured with and without the transmission grating. The lifetime is measured with the lattice laser frequency near the $1_u(23,1)$ state resonance. With the ASE noise truncated by the transmission grating, the molecule lifetime is greatly improved except in the region near the carrier where the grating response doesn't cover.

scatters the molecules and the contributions from the nearby 1_u states are well suppressed. This is corroborated in Figure 6.16, where the lifetime measured with the grating is substantially longer than that measured without the grating. Furthermore, with the grating implemented, the lifetime saturates at 140 ms, which nicely agrees with the conclusion in Section 6.3.3 about the collision-limited lifetime of deeply bound ground state molecules.

6.4.3.2 Spectral clean-up cavity

To suppress the ASE noise near the carrier, a spectral clean-up cavity is implemented. Figure 6.17 compares the molecule lifetime measured with and without the clean-up cavity. Without the cavity the molecule lifetime is typically around 5 ms. With the cavity implemented the molecule lifetime is consistently observed to be ∼20 ms. The fact

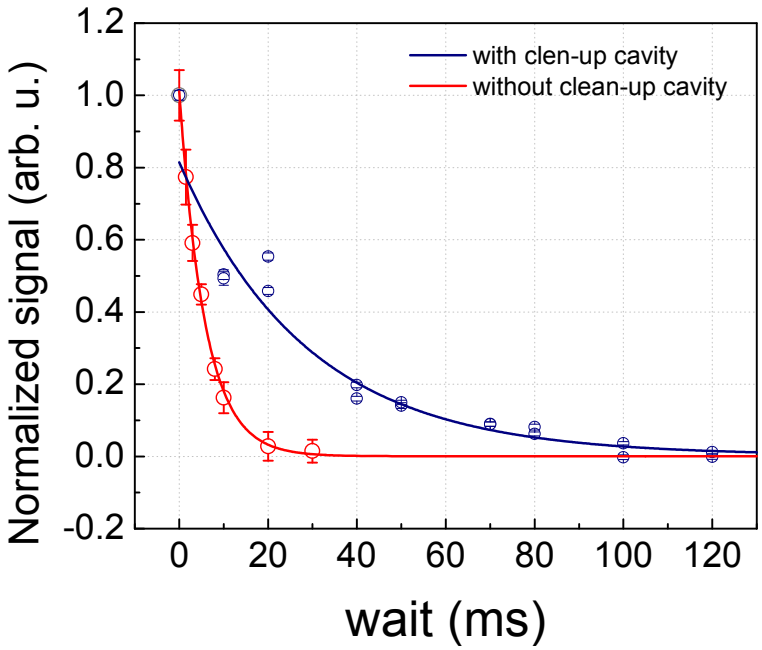

Figure 6.17: $X(6,0)$ molecule lifetime is measured with and without the spectral clean-up cavity. Without the cavity the molecule lifetime is typically around 5 ms. With the cavity implemented the molecule lifetime is consistently observed to be ∼20 ms. Both traces are fitted to the one-body loss model.

that implementing the clean-up cavity enhances the molecule lifetime again implies that the ASE noise plays an important role in the lifetime issue. However, scrutiny into these measurements throws some new puzzles.

6.4.3.3 Measurements that cannot be explained by lattice laser noise

It's great that several pieces of clues support that the TA ASE noise is a major reason for the lifetime problem. However, there are still several measurement that can not be explained (so far) by the TA background noise. First, with the clean-up cavity implemented, the amount of increase in the molecule lifetime is not enough. As elaborated in Section 5.1.3, the FWHM

of the cavity resonance is 17 MHz and the cavity finesse is about 155. This means that the lifetime should increase by at least two orders of magnitude after the cavity is implemented, but only an increase of a factor of $\sim$5 is observed. Second, the dependence of molecule lifetime on the lattice frequency, depicted in Figure 6.10 and 6.11, can't be intuitively explained by ASE noise. The parabolic dependence of lifetime on lattice frequency has a width of almost $\pm$1 GHz, which is a lot broader than the cavity linewidth. Even if the cavity linewidth is underestimated, the mechanism of how a tapered amplifier broadens a $\sim$1 kHz wide laser mode into a broad peak is obscure.

Fully resolving the lifetime puzzle requires understanding the ASE structure near the carrier better. This is not an easy task since directly resolving the laser spectrum down to sub-GHz level is technically difficult for common optical spectrum analyzers. If it were to be proven that the lattice spectrum is the culprit, a fine laser system with low background noise would be necessary for the next generation lattice trap.

Chapter 7

Measurements of dipole moments squared (DMS)

In this chapter I discuss the measurements of transition DMS. Precise knowledge in DMS is crucial for building the molecular clock from several aspects.

- First, it helps with determining the balanced ratio between Raman probe intensities. As elaborated in Section 5.2.1, the balanced probe intensity ratio is equal to the inverse ratio between transition DMS's, therefore the better the DMS's are known, the more precisely the balanced intensity ratio can be determined.

- Second, knowing the DMS values helps to design the magic wavelength. In Section 4.3.3, I demonstrate that a good lattice-driven resonance for the magic wavelength is the one that minimizes the lattice frequency instability transfer and causes the least lattice scattering. Therefore, the criteria for a good lattice-driven resonance include a strong transition strength and large decay branching ratio, which both indicates the importance of precise measurements of DMS's.

- Third, the measurements of DMS's can be employed to calibrate the theoretical molecular model. Having an accurate model is crucial for efficient progress in building the clock. For example, as demonstrated in Chapter 3 and 4, accurate binding energy predictions have saved us a lot of effort in the searches for deeply bound states. Also, the measurements of DMS's help characterize the 1_u potential with better precision, as discussed in Section 4.2.4.

- Forth, precisely knowing the DMS's enables convenient Rabi frequency calculations. The Rabi frequency is determined by two parameters, the transition DMS and the driving laser light intensity. Measuring the laser intensity is straightforward so having DMS's precisely pre-determined would make determining Rabi frequencies a lot easier.

In the following sections, I will discuss how to measure the transition DMS's using the techniques developed in previous chapters. The two main workhorses for the DMS measurements are the Autler-Townes spectroscopy and the light shift measurements. These two kinds of experiments allow precise measurements of Rabi frequencies, from which the transition DMS's can be backed out as follows.

For a transition with dipole moment d that is driven by a laser with electric field amplitude E, the Rabi frequency Ω is described by

$$\Omega = \frac{d \cdot E}{h}, \tag{7.1}$$

where h is the Planck constant. Note that the Rabi frequency in 7.1 is in the unit of Hz. In the version where the Planck constant is replaced by the reduced Planck constant $\hbar$, the Rabi frequency unit becomes rad/s. From Equation 7.1, the transition DMS d^2 is related to the Rabi frequency by

$$d^2 = \frac{h^2\Omega^2}{E^2} \tag{7.2}$$

For a monochromatic propagating wave, the field intensity is related to the electric field amplitude E by

$$I = \frac{1}{2}\varepsilon_0 c E^2, \tag{7.3}$$

where ε_0 is the vacuum permittivity and c is the speed of light in vacuum. In our experiment, the probe laser light is a Gaussian beam with a size that is typically larger than the molecule cloud size by an order of magnitude. This means that the light intensity seen by the molecules can be approximated to the peak intensity of the laser beam.

Given a Gaussian beam, the power $P(r, z)$ passing through a circle with radius r at position z can be written as

$$P(r, z) = P_0 \left[1 - \exp(-2r^2/w(z)^2)\right], \tag{7.4}$$

where P_0 is the total power transmitted by the beam and $w(z)$ is the beam radius at position z. By definition, the peak intensity $I(0, z)$ is

$$I(0, z) = \lim_{r\to 0} \frac{P(r, z)}{\pi r^2} = \frac{2P_0}{\pi w(z)^2} \tag{7.5}$$

In the DMS measurements, the $w(z)$ is the beam size measured at the position of molecule cloud. Together with Equations 7.3 and 7.5, the DMS can be rewritten as

$$d^2 = \left(\frac{\pi h^2 \varepsilon_0 c}{4}\right)\left(\frac{\Omega^2}{P_0}\right) w^2 \tag{7.6}$$

In Equation 7.6, the Rabi frequency is measured via spectroscopy and the total probe laser power P_0 can be easily measured with a power meter. The remaining challenging part is to

measure the beam size w, which will be discussed in Appendix B.

7.1 Autler-Townes spectroscopy

In Section 3.1, I derive the doublet frequencies in Autler-Townes spectroscopy. For a coupling laser that is detuned from a transition $|r\rangle \rightarrow |e\rangle$ by a frequency of Δ, it splits the $|g\rangle \rightarrow |e\rangle$ transition into a doublet which frequencies are described by Equation 3.2. The frequency difference $\delta_{\pm}$ between the doublet satisfies

$$\delta_{\pm}^2 = \Omega^2 + \Delta^2, \tag{7.7}$$

where Ω is the coupling laser Rabi frequency. Thus, the Rabi frequency squared can be obtained by fitting $\delta_{\pm}^2$ as a function of Δ. In the following sections, a few examples of DMS measurements via Autler-Townes spectroscopy are demonstrated.

7.1.1 Transitions from a ground state to a shallow excited state

For a transition that involves a ground state and a shallow excited state, the spectroscopy setup is straightforward. Shallow excited states have large Franck-Condon factors with shallow ground states and the $^1S_0$ atom so in this situation the depletion transition for the

Autler-Townes spectroscopy can be a bound-to-bound transition, depicted in Figure 7.1(a), or a free-to-bound transition, depicted in Figure 7.1(b)

7.1.1.1 $X(-1,0) \rightarrow 0_u^+(-4,1)$ transition

Figure 7.2 demonstrates an example of measurement pertaining to Figure 7.1(a). In this example, the DMS of $X(-1,0) \rightarrow 0_u^+(-4,1)$ transition is measured. The Autler-Townes

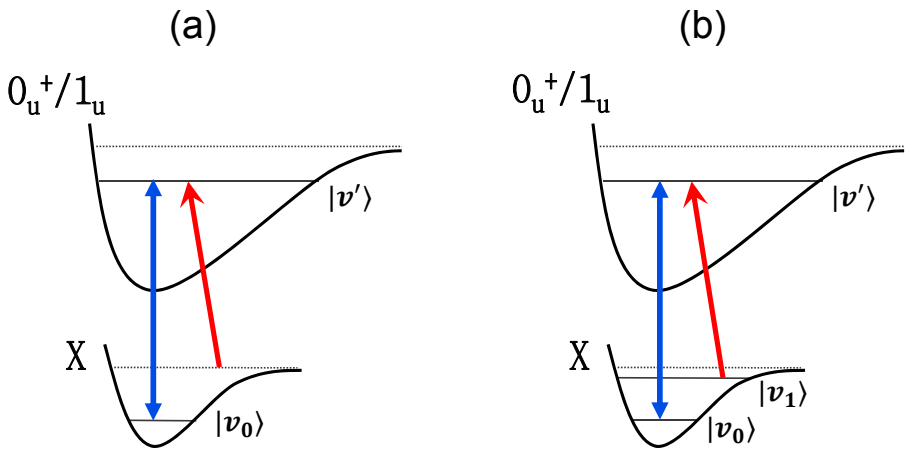

Figure 7.1: Spectroscopy scheme for DMS measurements for transitions from a ground state to a shallow excited state (blue). In this situation, the depletion transition (red) for the Autler-Townes spectroscopy can be (a) a free-to-bound transition or (b) a bound-to-bound transition.

spectroscopy is formed with the photoassociation transition from $^1S_0$ atom to $0_u^+(-4,1)$ state as the depletion laser. The coupling laser power is fixed at 57.4 μW and its beam waist is $(w_x, w_y) = (79.0(8)\ \mu\text{m}, 102(1)\ \mu\text{m})$ at the molecules. A Rabi frequency of 1.046(8) MHz is obtained from fitting the doublet frequency difference squared, depicted in Figure 7.2(b). Substituting these numbers into Equation 7.6 yields a DMS of

$$\begin{aligned} d^2 &= \left(\frac{\pi h^2 \varepsilon_0 c}{4}\right)\left(\frac{\Omega^2}{P_0}\right) w^2 \\ &= \left(\frac{\pi h^2 \varepsilon_0 c}{4}\right)\left(\frac{(1.046\ \text{MHz})^2}{57.4\ \mu\text{W}}\right)(79.0\ \mu\text{m} \times 102.5\ \mu\text{m}) = 1.97(4) \times 10^{-3}\ (ea_0)^2 \end{aligned}$$

This measured transition DMS is close to $3.13 \times 10^{-3}\ (ea_0)^2$ predicted by theoretical calculations. Note that the uncertainty in this DMS measurement is mostly contributed by the error in the beam waist estimation. Although a Gaussian distribution is a good approximation of the probe beam profile, a slight impurity could lead to an inaccurate estimation of

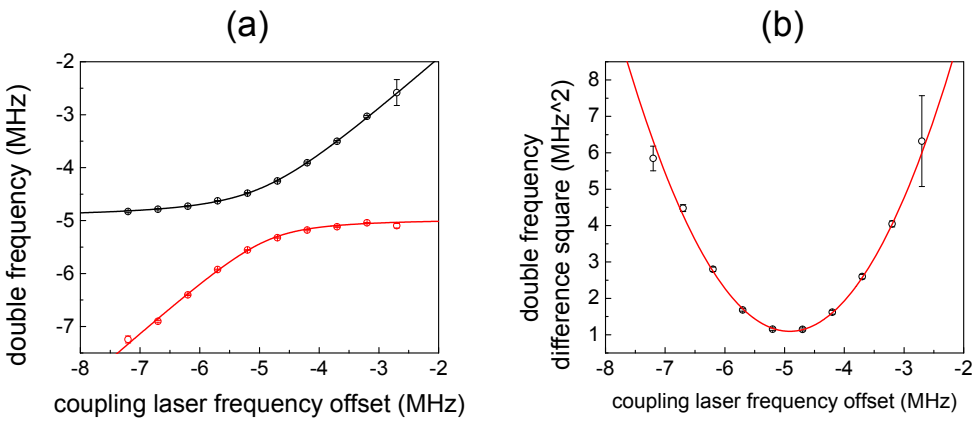

Figure 7.2: Demonstration of DMS measurement for the $X(-1,0) \rightarrow 0_u^+(-4,1)$ transition. The Autler-Townes doublet frequencies (a) and the doublet frequency difference squared (b) are plotted against the coupling laser frequency. The trace in (b) is fitted to Equation 7.7, which yields a Rabi frequency of 1.046(8) MHz.

beam waist and hence the laser beam peak intensity. An alternative method based on pixel intensity normalization can be applied to back out the peak intensity. With this method, it no longer requires the laser intensity profile to follow a certain distribution, which would lead to an even more precise measurement.

7.1.1.2 $X(6,0) \rightarrow 0_u^+(-4,1)$ transition

Figure 7.3 demonstrates another example that pertains to Figure 7.1(b). In this example, the DMS of $X(6,0) \rightarrow 0_u^+(-4,1)$ transition is measured. The Autler-Townes spectroscopy is formed with bound-to-bound $X(-1,0) \rightarrow 0_u^+(-4,1)$ as depletion transition. The coupling laser power is fixed at 92 μW and its beam waist is $(w_x, w_y) = (67.9(7)\ \mu\text{m}, 46.4(4)\ \mu\text{m})$ at the molecules. A Rabi frequency of 0.476(5) MHz is obtained from fitting the doublet frequency difference squared, depicted in Figure 7.3(b). Substituting these numbers into Equation 7.6 yields a DMS of

$$d^2 = \left(\frac{\pi h^2 \varepsilon_0 c}{4}\right)\left(\frac{\Omega^2}{P_0}\right) w^2$$
$$= \left(\frac{\pi h^2 \varepsilon_0 c}{4}\right)\left(\frac{(0.476\ \text{MHz})^2}{92\ \mu\text{W}}\right)(67.9\ \mu\text{m} \times 46.4\ \mu\text{m}) = 9.88(9) \times 10^{-5}\ (ea_0)^2,$$

which is comparable to $5.27 \times 10^{-5}(ea_0)^2$ predicted by theory calculations.

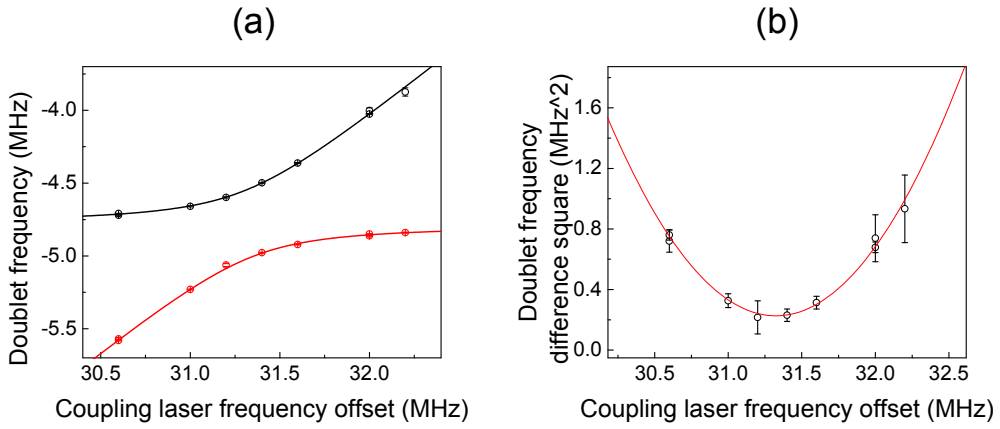

Figure 7.3: Demonstration of DMS measurement for the $X(6,0) \rightarrow 0_u^+(-4,1)$ transition. The Autler-Townes doublet frequencies (a) and the doublet frequency difference squared (b) are plotted against the coupling laser frequency. The trace in (b) is fitted to Equation 7.7, which yields a Rabi frequency of 0.476(5) MHz.

7.1.2 Transitions from a ground state to a deeply bound excited state

The Autler-Townes spectroscopy is more challenging for transitions from a ground state $X(v,J)$ to a deeply bound excited states, say $1_u(v',1)$ with $v' \sim 24$. In this situation, the Franck-Condon factor between the excited state and shallow ground states/$^1S_0$ continuum is small, making both depletion schemes depicted in Figure 7.1 unrealistic. Instead, the depletion transition in this case is formed by a two-photon transition between a weakly bound ground state and the ground state involved in the coupling transition, as shown in Figure 7.4.

Due to the complexity in this measurement, it is worth a few words to clarify the procedure for the spectroscopy. In this experiment, the molecules are prepared at a weakly bound ground state and the molecule number is detected with the recovery scheme. When the two-photon transition between ground states is tuned on resonance, a depletion signal is obtained. As the $X(v, J)$ state is addressed by the coupling laser, it is split into a doublet and scanning the depletion laser, the Raman transition in this case, resolves the Autler-Townes spectroscopy.

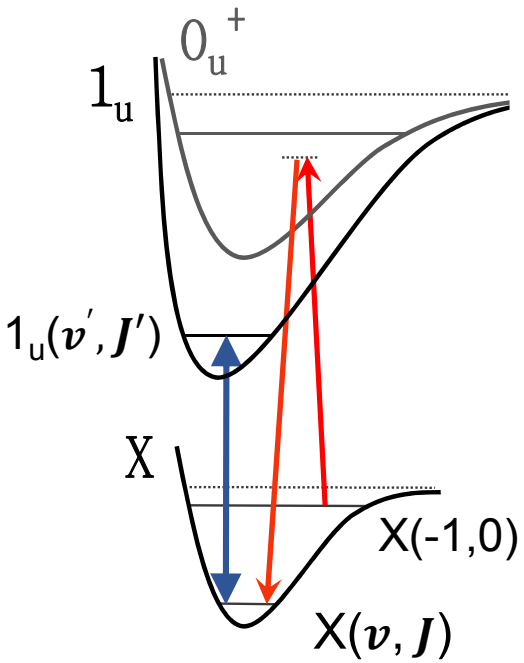

Figure 7.4: Spectroscopy scheme for DMS measurements for transitions from a ground state to a deeply bound excited state. In this case, a two-photon transition between ground states is adapted to be the depletion transition. The rovibrational quantum numbers v, J and J' are determined by the probe laser frequency and selection rules.

7.1.2.1 $X(6,0) \rightarrow 1_u(24,1)$ transition

An example of measurement on the DMS of $X(6,0) \rightarrow 1_u(24,1)$ is demonstrated in Figure 7.5. In this measurement, the coupling laser power is fixed at 1.2 mW and its beam waist

is $(w_x, w_y) = (81.2(8)\ \mu\text{m}, 86.6(8)\ \mu\text{m})$ at the molecules. A Rabi frequency of 0.49(4) MHz is obtained from fitting the doublet frequency difference squared, depicted in Figure 7.5(b). Substituting these numbers into Equation 7.6 yields a DMS of

$$\begin{aligned} d^2 &= \left(\frac{\pi h^2 \varepsilon_0 c}{4}\right)\left(\frac{\Omega^2}{P_0}\right) w^2 \\ &= \left(\frac{\pi h^2 \varepsilon_0 c}{4}\right)\left(\frac{(0.49\ \text{MHz})^2}{1.2\ \text{mW}}\right)(81.2\ \mu\text{m} \times 86.6\ \mu\text{m}) = 1.8(2) \times 10^{-5}\ (ea_0)^2 \end{aligned}$$

This value is comparable to the theory calculation which predicts $1.53 \times 10^{-5}(ea_0)^2$. Note that the DMS of a lattice-driven transition can be measured more precisely with the light shift, which is elaborated in the next section.

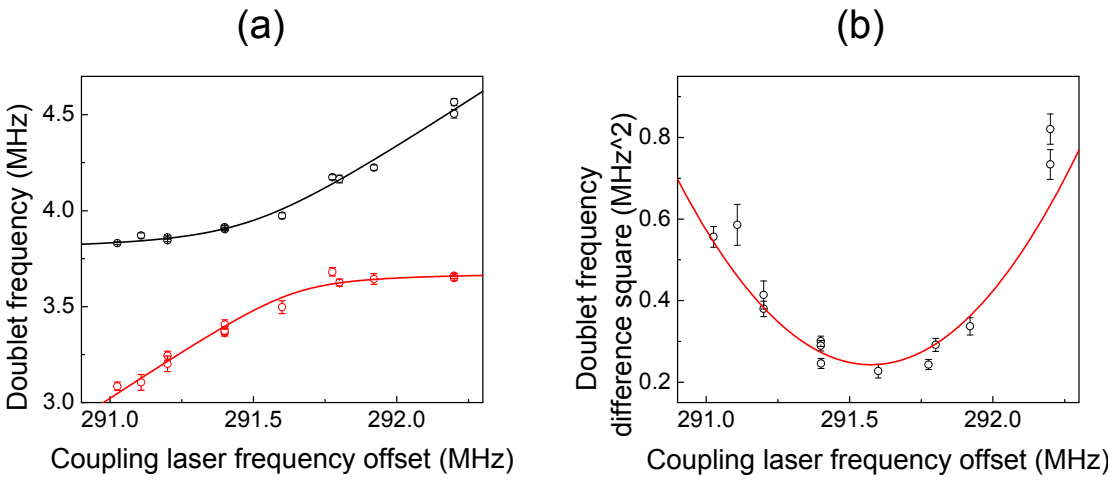

Figure 7.5: Demonstration of DMS measurement for the $X(6,0) \rightarrow 1_u(24,1)$ transition. The Autler-Townes doublet frequencies (a) and the doublet frequency difference squared (b) are plotted against the coupling laser frequency. The trace in (b) is fitted to Equation 7.7, which yields a Rabi frequency of 0.49(4) MHz.

7.2 Light shift measurements

In Section 4.2.2, the polarizability curves obtained with lattice-driven transitions are presented. As the lattice laser frequency is close to a vibronic transition resonance, a light shift is induced on the bottom clock state. The light shift δf, as described by Equation 4.5, is proportional to the Rabi frequency square,

$$\delta f = \frac{\Omega^2}{4\Delta}$$

Therefore, by fitting the light shift as a function of lattice detuning Δ, the Rabi frequency and the transition DMS can be backed out.

7.2.1 Lattice-driven transitions

In this section, the DMS measurement of the lattice-driven transition with $1_u(24, 1)$ state is demonstrated and the DMS values obtained via the Autler-Townes spectroscopy and the light shift measurement will be compared.

7.2.1.1 $X(6, 0) \rightarrow 1_u(24, 1)$ transition

Figure 7.6 demonstrates the DMS measurement for the $X(6, 0) \rightarrow 1_u(24, 1)$ transition. In this measurement, the lattice laser power is fixed at 200 mW and the lattice beam waist is 34.3 μm. A Rabi frequency of 29.0(2) MHz is obtained by fitting the dispersive curve to the light shift formula.

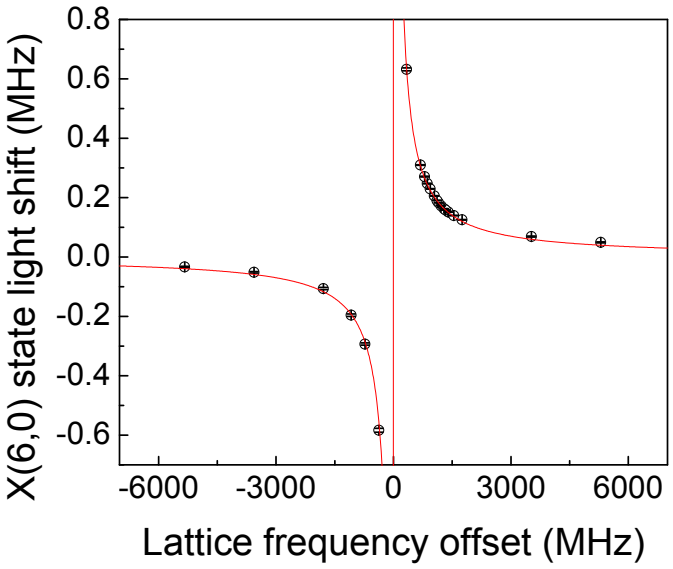

Figure 7.6: Demonstration of DMS measurement for the $X(6,0) \rightarrow 1_u(24,1)$ transition via light shift measurement. The light shift on X(6,0) state is fitted to Equation 4.5, which yields a Rabi frequency of 29.0(2) MHz. In this measurement, the lattice power is fixed at 200 mW and the lattice beam waist is 34.3 μm.

The DMS can be deduced from the Rabi frequency squared.

$$\begin{aligned} d^2 &= \left(\frac{\pi h^2 \varepsilon_0 c}{4}\right)\left(\frac{\Omega^2}{4P_0}\right) w^2 \\ &= \left(\frac{\pi h^2 \varepsilon_0 c}{4}\right)\left(\frac{(29.0\text{ MHz})^2}{4 \times 200\text{ mW}}\right)(34.3\ \mu\text{m} \times 34.3\ \mu\text{m}) = 1.57(2) \times 10^{-5}\ (ea_0)^2 \end{aligned}$$

Note that an additional factor of 4 appears before the laser power because the lattice is formed with two counter-propagating laser beams.

The DMS value for the lattice-driven transition obtained with light shift nicely agrees with theory calculations, which predict $1.53 \times 10^{-5}(ea_0)^2$. The value obtained with the light shift is comparable to that obtained with the Autler-Townes spectroscopy. Actually, the measurement via light shift should be more reliable because the spectroscopic laser also serves as the trapping laser, which naturally guarantees the precision in laser intensity estimation.

Chapter 8

Control of ultracold photodissociation with magnetic fields

8.1 Experiment overview

In this experiment we directly observe and record the photofragment angular distributions (PADs) in the millikelvin energy regime. The molecules are prepared at microkelvin temperatures in an optical lattice, as described in Chapter 2, and are subsequently fragmented with laser light. The one-dimension lattice is a standing wave of far-off-resonant light at 910 nm and is approximately 1 MHz (or 50 μK) deep. The geometry of the setup is defined in Figure 8.1. Photodissociation results in two counterpropagating photofragments, an atom in the ground state $^1S_0$, and an atom in the electronically excited state $^3P_1$ which decays to $^1S_0$ with a 22 μs lifetime. These atoms are absorption imaged using a charge-coupled device camera on the strong Sr transition at 461 nm. The imaging light is turned on for a short duration of ~ 10 μs, at a time τ (between 250 and 600 μs) after the 20–50 μs photodissociation pulse at

689 nm. During this time τ, the photofragments freely expand and effectively form spherical shells with radii determined by the frequency of the photodissociation light and the Zeeman shifts of the atomic continua. The camera is nearly on axis with the lattice, thus capturing a two-dimensional projection of the spherical shells since the atoms effectively originate from a point source. The laboratory quantum axis points along the applied magnetic field $\vec{B}$, which has a vertical orientation that defines the polar angle θ and azimuthal angle ϕ. The dependence of the photofragment density on these angles is our key observable and encodes the quantum mechanics of the reaction. The photodissociation light polarization is set to be either vertical or horizontal.

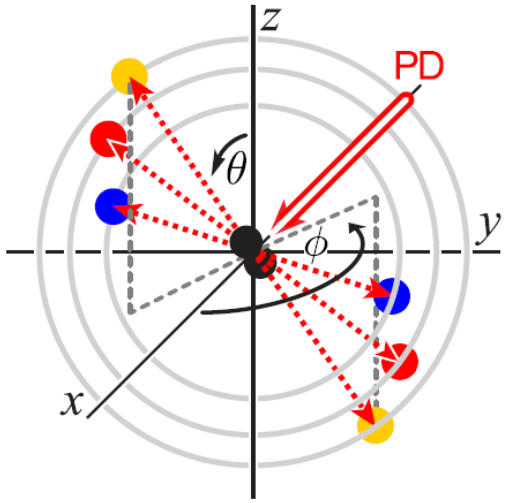

Figure 8.1: The molecules are trapped in an optical lattice at the origin, while the photodissociation (PD) laser propagates along the x-axis. The polar angle θ and azimuthal angle ϕ are defined as shown to describe the photofragment angular distributions. The radii of the spherical shells containing the fragments after a fixed expansion time are given by the frequency of the PD laser and the Zeeman shifts of different atomic continua. The largest shell corresponds to a negative shift (yellow), the medium shell to an absence of shift (red), and the smallest shell to a positive shift (blue). A camera points in the $-x$ direction and images a two-dimension projection of the nested shells.

8.2 Photodissociation with applied magnetic field

So how does an applied magnetic field influence photodissociation? Figure 8.2(a) illustrates the Sr_2 molecular structure relevant to this work. The molecules are created from ultracold atoms via photoassociation [71] in the least-bound vibrational level, denoted by $v = -1$, of the electronic ground state X (correlating to the $^1S_0 + ^1S_0$ atomic threshold). Initially, the molecules occupy two rotational states with the total angular-momentum quantum numbers $J_i = 0$ and 2, but the $J_i = 2$ population is mostly removed prior to fragmentation by a laser pulse resonant with an excited molecular state. The $J_i = 0$ molecules (with a projection quantum number $M_i = 0$) are coupled by the photodissociation laser to the singly excited continuum above the 0_u and 1_u ungerade potentials (correlating to the $^1S_0 + ^3P_1$ atomic threshold), where the numbers refer to the total atomic angular momentum projections onto the molecular axis. Under an applied field $B > 0$, the atomic energy levels split by the Zeeman interaction into the $m = -1$, 0, and 1 sublevels, where the energy separation between the neighboring sublevels is $h\Delta_Z = 1.5\mu_B B$ and μ_B is the Bohr magneton. The radius of each photofragment shell is $v\tau$ where $v = \sqrt{h(\Delta - m\Delta_Z)/m_{Sr}}$ is the velocity, h is the Planck constant, Δ is the frequency detuning of the photodissociation light from the $m = 0$ component of the continuum, and m_{Sr} is the atomic mass of Sr.

If the photodissociation laser detuning is large and negative, $\Delta < -\Delta_Z$, no photofragments should be detectable because the target energy is below the lowest threshold. If the detuning is small and negative, $-\Delta_Z < \Delta < 0$, then only one fragment shell should be visible, corresponding to $m = -1$. If the detuning is small and positive, $0 < \Delta < \Delta_Z$, we expect to observe two fragment shells, with $m = 1$ and 0. Finally, if the detuning is large and positive, $\Delta_Z < \Delta$, we expect three fragment shells with all possible values of m. This is the case in

the example of Figure 8.2(b) that shows a strong alteration of the PAD for $B = 10.15$ G compared to 0.5 G.

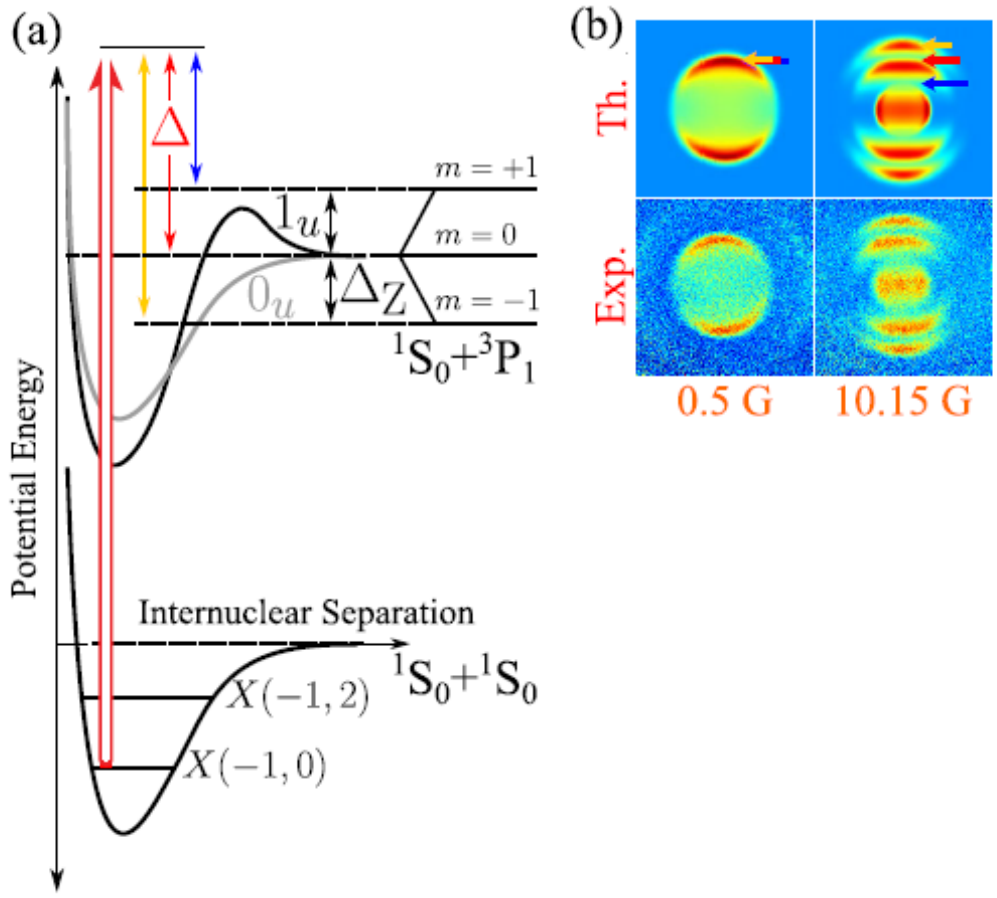

Figure 8.2: (a) Molecular potentials and quantum states relevant to the experiment. The photodissociation process is designated by the double arrow. The detuning of the PD light from the $m = 0$ Zeeman component of the continuum is Δ, and the symmetric Zeeman splitting has a magnitude ΔZ. The barrier of the 1_u potential has a height of ~ 30 MHz. The numbers in parentheses are v and J_i. (b) An example of calculated and measured PAD images for a process where a small applied magnetic field drastically alters the outcome of the reaction. The two pairs of images differ only by the magnitude of the applied field: $B = 0.5$ G on the left and 10.15 G on the right.

When a $J_i = 0$ diatomic molecule is photodissociated via a one-photon E1 process without an applied field, we expect and observe a dipolar-shaped PAD with an axis set by the laser polarization [12], as in the nearly field-free case of Figure 8.2(b). This can be understood either by visualizing a spherically symmetric molecule absorbing light with a dipolar probability distribution or by applying angular momentum selection rules that require $J = 1$ for the outgoing channel, which has a dipolar angular distribution with a single spatial node. We find that with a nonzero B this is no longer the case, and instead observe complicated structures with multiple nodes.

The main results of the experiment and theory are summarized in Figures 8.3 and 8.4. The two-dimensional projections of the PADs onto the imaging plane, with the detuning $\Delta = 29.2$ MHz, are shown in Figure 8.3 for a progression of magnetic fields B from 0.5 to 10.15 G. The removal of the $J_i = 2$ molecules is imperfect which results in the very faint outermost shell that can be ignored. The top pair of rows corresponds to parallel light polarization and the bottom pair to perpendicular polarization. We observe a transformation from simple dipolar patterns at $B = 0$ to more complex patterns that exhibit a multiple-node structure at 10.15 G. Figure 8.4 shows PADs that are observed when B is kept fixed at 10.15 G while Δ is varied from -13.8 to 50.0 MHz, again for both cases of linear light polarization. For the entire range of continuum energies, we observe PADs that exhibit a multinode structure. As Δ and B are varied, the angular dependence, or anisotropy, of the outgoing PAD is strongly affected. The zero-field evolution of the PADs with energy for this continuum is discussed in [4]. All additional features observed here are due to the continuum partial waves J being strongly mixed by the applied field.

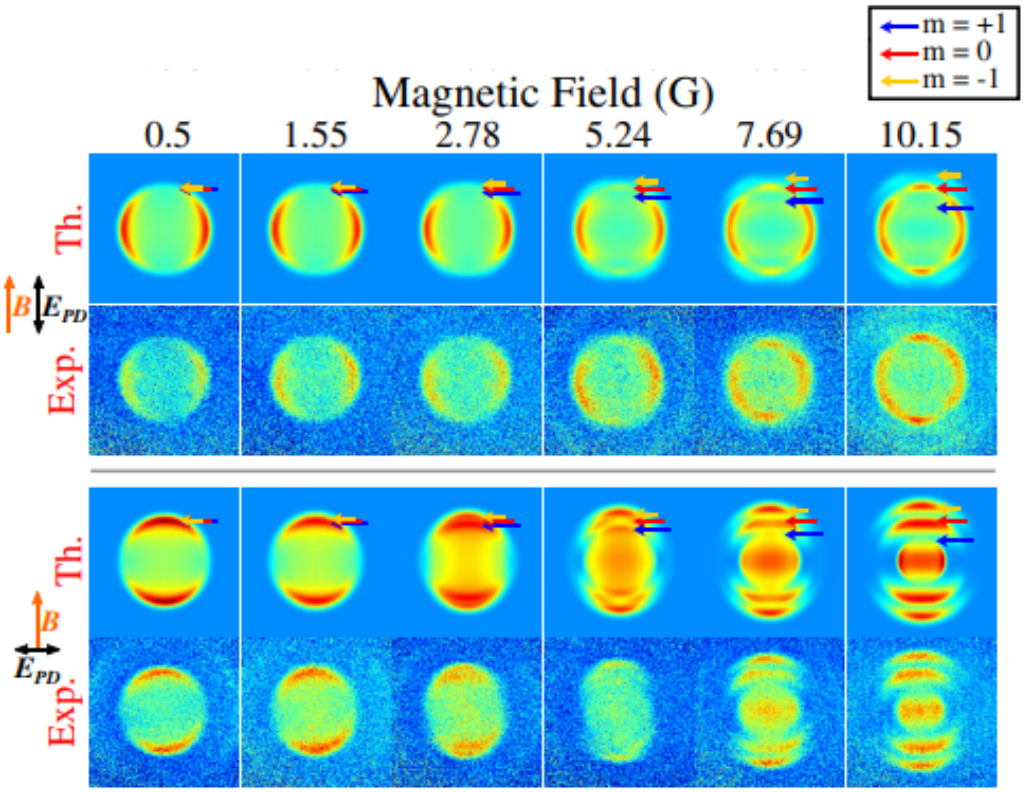

Figure 8.3: Tuning of the photodissociation reaction with small magnetic fields, across a range of energies. The color coding for the continuum Zeeman components is the same as in Figure 8.2. In this figure, theoretical and experimental images of PADs are shown as the magnetic field B is increased from 0.5 to 10.15 G, for the detuning $\Delta = 29.2$ MHz.

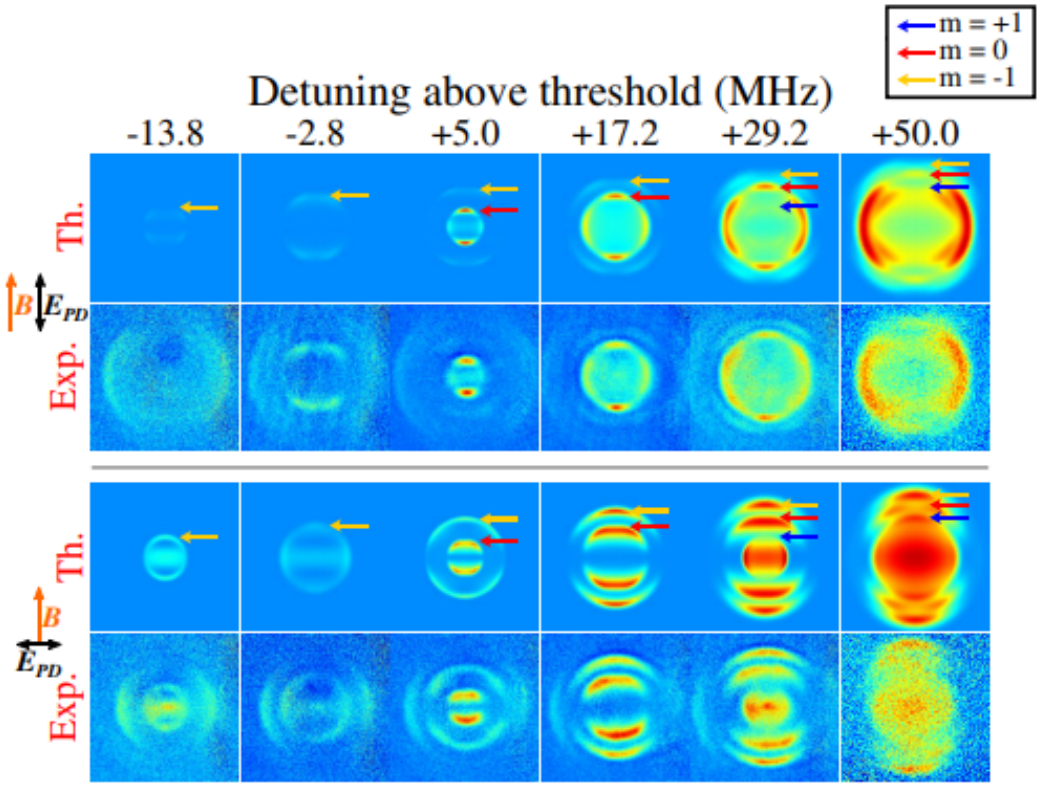

Figure 8.4: Tuning of the photodissociation reaction with small magnetic fields, across a range of energies. The color coding for the continuum Zeeman components is the same as in Figure 8.2. Here, theoretical and experimental PAD images at $B = 10.15$ G are shown, covering a range of Δ from -13.8 to 50.0 MHz. As indicated in Figure 8.2, additional channels ($m = -1$, 0, and 1) become available in the continuum as Δ increases, leading to extra photofragment shells. In some of the experimental images, the faint outermost shell is the result of incidental photodissociation of residual $J = 2$ molecules and can be ignored.

The top and bottom pairs of rows in both Figures 8.3 and 8.4 correspond to the light polarization parallel and perpendicular to $\vec{B}$, respectively. Typically, 300 experiments with atoms and 300 without atoms (for background subtraction) are averaged to obtain each experimental PAD image. The experimental images use an arbitrary brightness scale, and the relative transition strengths for different images can be inferred from this data only qualitatively. Within each PAD, however, relative transition strengths to different m's are more accurately reflected in the relative brightness of the rings.

As Figures 8.3 and 8.4 demonstrate, our theoretical results are in excellent agreement with the experimental data. The theory involves extending the standard treatment of diatomic photodissociation to the case of mixed angular momenta in the presence of a magnetic field and applying it to the quantum-chemistry model of the $^{88}Sr_2$ molecule [76, 81].

The PADs can be described by the expansion

$$I(\theta,\phi) \propto \beta_0 \left(1 + \sum_{\mu=1}^{\infty} \sum_{\nu=0}^{\mu} \beta_{\mu\nu} P_\mu^\nu(\cos\theta) \cos(\nu\phi) \right) \tag{8.1}$$

where $P_\mu^\nu(\cos(\theta)$ are the associated Legendre polynomials and the $\beta_{\mu\mu}$ coefficients are called anisotropy parameters. In the case of parallel light polarization, the PADs are cylindrically symmetric and we set $\beta_\mu \equiv \beta_{\mu 0}$ while all other $\beta_{\mu\nu}$ vanish. The μ are even for homonuclear dimers. The anisotropy parameters in Equation 8.1 can be evaluated from Fermi's golden rule after properly representing the initial (bound-state) and final (continuum) wave functions, including mixing of the angular momenta J_i and J by the magnetic field.

8.3 Summary

We have shown that the reaction of photodissociation can be strongly altered in the ultracold regime by small applied magnetic fields. In this work, the fragmentation of $^{88}Sr_2$ molecules

was explored for a range of fields from 0 to 10 G, and for a variety of energies above threshold in the 0–2 mK range. The near-threshold continuum has a high density of partial waves that are readily mixed by the field, resulting in pronounced changes of the photofragment angular distributions. The theory of photodissociation, after explicit accounting for field-induced mixing of angular momenta in the bound and continuum states, and combined with an accurate quantum-chemistry molecular model, has yielded excellent agreement with experimental data. The experiment and its clear interpretation are made possible by preparing the molecules in well-defined quantum states. We have shown that ultracold molecule techniques allow a high level of control over basic chemical reactions with weak applied fields. Moreover, this work serves as a test of *ab initio* molecular theory in the continuum.

Chapter 9

State-selected photodissociation pattern evolution with energy

9.1 Experiment description and overview

Collisions and reactions between molecules can be described by the quasiclassical model when the samples are at high energy. However, in the ultracold regime the quasiclassical model fails and we need a full quantum-mechanical approach to precisely understand the reaction. In Chapter 8, I discuss photodissociation of ultracold Sr_2 molecules in the near-threshold quantum regime and control of reactions by magnetic fields. Not surprisingly, the measured photofragment angular distributions disagreed with quasiclassical intuition to varying degrees. It remained an open question whether a crossover into quasiclassical behavior could be observed and explained from first principles. In this chapter, we observe the crossover from the ultracold, quantum mechanical to the quasiclassical regime of photodissociation. We show that photofragment angular distributions exhibit strong variations with the continuum energy near threshold, but stabilize to energy independent quasiclassical patterns at energies that exceed reaction barrier heights. This study includes an electronically excited

multichannel continuum in addition to the ground-state continuum. Furthermore, we find that quantum statistics of the photofragments can prevent the photodissociation outcome from reaching the quasiclassical limit even at high energies. Moreover, we also show that photodissociation of very weakly bound molecules can exhibit quantum mechanical behavior to higher energies, and we explicitly compare different levels of approximation for predicting the photofragment angular distributions.

In this experiment, ^{88}Sr atoms are laser-cooled and photoassociated in a one-dimensional optical lattice, yielding $\sim$7000 Sr_2 molecules trapped at a few microkelvin. The lattice trap at the wavelength of 910 nm has 30 μm radius and 730 μm length. The molecules predominantly occupy the most weakly bound vibrational level $v = -1$ in the electronic ground state that correlates to the atomic $^1S + {}^1S$ threshold. They are distributed between two angular momenta $J_i = 0, 2$, either of which can be chosen as the initial state for photodissociation, with the selectivity of the projection quantum number m_i. Alternatively, weakly bound levels that correlate to the excited $^1S + {}^3P_1$ continuum can be populated prior to photodissociation by 689 nm light that copropagates with the lattice, in which case the (J_i, m_i) notation would refer to these initial bound states. The photodissociation light pulses are $10 - 20$ μs long, the photofragment time of flight varies from 800 μs near threshold to 20 μs at higher energies, and the imaging pulse is $10 - 20$ μs. The absorption imaging beam is resonant with the strong 461 nm Sr transition, nearly coaligned with the lattice, and expanded to 300 μm in order to intercept the outgoing photofragments. The (vertical) quantization axis is set by the lattice polarization, or by a 3 G magnetic field when required for state selection, while the photodissociation light has polarization that is parallel ($P = 0$) or perpendicular ($|P| = 1$) to this axis. The continuum energy is determined by the frequency of the photodissociation light. Reaching high energies can be challenging because of diminishing bound-continuum

transition strengths and rapid expansion of the photofragments.

Figures 9.1(a) and 9.1(b) show two photodissociation processes studied in this chapter. In case (a), a single molecular quantum state (v, J_i, m_i) of the 0_u^+, 1_u electronic manifold is resonantly populated and immediately photodissociated to the ground continuum, while process (b) samples the electronically excited continuum from a single ground quantum state. The upper continuum has contributions from the barrierless 0_u^+ potential and the 1_u potential with a $\sim$1 mK electronic barrier, where the potentials are labeled by Ω_i, the atomic angular momentum projection onto the internuclear axis. Rotational barriers present for all continuum states with angular momentum $J \neq 0$ are not shown.

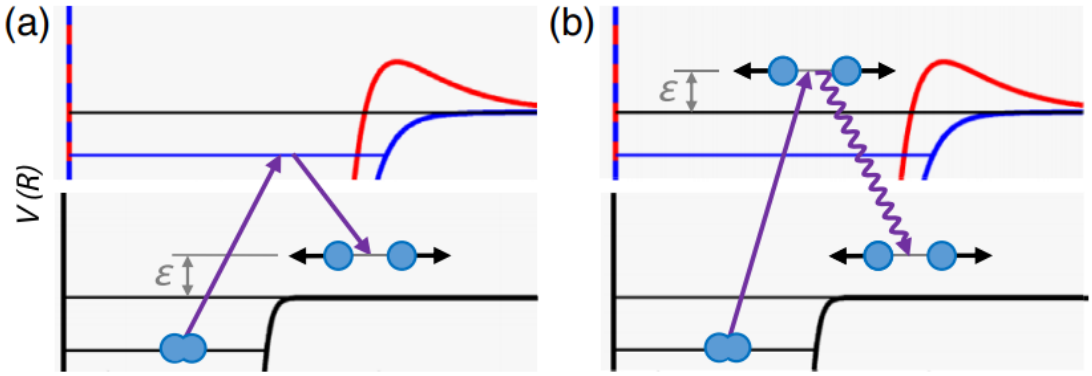

Figure 9.1: (a) Schematic of Sr_2 molecule photodissociation to the ground continuum. Weakly bound molecules are fragmented with a resonant two-photon process via the excited electronic state, which effectively serves as the initial molecular state. The photofragments have total energy ε that is determined by the bound-continuum laser frequency, and are detected with absorption imaging. (b) One-photon photodissociation to the excited continuum that corresponds to a pair of interatomic potentials, 0_u^+ and 1_u, where 1_u has an electronic barrier. The excited atomic fragments radiatively decay to the ground state, and the angular distributions can be imaged as in (a). Adapted from [6].

An image of a photofragment angular distribution and the data analysis procedure are illustrated in Figure 9.2. Panels (i)–(iv) show a time-of-flight image, a schematic three-dimensional distribution that results in this image via line-of-sight integration, the cross section of the distribution obtained with the inverse Abel transform of the data, and the radial average of the cross section showing the measured angular photofragment density.

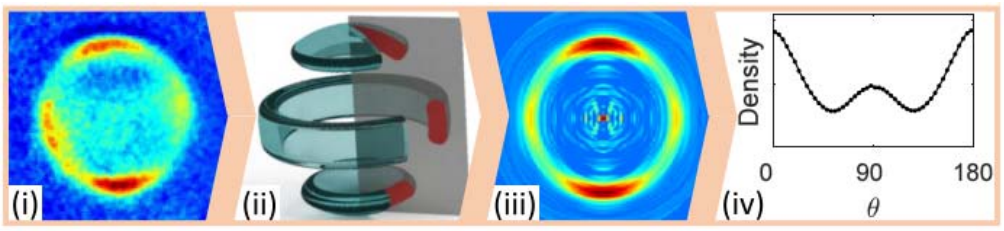

Figure 9.2: Data analysis for azimuthally symmetric photofragment distributions. A time-of-flight absorption image of photofragments, typically $0.3-0.5$ mm in diameter (i) where some asymmetry is introduced by inhomogeneities in the imaging beam profile, is a line-of-sight integral of the three-dimensional distribution [(ii), shown as a schematic surface of constant density]. A cross section of this distribution, shown in red, is retrieved from the data as in (iii) by slightly rotating the image and assuming symmetry about the horizontal axis, and radially averaged to yield an angular density profile (iv). Adapted from [6].

9.2 Key questions

We explore experimentally and theoretically the crossover from ultracold to quasiclassical chemistry. On the theory side, we explicitly compare the applicability of a range of approximations, including the Wentzel-Kramers-Brillouin (WKB) approximation and a semiclassical model that considers classical rotation of the molecule during photodissociation, to the full quantum mechanical treatment. This fully quantum treatment uses Fermi's golden rule with the bound and continuum wave functions to calculate the photodissociation cross sections. It

is in agreement with data across all sampled energies and for molecules in all initial quantum states, with further improvement possible only by introducing small corrections to the *ab initio* molecular potentials [76,81]. It is necessary to use the quantum mechanical method to model our observations near threshold. At high energy, the axial recoil limit is reached, where photodissociation is much faster than molecular rotation and the photofragments emerge along the molecular axis. The questions we address in this chapter are:

- At what energy scale do the angular distributions approach the axial recoil limit?
- How does this scale depend on the quantum numbers and binding energy of the molecule?
- How can quantum state selection prevent the axial recoil limit from agreeing with quasiclassical intuition?

9.2.1 Axial recoil limit

In this section we will find out at what energy scale the angular distributions approach the axial recoil limit and how this scale depends on the initial molecular state. Well, what does axial recoil actually mean? When molecules are dissociated at high energies, the photodissociation process is a lot faster than the speed at which molecules rotate so that the molecules can be approximated by classical rotors. In other words, the photodissociation outcome should have quasiclassical behavior if the photofragment energy in the continuum exceeds the height of any potential barriers. This regime is referred to as *axial recoil*, where the molecule has insufficient time to rotate during photodissociation and the photofragments emerge along the instantaneous direction of the bond axis.

Firstly let's look at a real example of dissociation pattern evolution. Figure 9.3 illustrates the evolution of an angular distribution as a function of the continuum energy ε for $0_u^+(v' =$

$-4, J_i' = 1, M_i' = 0$) molecules and $P = 0$. This energy dependence is characteristic of near-threshold photodissociation where there is a strong sensitivity to individual partial wave components of the outgoing photofragments. The molecules are photodissociated over ∼2 orders of magnitude of energy, with Figure 9.3(a) displaying the angular photofragment densities as a function of ε/k_B where k_B is the Boltzmann constant. Quantum chemistry calculations of the expected density curves, based on *ab initio* Sr_2 potentials, are overlayed with the data. The measured images for $\varepsilon/k_B = 1.6$ and 14 mK are shown in the leftmost panels of Figure 9.3(b) and 9.3(c), followed by theoretical images. Figure 9.3(c) also shows an image calculated for the axial recoil limit, which is already approached at 14 mK. The angular distribution in the axial recoil limit, $I_{AR}(\theta, \phi)$, agrees with the quasiclassical model: $I_{AR}(\theta, \phi) = I_{QC}(\theta, \phi)$, where the quassiclassical model is described by Equation 1.5. Note that the anisotropy parameter $\beta_2 = 2$ for a parallel photodissociation transition ($\Delta\Omega = 0$) resulting in a photofragment distribution mostly along the quantization axis and $\beta_2 = -1$ for a perpendicular transition ($\Delta\Omega = 1$) with a photofragment distribution mostly transverse to the axis.

For molecules composed of identical constituents such as bosonic ^{88}Sr atoms, spin statistics imposes selection rules on allowed angular momenta through the required symmetry under nuclear exchange. In the electronic ground state of $^{88}Sr_2$ only even J values are allowed, while in the 0_u^+ excited state only odd J values are possible. Since odd J are forbidden in the ground state, the quantum state of photofragments in this continuum [Figure 9.1(a)] can be described by only two parameters R, δ such that the amplitudes of finding the photofragments in $J = J_i - 1$ and $J = J_i + 1$ are $\sqrt{R}$ and $\sqrt{1-R}$, respectively, with the phase difference δ. The energy evolution of R and δ is plotted in Figure 9.3(d). In the axial recoil limit, $R \sim 1/2$ and $\cos\delta = 1$. More detailed theoretical discussions can be found in [8].

While the angular distributions in Figure 9.3(a)–(c) and R, δ in Figure 9.3(d) show a strong dependence on ε/k_B up to ∼5 mK, at higher energies significantly exceeding the rotational barrier heights the distributions become quasiclassical, with R showing faster convergence than δ.

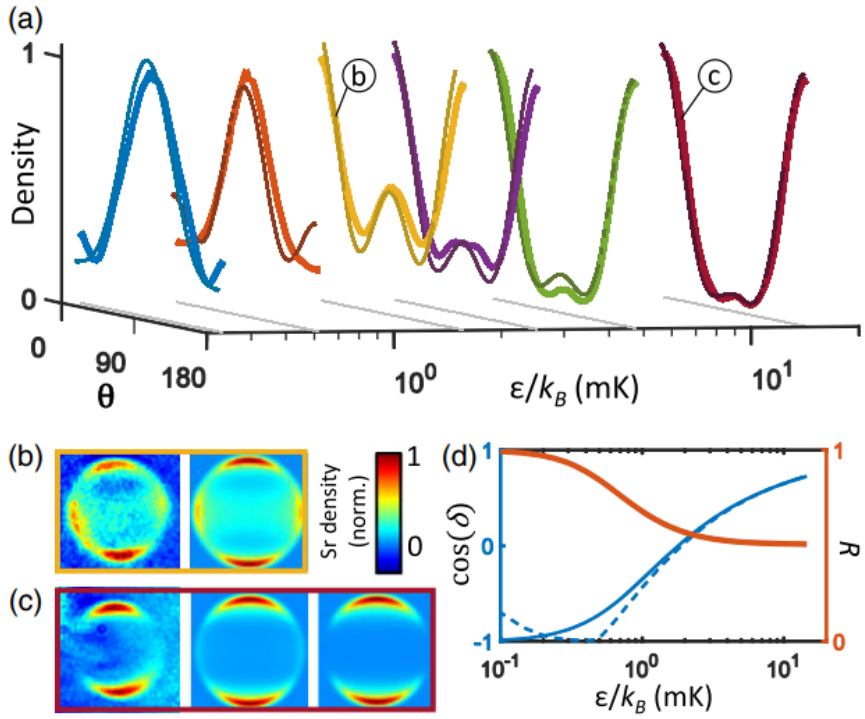

Figure 9.3: (a) Angular distribution of photofragment density from dissociation of the $0_u^+(v = -4, J_i = 1, M_i = 0)$ state as a function of energy ε. Thick curves: inverse Abel data. Thin curves: quantum theory prediction. The labeled curves correspond to panels (b),(c), where curve (c) nearly matches the quasiclassical expectation. (b) Absorption image and the corresponding quantum theory for the $\varepsilon = 1.6k_B$ mK $= 33h$ MHz dissociation ring, where h is the Planck constant. (c) Absorption image, quantum theory, and axial recoil approximation for the $\varepsilon = 14k_B$ mK $= 300h$ MHz dissociation ring. (d) Calculated energy evolution of R (thick line) and $\cos\delta$ (thin solid line) for the process in (a)–(c). The thin dashed line shows the WKB approximation and indicates its agreement with the quantum theory at $\varepsilon/k_B \gtrsim 1$ mK. Adapted from [6].

The experiments of dissociating molecules in different precisely prepared quantum states have also been carried out. In Figure 9.4, molecules in vibrational states $v' = \{-2, -3, -4, -5\}$ of the 0_u^+ potential are photodissociated with $P = 0$ at a continuum energies $\varepsilon/h = \{13, 33, 53, 100, 300\}$ MHz ($\varepsilon/k_B = 0.6 - 14$ mK). The photofragment angular distributions show a strong energy dependence and agree well with quantum-mechanical calculations regardless of initial states and continuum energies. Images calculated with the WKB approximation are also shown for comparison. At low energies the WKB approximation fails in predicting the photofragment angular distributions whereas the approximations are a lot better at high energies. Similarly, in Figure 9.5 molecules in vibrational states $v' = \{-1, -2\}$ of the 1_u potential are photodissociated with a variety of continuum energies. For 1_u molecules, due to the perpendicular nature of the $|\Delta\Omega| = 1$ transition to the ground state, at high energies the fragments emerge mostly horizontally (at 90° to the light polarization) rather than vertically as for 0_u^+ in Figure 9.4.

As implied by Figure 9.4 and 9.5, at very high continuum energies the quantum-mechanical calculations should converge to the WKB approximations. Figure 9.6 examines this speculation by comparing quantum theory and the WKB approximation at the continuum energy $\varepsilon/h = 1000$ MHz ($\varepsilon/k_B = 48$ mK). At this high energy, both methods approach the axial-recoil limit, which is also shown. Unfortunately, we couldn't directly compare experiments with theory at this extreme energy since the strength of dissociation processes decays rapidly with continuum energy. Anyway the experiments taken with $\varepsilon/h = 300$ MHz have shown decent qualitative agreements with the high energy situations. In the future if dissociation images at high continuum energies are really needed, one can try making more strontium molecules by increasing the oven temperature. When doing this, it is crucial to keep the oven valve temperature below 150°C to prevent it from breaking down.

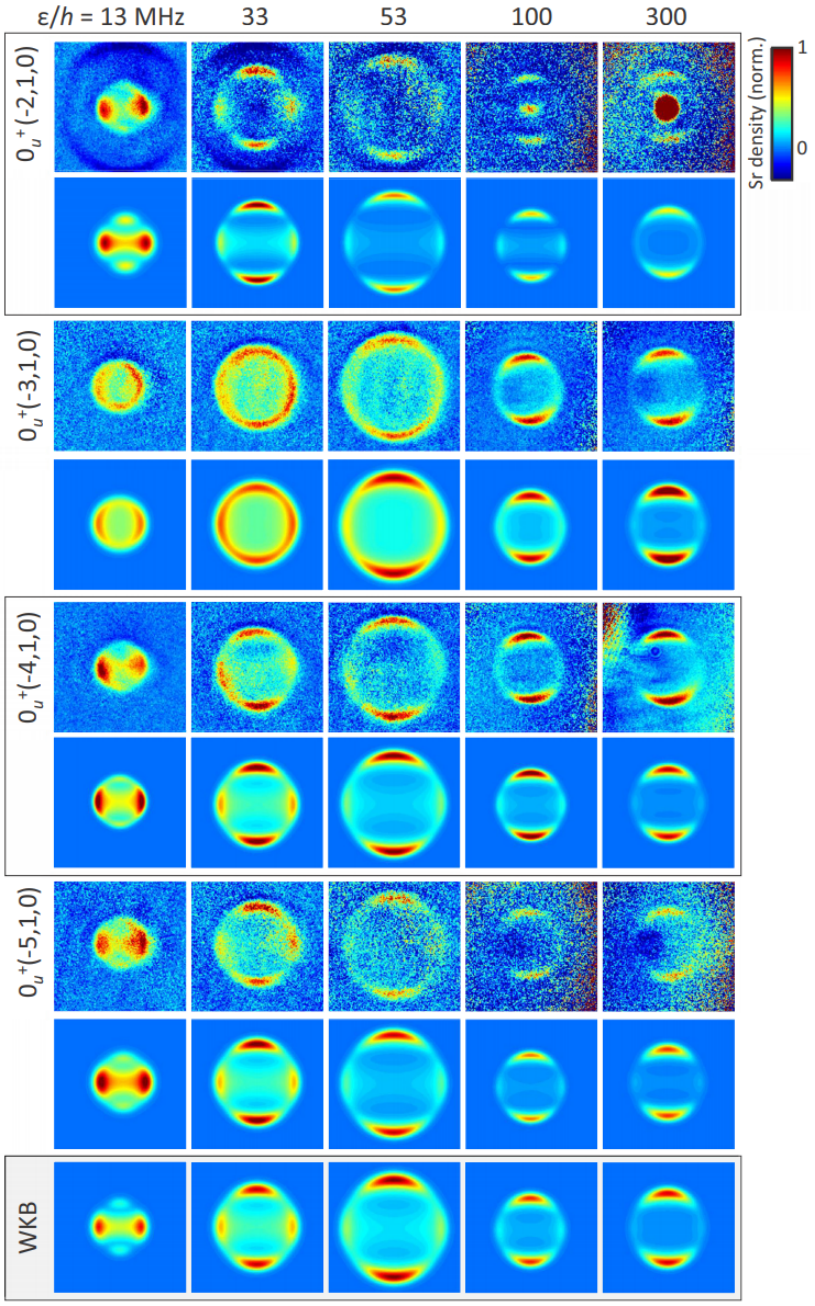

Figure 9.4: Measured and calculated photofragment angular distributions from 0_u^+ molecule dissociation in the ultracold quantum-mechanical regime. For each initial state, the upper and lower rows correspond to measurements and quantum-mechanical theory, respectively. The bottom row shows calculations obtained with the WKB approximation. Adapted from [8].

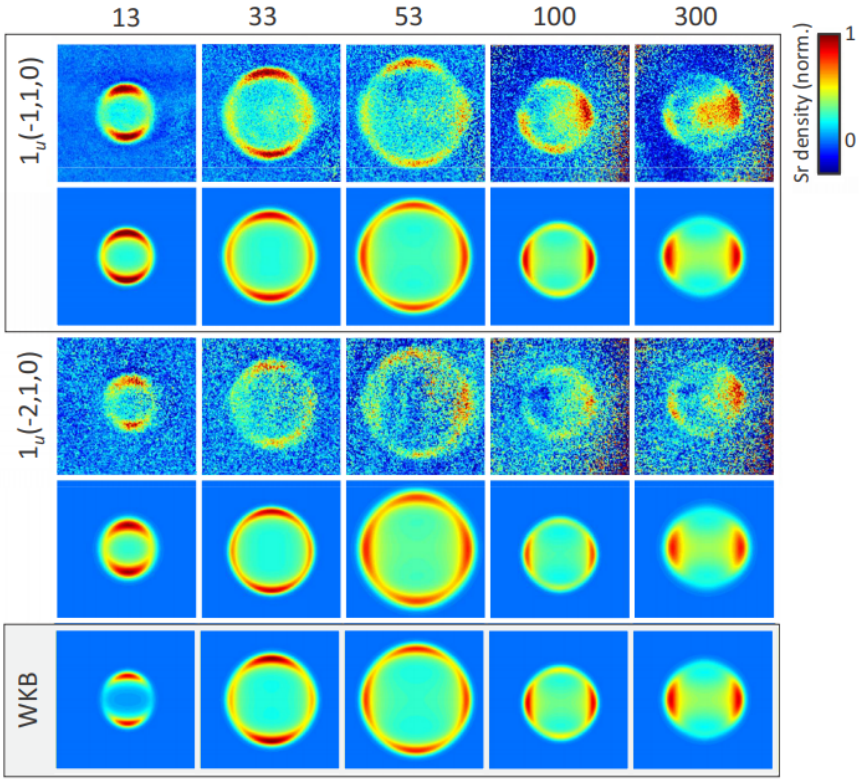

Figure 9.5: Measured and calculated photofragment angular distributions from 1_u molecule dissociation in the ultracold quantum-mechanical regime. For each initial state, the upper and lower rows correspond to measurements and quantum-mechanical theory, respectively. Adapted from [8].

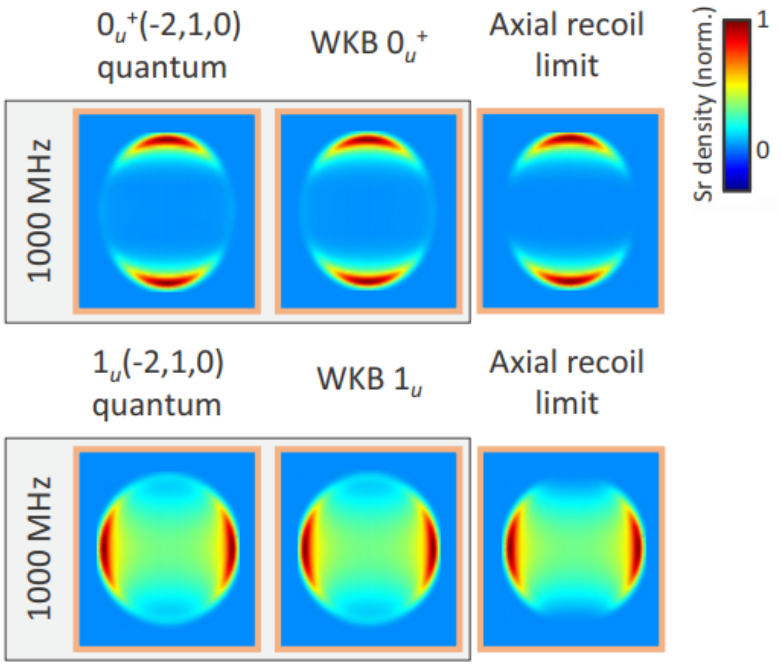

Figure 9.6: Angular distributions calculated for a pair of 0_u^+ and 1_u weakly bound states using both quantum theory and the WKB approximation at a high energy $\varepsilon/h = 1000$ MHz ($\varepsilon/k_B = 48$ mK), to show their close agreement with the appropriate axial-recoil limit. Adapted from [8].

In summary of this section, we find that the quantum-mechanical calculations precisely capture the observed photofragment angular distributions and their dependence on continuum energy. Moreover, the axial-recoil limit is reached at energies that exceed any potential barriers in the continuum and for the cases shown in this section the quasiclassical picture correctly describes the axial-recoil limit. However, it is not certain that the quasiclassical picture would always depict the axial-recoil limit. In the next section we will examine exceptional situations where the quasiclassical model fails to approach the axial recoil limit.

9.2.2 Quasiclassical model failure caused by quantum selection rules

In the previous section we saw a number of cases where the quasiclassical model is equivalent to the axial-recoil limit. However, there are cases where the quasiclassical approximation doesn't asymptote to the axial-recoil limit. We find that these two approaches are equivalent only when the reaction channels are well-defined. For molecules composed of distinguishable bosons or fermions, the reaction channels are always well-defined. However, as elaborated earlier, spin statistics imposes selection rules on allowed reaction channels for molecules composed of identical constituents such as bosonic ^{88}Sr atoms. As a result, in cases where dissociation partial waves are precluded by selection rules, the quasiclassical model would fail to describe the axial-recoil limit, no matter how large the continuum energy is.

We find that the photofragment angular distributions are insensitive to quantum spin statistics *only when* the dissociation laser polarization is parallel to the quantization axis and $\Omega_{inital} = \Omega_{final} = 0$ and $m_{initial} = m_{final} = 0$. In other cases the angular distributions depend on quantum statistics, leading to failure of the quasiclassical picture. In $^{88}Sr_2$ molecules photodissociation from the 1_u molecules with $|P| = 1$ fall into the latter category. Figure 9.7(a) shows the angular distributions of photodissociation from $1_u(-1, 1, 0)$ molecules. Because of the nature of dissociating light polarization, the output channel must have $m_J = 1, -1$. Because of the $\delta m_J = 1$ selection rule for $|P| = 1$ photodissociation of this initial state, only $J = 2$ is possible for the ground-state continuum (odd J are not allowed), and therefore no partial-wave interference or energy dependence is expected. The observations confirm an unchanging angular distribution that matches the quantum mechanical prediction and clearly fails to match the quasiclassical model. Figure 9.7(b) illustrates energy-dependent photodissociation of $1_u(-1, 3, 0)$ molecules. For $1_u(-1, 3, 0)$ molecules, the

near-threshold energy dependence arises from interference of the $J = 2$ and $J = 4$ continuum states. The right-hand panels show the calculated quantum mechanical angular distribution in the axial recoil limit that disagrees with the quasiclassical model. To demonstrate experimental agreement with the quantum mechanical treatment, the left-hand side shows angular distributions at 3.4 and 6.3 mK (70 and 130 MHz) above threshold that matches the calculated distributions in the insets. While the axial recoil regime (>50 mK) was not

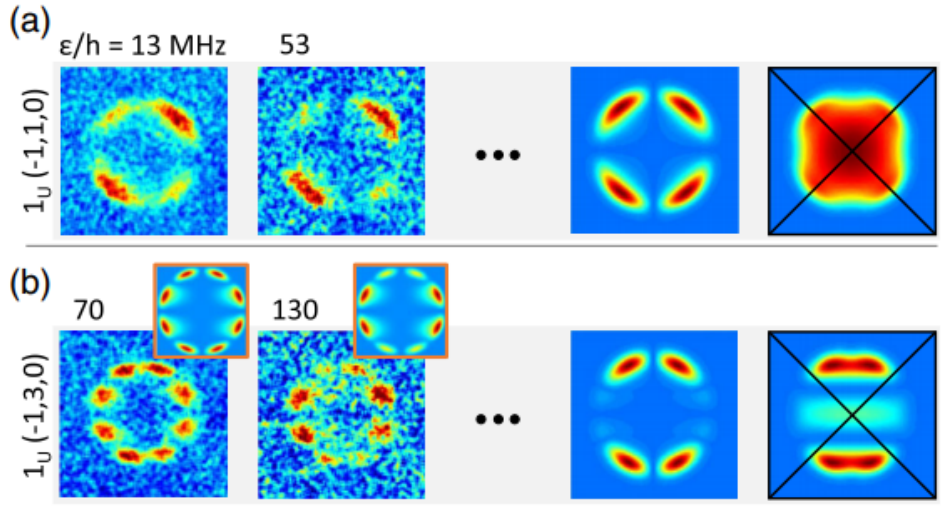

Figure 9.7: Quantum statistics of identical particles prevents agreement with quasiclassical predictions at large photofragment energies. Here $|P| = 1$. (a) Photofragment angular distributions for $1_u(-1, 1, 0)$ molecules at $\varepsilon/k_B = \{0.63, 2.5\}$ mK ($\varepsilon/h = \{13, 53\}$ MHz) on the left along with quantum mechanical and quasiclassical predictions on the right. This case is energy-independent. The quasiclassical picture fails to describe the process due to quantum statistics that leads to the missing $J = 1$ partial wave in the ground-state continuum. (b) Energy-dependent angular distributions for $1_u(-1, 3, 0)$ molecules at $\varepsilon/k_B = \{3.4, 6.3\}$ mK ($\varepsilon/h = \{70, 130\}$ MHz) are on the left, where the insets show the corresponding calculations. High energy quantum mechanical and quasiclassical predictions are on the right. While the highest energy regime could not be reached experimentally, at lower energies the experiment fully agrees with quantum mechanical calculations in the insets. Adapted from [6].

reached in this case due to weak bound-continuum transition strengths and insufficient photodissociation laser power, this limitation is not fundamental. Note that if optical selection rules (rather than spin-statistics restrictions) allow only a single partial wave J in the continuum, then quantum mechanical and quasiclassical angular distributions strictly agree [4].

9.2.3 Characterization of the molecular potential model

A key feature of photodissociation is the ability to select one of many possible continua. In Figure 9.8 we photodissociate ground state $X(-1,0,0)$ molecules to the $\{0_u^+, 1_u\}$ continuum, and sample energies in the range of 0.07–260 mK (1.5–5500 MHz). Here, the electronic potential barrier height is only $\sim$1 mK, being proportional to the very small C_3 dispersion coefficient that is determined by the inverse of the metastable $^3P_1$ atomic lifetime. The photofragments have angular momentum $J = 1$ and two possible $\Omega = \{0, 1\}$ that are mixed via nonadiabatic Coriolis coupling, especially at the lower energies [82]. This mixing has a strong and nontrivial effect on photofragment angular distributions. For the spherically symmetrical initial molecular state, the angular distributions can be described as $I_{QC}(\theta)$ for all continuum energies, but with a varying $\beta_2(\varepsilon)$ that becomes constant at the axial recoil limit.

Figure 9.8 shows the plot of $\beta_2(\varepsilon)$ across a wide energy range that is limited only by the photodissociation laser power, where the smaller error bars arise from the image quality and the larger ones conservatively estimate possible contamination by molecules initially in $J_i = 2$. In the case of mixed Ω in the continuum, the quasiclassical picture does not predict which Ω dominates at high energy and whether the observed pattern tends to a perpendicular dipole (for $\Omega = 1$) or a parallel dipole (for $\Omega = 0$). In this experiment, the *ab initio* pattern tends to a parallel dipole ($\beta_2 = 2$) in the axial recoil limit, but for the very weakly bound

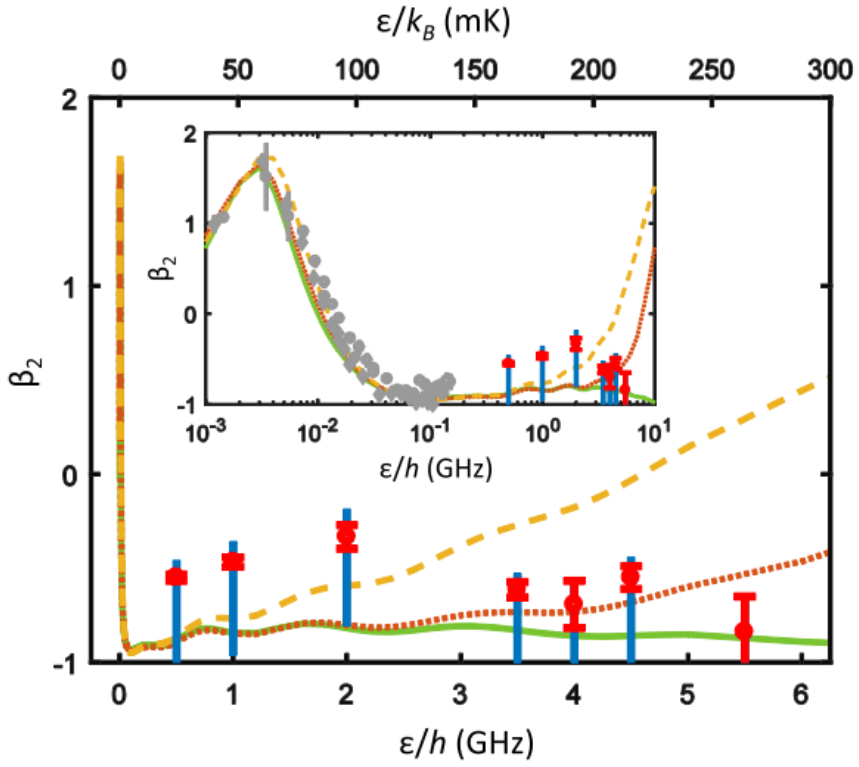

Figure 9.8: Anisotropy parameter β_2 measured for photodissociation of ground-state X(-1,0,0) molecules to the excited $\{0_u^+, 1_u\}$ continuum. Red capped error bars are determined from a bootstrap analysis of up to 1000 experimental realizations, and blue capless error bars result from possible contamination by molecules initially in $J_i = 2$. The dotted red line corresponds to the *ab initio* molecular potential [76], the solid green line to the potential that is optimized to reproduce long-range properties [81], and the dashed yellow line to the *ab initio* potential that was manually fitted for better agreement with measured spectra [83]. Photodissociation of these very weakly bound molecules does not yet reach the high-energy limit of $\beta_2 = 2$ at the accessible continuum energies up to 260 mK (5.5 GHz). The inset shows the high-energy data in the context of previous measurements [4] with improved *ab initio* theory. Adapted from [6].

molecules this regime is expected to be reached only at > 0.5 K above threshold. In the energy regime that is currently accessible, photofragment angular distributions vary steeply with energy in the region of the $\sim$1 mK electronic barrier, then stabilize at $\beta_2 \approx 1$. The energy interval where $\beta_2 \approx 1$ is sensitive to long-range molecular potentials, as we have confirmed by adjusting the C_6 coefficients. The measurements in this energy regime allow us to distinguish between the *ab initio* [76], long-range [81], and fitted ab initio [83] potentials to which the angular distributions are sensitive, as shown in Figure 9.8.

9.3 Summary

In conclusion, we have explored how ultracold, quantum mechanical state-selected photodissociation crosses over into the classical regime at increasing photofragment energies. The question of applicability of quasiclassical descriptions to photodissociation reactions has lingered in the literature for several decades [4, 60–62, 84], and in this work we experimentally access and probe the range of energies where the onset of the quasiclassical regime is expected. Besides, we find that the high-energy axial recoil limit is reached when the continuum energy exceeds any electronic and rotational barriers, although quantum effects can dominate to larger energies for very weakly bound molecules. We experimentally confirm with Sr_2 molecules that the commonly used quasiclassical formula for photofragment angular distributions [58, 59, 84] correctly describes the axial recoil limit for a variety of initial molecular states, while in the ultracold regime there is a strong nonclassical variation of the angular distributions with energy. We demonstrate that the effects of spin statistics for identical photofragments can persist to indefinitely large photodissociation energies and prevent the angular distributions from approaching the quasiclassical picture. We probe a molecular continuum with a mixture of Ω quantum numbers in an energy range of over three orders of

magnitude, distinguishing between the *ab initio* potentials and those that have been adjusted using molecular spectroscopy. Photodissociation of ultracold molecules with isolated quantum states uniquely enables studies of molecular continua, and for relatively simple molecules such as Sr_2, state-of-the-art quantum chemistry theory yields excellent agreement with measurements. These features allow us to directly observe and accurately model the crossover from ultracold to quasiclassical chemistry.

Chapter 10

Conclusions and outlook

In this thesis, I present the progress toward building a molecular lattice clock. Due to the long natural lifetime of the ground states, a two-photon Raman transition between two ground states forms an ideal clock transition that has metrological importance in testing fundamental physics. With Autler-Townes spectroscopy, we have successfully found several deeply bound ground states. Driving Raman transitions between ground states coherently requires eliminating the unbalance in clock states' polarizabilities, which is the heart of lattice clocks. In this thesis, the magic wavelength technique, which was developed for the atomic lattice clock, has been extended to molecules. With the lattice laser frequency tuned near a lattice-driven transition resonance, the polarizability of the bottom clock state can be strongly modified. By measuring the differential light shifts, the magic wavelength has been determined with a precision of $\sim$100 kHz for a couple of lattice-driven transitions. Implementation of a magic lattice trap has enhanced clock coherence by a factor over a thousand and narrowed the clock transition linewidth to 30 Hz, corresponding to a quality factor $Q = 8 \times 10^{11}$. To achieve a more stable environment for the molecular clock, several experimental upgrades have been carried out, which includes master laser frequency stability enhancement, lattice laser light

spectrum cleanup, fiber noise cancellation, and probe laser intensity stabilization.

A question that has remained perplexing is the issue with a short clock state lifetime. When the clock transition is driven with a magic lattice trap, the deeply bound clock state lifetime is observed to be 20 ms, a lot shorter than the collision-imposed lifetime of 140 ms. In this thesis, several hypotheses have been brought up to explain this mystery. Among them, we have initially precluded the possibilities of broad 1_u lattice-driven resonances and multi-photon excitation from the lattice light. So far, the scattering due to the ASE noise in the lattice laser spectrum is the only mechanism that is supported by solid evidence to be a culprit. The most concrete evidence is the lifetime measurement taken with the transmission grating. With the grating implemented to suppress the ASE noise, the clock state lifetime measured with non-magic lattice has increased to the collision-limited level. However, there are also two measurements that cannot be explained by the ASE noise. First, with the spectral clean-up implemented in an attempt to narrow the ASE window even further, the enhancement in clock state lifetime is lower than what was expected by orders of magnitude. Another piece of data that can't be described by ASE scattering is the quadratic dependence on lattice detuning of the clock state lifetime. To explain these observations, detailed modeling of the ASE structure needs to be performed. If the lattice spectrum is confirmed to be the culprit to the lifetime issue, a better high power source with clean spectral background would be necessary for the next generation lattice trapping.

The improvement in the frequency comb is another critical upgrade for achieving a better metrology system. The model of comb that we have been working with has issues with frequency instability. The f_{CEO} lock bandwidth is not high enough so that the entire comb spectrum suffers from a jittering of $\sim$400 kHz. Moreover, the repetition rate lock takes only $1 \times f_{CEO}$ subtraction instead of $2 \times f_{CEO}$, leading to an uncertainty of $\sim$10 mHz in

the repetition rate. This instability can be transferred to spectroscopic lasers and cause an overall uncertainty of ∼2 kHz on the clock transition frequency. To tackle the issues with the jittering f_{CEO}, Menlo System provides an upgrade scheme which allows ultra-low noise f_{CEO} lock. In the near future, this upgrade would be integrated to our comb to help achieve higher spectroscopic laser frequency control.

Apart from upgrading the comb, the future metrology improvement also includes a new ULE cavity which is ready to serve the next generation master laser reference. This new ULE cavity is coated for 780 nm light and allows a narrow laser linewidth of 1 Hz. In the future, the frequency comb will be stabilized to this new frequency reference and the 689 nm laser system will be used only for the red MOT cooling. It is worth mentioning that the new 780 nm light system will also serve as the first Raman laser for future clock transitions. Due to the weak transition strengths from the absolute ground state to weakly bound excited states, driving clock transition to $X(0,0)$ state via a weakly bound intermediate state implies an extremely unbalanced probe laser intensity ratio, which would add difficulties to the experiment. Instead, an intermediately bound excited state will be employed for the Raman transition, as illustrated in Figure 10.1.

For the future metrology experiments, the design of the magic lattice trap would need a slight adjustment. In this thesis, the lattice laser modifies the polarizability of the bottom clock state. However, in order to map out all the molecular states in the ground state potential, this is inconvenient because each ground state requires its own lattice-driven transition. Therefore, if the polarizability of an initial clock state can be tuned with a proper lattice-driven transition, the binding energy measurements would be much more convenient.

After the metrology system is fully developed with $^{88}Sr_2$ molecules, the techniques will be extended to other isotopes. To perform experiments with different isotopes, enhanced Sr

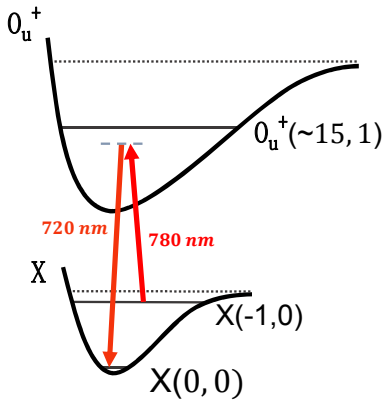

Figure 10.1: Clock transition between the least bound and the deepest bound ground state.

samples may be required. In the current oven, the isotopic abundance is low except for ^{88}Sr. Laser cooling and spectroscopy with other isotopes are pretty close to that with $^{88}Sr_2$ and have been demonstrated in a variety of experiments [85–87], which can be a guide to future measurements with the molecular clock.

Bibliography

[1] M. S. Safronova, D. Budker, D. DeMille, Derek F. Jackson Kimball, A. Derevianko, and Charles W. Clark *Search for new physics with atoms and molecules* Review of Modern Physics **90**, 025008 (2018)

[2] Cheng Chin and V. V. Flambaum *Enhanced Sensitivity to Fundamental Constants In Ultracold Atomic and Molecular Systems near Feshbach Resonances* Physical Review Letters **96**, 230801 (2006)

[3] G. Edward Marti, Ross B. Hutson, Akihisa Goban, Sara L. Campbell, Nicola Poli, and Jun Ye *Imaging Optical Frequencies with 100 μHz Precision and 1.1 μm Resolution.* Physical Review Letters **120**, 103201 (2018)

[4] M. McDonald, B. H. McGuyer, F. Apfelbeck, C.-H. Lee, I. Majewska, R. Moszynski, and T. Zelevinsky *Photodissociation of ultracold diatomic strontium molecules with quantum state control* Nature **535**, 122 (2016)

[5] M. McDonald, I. Majewska, C.-H. Lee, S. S. Kondov, B. H. McGuyer, R. Moszynski, and T. Zelevinsky *Control of ultracold photodissociation with magnetic fields* Physical Review Letters **120**, 033201 (2018)

[6] S. S. Kondov, C.-H. Lee, M. McDonald, B. H. McGuyer, I. Majewska, R. Moszynski, and T. Zelevinsky *Crossover from the ultracold to the quasiclassical regime in state-selected photodissociation* Physical Review Letters **121** 143401 (2018)

[7] T. Zelevinsky, S. Kotochigova, and Jun Ye *Precision Test of Mass-Ratio Variations with Lattice-Confined Ultracold Molecules* Physical Review Letters **100**, 4 (2008)

[8] I. Majewska, S. S. Kondov, C.-H. Lee, M. McDonald, B. H. McGuyer, R. Moszynski, and T. Zelevinsky *Experimental and theoretical investigation of the crossover from the ultracold to the quasiclassical regime of photodissociation* Physical Review A **98**, 043404 (2018)

[9] S. S. Kondov, C.-H. Lee, K. H. Leung, C. Liedl, I. Majewska, R. Moszynski, and T. Zelevinsky *Molecular lattice clock with long vibrational coherence* Nature Physics **15**, 1118 (2019)

[10] B. H. McGuyer, M. McDonald, G. Z. Iwata, M. G. Tarallo, W. Skomorowski, R. Moszynski, and T. Zelevinsky *Precise Study of Asymptotic Physics with Subradiant Ultracold Molecules* Nature Physics, **11**, 32 (2015)

[11] G. Herzberg *Molecular Spectra and Molecular Structure, Vol. I: Spectra of Diatomic Molecules* Van Nostrand, New York (1950)

[12] C. J. Foot *Atomic Physics* Oxford, London (1996)

[13] M. McDonald, B. H. McGuyer, G. Z. Iwata, and T. Zelevinsky *Thermometry via Light Shifts in Optical Lattices* Physical Review Letters **114**, 023001 (2015)

[14] M. McDonald *High precision optical spectroscopy and quantum state selected photodissociation of ultracold* $^{88}Sr_2$ *molecules in an optical lattice* Ph.D. thesis, Columbia University (2016)

[15] F. Apfelbeck *Photodissociation dynamics of ultracold strontium dimers* Master thesis, Columbia University (2015)

[16] C. B. Osborn *The physics of ultracold* Sr_2 *molecules: optical production and precision measurement* Ph.D. thesis, Columbia University (2014)

[17] C. Liedl *A molecular lattice clock* Master thesis, Columbia University (2018)

[18] D. W. Preston *Doppler-free saturated absorption: Laser spectroscopy* American Journal of Physics, **64**, 1432 (1996)

[19] K. B. MacAdam, A. Steinbach, and C. Wieman *A narrow-band tunable diode laser system with grating feedback, and a saturated absorption spectrometer for Cs and Rb* American Journal of Physics, **60**:1098–1098 (1992)

[20] C. Wieman, and T. W. Hänsch *Doppler-free laser polarization spectroscopy* Physical Review Letters, **36**, 1170 (1976)

[21] R. L. Targat, J.J Zondy, and P. Lemonde *75%-efficiency blue generation from an intracavity ppktp frequency doubler* Optics Communications **247**(4):471–481 (2005)

[22] A. Hemmerich, D. H. McIntyre, C Zimmermann, and T. W. Hänsch *Secondharmonic generation and optical stabilization of a diode laser in an external ring resonator* Optics letters, **15**(7):372–374 (1990)

[23] T. Ido, and H. Katori *Recoil-free spectroscopy of neutral Sr atoms in the Lamb-Dicke regime* Physical Review Letters, **91**, 053001 (2003)

[24] A. D. Ludlow *The Strontium Optical Lattice Clock: Optical Spectroscopy with Sub-Hertz Accuracy* Ph.D. thesis, University of Colorado at Boulder (2008)

[25] A. Ludlow *The Strontium Optical Lattice Clock: Optical Spectroscopy with Sub-Hertz Accuracy* Ph.D. thesis, University of Colorado (2008)

[26] S. K. Lee, and H.-W. Lee *Damped Population Oscillation in a Spontaneously Decaying Two-Level Atom Coupled to a Monochromatic Field* Physical Review A **74**, 063817 (2006)

[27] H.-R. Noh, and W. Jhe *Analytic solutions of the optical Bloch equations* Optics Communications, **283**, 11 (2010)

[28] S. Blatt, J. W. Thomsen, G. K. Campbell, A. D. Ludlow, M. D. Swallows, M. J. Martin, M. M. Boyd, and J. Ye *Rabi spectroscopy and excitation inhomogeneity in a one-dimensional optical lattice clock* Physical Review A **80**, 052703 (2009)

[29] T. H. Stievater, Xiaoqin Li, D. G. Steel, D. Gammon, D. S. Katzer, D. Park, C. Piermarocchi, and L. J. Sham *Rabi Oscillations of Excitons in Single Quantum Dots* Physical Review Letters **87**, 133603 (2001)

[30] Y. O. Dudin, L. Li, F. Bariani, and A. Kuzmich *Observation of coherent many-body Rabi oscillations* Nature Physics **8**, 790–794 (2012)

[31] Z. W. Barber, J. E. Stalnaker, N. D. Lemke, N. Poli, C. W. Oates, T. M. Fortier, S. A. Diddams, L. Hollberg, C. W. Hoyt, A. V. Taichenachev, and V. I. Yudin *Optical lattice induced light shifts in an Yb atomic clock* Physical Review Letters **100**, 103002 (2008)

[32] M. Boyd, T. Zelevinsky, A. Ludlow, S. Foreman, S. Blatt, T. Ido, and J. Ye *Optical Atomic Coherence at the 1-Second Time Scale* Science **314**, 1430 (2006)

[33] M. Takamoto, F.-L. Hong, R. Higashi, and H. Katori *An optical lattice clock* Nature **435**, 321–324 (2005)

[34] T. Legero, T. Kessler, and U. Sterr *Tuning the thermal expansion properties of optical reference cavities with fused silica mirrors* Journal of the Optical Society of America B **27**, 5 (2010)

[35] I. Ito, A Silva, T. Nakamura, and Y. Kobayashi *Stable CW laser based on low thermal expansion ceramic cavity with 4.9 mHz/s frequency drift* Optical Express **25**, 21 (2017)

[36] A. C. Wilson, J. C. Sharpe, C. R. McKenzie, P. J. Manson, and D. M. Warrington *Narrow-linewidth master-oscillator power amplifier based on a semiconductor tapered amplifier* Applied Optics **37**, 21 (1998)

[37] D. Voigt, E.C. Schilder, R.J.C. Spreeuw, and H.B. van Linden van den Heuvell *Characterization of a high-power tapered semiconductor amplifier system* Applied Physics B **72**, 3 (2001)

[38] E. Ji, Q. Liu, M. Nie, X. Fu, and M. Gong *Theoretical and experimental analysis of high-power frequency-stabilized semiconductor master oscillator power-amplifier system* Applied Optics **55**, 11 (2016)

[39] E. Gehrig, and O. Hess *Spatio-temporal dynamics of light amplification and amplified spontaneous emission in high-power tapered semiconductor laser amplifiers* IEEE Journal of Quantum Electronics, **37**, 10 (2001)

[40] L.-S. Ma, P. Jungner, J. Ye, and J. L. Hall *Accurate cancellation (to millihertz levels) of optical phase noise due to vibration or insertion phase in fiber-transmitted light* Photonics West, pages 165–175 (1995)

[41] L.-S. Ma, P. Jungner, J. Ye, and J. L. Hall *Delivering the same optical frequency at two places: accurate cancellation of phase noise introduced by an optical fiber or other time-varying path* Optics letters **19**, 21 (1994)

[42] B. E. A. Saleh, and M. C. Teich *Fundamentals of Photonics* Second Edition Wiley, Boston (2009)

[43] T. Okoshi, K. Kikuchi, and A. Nakayama *Novel method for high resolution measurement of laser output spectrum* Electronics Letters **16**, 16 (1980)

[44] B. J. Bloom, T. L. Nicholson, J. R. Williams, S. L. Campbell, M. Bishof, X. Zhang, W. Zhang, S. L. Bromley, and J. Ye *An optical lattice clock with accuracy and stability at the* 10^{-18} *level* Nature **506**, 71-75 (2014)

[45] T.L. Nicholson, S.L. Campbell, R.B. Hutson, G.E. Marti, B.J. Bloom, R.L. McNally, W. Zhang, M.D. Barrett, M.S. Safronova, G.F. Strouse, W.L. Tew, and J. Ye *Systematic evaluation of an atomic clock at* 2×10^{-18} *total uncertainty* Nature Communications **6**, 6896 (2015)

[46] K. Szymaniec, W. Chałupczak, E. Tiesinga, C. J. Williams, S. Weyers, and R. Wynands *Cancellation of the Collisional Frequency Shift in Caesium Fountain Clocks* Physical Review Letters **98**, 153002 (2007)

[47] A. C. Vutha, T. Kirchner, and P. Dubé *The collisional frequency shift of a trapped-ion optical clock* Physical Review A 96, 022704 (2017)

[48] A. M. Rey, A. V. Gorshkov, and C. Rubbo *Many-body treatment of the collisional frequency shift in fermionic atoms* Physical Review Letters 103, 260402 (2009)

[49] K. Gibble *Decoherence and collisional frequency shifts of trapped bosons and fermions* Physical Review Letters, **103**, 113202 (2009)

[50] M.D. Swallows, M. Bishof, Y. Lin, S. Blatt, M.J. Martin, A.M. Rey, and J. Ye *Suppression of collisional shifts in a strongly interacting lattice clock* Science, **331**, 1043–1046 (2011)

[51] G. K. Campbell, M. M. Boyd, J. W. Thomsen, M. J. Martin, S. Blatt, M. D. Swallows, T. L. Nicholson, T. Fortier, C. W. Oates, S. A. Diddams, N. D. Lemke, P. Naidon, P. Julienne, Jun Ye, and A. D. Ludlow *Probing Interactions Between Ultracold Fermions* Science **324**, 5925 (2009)

[52] R. Grimm, M. Weidemüller, and Y. B. Ovchinnikov *Optical dipole traps for neutral atoms* Advances In Atomic, Molecular, and Optical Physics **42** (2000)

[53] Y. Miroshnychenko, W. Alt, I. Dotsenko, L. Förster, M. Khudaverdyan, D. Meschede, D. Schrader, and A. Rauschenbeutel *An atom-sorting machine* Nature **442**, 151 (2006)

[54] Ch. Lisdat, J. S. R. Vellore Winfred, T. Middelmann, F. Riehle, and U. Sterr *Collisional losses, decoherence, and frequency shifts in optical lattice clocks with bosons* Physical Review Letters **103**, 090801 (2009)

[55] J. E. Bjorkholrn *Collision-limited lifetimes of atom traps* Physical Review A **38**, 3 (1988)

[56] A. Traverso, R. Chakraborty, Y. N. Martinez de Escobar, P. G. Mickelson, S. B. Nagel, M. Yan, and T. C. Killian *Inelastic and elastic collision rates for triplet states of ultracold strontium* Physical Review A **79**, 060702(R) (2009)

[57] H. Friedrich *Scattering Theory* Springer, Heidelberg (2013).

[58] S. E. Choi, and R. B. Bernstein *Theory of oriented symmetric-top molecule beams: precession, degree of orientation, and photofragmentation of rotationally state-selected molecules* The Journal of Chemical Physics **85**, 150–161 (1986)

[59] R. N. Zare *Photofragment angular distributions from oriented symmetric-top precursor molecules* Chemical Physics Letters **156**, 1–6 (1989)

[60] J. A. Beswick, and R. N. Zare *On the quantum and quasiclassical angular distributions of photofragments* The Journal of Chemical Physics **129**, 164315 (2008)

[61] R. N. Zare, and D. R. Herschbach *Doppler line shape of atomic fluorescence excited by molecular photodissociation* Proceedings of the IEEE **51**, 173–182 (1963)

[62] R. N. Zare *Photoejection dynamics* Molecular Photochemistry **4**, 1–37 (1972)

[63] D. Baugh, D. Kim, V. Cho, L. Pipes, J. Petteway, and C. Fuglesang *Production of a pure, single ro-vibrational quantum-state molecular beam* Chemical Physics Letters **219**, 3 (1994)

[64] G. Bazalgette, R. White, G. Trenec, E. Audouard, M. Büchner, and J. Vigué *Photodissociation of ICl molecule oriented by an intense electric field: Experiment and theoretical analysis* The Journal of Physical Chemistry A **102**, 7 (1998)

[65] L. Pipes, N. Brandstater, C. Fuglesang, and D. Baugh *Photofragmentation of M-state polarized molecules: Comparison of quantum and semiclassical treatments* The Journal of Physical Chemistry A **101**, 41 (1997)

[66] A. Carrington, and J. M. Brown *Rotational Spectroscopy Of Diatomic Molecules* Cambridge University Press (2004)

[67] N.F.Stepanov, and B. I.Zhilinskii *When and why Hund's cases arise* Journal of Molecular Spectroscopy **52**, 2 (1974)

[68] R. Ciurylo, E. Tiesinga, S. Kotochigova, and P. S. Julienne *Photoassociation spectroscopy of cold alkaline-earth-metal atoms near the intercombination line* Physical Review A **70**, 062710 (2004).

[69] K. M. Jones, E. Tiesinga, P. D. Lett, and P. S. Julienne *Ultracold photoassociation spectroscopy: Long-range molecules and atomic scattering* Review of Modern Physics **78**, 483 (2006)

[70] J. Ulmanis, J. Deiglmayr, M. Repp, R. Wester, and M. Weidemüller *Ultracold Molecules Formed by Photoassociation: Heteronuclear Dimers, Inelastic Collisions, and Interactions with Ultrashort Laser Pulses* Chemical Reviews **112**, 1890 (2012)

[71] G. Reinaudi, C. B. Osborn, M. McDonald, S. Kotochigova, and T. Zelevinsky *Optical Production of Stable Ultracold* $^{88}Sr_2$ *Molecules* Physical Review Letters **109**, 115303 (2012)

[72] A. Derevianko, and H. Katori *Colloquium: Physics of optical lattice clocks* Review of Modern Physics **83**, 2015 (2011)

[73] J. Ye, H. J. Kimble, and H. Katori *Quantum State Engineering and Precision Metrology Using State-Insensitive Light Traps* Science **320**, 1734 (2008)

[74] K. M. Jones, E. Tiesinga, P. D. Lett, and P. S. Julienne *Ultracold photoassociation spectroscopy: Long-range molecules and atomic scattering* Reviews of Modern Physics **78**, 2 (2006)

[75] B. H. McGuyer, M. McDonald, G. Z. Iwata, M. G. Tarallo, A. T. Grier, F. Apfelbeck, and T. Zelevinsky *High-precision spectroscopy of ultracold molecules in an optical lattice* New Journal of Physics **17**, 5 (2015)

[76] W. Skomorowski, F. Pawłowski, C. P. Koch, and R. Moszynski Rovibrational dynamics of the strontium molecule in the $A^1\Sigma_u^+$, $c^3\Pi_u$, and $a^3\Sigma_u^+$ manifold from state-of-art *ab initio* calculations The Journal of Chemical Physics **136**, 19 (2012)

[77] J. Ye, and S. T. Cundiff *Femtosecond optical frequency comb: principle, operation and applications* Springer Science and Business Media, (2005)

[78] N. Picqué, and T. W. Hänsch *Frequency comb spectroscopy* Nature Photonics **13**, 146–157 (2019)

[79] B. Widiyatmoko, K. Imai, M. Kourogi, and M. Ohtsu *Second-harmonic generation of an optical frequency comb at 1.55 μm with periodically poled lithium niobate* Optics letters **24.5** (1999)

[80] G. Ferrari, P. Cancio, R. Drullinger, G. Giusfredi, N. Poli, M. Prevedelli, C. Toninelli, and G. M. Tino *Precision Frequency Measurement of Visible Intercombination Lines of Strontium* Physical Review Letters **91**, 243002 (2003)

[81] M. Borkowski, P. Morzyński, R. Ciuryło, P. S. Julienne, M. Yan, B. J. DeSalvo, and T. C. Killian *Mass scaling and nonadiabatic effects in photoassociation spectroscopy of ultracold strontium atoms* Physical Review A **90**, 032713 (2014)

[82] B. H. McGuyer, C. B. Osborn, M. McDonald, G. Reinaudi, W. Skomorowski, R. Moszynski, and T. Zelevinsky *Nonadiabatic Effects in Ultracold Molecules via Anomalous Linear and Quadratic Zeeman Shifts* Physical Review Letters **111**, 243003 (2013).

[83] B. H. McGuyer, M. McDonald, G. Z. Iwata, M. G. Tarallo, A. T. Grier, F. Apfelbeck, and T. Zelevinsky *High-precision spectroscopy of ultracold molecules in an optical lattice* New Journal of Physics **17**, 055004 (2015)

[84] T. Seideman *The analysis of magnetic-state-selected angular distributions: A quantum mechanical form and an asymptotic approximation* Chemical Physical Letters **253**, 279 (1996)

[85] Y. N. Martinez de Escobar, P. G. Mickelson, M. Yan, B. J. DeSalvo, S. B. Nagel, and T. C. Killian *Bose-Einstein Condensation of* ^{84}Sr Physical Review Letters **103**, 200402 (2009)

[86] J. A. Aman, J. C. Hill, R. Ding, Kaden R. A. Hazzard, and T. C. Killian *Photoassociative Spectroscopy of a Halo Molecule in* ^{86}Sr Physical Review A **98**, 053441 (2018)

[87] F. Sorrentino, G. Ferrari, N. Poli, R. Drullinger, and G. M. Tino *Laser cooling and trapping of atomic strontium for ultracold atom physics, high-precision spectroscopy and quantum sensors* Modern Physics Letters B **20**, 1287 (2006)

Appendix A

Atomic shutter replacement

The atomic shutter is installed after the Sr oven to prevent hot atoms from disturbing the optical lattice loading. For a typical data-taking month, the shutter usually opens and closes over 40,000 times and therefore there is no guarantee that the shutter can last forever. The last time it broke down was in July 2016, which caused a five-month delay on the experiment. Thankfully no permanent damage was incurred on the experimental system. Since that event, some preventative steps have been developed to make fixing the future shutter failure (hopefully never!) easier.

Figure A.1 includes the critical components around the atomic shutter area.

- The oven is heated by four heating elements and wrapped by a couple layers of aluminum foils. The heating elements are powered by variacs.
- The oven valve (SG0063MCCF from Kurt J. Lesker) is installed right after the microtubule array. The purpose of this valve is to prevent the Sr oven from being contaminated by air when the vacuum is open. It is left open at normal time. Note that the highest bakeable temperature for this valve is 150°C.
- The triple flange is where the atomic shutter is. The shutter (L-0385 from Uniblitz)

sits in the middle flange, which design is shown in Figure A.2. This model of shutter is normally closed, which means it takes current to make it open. The drawing for the atomic shutter is shown in Figure A.3.

- The chamber valve is installed before the Zeeman slower tube. During the time when the experiment is off, this valve is closed to prevent the Zeeman slower window from being coated by Sr atoms.

- There are three ion pumps in place to maintain the vacuum. The one circled in Figure A.4 takes care of the region before the chamber valve.

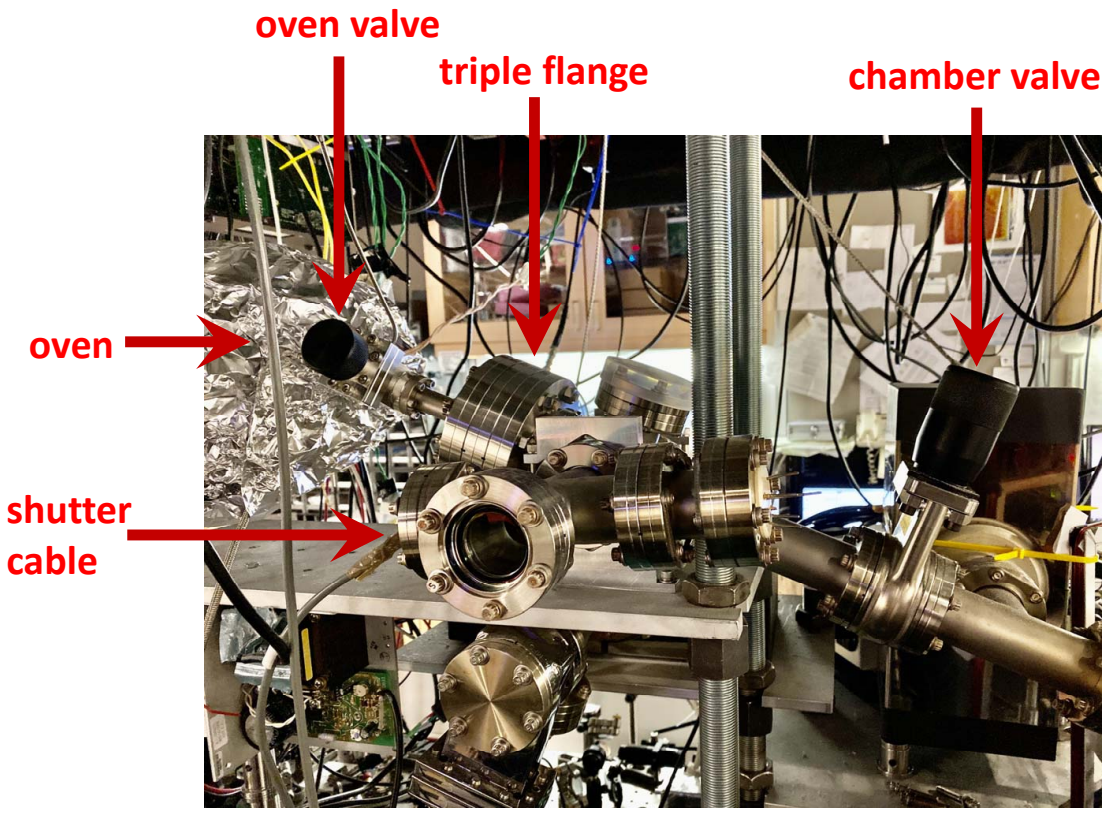

Figure A.1: Critical components near the atomic shutter area.

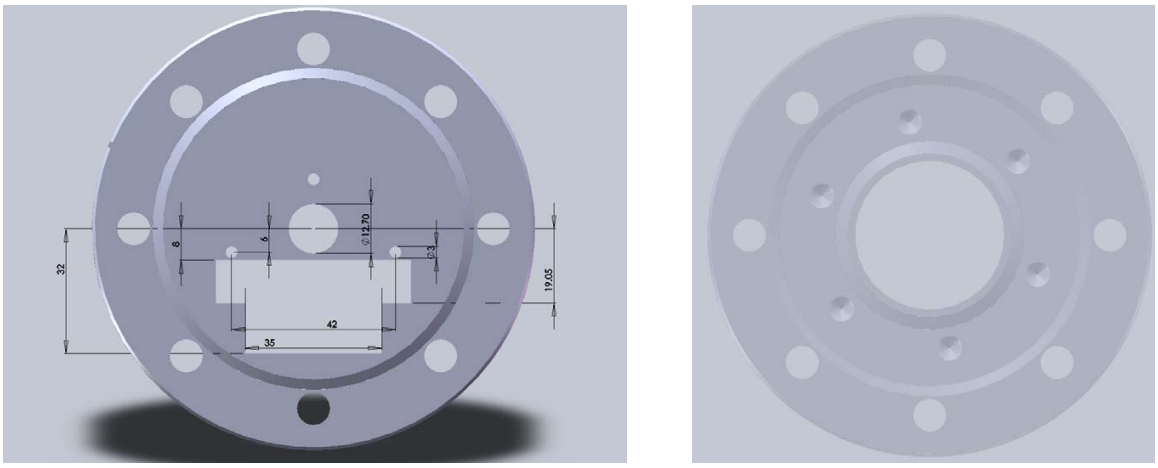

Figure A.2: Design drawing of the triple flange

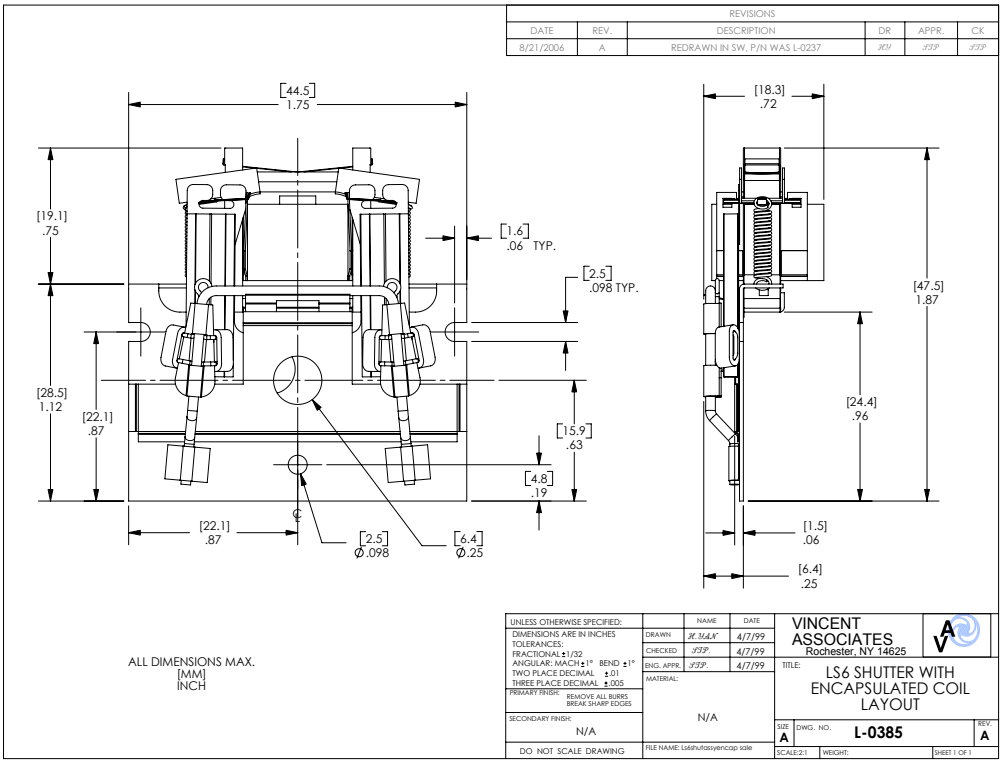

Figure A.3: Design drawing of the atomic shutter

Figure A.4: The ion pump circled in dashed red line takes care of the region before the chamber valve. On the left side of this figure is another ion pump, which takes care of the Zeeman slower tube area.

A.1 Diagnosis of shutter performance

When the atomic shutter misbehaves, its consequence is very obvious. It could occasionally skip few cycles or it could fail to open fully. In the former situation, it's most likely the shutter is stuck by Sr atoms. Gently hitting the triple flange with a wrench could help making it work again. However, if the situation appears to be worse, several checkpoints could help diagnosing the shutter condition.

If the shutter is alive,

- a click sound should be clearly heard when clicking the "Sr shutter" button in the

sequencer.

- the blue fluorescence should be observed when a resonant 461 nm light goes through the Zeeman slower window.

- a resistance of 50 Ohm should be measured across the shutter cables.

If it fails all these tests, the shutter needs to be replaced.

A.2 Shutter replacement procedure

The following is the suggested procedure to replace the shutter along with some lessons learned from the last shutter event.

- First things first, close the chamber valve and keep it closed until whole the replacement procedure is finished. Also, set up a vacuum monitor for the downstream areas. During the shutter replacing process, some gas and dust may leak into the downstream vacuum so it is important to have a vacuum monitor telling what's going on. The vacuum status

Figure A.5: The vacuum status can be monitored with high sensitivity from the ion pump voltage output reading. The vacuum level is indicated by the offset of the voltage output.

can be monitored with high sensitivity from the voltage output of the ion pump controller. Figure A.5 shows the ion pump reading for a well-maintained vacuum.

- Before opening the vacuum, the Sr oven has to be cooled down to room temperature. To prevent detrimental microtube clogging, it is suggested to crank down the temperature very slowly (over ∼5 hours). Also, during the cooling process, it has to be ensured that the nozzle temperature remains the highest among all the other parts of the oven.

- After the oven is completely cooled down, turn off the ion pump that is in charge of the shutter area.

- Then, close the oven valve and slowly remove the oven from the vacuum system. In this process, the vacuum reading in the downstream area may increase a little bit. Keep a close eye on that and make sure no serious leaking develops.

- Loosen the triple flange and take out the shutter. Then loosen the side feedthrough where the shutter cables come out and then disconnect the cables from the feedthrough, see Figure A.6. The shutter cables may need to be cut out because they are tightly glued on the vacuum wall.

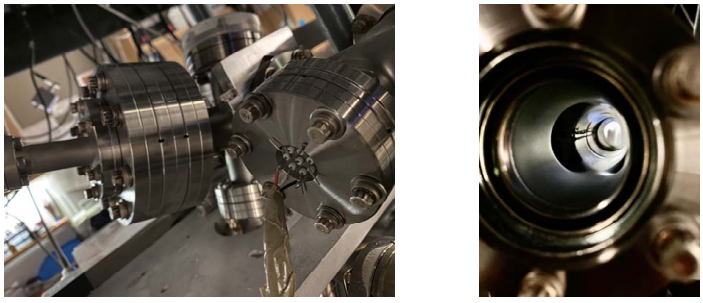

Figure A.6: The side feedthrough (left) and shutter cables (right) viewed from the transverse viewport.

- Replace the shutter and prepare *vacuum compatible glue* which will be used to attach the new shutter cables to the vacuum wall. Then connect the new shutter cables to the feedthrough. The polarity matters so be careful.

- Tighten the feedthrough and glue the shutter cables to the vacuum wall, then tighten up the triple flange.

- Put the Sr oven back and place the thermal sensors properly underneath the heating elements. It is crucial to confirm that the sensors are in good contact with the oven otherwise the inaccurate reading may cause harmful effect on the oven and Sr cells.

- Set up the vacuum gauge and turbo/scroll pumps through the connection underneath the feedthrough.

- Now the vacuum system is ready to be baked. To achieve better vacuum, the ion pump should also be baked. To do this, take out the ion pump magnets and cover the pump with heating elements and aluminum foils.

- A vacuum of 10^{-7} Torr is sufficiently good for this region. To reach this vacuum level, a continuous baking over a week is usually required. As the baking proceeds, the vacuum reading in both the shutter and the downstream areas should gradually drop.

- When the baking finishes, confirm the vacuum is stable and that there is no leaking. If everything is in good condition, it's done!

Appendix B

Measurements of laser beam size

To discuss the measurement of beam size let's first summarize the optics that directs the laser beams into the science vacuum chamber. A schematic for the optics layout is shown in Figure B.1. In our experiment the infrared lattice light and visible red probe laser beams are merged at a dichroic mirror. After being merged, the combined beams pass through a viewport lens that focuses the lattice beam at the molecule cloud. The lattice beam waist is tightly focused to 30 μm at the cloud while the probe laser beam waist is typically $\sim$150 μm. At the back of the chamber a second viewport lens is placed to reinstate the lattice beam

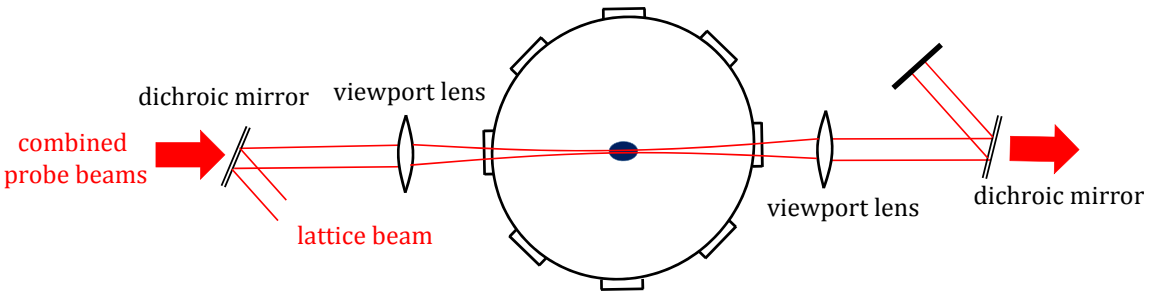

Figure B.1: A schematic for the optics layout.

collimation and another dichroic mirror separates the lattice and probe beams so that only the lattice beam is retro-reflected back into the chamber.

To measure the laser beam size, a mirror is placed between the first viewport lens and the chamber to detour the laser beam into a CMOS camera, shown in Figure B.2. The camera records the intensity profile of the laser beam from which the beam waist can then be obtained. In order to faithfully measure the beam waist that trapped molecules see, the camera needs to be placed at the position where the distance from the lens to the camera is equal to that from the lens to the trapped molecules. This is achieved by calibrating the camera position with the lattice beam. Because lattice trapping takes place where the laser intensity is maximized, the proper camera position can be determined by moving the camera back and forth until reaching the point where the lattice is focused.

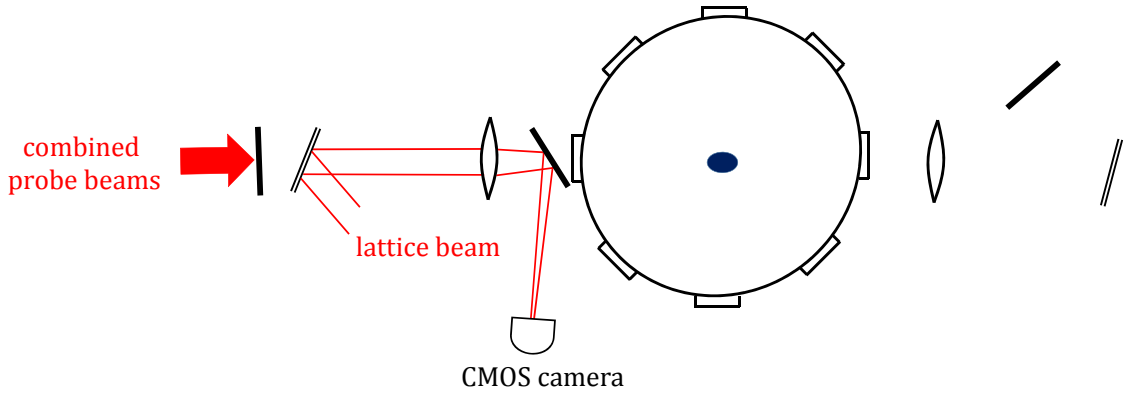

Figure B.2: Schematic for the measuring the laser beam waist. A mirror is placed between the first viewport lens and the chamber to detour the laser beam of interest into a CMOS camera, which records the laser beam intensity profile. The proper camera position is determined by finding the lattice laser focus point on the camera.

With the camera position calibrated the laser beam waist can be faithfully measured. Figure B.3 demonstrates an example where the intensity profile of a probe laser is recorded by the camera. When recording the intensity profile, it must be assured that the laser intensity is an optimal range. Too little power in the laser light would lead to a large uncertainty in the beam waist estimation whereas too much power would saturate the camera and lead to an incorrect estimation.

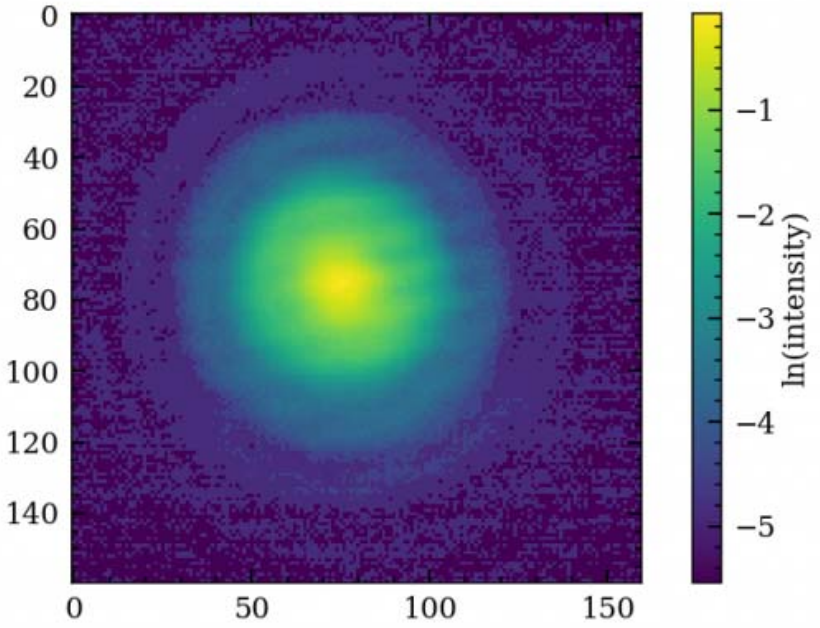

Figure B.3: An example where the intensity profile from a 689 nm laser beam is recorded by the camera. The figure dimensions are in the unit of pixel.

By fitting the intensity profile to the standard Gaussian formula, Equation B.1, the intensity distribution width can be backed out,

$$I(r) = I_0 e^{-r^2/2\sigma^2} \tag{B.1}$$

Note that the width σ in Equation B.1 is not the beam waist. By definition the beam waist w is defined with electric field via

$$E(r) = E_0 e^{-r^2/w^2} \tag{B.2}$$

Comparing these and recalling Equation 7.3 which says $I \propto E^2$, we get

$$w = 2\sigma \tag{B.3}$$

Lastly, the beam waist in the unit of pixel can be converted into the unit of μm by adapting the Thorlabs CMOS pixel size conversion 1 px = 5.2 μm.

In short, the laser beam waist measurement can be summarized into the following procedure, assuming the lattice and probe beams are collinear:

1. Turn down the laser powers, especially the lattice light, to protect the CMOS camera and researchers' eyes.

2. Place a mirror after the viewport lens to detour the beams onto the CMOS camera.

3. Block the probe laser beams and put the camera at the focus of the lattice light.

4. Record the intensity profile of the laser beam of interest and fit it to a Gaussian formula to get the intensity distribution width σ(px).

5. Obtain the beam waist via $w(\mu\text{m}) = 2 \times 5.2(\mu\text{m/px}) \times \sigma(\text{px})$.